Phase Behavior and Nonclassical Crystallization of Protein Solutions with Multivalent Salts

Dissertation

der Mathematisch-Naturwissenschaftlichen Fakultät

der Eberhard Karls Universität Tübingen

zur Erlangung des Grades eines

Doktors der Naturwissenschaften

(Dr. rer. nat.)

vorgelegt von

Ralph Andreas Maier

aus Singen am Hohentwiel

Tübingen

2022

Gedruckt mit Genehmigung der Mathematisch-Naturwissenschaftlichen Fakultät der Eberhard Karls Universität Tübingen.

Tag der mündlichen Qualifikation:	25.07.2022
Dekan:	Prof. Dr. Thilo Stehle
1. Berichterstatter:	PD Dr. Fajun Zhang
2. Berichterstatter:	Prof. Dr. Roland Roth

Contents

Abstract **9**

Zusammenfassung in deutscher Sprache **13**

I Introduction **17**
1.1 The universal relevance of crystallization 19
1.2 Protein-monovalent ion interactions 20
1.3 Soft matter phase behavior with multivalent salts 20
1.4 The crystallization pathway: classical vs nonclassical nucleation theory 21
1.4.1 Classical crystallization 22
1.4.2 Nonclassical crystallization 23
1.5 Crystallization of proteins vs small molecules/atoms 28
1.6 Membrane proteins 29

II Outline **31**

III Basic principles of small-angle X-ray and neutron scattering **35**

IV Protein crystallization in the presence of a metastable liquid-liquid phase separation **41**
4.1 Abstract 43
4.2 Introduction 44
4.3 Experiments and methods 47
4.3.1 Materials and sample preparation 47
4.3.2 Methods 47
4.3.3 Determination of the phase diagram 48
4.4 Results and discussion 49
4.4.1 Experimental phase diagram of the HSA-$CeCl_3$ system at room temperature 49
4.4.2 Crystal growth with unstable LLPS – Path 1 51

4.4.3 Crystal growth with a metastable LLPS – Path 2 55
4.4.4 Discussion of the role of metastable LLPS for protein crystallization 60
4.4.5 Crystal structure of HSA-Y^{3+} crystals by single crystal X-ray diffraction and the role of multivalent metal ions 61
4.5 Conclusions 65

V Human versus bovine serum albumin: A subtle difference in hydrophobicity leads to large differences in bulk and interface behavior 67
5.1 Abstract 69
5.2 Introduction 70
5.3 Experiments and Methods 71
5.3.1 Materials and sample preparation 71
5.3.2 Determination of the phase diagram 71
5.3.3 Optical microscopy 72
5.3.4 Small-angle X-ray scattering (SAXS) 72
5.3.5 Quartz-crystal microbalance with dissipation (QCM-D) 74
5.4 Results and discussion 74
5.4.1 Phase diagram 74
5.4.2 Crystallization 76
5.4.3 Effective bulk interaction characterized by SAXS 76
5.4.4 Adsorption studied by QCM-D 80
5.4.5 Discussion 83
5.5 Conclusions 85

VI Protein crystallization from a preordered metastable intermediate phase followed by real-time small-angle neutron scattering 87
6.1 Abstract 89
6.2 Introduction 90
6.3 Experimental section 91
6.3.1 Materials and sample preparation 91
6.3.2 Optical microscopy 92
6.3.3 Small-angle neutron scattering (SANS) 92
6.4 Results and discussion 93
6.4.1 Experimental phase diagram of BLG with $CdCl_2$ in D_2O . . . 93
6.4.2 Crystallization followed by optical microscopy 95
6.4.3 Crystallization followed by real-time SANS 98
6.5 Discussion on the role and the development of the MIP 105

6.6 Conclusions . . . 107

VII Structural insights into polymer-bounded lipid nanodiscs 109

7.1 Abstract . . . 111
7.2 Introduction . . . 111
7.3 Experimental . . . 114
7.3.1 Materials . . . 114
7.3.2 Polymer stock preparation . . . 114
7.3.3 Preparation of polymer-lipid nanodiscs . . . 115
7.3.4 SAXS measurements . . . 115
7.3.5 SAXS data analysis . . . 115
7.3.6 DLS . . . 116
7.4 Results . . . 116
7.4.1 Case A: Membrane architecture is affected with increasing copolymer concentrations . . . 116
7.4.2 Case B: Influence of temperature on size and shape of nanodiscs 121
7.5 Conclusion . . . 128

VIII Concluding discussion and outlook 129

List of publications 137

Bibliography 139

A Supporting information: Protein crystallization in the presence of a metastable liquid-liquid phase separation 167

B Supporting information: Human versus bovine serum albumin: A subtle difference in hydrophobicity leads to large differences in bulk and interface behavior 173

C Supporting information: Protein crystallization from a pre-ordered metastable intermediate phase followed by real-time small-angle neutron scattering 179

D Supporting information: Structural insights into polymer-bounded lipid nanodiscs 183

Acknowledgements 189

Abstract

Proteins are crucial and substantial for life. Their functions range from transporting molecules, being responsible for muscle movement to structural functions, e.g., in hair. Thereby, the form of the proteins strongly determines their function. Proteins are commonly divided into four subgroups (globular, disordered, fibrous, and membrane proteins) based on their structure with globular and membrane proteins being the focus in this work. Generally, globular proteins are spherical, water-soluble proteins and can show a rich phase behavior, including aggregation, liquid-liquid phase separation (LLPS), reentrant condensation (RC), and crystallization upon adding multivalent ions. Hence, understanding and being able to manipulate the phase behavior of proteins (e.g., through the addition of multivalent salts) is vital for a wide field of research. On the one hand, protein condensation is desired, since protein crystals are the basis of most structural resolution of proteins, giving hints toward their function. On the other hand, for example the formation of amyloid fibrils within the human body may result in diseases such as Alzheimer.

This dissertation aims to fulfill two main goals: As a first step, characterizing the respective protein-multivalent ion system, including determining the interactions and phase behavior, and as a second step, determining the respective crystallization pathway, i.e., the kinetics. In this regard, several theories exist that attempt to describe and predict the crystallization process (classical and nonclassical). However, these theories cannot be applied to every system, since no general crystallization pathway exists and even similar systems can crystallize following different crystallization pathways. In a classical process, the two parameters, structure and density, change simultaneously during crystallization, whereas in nonclassical crystallization, some kind of intermediate phase (such as the dense liquid phase after LLPS or clusters) exists in between the initial solution and the final crystal. To elucidate the protein phase behavior and crystallization pathway, different systems of negatively charged globular proteins in the presence of multivalent cations were investigated. Considerable parts of the present thesis are based on three own publications in peer-reviewed scientific journals.

In the beginning, the model systems containing the protein human serum albumin (HSA) with the salts $CeCl_3$ and YCl_3 were studied in detail to gain an overview of the phase behavior. Further, conditions inside and outside the region in the phase diagram where LLPS occurs were investigated in order to determine the role of the dense, protein-rich phase on the (nonclassical) crystallization pathway. A proposed nucleation within the dense phase, as suggested by simulations and theory, was

tested for its validity by the experiments performed for this system. In contrast to the predictions, the data led to the surprising conclusion that nucleation takes place within the dilute, protein-poor phase, and that the dense phase only acts as a reservoir. During crystal growth within the dilute phase, this reservoir of dense phase dissolves and facilitates further crystal growth.

Second, the two homologous proteins HSA and bovine serum albumin (BSA) were studied with $CeCl_3$ in solution and at a net negatively charged, hydrophilic surface to investigate their phase and adsorption behavior. These are crucial experiments to investigate the differences and similarities between these extremely similar proteins as well as to determine the driving force of crystallization, since only HSA was reported to crystallize in the presence of multivalent ions. While both proteins showed a similar phase behavior including RC and LLPS, the LLPS binodal was shifted toward much higher protein concentrations (c_p) in the case of BSA. These results indicate weaker intermolecular attractions for BSA, which was further supported with small-angle X-ray scattering (SAXS) experiments. Consistent with the literature, only HSA crystallized within the condensed regime in the respective phase diagram. Since HSA is slightly more hydrophobic than BSA, this behavior was attributed to additional hydrophobic interactions of HSA, which not only strengthen the attractions, but also provide additional oriented protein-protein contacts due to the hydrophobic patches, favoring crystallization. In turn, quartz-crystal microbalance with dissipation (QCM-D) data show that at a hydrophilic surface, a higher amount of the more hydrophilic BSA was adsorbed. Hence, even though the general protein phase behavior is strongly determined by electrostatic interaction due to ion binding and ion bridging, additional interactions such as hydrophobic interactions cannot be neglected, in particular when it comes to crystallization.

Third, the model system β-lactoglobulin (BLG) with $CdCl_2$ was studied in D_2O by real-time small-angle neutron scattering (SANS) and optical microscopy to shed light on the role of a preordered, metastable intermediate phase (MIP) in a nonclassical two-step crystallization process. With these techniques, it is possible to characterize the MIP during crystallization. A broad SANS peak was visible directly after preparation, indicating a correlation of the proteins within the clusters. Since the quantity of MIP and the characteristic length scale within these clusters evolved during crystallization, it was concluded that the proteins can still rearrange/reorient within the MIP, but that preordered domains with a length scale slightly larger than typical protein-protein distances within the crystal lattice serve as crystal precursors. In contrast to the dense droplets of the HSA system in the first result part, this MIP serves as a crystal precursor and due to its preordered nature, the system follows a completely different nonclassical crystallization pathway.

Finally, a topic that is not necessarily connected to the phase behavior and nonclassical crystallization of proteins was approached. Here, so-called nanodiscs, which are composed of a lipid bilayer surrounded by a polymer belt, were studied. These

nanodiscs are a promising tool to investigate membrane proteins in their native state, including techniques amenable for soluble proteins as well as crystallization and structural resolution of the membrane proteins. However, a complete characterization of the behavior of the nanodiscs is still lacking. For this purpose, different compositions of two polymers (styrene maleic acid (SMA) and diisobutylene maleic acid (DIBMA)) with the same lipid dimyristoyl-phosphocholine (DMPC) were mixed and characterized by dynamic light scattering (DLS) and SAXS. Using the two different polymers resulted in different structural arrangements of the nanodiscs. In addition, structural effects due to increasing polymer concentration and decreasing temperature were investigated. These results enable the biophysical and chemical investigation of membrane proteins in a much more controlled way.

Zusammenfassung in deutscher Sprache

Proteine sind ein wichtiger und substanzieller Bestandteil für jegliches Leben. Ihre Funktionen reichen vom Transport von Molekülen über Muskelaktivität bis hin zu strukturellen Funktionen wie z.B. in Haaren. Dabei bestimmt die Form der Proteine deren Funktion. Typischerweise werden Proteine in vier Gruppen entsprechend ihrer Struktur unterteilt: globuläre, ungeordnete, faserförmige und Membranproteine. In dieser Arbeit werden globuläre Proteine und Membranproteine behandelt. Globuläre Proteine sind sphärische, wasserlösliche Proteine, die ein vielfältiges und komplexes Phasenverhalten in Gegenwart von multivalenten Salzen aufweisen. Dieses kann Aggregation, flüssig-flüssig Phasentrennung (engl.: liquid-liquid phase separation, LLPS), "Reentrant Condensation"(RC) und Kristallisation beinhalten. Daher sind ein breites Verständnis über das Phasenverhalten von Proteinen sowie dessen Beeinflussung (z.B. durch die Zugabe von multivalenten Salzen) extrem wichtig in verschiedensten Bereichen. Einerseits ermöglichen kristalline Protein-Aggregate deren Strukturbestimmung mittels Röntgendiffraktometrie, wodurch Rückschlüsse auf die Funktion des Proteins gezogen werden können. Andererseits kann die Bildung von Amyloidfibrillen im menschlichen Körper zu Krankheiten wie Alzheimer führen.

Diese Dissertation verfolgt zwei Hauptziele: Zuallererst soll die Charakterisierung verschiedener Proteinsysteme mit multivalenten Salzen, einschließlich der Bestimmung der Interaktionen und des Phasenverhaltens, erfolgen. Darauffolgend ist die Bestimmung des Kristallisationsweges im jeweiligen System, d.h. die Kinetik der Kristallisation, geplant. In diesem Sinne existieren verschiedene Theorien zur Beschreibung und Vorhersage von Kristallisationsprozessen (klassische und nichtklassische Kristallisation). Jedoch können diese Theorien nicht für jedes System angewendet werden, da es keinen generellen Kristallisationsweg gibt und selbst ähnliche Systeme einem komplett unterschiedlichen Kristallisationsweg folgen können. Im klassischen Kristallisationsprozess ändern sich im Verlaufe der Kristallisation der Struktur- und der Dichteparameter simultan, wohingegen im nichtklassischen Prozess eine Zwischenphase zwischen der Lösung und dem finalen Kristall gebildet wird (wie z.B. die dichten Tröpfchen nach der LLPS oder Cluster). Um diese Ziele zu erreichen, wurden verschiedene Systeme bestehend aus negativ geladenen, globulären Proteinen und multivalenten Salzen untersucht. Wesentliche Teile dieser Arbeit basieren auf drei eigenen Publikationen in wissenschaftlichen Peer-Review-Zeitschriften.

Zuerst wurden Modellsysteme bestehend aus dem Protein Humanalbumin (engl.:

human serum albumin, HSA) mit den Salzen $CeCl_3$ und YCl_3 im Detail analysiert, um einen Überblick über das Phasenverhalten zu erhalten. Um die Rolle der dichten, proteinreichen Phase nach der LLPS im (nichtklassischen) Kristallisationsweg zu bestimmen, wurden Proben innerhalb und außerhalb der LLPS-Region präpariert und untersucht. Da Simulationen und theoretische Studien vorhersagen, dass Kristallnukleation in dieser dichten Phase stattfindet, wurde getestet, ob diese Beobachtungen experimentell bestätigt werden können. Im Gegensatz zu den Vorhersagen resultierte aus den Daten die überraschende Schlussfolgerung, dass die Nukleation in der dünnen, proteinarmen Phase stattfindet und die dichte Phase nur als Reservoir dient. Dieses Reservoir in Form von dichter Phase löst sich während des Kristallisationsprozesses auf, um weiteres Kristallwachstum zu ermöglichen.

Aufbauend darauf wurden die beiden homologen Proteine HSA und Rinderalbumin (engl.: bovine serum albumin, BSA) mit $CeCl_3$ sowohl in Lösung, als auch an einer negativ geladenen, hydrophilen Oberfläche in Bezug auf das Phasen- und Adsorptionsverhalten untersucht. Dies sind essenzielle Experimente, um einerseits Unterschiede und Gemeinsamkeiten zwischen den zwei ähnlichen Proteine zu finden als auch die treibende Kraft der Kristallisation zu bestimmen, da bisher nur für HSA Kristalle in der Anwesenheit von multivalenten Ionen gefunden wurden. Obwohl beide Proteine ein ähnliches Phasenverhalten einschließlich LLPS und RC aufweisen, ist die LLPS-Binodale von BSA zu deutlich höheren Proteinkonzentrationen (c_p) verschoben, was auf schwächere Interaktionen zwischen den Proteinen deutet. Dieses Ergebnis ist im Einklang mit Kleinwinkelröntgenstreuexperimenten (engl.: small-angle X-ray scattering experiments, SAXS experiments). Konsistent mit der Literatur wurden nur HSA Kristalle in der kondensierten Region im jeweiligen Phasendiagramm gefunden. Da HSA hydrophober als BSA ist, wurde dieses Verhalten den zusätzlichen hydrophoben Wechselwirkungen von HSA zugeschrieben, die nicht nur die Anziehungskräfte erhöhen, sondern auch zusätzliche gerichtete Protein-Protein-Kontakte durch hydrophobe Stellen an der Proteinoberfläche knüpfen können und damit Kristallisation ermöglichen und begünstigen. Im Gegensatz dazu belegen Quarzkristall Mikrowaage mit Dissipationsmessungen (engl.: quartz-crystal microbalance with dissipation, QCM-D), dass die hydrophilen BSA-Moleküle an einer hydrophilen Oberfläche stärker adsorbieren. Die Ergebnisse zeigen, dass die elektrostatischen Wechselwirkungen aufgrund von Bindung und Brückenbildung der Ionen ausschlaggebend für das generelle Phasenverhalten zu sein scheinen. Jedoch ist es wichtig, alle Interaktionen in Betracht zu ziehen, vor allem, wenn es um Kristallisation geht.

Im dritten Teil der Arbeit wurde das System β-Laktoglobulin (BLG) mit $CdCl_2$ in D_2O mithilfe von Kleinwinkelneutronenstreuung (engl.: small-angle neutron scattering, SANS) und optischer Mikroskopie untersucht, um Aufschluss über die Rolle einer geordneten, metastabilen, intermediären Phase (MIP) in einem nichtklassischen Zwei-Schritt-Kristallisationsprozess zu geben. Mit diesen Techniken ist es möglich, die MIP während der Kristallisation zu charakterisieren. Ein breiter SANS-Peak, der

auf eine Korrelation der Proteine innerhalb der Cluster hindeutet, war direkt nach Probenpräparation sichtbar. Da sich die Quantität der MIP und die charakteristische Längenskala innerhalb der Cluster während der Kristallisation änderten, wurde gefolgert, dass die Proteine innerhalb der MIP noch beweglich sind, aber das geordnete Domänen mit einer Längenskala, die minimal größer als die der Einheitszelle ist, als Vorstufe für die Kristalle dienen. Im Gegensatz zu den dichten Tröpfchen des HSA-Systems im ersten Ergebnisteil dient diese Zwischenphase wirklich als Vorstufe der Kristalle und aufgrund der strukturellen Anordnung der Proteine vor der Nukleation wird ein komplett anderer, nichtklassischer Kristallisationsweg vom System verfolgt.

Zu guter Letzt wurde ein Thema, welches nicht unbedingt mit dem Phasenverhalten und der nichtklassischen Kristallisation von Proteinen verknüpft ist, genauer beleuchtet. Dabei wurden sogenannte „Nanodiscs“untersucht, die aus einer Lipiddoppelschicht bestehen. Diese ist zusätzlich umrandet von einem stabilisierenden Polymergürtel. Nanodiscs sind ein vielversprechendes Werkzeug, um hydrophobe, unlösliche Membranproteine in ihrer nativen Form untersuchen zu können. Nichtsdestotrotz fehlt bisher eine komplette Charakterisierung des Verhaltens der Nanodiscs. Um weitere Einblicke zu erhalten, wurden verschiedene Zusammensetzungen aus den zwei Polymeren Styrol-Maleinsäure (engl.: styrene maleic acid, SMA) und Diisobutylenmaleinsäure (engl.: diisobutylene maleic acid, DIBMA) mit dem gleichen Lipid Dimyristoyl-Phosphocholin (engl.: dimyristoyl-phosphocholine, DMPC) gemischt und mit dynamischer Lichtstreuung (DLS) und SAXS untersucht. Dabei konnten strukturelle für die unterschiedlichen Systeme erfasst werden. Zudem wurden Strukturänderungen durch eine Erhöhung der Polymerkonzentration und eine Erniedrigung der Temperatur beobachtet. Die Ergebnisse ermöglichen eine besser kontrollierbare biophysikalische und chemische Untersuchung von Membranproteinen.

Part I

Introduction

1.1 The universal relevance of crystallization

For the last two years, our lives were tremendously affected by the corona virus disease (COVID-19), which is caused by the corona virus variant SARS-CoV-2.[1,2] To fight this pandemic, multiple approaches have been exploited. Concerning this matter, structural information are vital to obtain knowledge of how the virus can be made innocuous. For this purpose, complexes of antibodies with the virus have been crystallized.[1–3] Another approach was the crystallization of the main protease, which is responsible for the cleavage of the viral ribonucleic acid (RNA).[4] After crystallization, structure determination by X-ray or neutron diffraction was possible.[4] Consequently, for the latter case, inhibitors of the main protease were designed, having accurate knowledge of the required binding sites with the protease.[4] However, the formation of high-quality crystals (especially for proteins) is still the main bottleneck in biological structure analysis, since several parameters such as temperature can influence the crystal formation and many proteins are not prone to crystallize at all.[5,6]

Nevertheless, in the past, different macromolecules have been crystallized prior to structural analysis. Crystallization of polymers,[7,8] cytochrome c,[9,10] ribosomes,[11] transfer (t) RNA,[12] chaperones,[13] organic photovoltaics (OPVs),[14] human antibodies,[15,16] and many others has been exploited to obtain crucial information about the respective system. Besides structural resolution, crystallization is vital in many other research areas, ranging from the design of novel nanostructures for data storage to improved climate models.[17–20]

Although crystallization is of great relevance, the underlying mechanisms and interactions are nowadays not fully understood. Most of the time, protein crystallization is achieved by a trial-and-error approach, in which proteins and different precipitants/crystallizing agents are mixed and the presence or absence of crystals is recorded. Common variables to tune crystallization are temperature, pH, buffer, salt concentration, or polymer concentration and nature.[6,21–23] Besides, effects like stirring, shear or different flow velocities and modes can affect crystallization.[21,24,25] Other recent approaches to successfully induce and enhance protein crystallization comprise for example the usage of graphene quantum dots,[26] an ion-exchange membrane,[27] utrasound,[28] or seeding with, e.g., cyclic peptides.[22,29,30] In this context, new, optimized techniques were developed in order to perform high-throughput screens with simultaneous optimization of the protein crystallization conditions.[25,31–33]

Subsequently, different aspects regarding the phase behavior of proteins and crystallization in general, but highlighting protein crystallization, are presented. In this sense, in the beginning, a description of the phase behavior of protein solutions in the presence of a monovalent salt is given. Further, the thesis discusses the effects of adding multivalent ions, since the protein phase behavior is drastically changed compared to monovalent salts.[34]

1.2 Protein-monovalent ion interactions

In order to understand and control the crystallization process, knowledge of the underlying interactions is required. One rather simple model to describe the phase behavior of charged particles is the DLVO theory, which is named after the scientists, who contributed to its development, namely Derjaguin, Landau, Verwey, and Overbeek.[35,36] It is based on the Poisson-Boltzmann theory, which uses a mean-field approach to describe the ion distribution.[37,38] The DLVO potential contains three contributions: hard sphere repulsion, screened Coulomb repulsion and van der Waals (vdW) attraction. Increasing the ionic strength of the solution results in an increased charge screening of the particles, hence, an effective attraction. This approach is rather simplified, since, e.g., ion-ion correlations or hydration effects are neglected. Therefore, effects like the Hofmeister series cannot be explained by the DLVO theory. The Hofmeister series is an empirical study on protein condensation.[39] Hofmeister tested different salts (cations and anions independently) with regard to their ability to salt out (precipitate) or salt in (stabilize) different proteins in solution and put them into order.[39] In the DLVO theory, ions with the same valency are treated equally, hence, differences in the condensation behavior due to a different ion nature cannot be explained. Besides, the DLVO theory is only valid for monovalent salts. Thus, in the following, a proper description of the interactions and the phase behavior of proteins in the presence of multivalent salts is presented.

1.3 Soft matter phase behavior with multivalent salts

As mentioned above, salts are frequently used as precipitants to induce protein crystallization.[39–42] In this dissertation, systems of net negatively charged proteins and multivalent cations are used to investigate the protein phase behavior, highlighting crystallization. This is based on the fact that a rich phase behavior is observed for globular proteins in the presence of multivalent salts and the cations can even trigger crystallization.[40,42–45] Noteworthy, the use of multivalent salts does not only strengthen the effects of the ions, but also qualitatively changes these effects compared to monovalent ions.[34] In these protein systems with multivalent salts, for a given protein concentration c_p, the proteins initially repel each other due to their negative net charge (regime I).[40] Increasing the salt concentration c_s above a certain threshold concentration c^* results in a phase transition, where the proteins aggregate/condense (regime II), since the cations bind to the proteins, diminishing their charge, and are able to form intermolecular bridging contacts.[40–42] Increasing c_s even further, above the second phase boundary c^{**}, results in a clear and stable protein solution again (regime III). This behavior is called reentrant condensation (RC) and the underlying mechanism was found to be charge inversion of the proteins.[40,43,46] Inside the second regime, a liquid-liquid phase separation (LLPS) region can exist, and samples prepared at conditions within this area phase separate

into a dilute and a dense liquid phase.[47–50] Depending on the system, an additional glass line may exist, which results in an arrested state of the dense phase.[51,52]

This behavior is beyond the DLVO and Poisson-Boltzmann theories. In order to describe the phase behavior properly, the ion-activated patchy-particle model was developed based on the phase behavior and the crystal structures.[41] According to this model, each protein features patches which the multivalent cations can occupy and thereby activate.[41] If an occupied patch finds an unoccupied one, a short-range attraction occurs.[41] In contrast, if an occupied patch collides with another occupied one or two unoccupied patches meet, these patches repel each other.[41] Further Monte Carlo simulations could confirm that proteins are well-described as patchy particles.[53] Interestingly, it seems that not only the number of patches, but also their placement on the particle surface determine the phase behavior.[53,54] An an example for this, the critical point (the end point of a phase equilibrium curve) in the phase diagram is strongly affected by the placement of the patches.[53,54] Moreover, the number of patches influences the crystallization propensity.[53] Particles containing six patches crystallize much more likely than those with fewer patches.[53]

It is worth mentioning that the usage of multivalent cations is not only limited to proteins. Actually, DNA was the first type of soft matter showing RC upon adding cations, although the mechanism is different.[55] Besides, multivalent ions were also reported to be able to induce nanofibril formation of cellulose and synthetic copolymer systems due to their bridging effect.[56,57] Further studies indicate even reentrant transitions in these systems upon increasing c_s, i.e., swollen-collapsed-swollen transitions, translating into reentrant properties such as thermal properties, wettability, roughness, and nano-mechanical stiffness.[58–60] This leads to the conclusion that the phenomena mentioned are rather frequent in polyelectrolyte systems containing multivalent salts.[43,47–49,55,58–66]

1.4 The crystallization pathway: classical vs nonclassical nucleation theory

Multivalent cations can not only induce this rich phase behavior in polyelectrolytes, but are also able to induce crystallization of globular, net negatively charged proteins.[42,44–49] However, the exact pathways and corresponding energy landscapes resulting in the final crystal are still under debate. In this section, the classical nucleation theory (CNT) is compared to nonclassical nucleation theories. All of these theories describe different crystallization pathways. In general, the process of crystallization can be divided into two separate processes, namely nucleation and crystal growth. Changing the supersaturation of the solution enables the decoupling of the nucleation and growth of the crystals.[68] The supersaturation of a solution describes how much the concentration of a solute exceeds the equilibrium solubility under the same conditions. For crystal nucleation, a high supersaturation is required, whereas a low supersaturation is sufficient for subsequent crystal growth.[68]

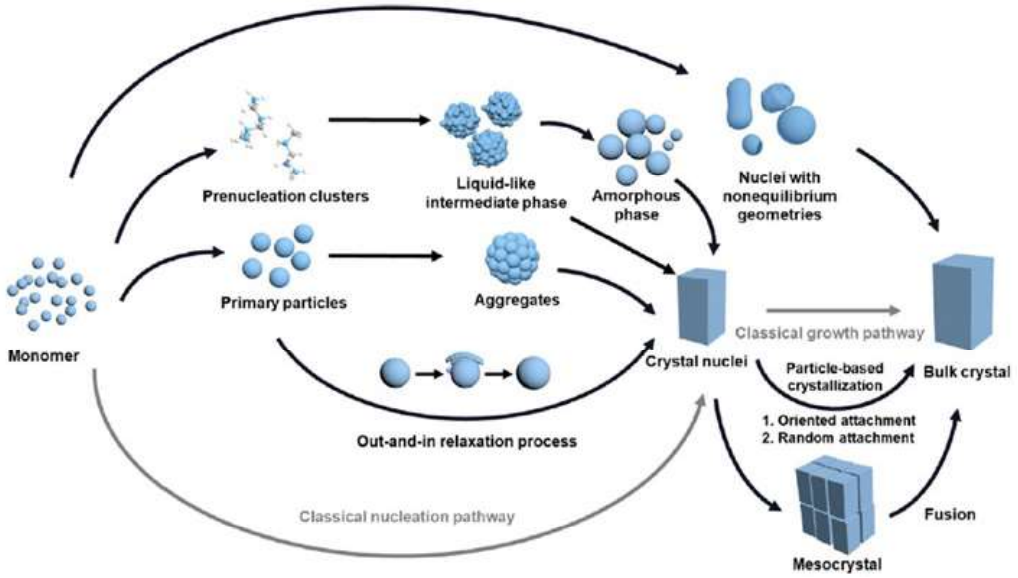


Figure 1.1: *Possible nucleation and crystal growth pathways. Classical pathways are drawn in grey, whereas nonclassical routes are colored black. Image adapted from Ref. 67.*

1.4.1 Classical crystallization

Classical nucleation theory states that a nucleus forms within a supersaturated solution. The nucleus grows further, having already the structure and the concentration of the final (bulk) crystal (see grey pathway in Fig. 1.1).[69,70] In this description, only the surface and bulk term of the free energy (G_S and G_V, respectively) are considered (Eq. 1.1).[71]

$$\Delta G = G_S + G_V = 4\pi r^2\gamma - \frac{4}{3}\pi r^3 \frac{k_B T \ln(S)}{\nu} \tag{1.1}$$

Here, r describes the radius of the cluster/nucleus, γ the interfacial free energy between cluster and solution, k_B the Boltzmann constant, T the temperature, S the solubility and ν the molar volume of the molecules. The positive G_S results from the energy cost to create a liquid-solid interface between solution and crystal while G_V represents the free energy gain due to molecule binding within the crystal. Above a critical radius r^*, the initially formed clusters become stable and are called nuclei. These nuclei grow further by single molecule attachment, while below r^*, the clusters are unstable and dissolve again. Noteworthy, one important aspect is that during this process, the order and density parameter change simultaneously, meaning the clusters already have the same structure as the final crystal.

Several experimental studies demonstrated this pathway to occur in their systems. Yau and Vekilov could show with atomic force microscopy (AFM) that the protein apoferritin crystallizes according to the CNT pathway.[72,73] AFM and cryo transmission electron microscopy (TEM) experiments revealed that glucose isomerase is

able to nucleate in a classical manner as well.[74–76] Similarly, template-directed nucleation on carboxyl self-assembled monolayers (SAMs) of calcite can be described by purely classical nucleation.[77]

1.4.2 Nonclassical crystallization

In contrast to the CNT discussed above, recent studies show nonclassical features during the crystallization process, which were first simulated by ten Wolde and Frenkel.[78] In their study, an intermediate phase formed from the solution due to density fluctuations and crystals nucleated within this intermediate phase.[78] Depending on the system and the respective sample compositions, different nonclassical crystallization pathways can occur, as to be seen from Fig. 1.1.[67] Following, several selected nonclassical nucleation pathways and crystal growth mechanisms which form a final bulk crystal are discussed.

1.4.2.1 Ostwald's rule of stages

The first theoretical description of a nonclassical pathway was probably Ostwald's rule of stages. It states that a system transforms from an energetically less stable into a more stable form through intermediate states.[79] These intermediate states have gradually less energy than the initial form.[79] This nonclassical pathway through Ostwald's rule of stages was observed in inorganic systems (metal phosphate).[80] However, in the case of gold and copper, molecular simulations revealed that a chemically-ordered intermediate, which is more organized than the final crystal, serves as a precursor in solid solution crystallization.[81] This ordered phase continues to promote nucleation later on as new clusters are formed at the solid-liquid interface during the development of the nucleus, resulting in a lower free energy barrier of nucleation.[81] These results are in contrast to Ostwald's step rule as the intermediate is actually more organized than the final phase, since it is both chemically and structurally more ordered.[81]

Another form of Ostwald's rule of stages was reported for water crystallization.[82] There, to lower the free energy barrier of nucleation, and thus, create a species with a lower free energy than the initial phase, a decrease of the interfacial free energy between the crystallites and liquid water was observed.[82] This decrease of the interfacial free energy originated from the solvation of the crystalline clusters by bilayer hexagons and resulted in an increase of the crystallization rate.[82] A similar pathway was recently reported for insulin.[83] In order to minimize the interfacial free energy, the insulin molecules form protein-rich clusters with radii between 160 and 200 nm, which eventually crystallize in a next step, leading to a nonclassical two-step crystallization.[83] Since minimizing the interfacial free energy directly reduces the barrier for crystal nucleation in solution, this two-step pathway is faster and favored compared to a classical pathway according to CNT.[83]

1.4.2.2 Phase separation/dense liquid or amorphous precursors

One possibility of how Ostwald's rule of stages can proceed is phase separation, i.e., the formation of a dense liquid or amorphous phase, which acts as metastable nucleation precursor. For example, scanning and photoemission electron microscopy observations are consistent with a dense liquid-like precursor being involved in regenerating sea urchin spines consisting of $CaCO_3$.[84]

Loh et al. showed by investigating supersaturated aqueous gold and silver solutions via in situ TEM that first, spinodal decomposition into dense and dilute phases occurs, second, amorphous nanoclusters nucleate within the metal-rich liquid phase, and third, these clusters crystallize.[85] The authors argue that a strong gold–gold atom coupling and water-mediated metastable gold complexes are responsible for this behavior.[85] Similarly, inside a dense liquid palladium (Pd) phase, metastable Pd nanocrystals were found to relax, restructure, and evolve into stable crystals.[86] During this process, the nanocrystals are able to merge, potentially facilitated by a mediation of mass transportation between particles of the dense phase.[86]

Using SANS, electron microscopy and electron tomography, a phase separation of ovalbumin in the presence of ammonium sulfate into core-shell particels (with a core radius of $\approx 2\,\mu m$ and a shell thickness of $\approx 0.5\,\mu m$) was reported.[87] Interestingly, the protein gel forming the shell composed a well-defined nanocrystalline network with branches, but was not completely crystalline in the end.[87] Here, a local crystallization within the protein gel of the shell occurred, but no complete crystallization of the shell and parts of the gel remained in the gel phase.[87]

Zhang et al. investigated the two-dimensional crystallization kinetics of a colloidal model system in real space and real time.[88] Forming first a dense, amorphous droplet, nucleation subsequently occurred within the metastable droplets.[88] Thermal fluctuations led to the formation and shrinkage/dissolution of subcritical nuclei, but only after the coalescence of these subcrystalline nuclei, larger crystalline nuclei were stable and did not dissolve again.[88] The grain boundaries after nuclei coalescence were eliminated gradually during the following growth, seemingly without an energy barrier.[88] Each dense droplet was only able to produce one mature crystalline nucleus.[88] Both the degree of order and density in the dense droplets decreased continuously from the crystalline core to its amorphous edge.[88] This gradual decrease in order gradient, from the core toward the exterior, was also reported for, e.g., aggregates of ferritin prior to crystallization.[89]

Combining classical density functional theory (DFT) with stochastic process theory can predict nonclassical nucleation pathways based solely on the interaction potential of the particles.[90] In this combined theory approach, crystallization is supposed to proceed in two steps: Initially, dense droplets are formed, which gradually order starting from the core of the droplet as a second step.[90] Importantly, over a wide range of supersaturations, the dense droplets are subcritical, and therefore unstable (and not metastable as Ostwald's rule of stages would predict).[90] Further crystal growth proceeds via freezing of a dense liquid layer of proteins on the surface of the crystal and not via single molecule attachment as compared to the CNT.[90]

Moreover, in other biological processes, such as in the phase separation of prion-like domains (low-complexity domain of the heterogeneous nuclear ribonucleoprotein A1), a multi-step nucleation was observed.[91] Interestingly, on the mesoscale, phase separation resembled a classic, homogeneous, nucleation-and-growth mechanism.[91] However, on the nanoscale, monomers first had to assemble into a condensed phase via unfavorable steps until the addition of additional monomers became energetically favorable.[91] This has a huge impact on the phase behavior: Solutions close to the liquid-liquid binodal may remain single-phased for an indefinite time in the absence of perturbations that facilitate nucleation.[91]

1.4.2.3 Prenucleation clusters

Contradictory to Ostwald's rule of stages is the rather recent observation of so-called prenucleation clusters found in biomineralization processes. These are stable, nanometer-sized clusters which are present in solution already before nucleation.[92] For example in $CaCO_3$ mineralization, the formation of prenucleation clusters was reported.[93] In fact, two types of clusters were observed: Small prenucleation clusters that coexisted with large clusters produced by spinodal decomposition.[93] The former long-lived nanometer-sized clusters acted as prenucleation clusters of $CaCO_3$ instead of unstable clusters as predicted by CNT.[93] In the CNT, clusters smaller than the critical nucleus size are unstable and dissolve again, and no stable clusters exist. Both types of $CaCO_3$ clusters led to different final phases.[93] For sample conditions prepared within the spinodal, growth and coalescence of the larger, dense liquid $CaCO_3$ clusters and subsequent dehydration resulted in the formation of amorphous calcium carbonate (ACC).[93]

Another example for prenucleation cluster formation can be found in the process of surface-induced calcium phosphate crystallization from simulated body fluid, in which prenucleation clusters act as precursors and building blocks.[92] In detail, cryo TEM and cryo electron tomography (ET) revealed that these prenucleation clusters first densified and aggregated at the templating surface (arachidic acid monolayer).[92] In this step, clusters with a diameter of $\approx 50\,\text{nm}$ were formed, which further aggregated into amorphous calcium phosphate (ACP) nanoparticles.[92] These nanoparticles grew further and developed crystallinity facilitated by the surface of oriented apatite crystals.[92] This pathway is illustrated in Fig. 1.1.

In contrast to the examples presented above, Smeets et al. stated that no stable prenucleation clusters (larger than 0.9 nm in size) exist in $CaCO_3$ formation.[94] The authors presented experimental and computational evidence that at high supersaturations, a dense liquid phase acts as a precursor for the formation of solid $CaCO_3$ in the form of vaterite, which grows via a net transfer of ions from solution.[94] In their opinion, the CNT can be successfully applied to describe the nucleation, although the growth mechanism involves intermediate phases.[94]

1.4.2.4 Out-and-in relaxation process

As indicated in Fig. 1.1, crystallization can also proceed via an out-and-in relaxation process. One example is the the transformation of poorly crystalline gold nanoparticles into nanocrystals, which was followed by in situ liquid-phase scanning TEM.[95] During this process, the crystalline core and the disordered shell around it exchanged matter, meaning poorly crystallized domains were expelled, and monomers and nanoclusters were reattached in a crystalline orientation.[95]

1.4.2.5 Secondary nucleation

Another possibility to obtain crystals is secondary nucleation. This process is strongly influenced by macroscopic crystals, meaning secondary nucleation occurs in the presence of the parent crystal within the solution.[96,97] Since the energy barrier for secondary nucleation is lower because of the already existing solid-liquid interface (i.e., the crystal surface), crystallization can occur at lower supersaturations.[97] In this regard, crystallization can occur directly at the crystal surface or from the solute layer on the crystal surface (and therefore in the close vicinity of the crystal surface).[97]

1.4.2.6 Mesocrystals

So far, only the nucleation process was discussed. However, one has to consider that not only crystal nucleation can be nonclassical, but also its growth (see Fig. 1.1). While CNT states solely monomers attach to the crystal surface as building blocks, mesocrystals have been found to consist of distinct nuclei or nanocrystals, which eventually merge, forming mesocrystals (Fig. 1.1).[98] Zhu et al. investigated haematite mesocrystals in the presence of oxalate by transmission electron microscopy (TEM).[98] The authors recorded the pathway of an interface-driven processes of nucleation and assembly by particle attachment, i.e., nuclei nucleated in the vicinity of preexisting crystals due to surface effects (but not directly on the surface itself), and then attached to the crystal, driven by attractive interactions.[98] These mesocrystals exhibited a spindle-like morphology.[98] In the same system, it was possible that single monomers attach to the crystal, resembling CNT growth and leading to a rhombohedral crystal.[98] In both cases, the inital precursor ferrihydrite was present as MIP, but dissolved into single ions, which then attached to the haematite crystals after its nucleation.[98]

1.4.2.7 Oriented attachment

Another specific pathway to result in (protein) mesocrystals was discovered by van Driessche et al. Cryo TEM experiments revealed the initial formation of facetted glucose isomerase (GI) nanocrystals in the presence of polyethylene glycol (PEG).[75] These nanocrystals later merged lattices by means of oriented attachment (OA) alignment prior to their conjunction (see Fig. 1.1).[75] Due to the symmetry of the

space group, only three distinct crystal contacts are allowed, which makes a proper alignment essential before the contact formation can occur.[75] Based on classical density functional theory (cDFT) calculations of Liu et al., it was proposed that local water structuring plays a crucial role in the OA process, resulting in an aligning torque for the single nanocrystals.[75,99] These cDFT calculations showed that the combination of electrostatic, solvation, ion correlation and vdW interactions establishes a short-raged ($\approx 2\,\mathrm{nm}$) attractive interaction potential with little or no barrier to attachment ($\leq k_B T$).[99] As a last step, desolvation of the buried interfaces of the separate nanocrystals is believed to occur.[75] These results highlight the crucial role of the interaction between crystalline nuclei and lead toward a new mechanism of OA in protein crystallization.[75] Interestingly, the authors observed an initial nucleation of the GI molecules according to CNT,[75] although they have reported both classical and nonclassical nucleation pathways for this system.[74,76] They concluded that even within the same system, multiple crystallization (nucleation and growth) pathways can occur, which are conceptually diverse.[75]

1.4.2.8 Polymorphs and solid-solid-transition

Previously, only crystal nucleation of a specific crystal structure and its subsequent growth were discussed. However, many solutes exhibit polymorphism.[100–103] The ability of a compound to crystallize in more than one distinct crystal species, i.e., crystal arrangements, in case of the same chemical composition is called polymorphism.[104,105] In the following, it is briefly discussed, which polymorph is preferred, i.e., how polymorph selection takes place.

According to theoretical calculations and simulations (not taking into account kinetic effects), polymorph selection far away from the equilibrium is controlled by surface tension.[106] Given the case that the polymorph with the lowest surface tension does not have the lowest free energy, a transformation into the most stable phase will occur subsequently.[106] This scenario resembles closely Ostwald's step rule, where rather the surface tension than the chemical potential dominates.[106] In this case, the chemical potential of the final polymorph might even be higher than that of the initial polymorph.[106]

In this respect, lattice defects (voids) as well as proteins were found to be highly mobile within a crystal.[107] Especially molecules located within the grain boundaries need to be mobile and to be able to undergo rapid bond breaking as well as recombination.[107] This also explains the reduced thermodynamic cost of a solid-solid phase transition, i.e., the sudden transformation from one polymorph to a more stable one. During this transformation, no crystal dissolution was observed, but a solid-state mediated transformation.[107]

In contrast, Peng et al. demonstrated with single-particle-resolution video microscopy of colloidal films that transitions between square and triangular lattices follow a two-step diffusive nucleation pathway with an intermediate liquid nuclei.[108] Since the energy of the solid-liquid interface was lower than that between solid phases, this pathway took place instead of a direct solid-solid transition.[108] To be

more precise, this pathway is supposed to occur when the solid-liquid interfacial energy is lower than the solid-solid interfacial energy.[108] The authors generalized these findings and stated that similar kinetic pathways with an intermediate liquid should be observed in two and three dimensions (2D, 3D) as well as in thin-film single crystals and polycrystals.[108]

1.5 Crystallization of proteins vs small molecules/atoms

In the previous sections, multiple nucleation and crystal growth pathways for various systems were discussed. Nevertheless, not all pathways can be applied to proteins, since several crucial differences between protein crystals and crystals consisting of small molecules or atoms exist. While crystals formed by small molecules and protein crystals have comparable binding energies, proteins feature a heavier molecular weight and the crystals contain fewer contacts, hence, the overall intermolecular contacts are weaker.[6] An additional aspect why protein crystallization is (more) difficult to facilitate is that protein purification remains very challenging.[6] Even with a 100 % chemical purity, proteins can exist in different conformations, which hinders the formation of highly ordered crystals.[6] Besides the named factors, each protein is unique in its overall physicochemical properties and differently affected by varying the pH, ionic strength, temperature or concentration, having an effect on the crystallization probabilities.[6,109] Small molecules, can potentially form crystal contacts with every collision due to their isotropic shape. In contrast to that, the anisotropic shape and the anisotropic distribution of charges etc. of proteins lead to steric restrictions to form crystal contacts and the whole crystallization proceeds substantially slower.[68,110] For proteins, the formation of a crystal contact requires not only a sufficiently close distance between the molecules, but also their proper spatial orientation.[68] Hence, it is immensely more difficult to crystallize proteins compared to atoms or small molecules and the crystallization pathways can differ between proteins and atoms as well as between different proteins with different properties.[67,109,111–116]

As a result, attractive interactions between the different molecules appear to be of significance for protein crystallization.[117] George and Wilson could show in an empiric study that a so-called crystallization slot exists.[117] While too weak attractions may be insufficient for crystallization or too slow, too strong attractions can cause arrested aggregates, but not induce crystallization.[117] Only within an area of optimum attractive interactions, protein crystals were observed.[117] This crystallization slot was found to be close to the critical point of LLPS, hence, at reduced second osmotic virial coefficient (B_2/B_2^{HS}) values of roughly -1.5.[78,118] In other words: The attraction between the proteins needs to be large enough to enable crystallization, but not too large to provoke amorphous precipitation.[119,120] In this sense, a subtle fine-tuning is required.

1.6 Membrane proteins

Previously, the phase behavior and crystallization of globular proteins were discussed. In the following, attention will be drawn toward membrane proteins (MPs). Out of the 30000 genes humans carry, 25-35 % encode MPs.[121] Despite this importance, only roughly 3 % of all structures deposited in the Protein Data Bank (PDB) are MPs.[122] Clearly, we still know little about biological membranes and the proteins connected although they exploit vital functions and are involved in a multitude of physiological processes.[121,122] MPs transfer chemical molecules through different cell compartments and play an important role in localizing and organizing cells.[121] Due to their exposure on the surface of the cells, 60 % of the pharmaceutical drugs target MPs.[121,123,124] Hence, they are of general interest regarding human health as well as the preferred target of drugs.[121,123,124] In order to solve their structure, several methods have come into view. One of the most popular ones is to transfer the MPs embedded in the lipid bilayer into a cubic phase.[125] Since the MPs are still in their native environment, they are less prone to losing their activity than in an in meso crystallization approach.[125] The cubic phase resembles an open, porous, and bicontinuous structure that disposes the protein for interaction and complex formation with other membrane proteins and soluble components.[125] Afterward, X-ray diffraction is used to solve the crystal structures.[125]

Since MPs are mostly embedded in the hydrophobic part of membranes, they are also of hydrophobic nature and thus insoluble in water.[122,125] In order to study MPs in their native-like environment, so-called "nanodiscs" have emerged.[122,126] Originally, they consisted of a phospholipid bilayer surrounded by a belt of membrane scaffold proteins (MSPs).[127,128] The MPs can be extracted and embedded in this lipid bilayer whilst remaining active in their native environment.[129] These nanodiscs exerted a disc-like shape with their diameter varying between 7.8 and 13 nm.[126] Due to their monodisperse size and composition, they enable physiochemical investigations of the MPs, e.g., electron microscopy or solution nuclear magnetic resonance (NMR) studies.[130–133] Furthermore, structural resolution of the MPs is facilitated.[129]

In this dissertation, a new approach to form nanodiscs is studied. For this, polymers are used instead of proteins in order to form the belt around the lipids, retaining the disc-like shape.[134–136] Yet, little is known about the effects of variables such as polymer concentration, temperature, etc. on the nanodisc structure and with that the possibilities and limitations to investigate MPs.[134–136]

Part II

Outline

Protein crystallization is relevant for research fields like pharmacy and structural biology. However, most of the time, protein crystallization is achieved by trial-and-error, while the exact crystallization pathway is not yet fully understood and can differ even within same system, depending on the parameters such as temperature or precipitant concentrations.[6] Hence, this thesis aims to first characterize different protein-multivalent salt systems (i.e., the phase behavior and the respective interactions), and, second, to resolve their crystallization pathways. In the following, specific questions for each result part (Chapter IV–VII) of this thesis are highlighted.

Chapter IV: In many of these protein-multivalent salt systems, a clearly visible LLPS can be observed for selected conditions within the second regime. According to theory and simulations, nucleation should occur in the dense phase.[78,137,138] Therefore, the main questions to be answered for the first part were:

- Does crystallization indeed occur within the dense phase or not?
- Are there any other precursors?
- Where exactly does the nucleation start?
- Does the exchange in solvent alter the phase behavior and/or the crystallization pathway, i.e., are there any isotope effects due to the exchange of H_2O by D_2O as the solvent?

To answer these questions, the systems HSA with $CeCl_3$ in both H_2O and D_2O as well as HSA with YCl_3 in H_2O were investigated in the first part of this thesis.

Chapter V: After establishing the phase behavior and crystallization pathway of HSA with $CeCl_3$, we focused on its homolog, BSA, in the second result part. In the past, a similar phase behavior (including RC and LLPS) has been observed for BSA and HSA with multivalent salts, but only HSA crystals have been reported. Thus, in this follow-up study, the main questions focused on:

- Is it true that only HSA crystallizes with multivalent salts although both proteins have a sequence identity of 75 %?[139]
- What could be the origin for the behavior observed?
- Using $CeCl_3$ as an identical precipitant can differences in the phase or adsorption behavior between the two proteins be observed that could explain the absence of BSA crystals?
- What are the respective effective bulk and interface interactions?
- In general, what is the driving force for crystallization?

Chapter VI: In the third result part, the system BLG with $CdCl_2$ was investigated. Previous studies concluded a two-step crystallization pathway with a MIP as precursor in H_2O for specific sample compositions.[42,44,45] In order to study the system with non-invasive neutron experiments, using D_2O as solvent is extremely beneficial. Thus, the questions for this part focused on the solvent and the precise crystallization behavior:

- Does the system behave similarly in the new solvent (i.e., D_2O)?
- Can we obtain new insights into the crystallization pathway using neutron scattering experiments?
- Does the system still crystallize according to a two-step crystallization process in D_2O?
- How do the crystal precursors evolve with time?
- What is their exact role during crystallization?

Chapter VII: As a last goal, fundamental steps regarding the investigation of membrane proteins were attempted. Although nanodiscs composed of lipids and polymers are relatively easy to produce, their precise characterization and behavior upon changing several parameters (such as temperature and concentrations of both lipid and polymer) is still unknown. Hence, nanodiscs from one common lipid (DMPC) with two different polymers, DIBMA and SMA, acting as stabilizing belts were solubilized. Our primary questions were:

- Are there differences between the structure of the nanodiscs using the different polymers?
- What happens to the nanodisc structure if one increases the polymer concentration?
- How does a temperature change alter the structure of the nanodiscs?
- Do lipid bilayer phase transitions also occur within the nanodiscs?
- Do additional charges (due to the addition of multivalent ions) affect the nanodisc architecture?

These studies lead to a more in-depth understanding of the protein phase behavior as well as of nonclassical protein crystallization, which is not only relevant from a fundamental point, but can also aid fields such as structural resolution. In addition, a comprehensive picture of the behavior of different polymer-lipid nanodiscs for subsequent membrane protein investigations can be drawn.

Part III

Basic principles of small-angle X-ray and neutron scattering

To answer most of the questions asked in Chapter II, the main method used in this thesis is small-angle scattering (SAS). SAS is usually applied to gain information about the size and shape of particles and/or aggregates in a solution, as well as to investigate the underlying interactions within the system studied.

Although X-rays interact with the electrons of an atom, whereas neutron interact with the respective cores, the basic principle of the scattering processes and the mathematical formalism are similar for both SAXS and SANS.[140] For this reason, both SAS techniques will be treated simultaneously in this section. In particular, this section contains its basic principles, while further information on the respective experiments, set-ups, etc. will be given in the respective results chapters (Chapter IV–VII). For further information about applications and theory of SAS, the reader is referred to the literature such as Refs. 140–146.

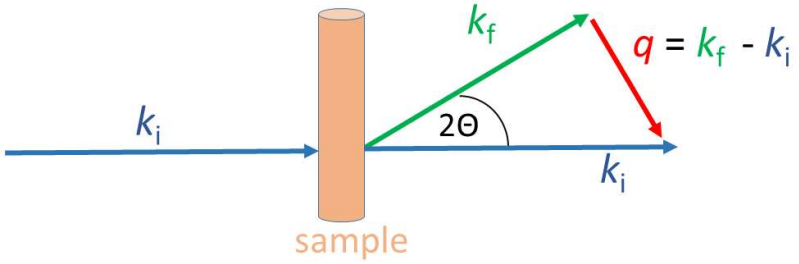


Figure 3.1: *Geometry of a scattering process. $\vec{k}_i$ represents the incoming, $\vec{k}_f$ the outgoing wave vector, $\vec{q}$ the scattering vector, and 2θ is the scattering angle.*

In Fig. 3.1, the schematic set-up of a typical SAS measurement is illustrated. The incoming beam is scattered by the sample and deviates from its initial trajectory. This deviation is usually expressed by the scattering vector $\vec{q}$, which can be expressed as:[140]

$$\vec{q} = \vec{k}_\mathrm{f} - \vec{k}_\mathrm{i} \tag{3.1}$$

In Eq. 3.1, 2θ is the scattering angle, and $\vec{k}_\mathrm{f}$ and $\vec{k}_\mathrm{i}$ are the outgoing and incoming wave vector, respectively. For elastic scattering, the energies and wavelengths λ of the incoming and outgoing waves are the same, hence, their absolute values can be characterized by $|\vec{k}_\mathrm{f}| = |\vec{k}_\mathrm{i}| = 2\pi/\lambda$.[140] Thus, the magnitude of the scattering vector, which is also called the momentum transfer and graphically illustrated in Fig. 3.1, can be described by Eq. 3.2.[140]

$$q = |\vec{q}| = |\vec{k}_\mathrm{f} - \vec{k}_\mathrm{i}| = \frac{4\pi}{\lambda} \sin\left(\frac{2\theta}{2}\right) \qquad [1/\mathrm{m}] \tag{3.2}$$

Mathematically, the measured total scattering intensity of different types of non-interacting particles can be written as a linear combination of their individual scat-

tering intensities.[140] Thereby, the fraction of radiation that is scattered depends on the scattering length density $\rho_j(\vec{r})$ from each type of particle j that scatters.[140] Summing up each contribution results in Eq. 3.3, in which b_j is the scattering length of scatterer j, and $\vec{r}$ describes its position.[147]

$$\rho(\vec{r}) = \sum_j \rho_j(\vec{r}) b_j \tag{3.3}$$

As mentioned above, scattering and therefore also the scattering length result from fundamentally different processes/origins in X-ray and in neutron scattering: While X-rays interact with the electrons of the atom shells, neutrons interact with the nuclei.[140] The latter interaction depends strongly on the spin of not only the nucleus, but also the incoming neutrons.[140] Nevertheless, for both SAXS and SANS, the Born approximation can be applied. It assumes that the interactions of the beam with one scatterer are not influenced by the scattering of others. Hence, the total scattering amplitude $A(\vec{q})$ for the illuminated volume V_S is described by Eq. 3.4.[140]

$$A(\vec{q}) = \int_{V_S} \rho(\vec{r}) \mathrm{e}^{-i\vec{q}\vec{r}} d\vec{r} \tag{3.4}$$

Since the intensity is given by the product of the scattering amplitude with its complex conjugate, this relation results in Eq. 3.5.[140]

$$I(\vec{q}) = \frac{A(\vec{q})A^*(\vec{q})}{V_S} = \frac{1}{V_S} \int_{V_S} \int_{V_S} \rho(\vec{r})\rho(\vec{r'}) \mathrm{e}^{-i\vec{q}(\vec{r}-\vec{r'})} d\vec{r} d\vec{r'} \tag{3.5}$$

For systems with more than one diffusing particles that (can) interact with each other, to access the structural information, a time-averaged intensity has to be measured. If the particles are spherical (which is the case for globular proteins), the total scattering intensity can be described according to Eq. 3.6.[141] n is the number density of particles, $P(\vec{q})$ is the particle form factor, giving information about the particle shape, and $S(\vec{q})$ is the structure factor, describing the relative position of the particles to each other and their interactions.

$$\langle I(q) \rangle = b^2(q) \sum_{i=1}^{n} \sum_{j=1}^{n} \left\langle \mathrm{e}^{-i\vec{q}(\vec{r}-\vec{r'})} \right\rangle = n b^2(0) P(q) S(q) \tag{3.6}$$

Here, the form factor is given by

$$P(\vec{q}) = \frac{1}{V^2} \int \int \rho(\vec{r})\rho(\vec{r'}) \mathrm{e}^{-i\vec{q}(\vec{r}-\vec{r'})} d\vec{r} d\vec{r'} \tag{3.7}$$

with V being the volume of the particles.[147] For a sphere, the form factor can be described by:[148]

$$P(q) = \frac{3[\sin(qr) - qr\cos(qr)]}{(qr)^3} \tag{3.8}$$

In Eq. 3.6, $S(q)$ is the structure factor given by:[141]

$$S(q) = 1 + 4\pi\frac{n}{V_s}\int_0^\infty [g(r) - 1]r^2\frac{\sin(qr)}{qr}dr \tag{3.9}$$

with $g(r)$ being the pair correlation function of the particles.[141] Note that in several fitting procedures, an effective structure factor is introduced, considering polydisperse and nonspherical particles.[149] Please also note that further models and procedures to analyze scattering data are described in the respective result chapters (Chapter IV–VII).

Part IV

Protein crystallization in the presence of a metastable liquid-liquid phase separation

Chapter IV is based on the following publication:
Protein crystallization in the presence of a metastable liquid-liquid phase separation
Ralph Maier, Georg Zocher, Andrea Sauter, Stefano Da Vela, Olga Matsarskaia, Ralf Schweins, Michael Sztucki, Fajun Zhang, Thilo Stehle, and Frank Schreiber
Crystal Growth & Design 2020, 20, 12, 7951-7962

Contributions:	
Research design	RM, AS, FZ, FS
Experiments	RM, GZ, AS, SDV, OM
Technical assistance	MS, RS
Data analysis and interpretation	RM, GZ, AS, FZ, TS, FS
Paper writing	RM, GZ, AS, FZ, FS

Reprinted with permission from *Cryst. Growth Des.* 2020, 20, 12, 7951–7962. Copyright 2021 American Chemical Society.

4.1 Abstract

We study protein crystallization in solutions of human serum albumin (HSA) exhibiting a metastable liquid-liquid phase separation (LLPS) in the presence of trivalent salts. Specifically, we focus on the effects of dense liquid phases (DLPs) on the crystallization pathways. Based on the phase diagram, we choose two conditions around the LLPS binodal: one condition is located close to, but outside the LLPS region, resulting in protein clusters, but no macroscopic LLPS. Yet, a surface-enhanced unstable DLP layer is observed at the surface of the cuvette (wetting). The second condition, inside the LLPS binodal, leads to a macroscopic metastable DLP. The crystallization is followed by optical microscopy and small-angle X-ray and neutron scattering (SAXS/SANS) as well as by ultraviolet-visible absorption spectroscopy to explore the role of LLPS. In no case, evidence of nucleation inside the DLP is observed. SAXS and SANS show a monotonous growth of the crystals and a decrease of the remaining overall material in the sample. We thus conclude that the existence of a metastable LLPS is not a sufficient condition for a two-step nucleation process. The DLP serves as a reservoir and crystal growth can be described by the Bergeron process, i.e., crystals grow directly into the dilute phase at the expense of the DLP. Furthermore, the crystallographic analysis of the resulting crystals shows that crystals with different morphology grown under different conditions share a similar crystal structure and that the metal ions create two bridging contacts within the unit cell and stabilize it.

4.2 Introduction

Knowledge of protein structures is essential for the mechanistic understanding of their functions. Crystallography remains the most powerful tool in this context, but crystal structure determination of macromolecules is often hampered by a lack of high-quality crystals suitable for diffraction. One of the main challenges in the process of crystallization is the quantitative understanding and control of protein-protein interactions under various conditions and at different length scales and how these translate ultimately into crystallization. Since multiple parameters such as temperature, concentration of both protein and potential precipitants, the nature of the precipitants, solvent, etc. are involved in protein crystallization, predictions about the process are difficult to make.

For many years, classical nucleation theory (CNT) has been used to describe crystallization.[69,70,150] It states that a nucleus forms directly from a supersaturated solution. Nevertheless, recent theoretical, experimental and simulation studies have revealed nonclassical features in the early stage of nucleation for several systems.[76,138,151–156]. In particular, the decoupling of the order parameters involved during a fluid-to-solid transition leads to the so-called two-step nucleation mechanism, in which a metastable intermediate phase (MIP) exists between the initial supersaturated solution and the final crystals. Depending on the exact free energy landscapes, the MIP can be a high density liquid phase, mesoscopic clusters, or a preordered state.[78,137,157,158]

For colloid and protein systems, dominating short-ranged attractive interactions lead to a metastable liquid-liquid phase separation (LLPS) with respect to the fluid-to-solid transition.[159] As illustrated in Fig. 4.1 a, the LLPS coexistence line is located below the solubility line, indicating the metastability with respect to the crystalline phase. LLPS may be interrupted by glass formation of the dense phase and result in an arrested state.[52]

In terms of protein crystallization, the existence of a metastable LLPS region may be the main reason underlying the formation of MIPs, as indicated by three possible pathways of two-step nucleation associated with LLPS (paths 1-3) which can be identified in Fig. 4.1. The exact pathways depend on the respective quench depths and their resulting locations in the phase diagram.[152] Starting point for the respective paths is always the single-phase region with higher reduced second virial coefficients, $B_2' = B_2/B_2^{\mathrm{HS}}$, thus, a stable fluid solution. B_2' is a measure of the interaction strength between two proteins and B_2^{HS} is the second virial coefficient of hard spheres with a radius R. Lower negative B_2'-values indicate an increased attraction between the proteins. B_2' can be tuned by, for example, varying the temperature or the solvent.[51,160–164]. Path 1 (quench down to *1* in Fig. 4.1 a representing the region near the critical point of LLPS where density fluctuations occur) leads to a two-step nucleation as initially proposed by ten Wolde and Frenkel[78]. Path 2, quenching down to *2* in Fig. 4.1 a, representing conditions inside the LLPS binodal, suggests that LLPS occurs before nucleation and both dilute and dense phase are liquid-like. The two-step theory predicts crystal nucleation inside the macroscopically dense

liquid.[78,137,138] Path 3, quench down to *3*, suggests that for a deeper quench the binodal of the high density branch is intercepted by the glass line (black), resulting in an arrested non-equilibrium state of the dense phase.[51,52] In this case, nucleation within the dense phase is hindered by dynamical arrest.[52] Compared to the CNT, the respective free energy landscapes of these nonclassical pathways thus show an additional free energy minimum (Fig. 4.1 b), corresponding to the intermediate phase. If the free energy of the intermediate phase is higher than that of the initial solution (top curve in Fig. 4.1 b), it is unstable with respect to the initial solution (but still in a local free energy minimum) and the MIP exists as mesoscopic clusters. If the free energy of the intermediate phase is lower than that of the initial solution (bottom curve in Fig. 4.1b), then the MIP can be a metastable dense liquid phase (DLP).[165] In both cases the MIPs have a higher free energy than the crystals and thus are not stable with respect to crystallization.

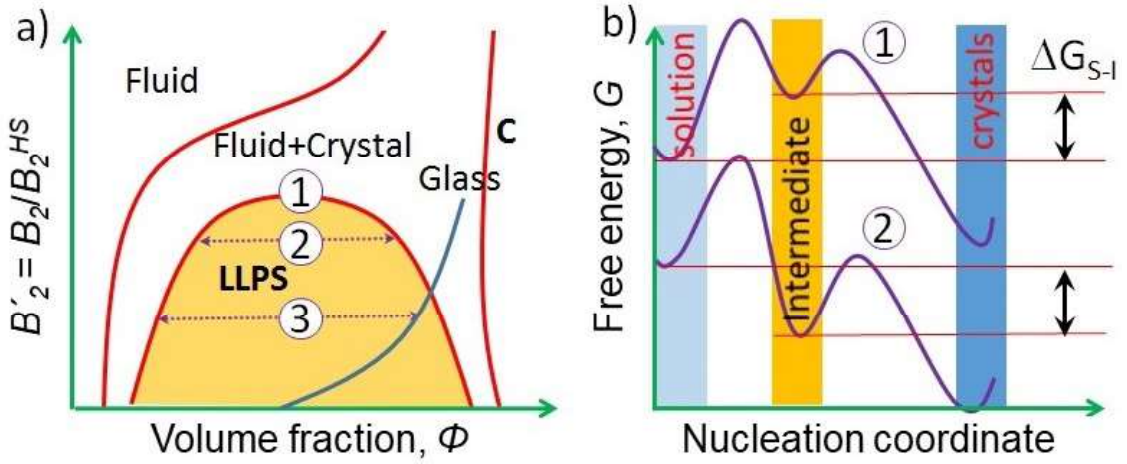


Figure 4.1: *a) Typical phase diagram for colloidal systems with short-range attractions including protein solutions. Three possible nucleation paths associated with LLPS are indicated (see text for details). b) Free energy landscapes for the nucleation paths 1 and 2 labeled in Fig. 4.1 a.*

In our previous work, we have demonstrated that multivalent salts can be used to induce a phase behavior similar to that described in Fig. 4.1 a as well as crystallization of globular proteins.[42,44–46,48] Transition metals, including especially lanthanides and yttrium, have recently become more and more popular since they are used for the structure determination of hundreds of proteins by X-ray diffraction and nuclear magnetic resonance (NMR) and are found in lanthanide-dependent metalloenzymes in bacteria.[34,166,167] One example is their presence in the active site of methanol dehydrogenase, which is involved in the metabolism of multicarbon substrates.[167,168] We have shown that negatively charged globular proteins at neutral pH undergo a reentrant condensation (RC) phase behavior in the presence of trivalent salts. RC has been originally observed for DNA[169] and has also been described

in systems of globular proteins in the presence of multivalent ions.[41,43,46–48,152,170,171] Since HSA is initially net negatively charged at neutral pH, the proteins repel each other at a given protein concentration and form a clear and stable solution (regime I, see also Fig. 4.2 further below).[43] By increasing the salt concentration (c_s) above a well-defined salt concentration (c^*), the proteins aggregate or condense due to binding the multivalent ions, diminishing their negative charge (regime II). The solution thereby turns turbid. Increasing c_s even further, above the second well-defined salt concentration c^{**}, leads to an effective charge inversion of the proteins.[41,46] Thereby, the attraction between the proteins becomes weaker and a stable and clear solution is observed again (regime III). This charge inversion of proteins can also be obtained *vice versa*, i.e., by adding negatively charged polyoxometalates (POMs) to positively charged proteins in sufficient concentrations.[172] For details, see Refs. 40, 43 and 48.

Having illustrated the phase behavior of aqueous solutions of globular proteins in the presence of multivalent salts, we proceed to explain its implications for crystallization. In our system, a metastable LLPS region exists inside regime II (see Fig. 4.2).[41,47,48,50]

According to literature, crystallization from the condensed regime may follow different pathways. Near c^*, crystals grow directly from the supersaturated solutions; near or inside the LLPS binodal, metastable LLPS occurs first and is followed by crystal growth.[42,44–48,152,173,174] An important theoretical prediction for the two-step theory is that nucleation is favored inside the dense liquid intermediate phase compared to the dilute phase, since the surface energy of the dense phase is closer to the final crystalline state, and thus the free energy barrier for nucleation is lower.[78,137,138] However, experimental observations in several protein systems suggest that crystals nucleate mainly from the dilute phase or at the interface of the dense liquid droplets and grow outside of it into the dilute phase.[175–177] These observations are often ascribed to the high viscosity or even gel state of the DLP.[52]

In spite of significant progress, many questions are still open regarding the role of this metastable LLPS for nucleation and the subsequent crystal growth. In this study, we use the protein HSA with yttrium chloride (YCl_3) and cerium chloride ($CeCl_3$) as a model system to study the effect of metastable LLPS on crystallization. For HSA with $CeCl_3$, we use both H_2O and D_2O as solvents since one can tune protein-protein interactions by exchanging hydrogen with deuterium.[161–164] In particular, we focus on whether crystals can nucleate and grow inside the DLP after LLPS. For this purpose, conditions inside and near the LLPS binodal, corresponding to metastable and unstable LLPS, respectively, are chosen for the crystallization study. We note that, in the present article, the term "unstable LLPS" implies that the LLPS is unstable with respect to both the initial solution and the crystalline phase (see *1* in Fig. 4.1 b). In contrast, metastable dense phases are more stable than the inital solution, but have a higher free energy than that of crystals (see *2* in Fig. 4.1 b).

The results presented here provide insights into the role of LLPS in crystallization processes. Importantly, in addition to the kinetic insights, we further report a

new crystal structure of HSA with metal ions incorporated in the crystal lattice, highlighting the crucial role of the multivalent ions in the crystallization process by forming intermolecular contacts.

4.3 Experiments and methods

4.3.1 Materials and sample preparation

Protein, salts and D_2O were purchased from Sigma-Aldrich, now Merck, and used as received. The guaranteed purities were 97 % for HSA (A9511), 99.99 % for $CeCl_3$ (429406) and YCl_3 (451363), and 99.9 % for D_2O (151882).

All samples were prepared by mixing the required amount of salt stock solution, deionized (18.2 MΩ) degassed Millipore water or D_2O (for neutron scattering experiments) and protein stock solution. Stock solutions were prepared by dissolving the protein and salt powders in deionized degassed Millipore water or D_2O, respectively. The concentration of HSA solutions was determined by ultraviolet (UV) absorption measurements using an extinction coefficient of $0.531\,\mathrm{L}\cdot\mathrm{g}^{-1}\cdot\mathrm{cm}^{-1}$ at a wavelength of 278 nm.[178] A Seven Easy pH instrument from Mettler Toledo was used to monitor the pH of the protein solutions. All samples had a pH (between 6.2 and 6.9) above the pI of HSA. No additional buffer was used to avoid the effect of co-ions.

4.3.2 Methods

4.3.2.1 Optical microscopy

An optical microscope (Axio Scope.A1, Carl Zeiss AG) was used for optical investigations of the samples. Images were recorded by a camera (AxioCam ICc5, Carl Zeiss AG) in combination with the software ZEN Lite 2012. The samples were prepared in two different ways. In the first case, ∼ 50 µl of solution were pipetted into a silicone ring on a glass slide and covered with a cover slide. Alternatively, ∼ 350 µl were filled into a type 120 quartz glass cuvette (Hellma GmbH, Müllheim, Germany) with a path length of 1 mm. After mixing the samples in a separate tube, they were filled into the quartz cuvettes which were subsequently sealed by Parafilm®. The software ZEN Lite 2012 was used to conduct the imaging as well as to measure the crystal lengths.

4.3.2.2 UV-visible spectroscopy (UV-vis)

UV-vis was used to follow the change in protein concentration of the dilute phase during crystal growth in the presence of a metastable DLP. The experiments were performed with a UV-vis spectrophotometer (Cary 50 UV-vis spectrometer, Varian Technologies, USA). The solutions were probed in a quartz cuvette with a path length of 1 mm. UV-vis spectra were collected every 10 min over a period of several days.

4.3.3 Determination of the phase diagram

The phase diagram of Fig. 4.2 was determined following the procedure established in our group as reported in previous work.[47,50] The respective c^* and c^{**} phase transition boundaries (with $c^* < c^{**}$) were determined by visual inspection of 200 µl samples at c_p = 10, 15, 20, 22.5, 25, 30 35, 40 and 50 mg/ml HSA in H_2O and c_p = 10, 20, 35 and 50 mg/ml HSA in D_2O and varying c_s. The mean of the c_s of the last clear and first turbid or last turbid and fist clear sample is referred to as c^* or c^{**}, respectively. The LLPS binodals in the phase diagram (Fig. 4.2) were determined using UV-vis spectroscopy. Samples were prepared at 35 and 45 mg/ml HSA and varying c_s for both solvents H_2O and D_2O. The macroscopically liquid-liquid phase-separated state of these samples was verified by visual inspection. The sample tubes were centrifuged for 2 min with 21030 x g to separate the dilute and the dense phase. The concentration of the dilute phase was determined by the UV-vis spectrophotometer.

4.3.3.1 Small-angle X-ray scattering (SAXS)

SAXS measurements were performed at the European Synchrotron Radiation Facility (ESRF), Grenoble, France, at beamline ID02.[179] The sample-to-detector distance was set to 2 m. The photon energy of the incoming X-rays was 12 keV, covering a q-range from 0.25 to 3.2 nm^{-1}. The exposure time was 0.1 s for each measurement. The crystals were collected and filled into a quartz capillary with a wall thickness of about 10 µm and a diameter of 2 mm. The sample capillary was inserted into the beam vertically. Between the measurements, the capillary was shifted up and down to measure the scattering pattern at different positions. The 2D intensity pattern was calibrated to absolute intensity and azimuthally averaged to obtain the intensity profiles. The averaged profiles from different positions were used to index the Bragg peaks. More detailed information on data reduction and q-resolution calibration can be found in the literature.[180,181]

Additional SAXS data were collected on a laboratory instrument (Xeuss 2.0, Xenocs, Grenoble, France) employing a GeniX 3D microfocus X-ray tube with a copper anode, using an X-ray wavelength of 1.54 Å. With a sample-to-detector distance of 1850 mm, the employed Pilatus 300K detector covered a q-range from 0.055 to 2.25 nm^{-1}. Quartz capillaries with a diameter of 2 mm were used. The acquisition time per run was 10 min.

4.3.3.2 Small-angle neutron scattering (SANS)

SANS measurements were carried out at beamline D11 at the Institut Laue-Langevin (ILL), Grenoble, France.[182] The sample-to-detector distance was 2 m which covers a q-range from 0.03 $Å^{-1}$ to 0.33 $Å^{-1}$ at a wavelength of 6 Å ($\Delta\lambda/\lambda$ = 10 %). Protein-salt solutions in D_2O were filled into rectangular quartz cells with a path length of 2 mm. The beam size on the sample was 7 mm x 10 mm. The acquisition time per run was 240 s. Runs were repeated in appropriate time intervals in order to

follow the crystallization process over a period up to several days. H_2O was used as secondary calibration standard to calibrate the absolute scattering intensity. Data were stored in NeXus data format.[183] The data correction and absolute intensity calibration were performed using the software LAMP.[184] Data can be accessed via the DOI: 10.5291/ILL-DATA.9-13-672.[185]

4.3.3.3 Protein crystallization and crystal structure analysis

High-quality protein single crystals were obtained for a sample containing 31.0 mg/ml HSA and 2 mM YCl_3 at 293 K by batch crystallization in small glass vials.

Single crystals were pipetted onto a siliconized glass plate and subsequently subjected to a stepwise cryo-protection using the mother liquor, i.e., H_2O with the respective c_s, supplemented with 26 % (v/v) glycerol. Crystals were mounted into a loop prior to flash-freezing in liquid nitrogen. X-ray diffraction data were recorded at beamline X06SA at the Swiss Light Source (SLS), Villigen, Switzerland. A highly redundant data set was recorded at a wavelength of 1.7 Å to maximize the anomalous signal of the yttrium ions (Tab. A.1). The data were reduced using the XDS package.[186] Phases were obtained by the molecular replacement procedure of PHASER[187] using HSA as template structure (PDB code: 2BXI) followed by a simulated annealing approach as implemented in PHENIX[188] to reduce the model bias. The following refinement was done in several cycles of reciprocal space refinement as implemented in REFMAC5[189] followed by real space model corrections using COOT.[190] Positions of the metal ions were determined on the basis of a $|F^+ - F^-|$-electron density map. The structure was validated using MOLPROBITY,[191] visualized with PYMOL[192] and deposited to the Protein Data Bank with accession code 7A9C.

4.4 Results and discussion

4.4.1 Experimental phase diagram of the HSA-$CeCl_3$ system at room temperature

First, we present the phase diagram and the crystallization conditions of our systems. Fig. 4.2 summarizes the phase behavior including reentrant condensation and LLPS of HSA-$CeCl_3$ in H_2O and in D_2O. For this system, the second regime and the LLPS region in D_2O are significantly broadened in comparison to H_2O. In essence, the c^{**} boundary is shifted to higher salt concentrations, whereas c^* remains approximately at the same location. The LLPS binodal is also shifted to much lower protein concentrations in D_2O. The shift of the phase boundaries results from enhanced attractive interactions in D_2O as reported in our previous work on a similar system.[164] This solvent isotope effect has been observed for several other proteins, such as lysozyme and γB-crystallin solutions.[161–163] In contrast to its bovine variant bovine serum albumin (BSA), which we have also investigated in detail (see Refs.

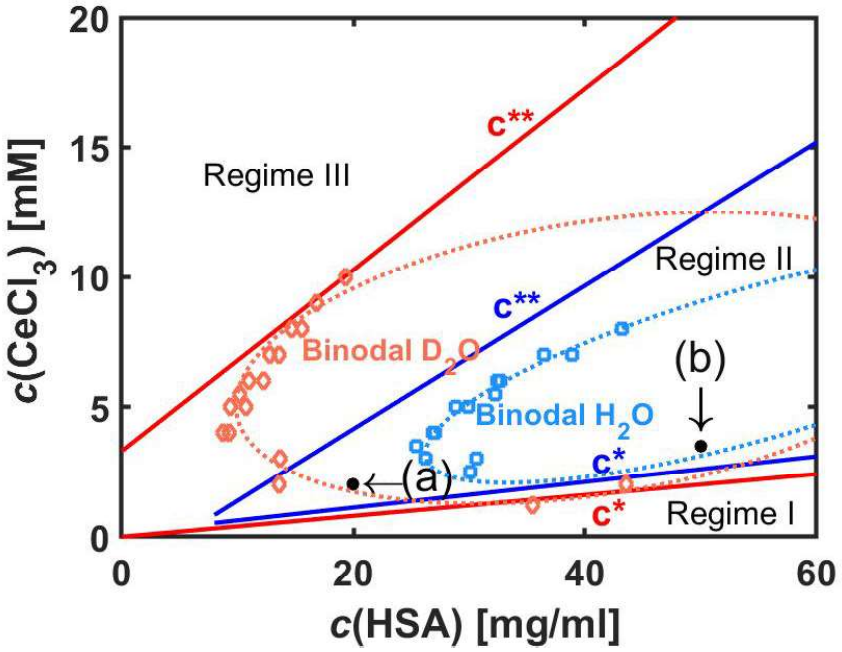


Figure 4.2: *Experimental phase diagram of HSA with $CeCl_3$ in H_2O (blue) and in D_2O (red) at room temperature. Both RC and LLPS exist in both solvents, but replacing H_2O by D_2O significantly broadens the phase boundaries due to an enhanced interprotein attraction.*[164] *The crystallization conditions examined in this paper are labeled as (a): outside the LLPS area in H_2O, and (b): inside the LLPS area for both solvents. The dotted binodal ellipses are guides to the eye. The solid lines represent fits for c^* and c^{**} in the respective system, determined by visual inspection as described in the text.*

40,43,160,164,170,193–195) and which also shows RC, LLPS and a tunable phase behavior using a deuterated vs. protonated solvent,[164] HSA is able to crystallize in the presence of multivalent salts. We have investigated HSA with YCl_3 before as well,[50] but the HSA-$CeCl_3$ system crystallizes more controllable and is therefore used as model system. Another advantage for the purpose of this work is the clear LLPS binodal, which is mostly not the case for β-lactoglobulin systems.

The experimental phase diagram provides a guide for optimal conditions of protein crystallization. Slightly below c^*, macroscopic needle-like crystals are formed and no visible intermediate phase is observed. Crystals appear directly in the clear supersaturated solution.[42,44] For HSA with $CeCl_3$, the crystals feature predominantly lenticular shapes (see Fig. 4.3 and Fig. 4.5). Different morphologies of crystals grown in the presence of YCl_3 are shown in Fig. A.1. We found that near c^* and at the lower boundary of the LLPS binodal, proteins crystallize reproducibly.[47] In the present work, we choose two typical conditions around the LLPS binodal as labeled with (a) and (b) in Fig. 4.2. The first condition (a) is located outside of the binodal.

Under this condition, protein clusters exist, but macroscopic LLPS is impossible. However, at the liquid/solid interface, a surface-enhanced wetting layer of dense phase may form, meaning the DLP can only exist at a surface stabilizing it due to its location outside the binodal in the phase diagram.[196] Thus, the free energy of the dense phase is even higher than that of the initial supersaturated solution and corresponds to path 1 shown in Fig. 4.1. The second condition ((b) in Fig. 4.2) is located inside the LLPS region, where macroscopic LLPS leads to a protein-rich and a protein-poor phase. Both are metastable with respect to the crystalline phase. This condition corresponds to path 2 in Fig. 4.1. These crystallization areas at constant temperatures in the phase diagram are consistent with theoretical predictions.[47,118]

4.4.2 Crystal growth with unstable LLPS – Path 1

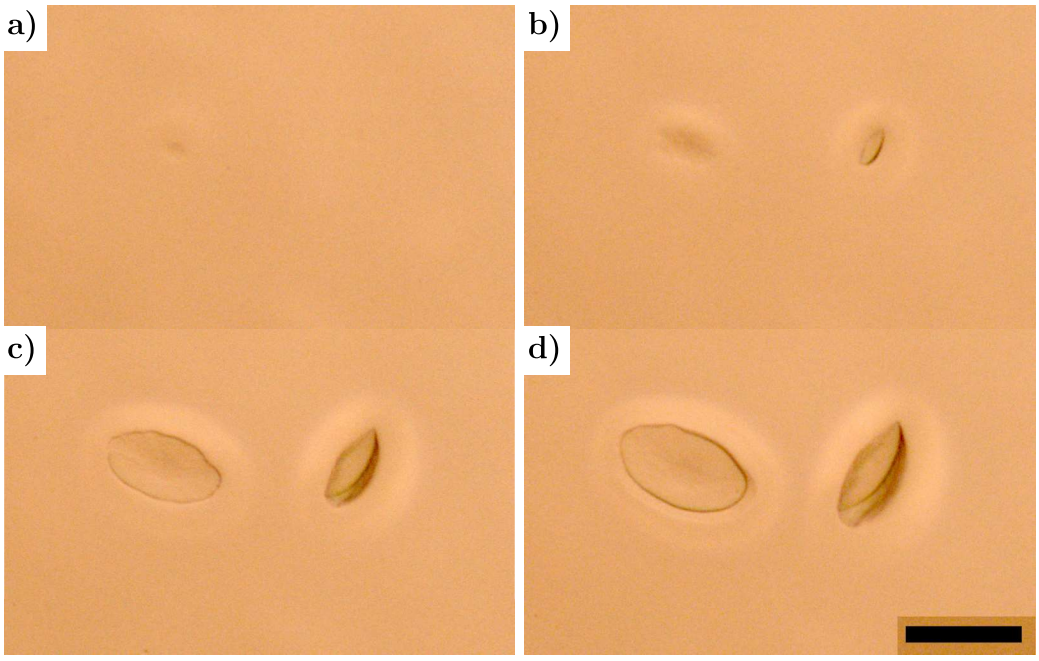


Figure 4.3: *Bright field optical microscopy observations of crystallization of a sample containing 20 mg/ml HSA and 2.5 mM $CeCl_3$ at different times after preparation. The sample was briefly centrifuged in the cuvette before examination under the microscope in order to concentrate the protein aggregates on one site. a) 4.3 h, a small crystal appears at the wetting layer; b) 5.7 h, a second crystal appears; c) 7 h and d) 7.7 h, crystal growth and consumption of the DLP lead to the formation of a depletion zone around the crystals. The scale bar corresponds to 50 µm for all panels.*

We will first discuss the crystallization experiments for the samples located at position (a) in Fig. 4.2. Fig. 4.3 shows the crystallization process of a sample which is located outside the lower part of the LLPS region (20 mg/ml HSA and 2.5 mM $CeCl_3$ in H_2O). A depletion zone appears around the crystals. The formation of a depletion zone for a different salt concentration is shown in Fig. A.2, indicating

reproducibility. In the phase diagram (Fig. 4.2), condition (a) is located outside the LLPS binodal for H_2O. Nevertheless, it is visible that the unstable microscopic dense droplets sediment to the bottom, where they are able to form a layer on the glass surface. Since the dense droplets are visible only for several minutes by microscopy (in contrast to path 2), we expect them to be unstable with respect to the initial solution (see Fig. 4.1 b) and to completely dissolve again without an interface to sediment onto. Hence, this layer of dense phase is presumed to be a surface-enhanced phenomenon.[196]

Crystal growth kinetics for the same conditions was further studied using real-time SAXS and SANS. Real-time SAXS data of a sample containing 20 mg/ml HSA and 2 mM $CeCl_3$ are shown in Fig. 4.4 a. The SAXS profiles are initially smooth and the scattering intensity mainly stems from the protein form factor in the high q ($> 0.1\,\text{Å}^{-1}$) region. In the intermediate q-range, the overall attraction leads to an intensity increase with decreasing q. The low q ($< 0.01\,\text{Å}^{-1}$) upturn indicates the formation of protein clusters. No additional structural features from the protein clusters were seen, which is in contrast to the β-lactoglobulin (BLG)-$CdCl_2$ system we studied previously where an additional protein-protein correlation peak reflects the presence of an intermediate phase.[44,45] Over time, the overall intensity decreases in the q-range measured, and after 10 h the first Bragg peak appears at $q = 0.069\,\text{Å}^{-1}$.

For a quantitative analysis of the growth kinetics, we have integrated the intensities in the range from 0.03 to $0.06\,\text{Å}^{-1}$ and plotted the resulting values as a function of time in Fig. 4.4 b to follow the process of protein consumption from solution. This range was chosen for several reasons. First, since no additional structural feature is visible in the raw data indicating scattering from a different phase, one cannot distinguish contributions in the scattering signal from the wetting layer observed under the microscope and the dilute phase. Importantly, the structure factor dominates the signal in this q-region. The decrease in intensity is therefore attributed to the overall material consumption during crystallization. Second, it is accessible with both SAXS and SANS, and therefore the data can be easily compared. Third, it does not overlap with the Bragg peaks, so these different contributions can be well separated. We have also integrated the q-range between the first and the second Bragg peak for all samples, leading to the same results. Last but not least, the statistical data quality is higher for lower q-values.

The values for the area of the Gaussian fit of the Bragg peak at $q = 0.069\,\text{Å}^{-1}$ after subtracting a linear background are also plotted in order to follow crystal growth. One can see that the scattering intensity from the solution begins to decrease after ~ 8 h. At the same time, the Bragg peak starts to grow. Both changes proceed monotonously and no stepwise change is visible. After ~ 20 h, the Bragg peak intensity reaches a maximum value which remains nearly constant. In Fig. 4.4 b, data points of the Bragg peak fit were binned in groups of three to improve the statistics. The error bars represent the respective standard deviation. This procedure was not necessary for the SANS data, because the R^2-values of the Gaussian fits are all higher than 0.92. The error of the integrated scattering intensity of the overall

material is always much smaller than the symbols, and thus not plotted for clarity. For all data sets (SAXS and SANS), both the intensity of the Bragg peak and of the proteins inside dense and dilute phase were fitted by a logistic function (Eq. 4.1), where A is the maximum of the curve, k its logistic growth rate or steepness and t_1 the time of its midpoint.[197]

$$f(t) = \frac{A}{1 + \mathrm{e}^{-k(t-t_1)}} \tag{4.1}$$

According to Arrhenius' law, the initial exponential increase in the intensity of the Bragg peak is caused by nucleation,[198] which is the rate-limiting step at this time. Later, the growth of the crystals is linear until it eventually reaches a plateau due to limited material in solution. Depending on how far away the solubility line is located from the LLPS binodal, crystals can still grow after all dense phase is consumed, since the dilute phase is then consumed (see also later). The midpoints for both curves in Fig. 4.4 b are $t_{1,\mathrm{Bragg}} = 15.59\,\mathrm{h}$ and $t_{1,\mathrm{solution}} = 16.04\,\mathrm{h}$. The time of the midpoint, t_1, is also the time of the turning point of the curves and can be seen equal to the respective time of the extremum of the first time derivatives. Since the t_1-values are similar, indicating that proteins are consumed the fastest when crystals grow the fastest, this result suggests again a one-step process. All fit parameters are listed in Tab. A.2.

A similar condition (inside the second regime, but outside the LLPS binodal) for the system in D_2O (10 mg/ml HSA with 2 mM $CeCl_3$ in D_2O) was studied by SANS. The results are shown in Fig. A.3. Both SAXS and SANS measurements show a similar growth behavior: first, around the Bragg peaks, no additional structural feature is visible, which could be used to identify the intermediate phase. Due to the crystal size, the crystals sediment to the bottom of the container once they are big enough. SANS has the advantage of a large scattering volume with a large number of crystals contributing to the intensity. The results shown above indicate that given the current conditions, crystal growth can be described by a one-step crystallization. Combining with results from microscopy and UV-vis, we conclude that after nucleation in the dilute phase or at its interface with the dense phase or the container, the crystals grow into the dilute phase while they first consume the dense phase/wetting layer, followed by the dilute phase.

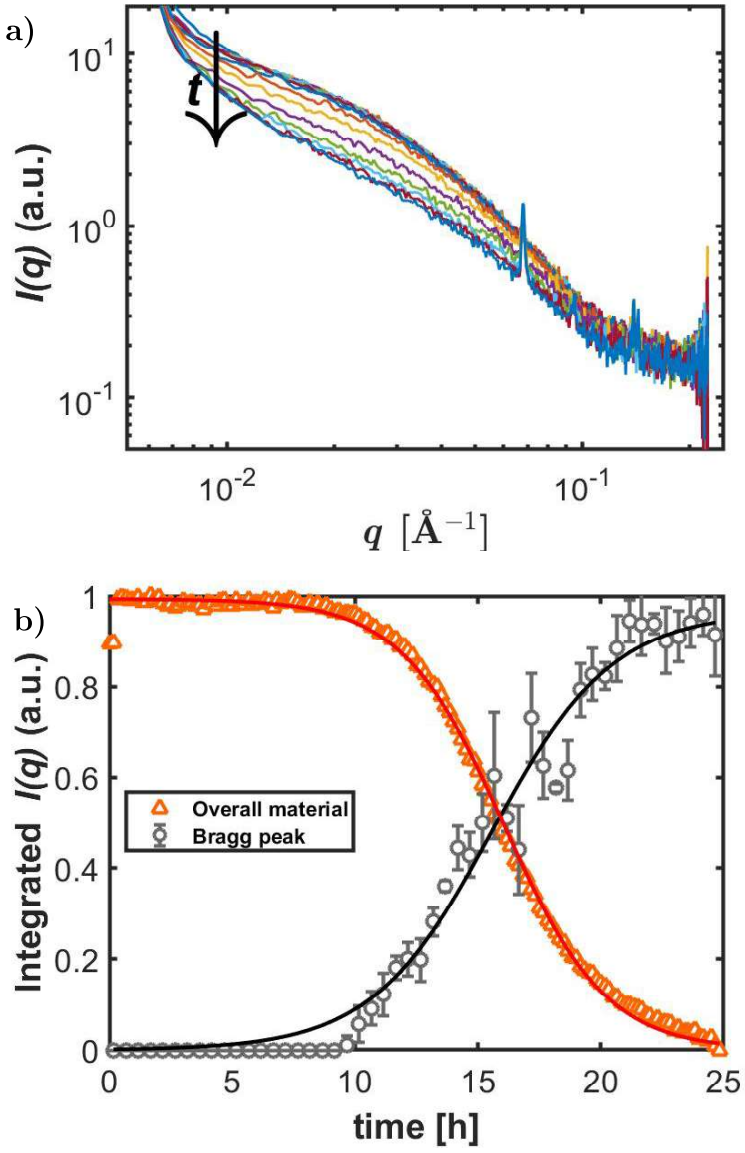


Figure 4.4: *SAXS data of a sample containing 20 mg/ml HSA and 2 mM $CeCl_3$. a) Scattering intensity curves between 0 and 25 h after sample preparation as functions of q, and b) analysis of the kinetics based on the integrated area covered by Bragg peaks and the low q-intensity between 0.03 and 0.06 Å^{-1}. The solid lines represent the corresponding fits (Eq. 4.1).*

4.4.3 Crystal growth with a metastable LLPS – Path 2

We now present the results of crystal growth at position (b) in Fig. 4.2, i.e., inside the LLPS binodal. We prepared one set of samples containing 50 mg/ml HSA and 3.5 mM $CeCl_3$, located at the lower binodal boundary of LLPS in the phase diagram. In this case, the amount of dense phase is small and it appears rather liquid-like than gel-like.

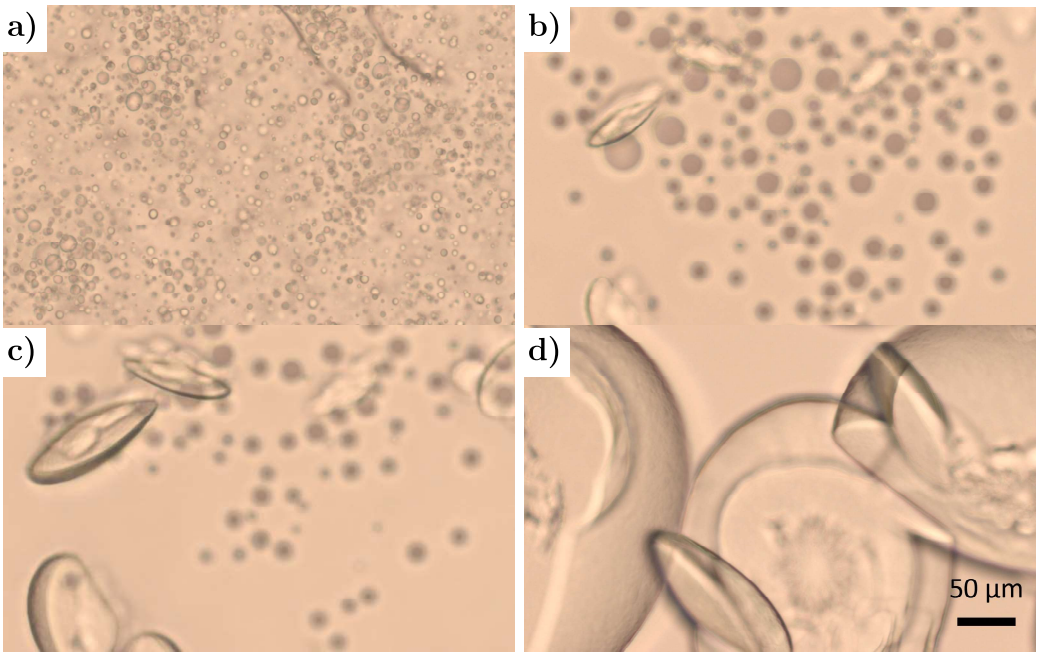


Figure 4.5: *Crystal growth of a sample containing 50 mg/ml HSA and 3.5 mM $CeCl_3$ at different times after sample preparation: a) 10 min; b) 6 h; c) 8 h and d) 17 h. The scale bar corresponds to 50 µm.*

The crystal growth of this sample followed by optical microscopy is shown in Fig. 4.5. Tiny droplets of DLP are visible right after preparation. Some of them sediment to the bottom surface while some stay in solution. The latter merge and disappear with time. In contrast to path 1 described previously, the droplets appear stable with respect to the initial solution (see Fig. 4.1 b), evidenced by their increased lifetimes. Crystals appear $\sim$2 h after preparation. While nucleation is not observed in the dense phase, it is seen in the dilute phase or at its interface with the container, which suggests a one-step crystallization. The latter two scenarios cannot be distinguished due to the limited resolution of the optical microscope. After 17 h, the system is crystallized and no further changes can be observed on a reasonable timescale. Crystal growth first consumes the material (dense phase) around the crystals, leading to a depletion region or "buffer zone". Similar observations have been reported for crystal growth in lysozyme solutions undergoing LLPS.[177]

An interesting observation concerns the consumption of the dense phase upon crystal growth. Under the microscope, one can see that the droplets are shrinking,

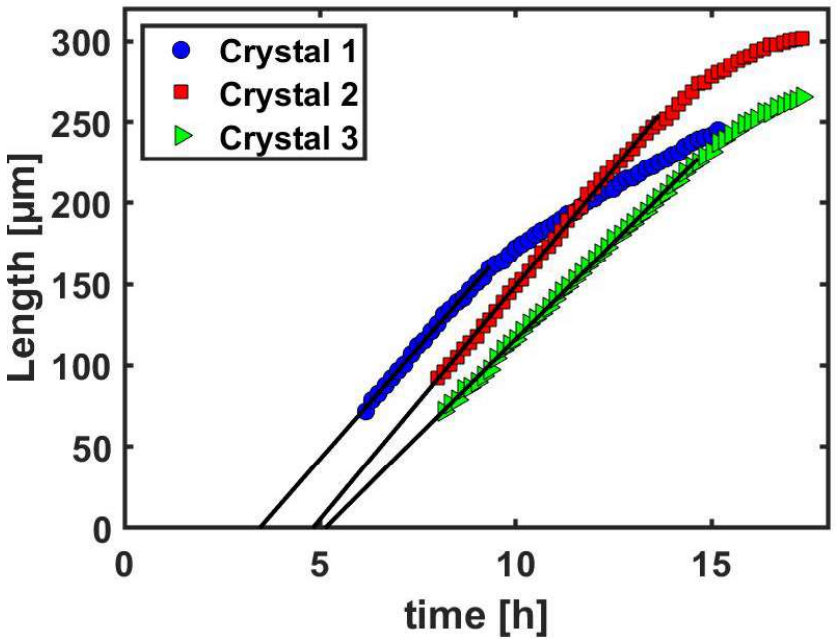


Figure 4.6: *Crystal length as a function of time for the sample shown in Fig. 4.5. After 11.7 h, no dense droplets can be observed anymore.*

but neither do crystals grow into the droplets nor do droplets incorporate into the crystals. This suggests crystal growth via the deposition of proteins from the dilute phase. While the dilute phase feeds crystal growth, the droplets dissolve, i.e., the crystal growth does not consume the droplets directly.

In Fig. 4.6, size measurements for three different crystals of the sample containing 50 mg/ml HSA and 3.5 mM $CeCl_3$ are shown. In every case, the initial crystal growth follows a linear relationship. The fits are further extrapolated to obtain the induction times $t_0 = 3.5, 4.8$ and 5.1 h for crystals 1-3, respectively. Note that these measurements are performed for crystals in the focal area, which are not necessarily the ones that grew first. In addition to the growth rates and the induction times, the final sizes of the crystals (250 to 300 µm) are similar. The disappearance of the dense droplets seems to have no direct impact on their growth rate. The late stage saturation of the size can be explained by the limited amount of material in the solution. This linear growth behavior would be consistent with a one-step nucleation process.

The crystal growth kinetics was further characterized using SANS. Fig. 4.7 shows SANS data and the corresponding analysis of a sample containing 50 mg/ml HSA with 3.5 mM $CeCl_3$ in D_2O. The corresponding optical microscopy images of the crystal growth in D_2O are presented in Fig. A.4. Although the appearance of the DLP is different in D_2O (network) than in H_2O (droplets) because of enhanced interprotein attractions in D_2O, crystal growth in H_2O and D_2O is comparable. Again, the overall smooth SANS curves show a decrease in intensity in the low

q-region as shown in Fig. 4.7 a. With time, Bragg peaks appear and their areas increase. In addition to the overall material consumption, the area of the Gaussian fit of the first Bragg peak at $q = 0.07\,\text{Å}^{-1}$, representing the crystalline phase, is plotted in Fig. 4.7 b. It increases with time, indicating crystal growth. Similarly to Fig. 4.4 b, both changes are monotonous and no stepwise change is visible.

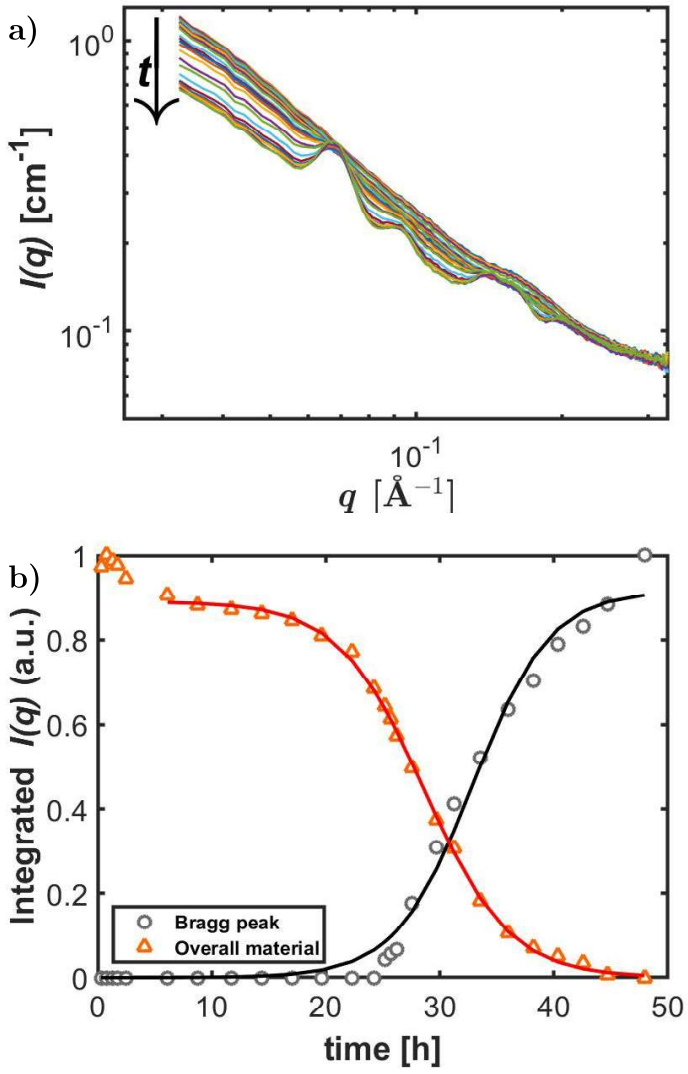


Figure 4.7: *a) SANS profiles of crystal growth of a sample containing 50 mg/ml HSA and 3.5 mM $CeCl_3$ in D_2O between 0 and 48 h. b) Analysis of the kinetics based on the areas of the Bragg peak at $q = 0.07\,\text{Å}^{-1}$ and the normalized integral of intensity in the q-range from 0.03 to 0.06 Å^{-1} for the crystalline phase and the overall material, respectively. The solid lines represent the corresponding fits (Eq. 4.1).*

The slight decrease in intensity in the beginning may be due to the temperature difference between sample preparation and the measurement (Fig. 4.7 b). Therefore, these data points were not taken into account for the fit. Afterward, an initially

exponential increase followed by a linear part of the Bragg peak area is visible again. The increase at later stages is more pronounced compared to the samples discussed before (Fig. 4.4 b). The solubility line may be located further away from the LLPS binodal or some crystals may have sedimented from the top of the cuvette into the beam region, causing this increase. However, the respective t_1-values are similar again. This result is also consistent with a one-step crystallization where the metastable dense phase serves as a reservoir for the crystal growth and is consumed during the process. We would expect a stepwise growth for a two-step nucleation as it can be, for example, observed for BLG with $CdCl_2$.[44,45]

To further clarify the role of the DLP in crystallization, we have determined the protein concentration of the dilute phase during crystal growth. After preparation, the samples were briefly centrifuged in order to deposit the dense phase at the bottom of the cuvette. The protein concentration of the dilute phase was followed by UV-vis as shown in Fig. 4.8 a. The protein concentration in the dilute phase as a function of time is plotted in Fig. 4.8 b and can be divided into three stages: first (from the beginning to about 15 h) the protein concentration is almost constant and corresponds to the dilute phase resulting from LLPS. During this time, crystals are already formed, but crystal growth consumes the dense phase, and thus, the dilute phase has an almost constant concentration. The minor increase in protein concentration can be caused by a slight temperature difference between the centrifuge and the UV-vis spectrophotometer. In the second stage, the concentration decreases quickly with time, corresponding to a growth procedure of the crystals while consuming the dilute phase. In the third stage, the protein concentration of the dilute phase is low, corresponding to the gas-solid (solution-crystal) equilibrium, i.e., the solubility line.

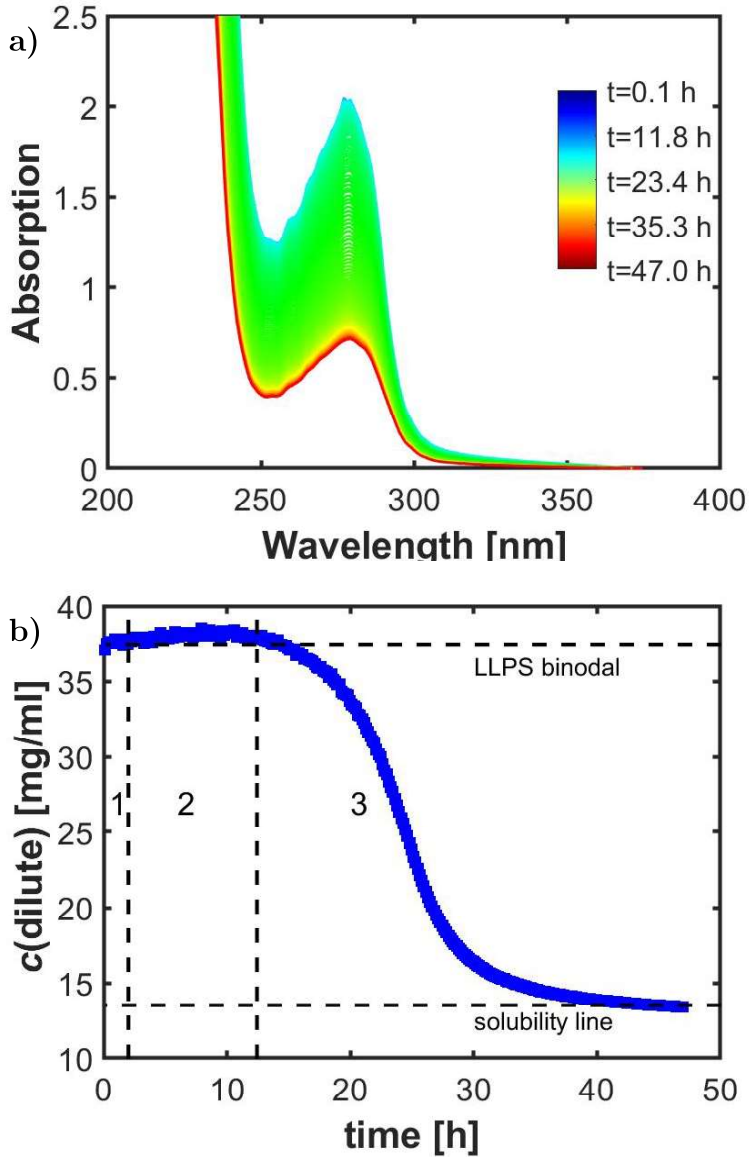


Figure 4.8: *Protein concentration of the dilute phase during crystal growth of a sample containing 50 mg/ml HSA and 3.5 mM $CeCl_3$ monitored by UV-vis. a) Real-time UV-vis spectra, and b) protein concentration as a function of time. Based on microscopy data (exemplarily shown in Fig. 4.5), we distinguish three sections. In section 1, no crystals are formed yet, while they nucleate and consume the dense droplets in section 2 and grow further without visible dense phase in section 3.*

4.4.4 Discussion of the role of metastable LLPS for protein crystallization

In summary, our growth kinetics studies by optical microscopy for individual crystals as well as by real-time SANS/SAXS and UV-vis for the overall growth kinetics lead to the consistent conclusion that the crystal nucleation for the present system follows a one-step process and the intermediates (dense liquid droplets/wetting layer or protein clusters) serve as a reservoir. Such a growth pathway is illustrated in Fig. 4.9.

Two-step nucleation theory predicts that a metastable high density liquid phase is favored for crystal nucleation because of the lower free energy barrier. However, any experimental studies indicate that crystals form either inside the dilute phase or at the interface between the dense and dilute phase and grow into the dilute phase. This has been attributed to the arrested state of the dense phase.[175–177] This may indeed be the case for lysozyme.[52] The fact that the dense phases studied in the present work are always able to merge as well as dissolve again, similar to the study by Ray and Bracker,[176] indicates, however, that they are liquid-like. Thus, the slow dynamics cannot be used to explain the absence of nucleation inside the dense phase. We expect that a combination of heterogeneous and homogeneous nucleation may be the alternative. Due to the low resolution limit of the optical microscope, one cannot unambiguously determine if nucleation takes place at impurities, at interfaces of the dilute phase with the dense phase or with the sample container, or directly in the dilute phase. Nevertheless, nucleation inside the dense phases was not visible in any of our experimental conditions, even with extremely long lifetimes of the metastable ones. We speculate that to some extent the mechanism of enhanced adsorption (and possibly crystal nucleation) at the interface of the glass container may play a role, but a detailed study of this is beyond the scope of the present work and can be found in Refs. 194 and 195.

We note that observations of two-step processes involving manifold kinds of precursors have been made for several proteins.[42,44,45,137,151,152,158,199–202] We do not completely rule out the possibility that different precursors with a short lifetime in solution may initiate crystal nucleation (which is beyond the resolution limitation of the microscope and which we also do not observe with SAXS/SANS). In our work, we aim to investigate the role of macroscopic LLPS on nucleation. The macroscopic dense droplets are clearly visible under the microscope and their lifetime is extremely long (hours). Under our experimental conditions, we can demonstrate that no nucleation occurs inside the macroscopic DLP after LLPS. We also note that protein crystallization pathways depend strongly on the specific systems and the respective conditions. This work provides evidence of a scenario where an MIP forms, but does not initiate interior nucleation. This scenario is not described in Fig. 4.1 a.

Furthermore, we note that the crystallization behavior discussed here (Fig. 4.9) is very similar to the "Bergeron process", i.e., crystal growth via vapor deposition at the expense of the metastable DLP. The Bergeron process has been used to describe the water condensation process at high altitudes and the fluid-solid phase

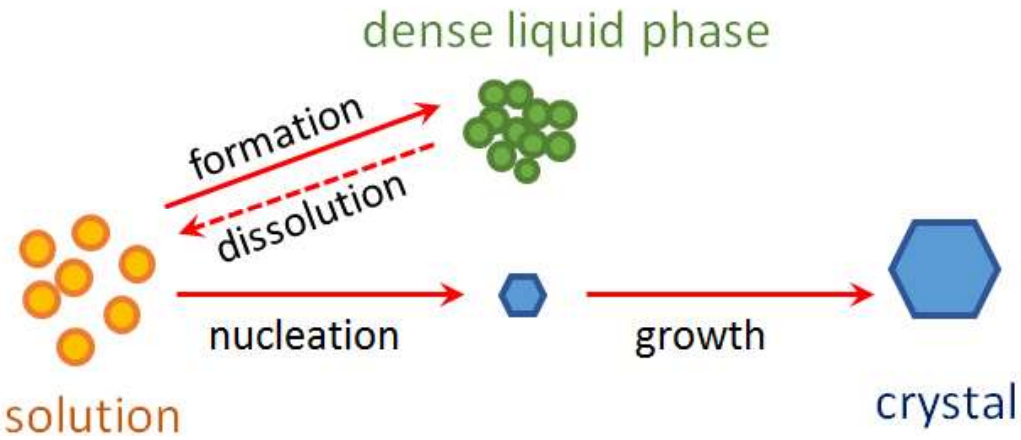


Figure 4.9: *Schematic of the nucleation pathway of protein crystallization in the presence of a metastable LLPS as revealed from this study.*

transition in colloidal systems.[203] Once crystals are formed, crystal growth via vapor deposition (here: from the dilute phase) is more favored than growth through the supercooled water droplets (here: DLP) due to different saturation vapor pressures of the crystals and the metastable droplets. We can easily compare these two cases because of the existence of a metastable LLPS, resulting in a gas (dilute) and a liquid (dense) phase. This can also explain why crystals are observed to grow into the dilute phase instead of into the dense phase after nucleation.

4.4.5 Crystal structure of HSA-Y^{3+} crystals by single crystal X-ray diffraction and the role of multivalent metal ions

Optimizing crystallization conditions of HSA with YCl_3 led to high-quality crystals, the structure of which is presented in the following. Before we introduce the crystal structure analysis, we first compare the overall crystal structure of crystals grown with different salts under various conditions. Crystals grown under different conditions and with different morphologies were collected and filled into quartz capillaries for SAXS measurements. As shown in Fig. 4.10, the SAXS profiles of all crystals have Bragg peaks at very similar positions and with similar intensities. The corresponding Miller indices for the first Bragg peaks are also shown. From this agreement, it can be concluded that the crystals of different shape and of different salts have a similar crystal structure. This result is in good agreement with the fact that yttrium and cerium are chemically similar to each other[167] and the phase behavior of HSA solutions in the presence of the two cations is also similar. Nevertheless, for growing high-quality single crystals suitable for X-ray diffraction, HSA with YCl_3 turned out to be the more reliable system. Hence, the crystal structure

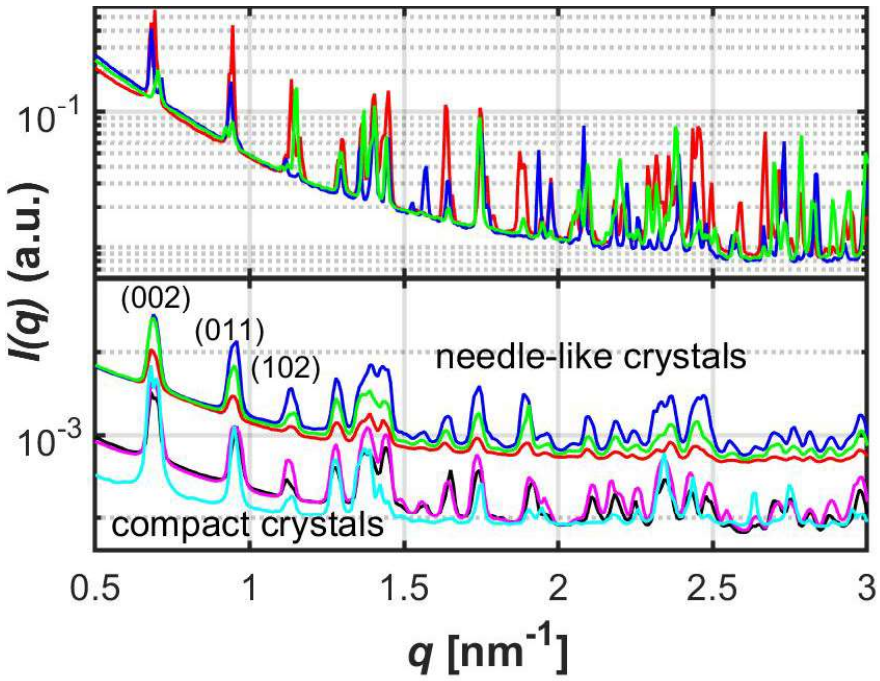


Figure 4.10: *Comparison of SAXS profiles of HSA crystals grown under different conditions with different morphologies and different salts measured at different positions in the capillary. Top: 150 mg/ml HSA with 10 mM $CeCl_3$; bottom: 30 mg/ml HSA with 3 mM YCl_3 resulting in different morphologies, which are shifted for clarity (top: needle-like crystals, bottom: compact crystals). The Bragg peaks can be assigned to the corresponding Miller indices using the HSA crystal structure determined in this article (PDB code: 7A9C).*

analysis was performed with HSA-YCl_3 crystals.

Yttrium causes HSA to crystallize in a so-far not-described crystal form with spacegroup $P2_12_12_1$ and unit cell dimensions of $a = 55.27$ Å, $b = 71.93$ Å, $c = 180.13$ Å, respectively. Nonetheless, the overall fold of the protein is not influenced by the metal ions and is virtually identical to the HSA structures deposited in the PDB data base possessing a Cα-rms deviation of 0.84 Å for 579 out of 581 aligned amino acids. The model quality is reasonable for the given resolution of 2.75 Å and allowed to clearly identify the yttrium ions on the basis of an anomalous difference map (coefficient: $|F^+\text{-}F^-|$) in combination with the chemical environment.[204] Two chemically different metal ions were identified that interconnect the HSA protomers in the crystal (Fig. 4.11 b and c), resulting in an overall stoichiometry of HSA to Y^{3+} of 1:2. Each HSA protomer is in contact with ten symmetry-related HSA molecules, but only four protomers out of these are mediated by yttrium interactions. The coordination of the yttrium ions is comparable to the interactions observed for BLG (PDB code: 3PH5, 3PH6) and shows that each yttrium ion is coordinated by three negatively charged glutamate side chains, thereby compensating the positive charge of the metal ion.

We performed an interface calculation, i.e., the ratio between the surface of the binding sites and the total surface of the protein, using PISA [205] to analyze the metal ion contribution for the crystallization of HSA and BLG (PDB code: 3PH5) in the presence of yttrium. The total interface area in the HSA:Y^{3+} crystals is calculated to be 2052 Å^2 out of which 316 Å^2 (15.4 %) is mediated by Y^{3+}-protein interactions. This is in good agreement with the observation that most of the contacts of the 585 amino acid long protomers are formed by protein-protein interactions and the influence of the metal ion is less pronounced for HSA. This is different for BLG-Y^{3+} crystals where the yttrium ions contribute more substantially to the crystal contact formation. Here, the four yttrium ions of the dimeric protein make up 30.2 % of the total crystal contact area (577 Å^2 out of 1907 Å^2).

In summary, we show that the high valency metal ions bridge the proteins and develop two new protein contacts, which stabilize the crystal lattice for both metal salts used. This is in contrast to the crystal structure of BLG in the presence of YCl_3 where all four binding sites contribute to the bridging contacts between the unit cell. [46] In addition to their crucial role in inducing crystallization, the trivalent cations can be used to solve the phase problem using anomalous dispersion methods, since they are an integral part of the crystal lattice. Both yttrium ions are coordinated by three glutamate side chains. In addition, a carbonyl coordination of the peptide backbone is found for one yttrium ion (Fig. 4.11 b). A stable crystal lattice is formed due to the cation-based contacts interconnecting the proteins. This bridging effect has resulted in the development of an ion-activated patchy colloidal model, which describes theoretically the phase behavior observed experimentally. [41] The significant improvement of both crystal yield and quality using multivalent metal ions and the physical mechanisms revealed in our study provide not only a practical guide for protein crystallization, but also an efficient way to tune the effective interactions, phase behavior and even the exact nucleation pathways of protein crystallization. Furthermore, the ion-activated patchy particle model [41] provides a theoretical framework for future developments in this field.

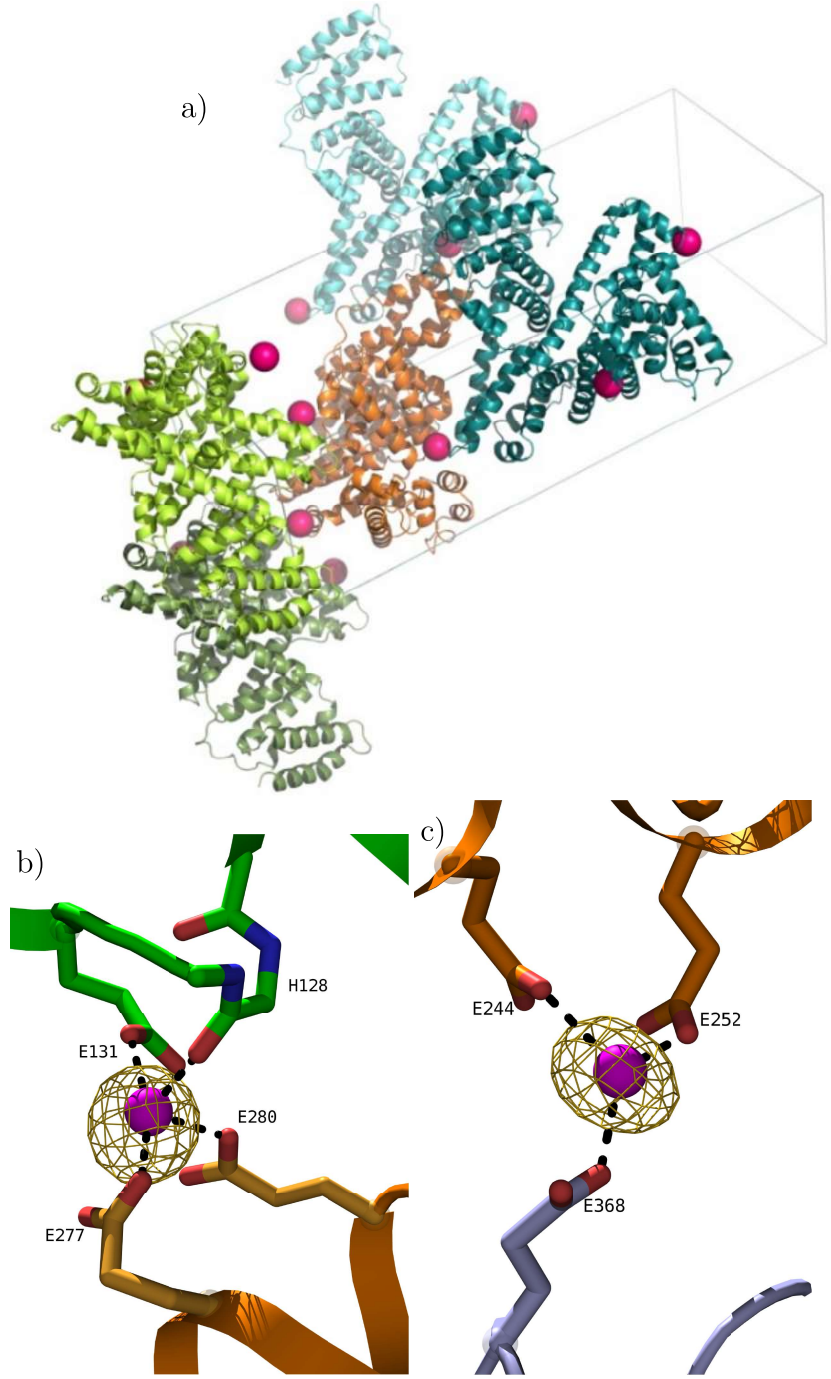


Figure 4.11: *Crystal structure of HSA crystallized in the presence of yttrium ions. The crystal packing is shown for a single protomer. All protomers which contact the central protomer (orange) by metal (pink) coordination are colored (green, blue). All attached protomers interacting exclusively by protein-protein interactions are not visualized. A similar figure showing all crystal contacts of a single protomer can be found in Fig. A.5. Four of the ten protomers contact the central protomer by two chemically different metal sites (hot pink) (b, c). The metal sites were placed on the basis of an anomalous electron density map (yellow, contour level 6.0) using the Bijvoet pairs as map coefficients.*

4.5 Conclusions

In summary, we have studied protein crystallization in solutions exhibiting a metastable LLPS. We focus on the effects of unstable and metastable DLPs on the crystallization pathways of HSA. Based on the phase diagram, for the first condition outside the LLPS region, but still inside the condensed regime, the DLP is unstable with respect to crystals and the solution. However, the surface of the quartz cuvette containing the sample may lead to a wetting layer of surface-enhanced dense phase. The second condition is located inside the LLPS binodal, leading to a small amount of metastable DLP. Optical microscopy and SAXS/SANS measurements solely show a monotonous crystal growth. We note that no evidence of nucleation inside the DLPs has been found. Thus, the existence of a metastable LLPS seems not to be a sufficient condition for two-step nucleation. In our systems, the crystallization process can be better described as a Bergeron process, i.e., crystal growth via vapor deposition (here: from the dilute phase) at the expense of the metastable (or unstable) phase (see Fig. 4.9). The Bergeron process also explains the fact that experimental observations often reveal that the crystals grow inside the dilute phase instead of the dense phase. Furthermore, all crystals grown under different conditions and with different trivalent salts share the same crystal structure. Crystallographic analysis shows that two metal ions are coordinated by negatively charged acidic residues to form intermolecular crystal contacts, hence contributing to the formation of the crystal lattice and supporting the ion-activated patchy particle model.[41]

Part V

Human versus bovine serum albumin: A subtle difference in hydrophobicity leads to large differences in bulk and interface behavior

Chapter V is based on the following publication:
Human versus bovine serum albumin: A subtle difference in hydrophobicity leads to large differences in bulk and interface behavior
Ralph Maier, Madeleine R. Fries, Cara Buchholz, Fajun Zhang, and Frank Schreiber
Crystal Growth & Design 2021, 21, 5451-5459

Contributions:	
Research design	RM, MF, FZ, FS
Experiments	RM, CB
Data analysis and interpretation	RM, MF, FZ, FS
Paper writing	RM, MF, FZ, FS

Reprinted with permission from *Cryst. Growth Des.* 2021, 21, 9, 5451–5459. Copyright 2021 American Chemical Society.

5.1 Abstract

The protein human serum albumin (HSA) is able to readily crystallize in the presence of trivalent cations, whereas this is not the case for the homologous protein in cattle, bovine serum albumin (BSA), although both have analogous functions as well as similar physicochemical properties. To understand the underlying interactions and mechanisms, we investigated their bulk phase behavior with $CeCl_3$ by visual inspection, optical microscopy, and small-angle X-ray scattering (SAXS). The results reveal that both proteins undergo reentrant condensation and liquid-liquid phase separation (LLPS). However, the LLPS binodal for HSA shifts toward lower protein concentrations than that for BSA, indicating a stronger intermolecular attraction in HSA solutions at the same compositions, consistent with SAXS measurements. Moreover, crystallization occurs within the condensed regime of HSA, but no crystallization was observed for BSA. Adsorption studies at a hydrophilic SiO_2 surface demonstrate that both systems show reentrant adsorption with a higher amount of adsorbed BSA, likely due to enhanced cation-mediated interactions and/or hydrogen bonds. We conclude that the higher surface hydrophobicity of HSA could explain the experimental observations. These additional hydrophobic interactions not only strengthen the attraction between the proteins but also provide directional and specific protein–protein contacts, which are favored for protein crystallization. This work further demonstrates the sensitivity and complexity of protein interactions in solution: Subtle differences in molecular structure lead to a dramatic change in their phase behavior. Generalization of these findings can pave the way toward, e.g., better drug design and improve medical treatment.

5.2 Introduction

Crystallization of macromolecules, e.g., proteins, is relevant in many fields such as pharmacology or structural biology. Although much effort is put into this research, the underlying mechanisms and interactions triggering crystallization are until now not fully understood. In order to elucidate the question which intermolecular interactions are required for crystallization, we performed systematic investigations on the interactions in aqueous HSA as well as in BSA solutions in the presence of solely multivalent cations as additives since only the former were reported to crystallize.

Serum albumin is the most abundant protein in the blood stream with a physiological concentration of roughly 40 mg/ml.[206] In general, albumins have two key physiological functions: maintaining the fluid balance by virtue of their colloid osmotic pressure and serving as carriers of small molecules.[207] Each mammal has its own albumin version (e.g., human serum albumin (HSA) for humans and bovine serum albumin (BSA) for cattle) since the respective primary and tertiary structures underwent a different evolution within the respective species.[139] Universally, however, the heart-shaped serum albumin molecules are formed by three homologous domains (I, II and III), which consist themselves of two subdomains of similar structural motifs.[139,208] The subdomains IIA and IIIA contain hydrophobic cavities, which are mainly responsible for ligand binding.[139,208] Several structural features are conserved in all mammalian serum albumins such as the highly helical tertiary structure and the characteristic pattern of the 17 disulfide bridges, indicating a canonical structure.[139] Due to their important role in the body, the binding to different ligands and the phase behavior of serum albumin were and still are investigated in great detail.[50,194,206,208–218] In numerous scientific studies, however, BSA is used instead of HSA because of its easier accessibility, and the subsequent results are transferred to HSA.[139] While the two homologs do indeed share multiple similar properties, there are also vital differences, since HSA is for example thermally more stable than BSA as well as more hydrophobic.[219,220]

Several of the different properties between the homologs can be explained with their structural differences and the resulting interactions. Regarding the primary structure, mature HSA contains 585 amino acids whereas BSA contains only 583 amino acids.[139] In combination with slight differences in their sequence, this results in the fact that HSA and BSA only have 75.8 % sequence identity.[139] Therefore, changes in the primary structure can be found, which are highly correlated with the evolution of the respective species.[139] Although there is a large degree of similarity between BSA, HSA, ESA (equine serum albumin) and LSA (leporine serum albumin), a number of differences in the binding pockets, and especially variations in the respective surface structures and charge distributions were found.[139]

From a colloidal point of view, HSA and BSA are both globular proteins with a net negative charge at neutral pH.[43] They are not only of physiological interest, but also considered as model proteins and used for studies investigating protein adsorption, protein-protein interaction, gelation or crystallization.[50,170,194,195,214,215,221,222]

In previous work, it was established that trivalent salts induce a rich phase be-

havior, similar to that shown in Fig. 5.1, and possibly even crystallization of globular proteins.[34,40,46,50,170,194,195,214,215,222] In this context, crystallization of HSA with YCl_3 and $CeCl_3$ was observed, but no crystallization of BSA in the presence of multivalent salts was reported.[40,43,47,194,195,214,215,222] In order to investigate this dissimilar crystallization behavior and the underlying interactions, in this work, we systematically studied the bulk phase behavior of HSA and BSA in the presence of $CeCl_3$ by visual investigation, optical microscopy, and small-angle X-ray scattering (SAXS). In addition, we studied the adsorption behavior of these two systems at a solid-liquid interface to further evaluate the interactions of these two homologous proteins to obtain a better understanding about why HSA crystallizes in the presence of multivalent cations, whereas BSA does not.

5.3 Experiments and Methods

5.3.1 Materials and sample preparation

The proteins and the salt used were purchased from Sigma-Aldrich, now Merck, and used as received. The purities were 97 % for HSA (product no. A9511), 98 % for BSA (product no. A7906) and 99.99 % for $CeCl_3$ (product no. 429406). Stock solutions were prepared by dissolving the protein and salt in deionized (18.2 MΩ), degassed Millipore water. The concentration of the protein solutions was determined with an ultraviolet-visible (UV-vis) spectrophotometer (Cary 50 UV-vis spectrometer, Varian Technologies, USA) using an extinction coefficient of $0.531\,\mathrm{ml\,mg^{-1}\,cm^{-1}}$ at a wavelength of 278 nm for HSA and $0.667\,\mathrm{ml\,mg^{-1}\,cm^{-1}}$ for BSA.[178] All samples were prepared by mixing the required amount of deionized, degassed Millipore water, protein stock solution and salt stock solution. All samples had a pH (between 6.2 and 6.9) above the respective pI of the proteins, measured with a pH meter from Mettler Toledo (Germany). No additional buffer was used to avoid the effect of co-ions. All samples were prepared and investigated at $21 \pm 1\,^{\circ}\mathrm{C}$.

5.3.2 Determination of the phase diagram

The phase diagrams of BSA and HSA with $CeCl_3$ were determined by visual inspection. Samples of protein concentrations (c_p) at 5, 20, 50, 80 and 100 mg/ml were prepared for HSA and c_p = 5, 20, 50, 60, 80, 100, 150 and 160 mg/ml for BSA at varying salt concentrations (c_s). The mean c_s of the last clear and first turbid or last turbid and first clear sample is referred to as c^* or c^{**}, respectively. The respective c^* and c^{**} phase boundaries (with $c^* < c^{**}$) are plotted in Fig. 5.1.

The dilute branches of the LLPS binodals (triangle markers in Fig. 5.1) were determined by UV-vis spectroscopy. Samples were prepared with two different c_p, i.e., with c_p = 150 and 160 mg/ml for BSA, and with c_p = 80 and 100 mg/ml for HSA, and varying c_s to ensure reproducibility. Since the binodals thus obtained for different protein/salt conditions are nearly identical within one protein, only

one data set is shown for better clarity. The macroscopic phase separation was ensured by visual inspection (see exemplarily Fig. B.1 for BSA). For the binodal determination, the samples tubes were centrifuged for 8 min with 5000 x g to separate the dilute and the dense phase. Afterward, the concentration of the dilute phase was determined with a the UV-vis spectrophotometer. Note that the complete LLPS binodal needs to consider both protein and salt partitioning in the two liquid phases, which leads to an ellipsoidal-shaped closed loop in regime II (see Refs. 47,50,222). In this work, we focus on the minimum protein concentration needed for LLPS in BSA and HSA solutions in the presence of trivalent salt; thus, only the protein concentrations in the dilute phases were determined.

5.3.3 Optical microscopy

An optical microscope (Axio Scope.A1, Carl Zeiss AG) was used for optical investigations of the samples. Images were recorded with a camera (Axio-Cam ICc5, Carl Zeiss AG) using the software ZEN Lite 2012. Samples were prepared in a separate tube. Afterward, 25 µl were transferred into a Gene Frame (1×1 cm with a thickness of 0.25 mm from Thermo Scientific™, Germany) on a glass slide and subsequently covered with a cover slide.

For crystallization experiments, multiple conditions were investigated to check for the optimal crystallization conditions. Samples were directly transferred into the Gene Frame and after 14 days, the presence or absence of crystals was recorded. This study was carried out for samples containing 20, 35, 50, and 80 mg/ml HSA with varying $CeCl_3$ concentrations. For BSA solutions, the samples used for the determination of the phase diagram were kept for several weeks to monitor the crystallization behavior.

5.3.4 Small-angle X-ray scattering (SAXS)

SAXS measurements were performed at the Petra III beamline P12 (Hamburg, Germany).[223] With a sample-to-detector distance of 3 m and an X-ray energy of 10 keV, a q-range from 0.03-7.3 nm^{-1} was achieved. The sample was exchanged using a flow cell. For each sample, 40 exposures of 0.045 s were checked for radiation damage and averaged. The 2D intensity pattern was azimuthally averaged to obtain the intensity profiles. Afterward, the solvent background was measured the same way and subtracted.

Additional SAXS data were collected with a Xeuss 2.0 instrument (Xenocs, Grenoble, France) employing a GeniX 3D microfocus X-ray tube with a copper anode, using an X-ray wavelength of 0.154 nm. With a sample-to-detector distance of 1850 mm, the employed Pilatus 300K detector covered a q-range from 0.055 to 2.25 nm^{-1}. Quartz capillaries with a diameter of 2 mm were used for this setup. Each acquisition time was 30 min.

In order to determine the reduced second osmotic virial coefficient $B_2' = B_2/B_2^{HS}$ with $B_2^{HS} = 16\pi R^3/3$ being the second virial coefficient of hard spheres, the data

were fitted with a sticky hard sphere (SHS) model[224] using IGOR Pro 6.37 in combination with macros provided by NIST.[225] The potential for particles with radius R is described as

$$\beta U(r) = \begin{cases} \infty & r < \sigma = 2R \\ -\beta U_0 = \ln\left(\frac{12\tau\Delta}{\sigma+\Delta}\right) & \sigma < r < \sigma + \Delta \\ 0 & r > \sigma + \Delta \end{cases} \tag{5.1}$$

with $\beta = 1/k_B T$. τ stands for the stickiness parameter and Δ for the width of the square well. A pertubative solution of the Percus-Yevick closure relation was used to calculate the structure factor.[193,226]

Prior to their investigation, the samples were briefly centrifuged and only the clear supernatant was examined. The protein concentration of the HSA samples was determined with the help of the binodal in the phase diagram (Fig. 5.1) in a 10 mg/ml range and for the BSA samples, a concentration range between 40 and 50 mg/ml was assumed since the initial concentration was 50 mg/ml and no LLPS occured for these conditions. With the specific volumes of 0.735 ml/g for BSA[227] and 0.754 ml/g for HSA,[228] the respective volume fractions were calculated. Similar to Refs. 229 and 193, Δ was set to $0.01\,\sigma$ to avoid artificial coupling with τ, the axes of the ellipsoid were fixed to $r_a = 1.8\,\mathrm{nm}$ and $r_b = 6.1\,\mathrm{nm}$ and the scattering length density (SLD) of the ellipsoid was set to $1.24 \cdot 10^{-7}\,\mathrm{nm}^{-2}$. Since HSA and BSA are similar in size and shape (see Tab. 5.1), the same values are used for both proteins.

In the limit $\Delta \to 0$, which is used here, the reduced second virial coefficient can then be calculated by:

$$\lim_{\Delta \to 0} \frac{B_2}{B_2^{HS}} = 1 - \frac{1}{4\tau} \tag{5.2}$$

Due to aggregation or further LLPS within the samples indicated by a strong increase of intensity at low q-values ($< 0.1\,\mathrm{nm}^{-1}$) (see Fig. 5.3), the model was only applied for q-values $\geq 0.1\,\mathrm{nm}^{-1}$. Representative fits are plotted in Fig. B.2.

For protein solutions with a c_s of 1 mM, a screened Coulomb (SC) potential[230,231] was used to describe the effective interactions. According to Ref. 232, the axes of $r_a = 1.7\,\mathrm{nm}$ and $r_b = 4.2\,\mathrm{nm}$ for low c_s were used. The SLD of the ellipsoid was again set to $1.24 \cdot 10^{-7}\,\mathrm{nm}^{-2}$, the temperature to 293 K, the monovalent salt to 0.006 M (having the same Debye length as 1 mM $CeCl_3$) and the volume fraction was calculated similarly to the SHS fits. Similar to the procedure above, the model was applied only for q-values $\geq 0.1\,\mathrm{nm}^{-1}$. The respective fits can be seen in Fig. B.3.

5.3.5 Quartz-crystal microbalance with dissipation (QCM-D)

Protein adsorption measurements were performed with a Q-Sense Analyzer (Biolin Scientific, Sweden).[174,233,234] The samples were mixed and 5 ml of the protein/salt mixtures was pumped into a previously degassed-MilliQ-water-calibrated QCM-D cell. The signal of the adsorption process was recorded for approximately one hour and the cell was subsequently rinsed by MilliQ water in order to detect irreversibly bound proteins. Native silica-coated quartz sensors (product no. QS-QSX303 from Quantum Design, Germany) were used as substrates for this setup. The flow cell was inverted during the complete measurement and cleaning, i.e., with the substrate on top of the solution, in order to avoid sedimentation effects. After each measurement, the flow cell was cleaned in situ in three steps with 2 % Hellmanex, ethanol and water. The QSoft software was used for data collection while Dfind and QTools (Biolin Scientific) were used for data analysis and figure generation. Since the dissipation (D) was > 0, a viscoelastic (Voigt) model was applied for the data collected.[235,236] More details regarding data analysis and fitting parameters can be found in Refs. 194, 195, and 215. Each adsorbed protein layer thickness d at the solid-liquid interface is the mean of at least three individual measurements to check for reproducibility and to estimate the error of the measurement. Thus, the error bars indicate the respective standard deviations.

5.4 Results and discussion

5.4.1 Phase diagram

As a first step, the respective phase diagrams were established. Fig. 5.1 shows experimental phase diagrams of HSA and BSA in the presence of $CeCl_3$. While parts of the phase diagram of HSA-$CeCl_3$ were already discussed in a previous work,[214] the BSA system was newly established in the context of this study. One can see that HSA and BSA both show a rich phase behavior including reentrant condensation (RC) and liquid-liquid phase separation (LLPS) in the presence of $CeCl_3$ (see Fig. 5.1). This rich phase behavior has been established for net negatively charged, globular proteins in the presence of multivalent salts, but can also be found in solutions of positively charged proteins and negatively charged polyoxometalates.[41,46,170,172,194,195,214,215,222] The proteins initially repel each other by virtue of their negative charge, forming a clear and stable solution (regime I). By increasing c_s and crossing c^*, the proteins macroscopically aggregate/condense, which leads to an optically turbid solution. In this turbid solution, the multivalent cations bind to the carboxyl groups at the protein surface, therefore weaken the repulsive forces between the initially negatively charged proteins, and the effective attraction is strong enough to cause protein condensation (regime II).[41,46] By further increasing c_s, above c^{**}, the attractive interactions between the proteins become weaker

and the solution becomes clear and stable again (regime III), which is defined as RC.[40,41,43,46] The driving force for this behavior was found to be an effective charge inversion of the proteins.[41,46] In regime II, a metastable LLPS regime can occur, if the effective attractive protein-protein interactions are sufficiently strong.[50,118] Samples prepared at conditions inside this LLPS regime phase separate into a dense and a dilute liquid phase.

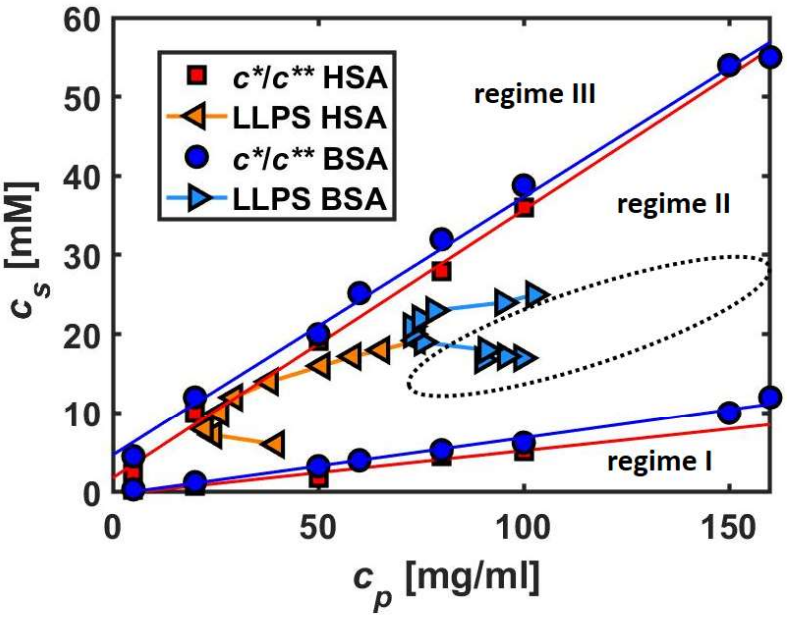


Figure 5.1: *Phase diagram of HSA-$CeCl_3$ (red) and BSA-$CeCl_3$ (blue). Both phase diagrams were determined at 21 °C. The straight lines corresponding to c^* and c^{**} are fits to the respective values determined by visual inspection. Note that the experimental data for LLPS (triangles) include only the determination of protein concentration within the dilute phase at different c_s, since we focus on the minimum protein concentration needed for LLPS (onset) in BSA and HSA solutions in the presence of $CeCl_3$. The determination of the complete LLPS loop would require the determination of the salt and protein partitioning within the respective liquid phases. A hypothetical complete LLPS loop for BSA is drawn as black dotted ellipse based on Refs. 47,50,222 (which used other conditions).*

The comparison of the HSA with the BSA phase diagram shows a shift of the LLPS binodal about three-fold higher protein concentrations for BSA (72 vs 22 mg/ml), indicating stronger attractions in HSA than BSA solutions under the same condition. The slight shift of c^* and c^{**} can be explained by the fact that BSA has two acidic residues more than HSA, meaning is more negatively charged (see Tab. 5.1),[43] and thus more cations are required to balance the electrostatic repulsion and induce the phase transitions.

5.4.2 Crystallization

After establishing the phase boundaries and the LLPS binodal, we focused on protein crystallization and the crystallization conditions within the phase diagram. Crystallization of HSA in the presence of multivalent salt has been reported in the literature, but so far not for BSA.[40,43,47,194,195,214,215,222] The conditions of HSA-$CeCl_3$ crystals or their absence after 14 days for numerous conditions are plotted in Fig. 5.2. Representative images of HSA crystals grown under different conditions are shown in Fig. B.4. It is clearly visible that crystallization mainly occurs in regime II, especially in the lower half, including both conditions outside and inside the LLPS area. A detailed study of the role of LLPS on nucleation has been performed for this system and the reader is referred to Ref. 214 for more information. The absence of crystallization in the upper part of regime II will be discussed in the Discussion Section.

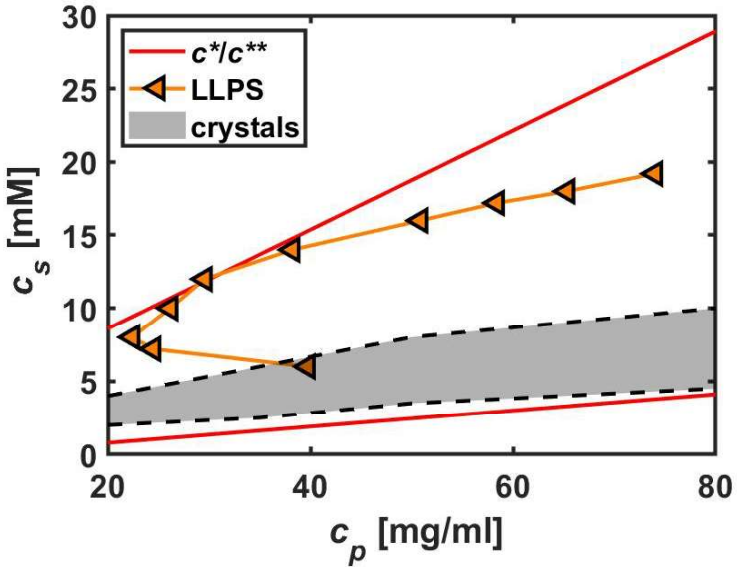


Figure 5.2: *Conditions of HSA-$CeCl_3$ crystallization recorded after 14 days. 20, 35, 50 and 80 mg/ml HSA samples were investigated at varying c_s. Conditions which showed crystals are shaded grey within the HSA-$CeCl_3$ phase diagram.*

In contrast to HSA, none of the BSA samples crystallized. In fact, no BSA crystals were observed for any set of conditions studied in our work. This is also true for BSA with other multivalent salts, namely YCl_3, $HoCl_3$, $LaCl_3$, LaI_3, YI_3 (see exemplarily SAXS data of BSA-LaI_3 in Fig. B.5), and thus apparently a rather general effect.

5.4.3 Effective bulk interaction characterized by SAXS

As a next step, the effective intermolecular bulk interactions resulting in the different crystallization behavior were characterized by SAXS. Fig. 5.3 a shows raw SAXS

data of a set of samples containing 50 mg/ml HSA and varying c_s and Fig. 5.3 b shows the corresponding data for 50 mg/ml BSA. In both figures, first an increase in the low q-intensity can be observed upon increasing c_s, indicating increasing attractive interactions. Simultaneously, the correlation peak at $q \approx 0.5\,\mathrm{nm}^{-1}$, which denotes a dominant electrostatic repulsion between the particles in solution, vanishes. At moderate c_s, a maximum of the low q-intensity is visible, and for high c_s, it decreases again. This behavior corresponds well with the phase diagrams shown in Fig. 5.1, in which the three different regimes are observed. In the condensed regime (regime II), the interparticle attraction is strong enough to induce protein aggregation/condensation. The trend of SAXS profiles observed in Fig. 5.3 is consistent with previous works investigating intermolecular interactions of RC systems.[170,193,194,229]

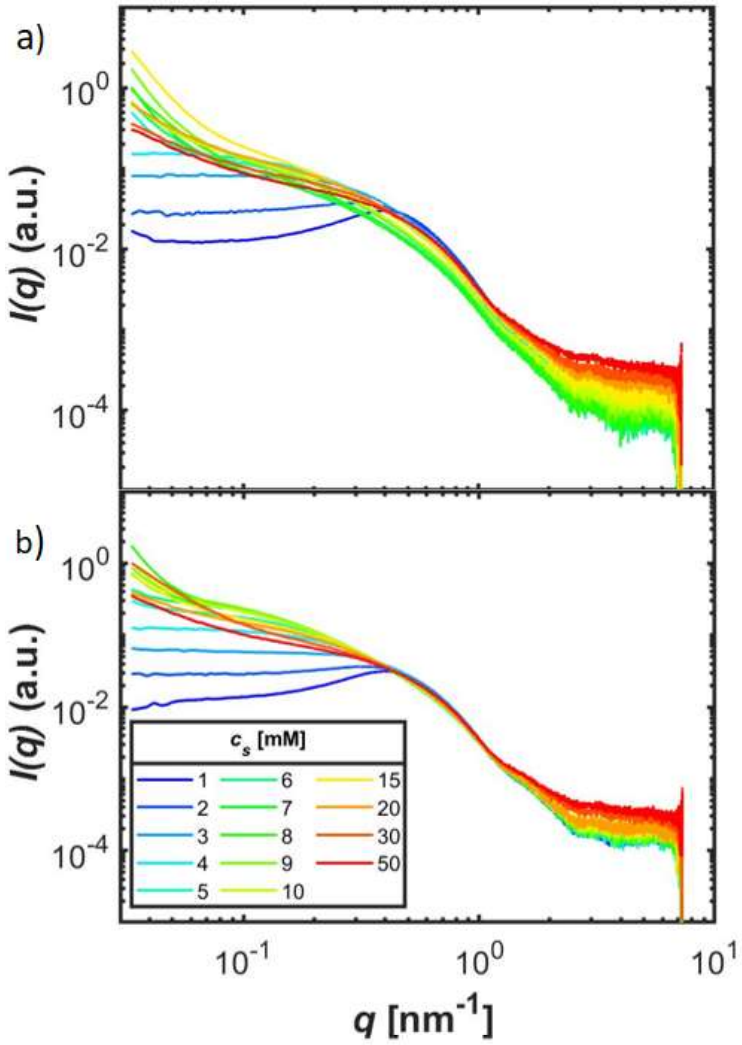


Figure 5.3: *SAXS intensity curves of samples containing a) 50 mg/ml HSA and b) 50 mg/ml BSA and varying $CeCl_3$ concentrations of 1-50 mM.*

In order to quantify these observations, B_2' values from the model fit are plotted

in Fig. 5.4. B_2' is a measure of the intermolecular interactions of a system. $B_2' < 0$ implies a net attraction, whereas $B_2' > 0$ represents a net repulsion. The B_2'-values slightly decrease for both proteins upon increasing c_s, reach a minimum (which is negative, hence attractive) in regime II and increase again in regime III. Unfortunately, the model is physically limited to attractive interactions, hence, the B_2'-values of regime I, approaching c^*, could not be determined by this procedure. However, the results are in good agreement with the phase diagrams shown in Fig. 5.1, showing a reentrant strength of attraction with the strongest attractions in regime II. Comparing HSA with BSA shows that HSA has lower B_2'-values and therefore stronger attractions in regime II while this trend is opposite when crossing c^{**}.

For further understanding of the effective interactions, a model-free analysis was applied. $1/I(q \to 0)$, i.e., the inverse intensity at low q-values (close to 0), is also a measure of the intermolecular interactions of a sample, since it is proportional to the isothermal compressibility of the system investigated and the respective second osmotic virial coefficient B_2.[141] The respective curves can be found in Fig. 5.4 b. Since it is a model-free analysis, it is not limited to attractive conditions like the SHS analysis, but also low c_s can be investigated. Here, the sharp decrease from repulsive forces to attractive forces is visible when crossing c^*. Otherwise, they exhibit the same trend as the respective B_2'-curves with the only difference being the additional bump in the second regime for HSA. This additional increase and decrease was found to be caused by LLPS. In the virial expansion of the structure factor (Eq. 5.3), ρ is proportional to c_p, hence, a change in c_p of the measured dilute phase due to LLPS affects the $1/I(q \to 0)$-behavior and causes this bump at $c_s = 8\,\mathrm{mM}$.[193,237] These results are consistent with the phase diagrams which show LLPS for HSA at 50 mg/ml, but not for BSA (see Fig. 5.1).

$$1/S(q \to 0) = 1 + 2B_2\rho + ... \tag{5.3}$$

As a last step of the SAXS analysis, an SC potential was fitted to the protein samples with the lowest c_s, i.e., with 1 mM $CeCl_3$ (see Fig. B.3), in order to compare the pure proteins (without or with little salt). The curves and fits are nearly identical with the only difference being a decrease at very low q-values for BSA compared to an increase for HSA, which might stem from HSA aggregation. The net charges resulting from the fits are $-14\,\mathrm{e}$ and $-13\,\mathrm{e}$ for BSA and HSA, respectively. Similar to Ref. 43, a slightly more negative charge is obtained for BSA. These results indicate that the proteins behave similarly without (or with little) salt added, but BSA is slightly more negatively charged.

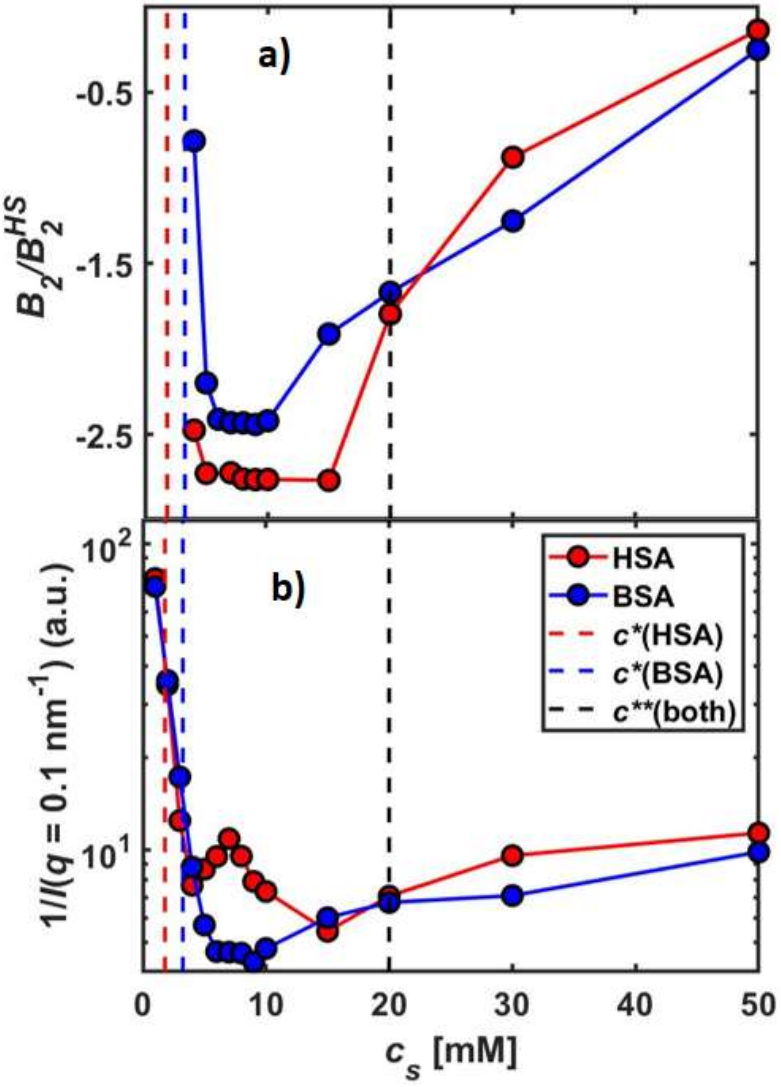


Figure 5.4: *a) Reduced second virial coefficients B_2/B_2^{HS} and b) $1/I(q \to 0)$-behavior of the raw SAXS data of HSA and BSA samples with $c_p = 50\,\mathrm{mg/ml}$ and varying c_s presented in Fig. 5.3. The respective phase boundaries are plotted, as well. c^{**}(both) represents the c^{**} boundary, which is identical for HSA and BSA. For all images, the errors are typically at least one order of magnitude smaller than the respective data values and therefore not plotted for clarity.*

5.4.4 Adsorption studied by QCM-D

In this section, the adsorption behavior of HSA and BSA solutions at a hydrophilic, negatively charged SiO_2 surface is presented to further elucidate the strength and nature of the interactions of these two proteins. Fig. 5.5 shows the raw data of samples containing a protein concentration of 20 mg/ml and different salt concentrations (0, 1, 2, 5 and 20 mM). Similar frequency decreases (roughly proportional to the amount of adsorbed protein) can be seen for both BSA and HSA samples, whereas the dissipation increases are more pronounced for BSA. In Fig. 5.6, the respective calculated thicknesses based on a full fit following Ref. 194 are shown. A complex adsorption behavior is recorded for both HSA and BSA. Initially, an increase in adsorbed protein layer thickness d can be observed until a maximum value is reached. Increasing c_s further results for both proteins in a decrease in d until the adsorption layer saturates in regime III, known as reentrant adsorption (RA).[194,195,215] This result is in line with previous work on similar systems.[194,195,215,238] The observation of a maximum adsorbed amount is also consistent with the bulk data, which show a maximum of attraction in the second regime. Fig. 5.6 b presents the irreversibly adsorbed protein layer after rinsing for both systems. The overall thickness is significantly reduced, but the similar trends remain.

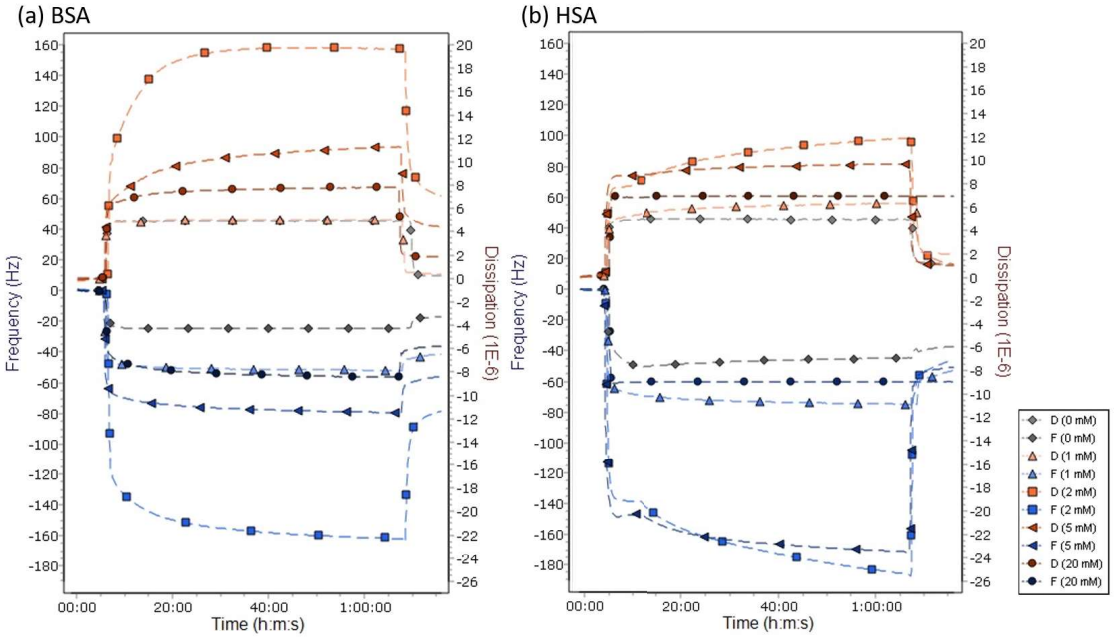


Figure 5.5: *Raw QCM-D data of samples containing (a) 20 mg/ml BSA or (b) 20 mg/ml HSA with different c_s. The frequency of the 9th overtone is plotted in blue, whereas the dissipation is plotted in red. For clarity, only one condition of each regime is plotted. The different c_s represent all individual regimes in the phase diagram.*

With no or low c_s, the adsorption thickness d is slightly higher for HSA than that for BSA, which is expected as HSA is more hydrophobic and has less surface charge. This observation is consistent with the literature: Kurrat et al. reported that in HEPES and PBS buffer, HSA has a thicker adsorption layer than BSA.[239] The interesting observation is that in regime II and III, more BSA adsorbs at the surface than HSA. If we only consider the bulk behavior, it may seem surprisingly at first glance that more BSA are adsorbed at the surface than HSA including the irreversible bound proteins (see Fig. 5.6) since weaker intermolecular interactions are observed in bulk for BSA. This can be explained, though, by the fact that BSA is more hydrophilic than HSA,[220] hence, more BSA proteins adsorb at the hydrophilic surface. In addition, BSA is more negatively charged than HSA (see Tab. 5.1),[43] In our previous work on protein adsorption in the presence of multivalent cations (see Refs. 194,195,215,238), we have demonstrated that indeed the cation-mediated interactions lead to an enhanced adsorption at hydrophilic interfaces, i.e., the trivalent cations preferentially adsorb to the natively negatively charged silicon wafer. Further, the specific interactions between these adsorbed cations and the carboxyl groups on the protein surface enhance the protein adsorption. Therefore, as BSA has two acidic residues more than HSA,[43] BSA provides more possible binding sites for the cations, thus induces stronger binding to the surface and the cation-mediated adsorption leads to a thicker layer for BSA compared to HSA in regime II and III.

Note that all samples used in the QCM-D were below the LLPS binodal, and were thus not phase separated. In a recent publication, we have shown that the adsorption is enhanced inside or close to the LLPS binodal.[195] Since the HSA conditions are located just outside the binodal compared to the BSA conditions, which are far away from the binodal, one would expect a higher d for the HSA samples. Since actually the opposite is the case, we attribute this to strong cation-mediated adsorption and/or hydrogen bonds of BSA with the substrate. Another aspect one has to take into account is that QCM-D also detects water in the adsorbed layer. Since BSA is more hydrophilic,[220] more water molecules should be coupled to the protein and hence an increased thickness should be observed compared to HSA.

As shown in Fig. 5.5, QCM-D provides also the dissipation parameter D, which is a measure for the viscoelastic properties of the media investigated. In regime II, D is roughly twice as high for BSA as for HSA (see Fig. 5.5), suggesting a denser and stiffer (i.e., more "solid-like") layer for HSA. In accordance with this, the viscosity of the HSA layer is approximately twice of the BSA layer. A high viscosity may be due to strong protein-protein interactions and may correspond to binding and cluster formation,[240] which is consistent with the SAXS measurements in Fig. 5.4.

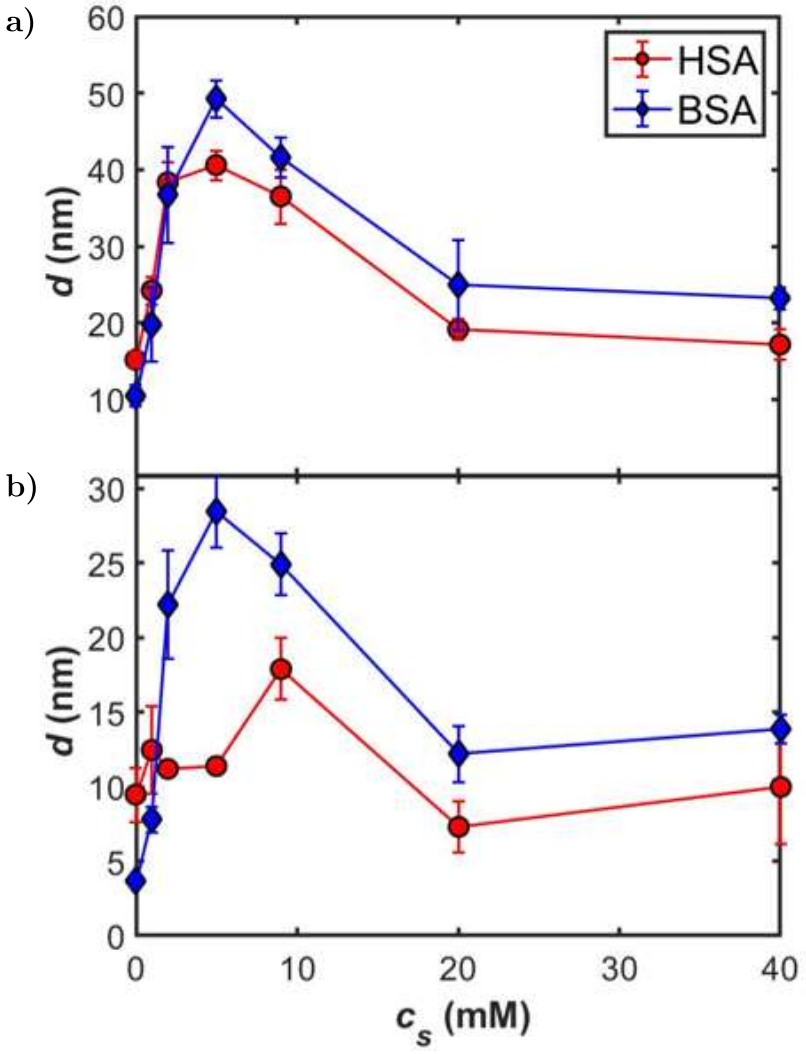


Figure 5.6: *a) Adsorbed protein layer thickness (d) of 20 mg/ml BSA (blue diamonds) and HSA (red circles) on a SiO_2 quartz calculated from the raw data exemplarily shown in Fig. 5.5 with the Kelvin-Voigt model and b) data after subsequent rinsing with water. Each data point is the mean of at least three individual measurements. The error bars indicate the respective standard deviation. Note that 20 mg/ml is outside and just at the border of the LLPS region for BSA and HSA, respectively (see text for details).*

5.4.5 Discussion

Due to the highly complex structure of globular proteins, different properties and parameters simultaneously influence their bulk and interface behavior. In order to provide a comprehensive discussion, the following section highlights similarities as well as differences of HSA and BSA deducing key mechanism triggering the different bulk (crystallization) and adsorption behavior of BSA versus HSA. Here, the main focus lies on their secondary structure, the binding behavior of various ligands and the respective behavior at interfaces as well as in bulk. Some physicochemical parameters are listed in Tab. 5.1.

HSA was found to bind lanthanides in blood serum.[245] The ions of cerium and the transition metal ions of yttrium were found to bind at negatively charged glutamate residues of HSA, forming intermolecular crystal contact sites.[214] Since each HSA molecule binds four ions, 15.4 % of its surface area is responsible for cation binding within a crystal.[214] We note that the role of the multivalent cations on protein crystallization is similar to the one of anionic calixarene scaffolds, which are used to mold to cationic proteins, and induce oligomerization and crystallization.[246] Further studies on BSA show that the lanthanide metal ions Yb^{3+} and Gd^{3+} bind to BSA with four equivalent affinity sites in a pH range of 6-7 (with association constants Yb^{3+}-BSA $\gg$ Gd^{3+}-BSA).[247] The authors conclude that the Yb-ions bind to histidine while the binding site of the Gd-ions is not fully clear.[247] Hence, both proteins easily bind lanthanide cations, which is also revealed in the RC phase diagrams due to ion binding and bridging.[40,43,248]

Regarding their secondary structure, Blaber et al. report that the helix propensity depends strongly on the hydrophobic effect of the respective amino acids, which stabilizes the helical structure.[249] Since HSA has a higher fraction of α-helices, it is reasonable to conclude that more or stronger hydrophobic interactions are present compared to BSA. Akdogan et al. actually report that the differences in hydrophobicity between the albumins often occur at surface-exposed residues, which is crucial for the consideration that HSA is less hydrophilic than BSA as evidenced by their hydropathy Ω (see Tab. 5.1).[220] In terms of intermolecular interactions, HSA is

Table 5.1: *Physicochemical properties of BSA and HSA.*

	BSA	HSA
Molecular weight [kDa][241,242]	67	66.5 – 69
Hydrodynamic radius R_H [nm][241]	3.3 - 4.3	3.3 – 4.1
# Amino acids[139,243]	583	585
# Positive/negative residues[43]	80/91	80/89
pI[43]	4.6	4.6
Charge (pH 7) [e][43]	-11	-9
Overall hydropathy Ω[220]	-279.2	-230.8
Secondary structure [%][216,244] (α-helix/β-sheet/β-turn)	(53/14/4)	(66/4/22)

supposed to be better at attracting and binding hydrophobic and amphiphilic ligands.[210,220] In contrast, interactions with water and hydrogen bonding are hindered compared to BSA. These findings are consistent with the adsorption data presented (see Fig. 5.6).

In addition to the LLPS binodal shift, the biggest difference in the respective bulk behavior is that HSA crystallizes in the presence of multivalent cations and BSA does not. George and Wilson stated in an empirical study that the intermolecular attractions have to be in a relatively narrow range for crystal nucleation.[117] According to this study, the optimum crystallization conditions are around or slightly below the critical point of LLPS. Vliegenthart and Lekkerkerker calculated the B_2'-value at the critical point to be approximately -1.5.[118] This empirical study was rationalized by a kinetic model for the growth rates of protein crystals. Schmit and Dill assume that the protein can bind to the crystal surface in two ways: productively (in the correct crystal orientation and alignment), or nonproductively (in a noncrystalline orientation).[120] Crystal growth only occurs when proteins bind productively.[120] They propose that too strong attractions lead to nonproductive attachment of proteins to the crystals.[120] Since LLPS can be observed for both HSA and BSA in the presence of multivalent salts (see Fig. 5.1) and both proteins show B_2'-values ≤ -1.5 (see Fig. 5.4), both proteins should theoretically have attractions strong enough to induce crystallization. However, we only monitor HSA crystals in our systems. This indicates clearly that some differences between HSA and BSA (most likely at the protein surface) do have to exist, which are responsible for this dissimilar behavior.

It is also known that an interplay between anisotropic and isotropic interactions is crucial for protein crystallization.[250,251] It seems that only ion bridging is not sufficient for serum albumin to crystallize. It is able to induce an RC bulk behavior and LLPS, but for crystallization additional forces are required. This can also be seen from the fact that some crystal contacts of HSA-Y^{3+} crystals are formed by solely protein-protein interactions,[214] which are assumed to be of hydrophobic nature. These additional intermolecular contacts are believed to aid in orienting and aligning proteins, resulting in a productive binding in order to promote crystallization.[120] The absence of HSA crystallization at high c_s may be due to the high occupation of binding sites by metal ions, which could block the protein-protein contacts, or change the crystallization pathway (or crystals simply need a much longer induction time, beyond the observation time). We note in another system (BLG with YCl_3), crystallization near c^* and c^{**} shows different pathways.[46]

The hypothesis that the additional hydrophobic interactions of HSA drive crystallization is supported by the fact that either highly hydrophobic or highly polar surface regions were reported to have an increased probability of establishing crystal lattice contacts.[114] By increasing the hydrophobicity at the protein surface, proteins can assemble in new crystal packings.[114] Approximately 68 % of the contact area in cutinase crystals is hydrophobic while around 30 % of the total hydrophobic area of the protein is involved in contact formation, indicating the crucial role of the hydrophobic interactions for protein crystallization.[114] The hydrophobic patches favor protein-protein interactions and counteract the repulsive forces arising from

charged functional groups, hence contributing significantly to the formation of protein crystals.[252] Further support is obtained by recent models indicating that the fraction of exposed residues in combination with their hydrophobicity plays a vital role in protein crystallization propensity.[115]

We note that, while we have not observed BSA crystallization in the presence of multivalent cations, BSA was crystallized in specific systems using polyethylene glycol (PEG) as precipitant or at gas-liquid interfaces.[139,253,254] In Refs. 253 and 139, however, BSA was further purified by removing fatty acids bound to the protein and/or eliminating dimers.[255] In Ref. 254, the protein was purchased from a different company, which gives no information about its purification methods, and acidic solutions (pH 4.3) were used. Hence, the degree of purification of the proteins and the aqueous environment differ compared to our system, which seemingly affects the phase behavior substantially. In our work, we have observed a variation of phase boundaries (such as c^* and c^{**}) due to the usage of different batches, but in all batches HSA, crystallizes under certain conditions. BSA, however, never crystallizes under any experimental conditions employed by us.

5.5 Conclusions

In summary, we have studied the protein bulk phase behavior and the adsorption at an interface for HSA and BSA solutions in the presence of the trivalent salt $CeCl_3$. Both systems exhibit a rich phase behavior including RC and LLPS, however, only HSA crystallizes in regime II, but BSA does not. SAXS measurements confirm stronger intermolecular attractions for HSA compared to BSA solutions in regime II. Protein adsorption experiments at a hydrophilic, negatively charged SiO_2 substrate show a thicker layer for BSA in regime II and III, which is in good agreement with the cation-mediated protein adsorption,[194,195,215,238] where the more hydrophilic BSA shows an enhanced adsorption behavior.

Although many physicochemical properties are similar (see Tab. 5.1), both bulk and adsorption results show that crucial differences between HSA and BSA exist. Especially for crystallization, an interplay of isotropic and anisotropic interactions is essential. While the multivalent cation binding and bridging induce RC and RA, hydrophobic interactions and hydrogen bonding fine-tune this behavior. Hence, the more hydrophilic BSA seems to bind stronger to water and to negatively charged, hydrophilic surfaces, whereas the additional hydrophobic forces of HSA are able to induce crystallization. In conclusion, depending on the favorable or unfavorable binding to ligands or surfaces, the whole range of interaction types needs to be considered and accurately chosen for the desired application. These findings are of vital importance in many research areas, ranging from drug design to food processing.

Part VI

Protein crystallization from a preordered metastable intermediate phase followed by real-time small-angle neutron scattering

Chapter VI is based on the following publication:
Protein crystallization from a preordered metastable intermediate phase followed by real-time small-angle neutron scattering
Ralph Maier, Benedikt Sohmen, Stefano Da Vela, Olga Matsarskaia, Christian Beck, Ralf Schweins, Tilo Seydel, Fajun Zhang, and Frank Schreiber
Crystal Growth & Design 2021, 21, 6971–6980

Contributions:	
Research design	RM, BS, FZ, FS
Experiments	RM, BS, SDV, OM, CB, TS
Experimental assistance	RS
Data analysis and interpretation	RM, BS, FZ, FS
Paper writing	RM, BS, FZ, FS

Reprinted with permission from *Cryst. Growth Des.* 2021, 21, 12, 6971–6980. Copyright 2021 American Chemical Society.

6.1 Abstract

We present a systematic study using real-time small-angle neutron scattering (SANS) and optical microscopy to follow the protein crystallization process in the presence of a metastable intermediate phase (MIP). Using bovine β-lactoglobulin (BLG) in the presence of the divalent salt $CdCl_2$ as a model system, we first determine the experimental phase behavior in D_2O. The protein solutions become turbid after crossing the first threshold salt concentration c^*, and upon further increasing the salt concentration, the solutions become less turbid but not completely clear again. Thus, the second border is called $pseudo - c^{**}$. Near $pseudo - c^{**}$, crystallization follows a nonclassical process with a MIP, which is further explored with a focus on the structural evolution and the growth kinetics of the MIP prior to crystal nucleation. Real-time SANS measurements show that a correlation peak develops inside the MIP, and its peak position shifts to higher q-values with time, finally stabilizing at a characteristic length scale of $d_{MIP} \approx 84\,\text{Å}$. The area of this peak (proportional to the amount of MIP in the sample) increases with time first, reaches a maximum, and then decreases quickly upon crystallization due to consumption by crystal growth. The evolution of the correlation peak indicates a "preordering" nature of the MIP as precursors of crystal nucleation, which lowers the nucleation barrier for subsequent crystallization. These results of structural evolution and the role of MIPs during a nonclassical crystallization process may be relevant for other fields ranging from structural biology to pharmacy.

6.2 Introduction

Crystallization, especially of proteins, is important not only for structural biology, where high-quality crystals are required for structure determination, but also in research areas like pharmacological drug delivery, where protein crystals are used for stability reasons while simultaneously allowing for a controlled drug release in the body.[256,257] However, the molecular interactions in protein solutions and their connections to the crystallization process are not fully understood and crystal growth is typically performed by screening several conditions and optimizing those which result in protein crystals.[6]

The early stage of crystallization, i.e., the nucleation process, is often interpreted following the classical nucleation theory (CNT).[258,259] One of the main assumptions of CNT is that molecules form nuclei in a supersaturated solution with the exact density and structure of the crystals in the final stage.[260–262] Recent studies in protein and colloid crystallization as well as biomineralization have shown nonclassical features in the early stage of nucleation.[42,44,45,78,93,137,138,157,165,175,201,260,263–273] Hence, according to the nonclassical nucleation theory, a metastable intermediate phase (MIP) (clusters or dense liquid phases) exists in between the initial solution and the final crystalline state.[78,137,138,152,260] The free energy landscapes of nonclassical pathways show an additional local free energy minimum corresponding to this intermediate phase.[165]

In the nonclassical nucleation theory, the order parameters, i.e., density and structure, are decoupled. In most studies, the liquid precursors gain higher density prior to reaching their final structure.[78,88,137,156,263,274,275] Nevertheless, also the scenario of preordered MIPs serving as a nucleation precursor was reported.[165,276,277] One example is the solid-solid transformation from an initially formed polymorph toward a more stable crystal structure, where the less stable crystals serve as preordered precursors.[80,278–280] Another example is the so-called "oriented attachment" in crystallization, in which building blocks (which might be crystalline or not) form independently and then attach to the crystal surface in the required orientation, forming mesocrystals in the case of crystalline precursors.[76,281–285]

In solution crystallization, preordered precursors have been observed for small molecules, colloids as well as for protein systems.[273,275,277,282,286–289] For minerals such as calcium carbonate ($CaCO_3$), a partial dehydration of the prenucleation clusters was found to be crucial for liquid-liquid phase separation (LLPS) and further solidification.[273,275] A different nature of additives (such as polyaspartic acid or magnesium) can lead to different types of short-range order within the amorphous precursors.[286] In a second step, water is expelled from these precursors, resulting in long-range order.[286] In simple aromatics (perylene diimides), cryogenic electron microscopy revealed an initial densification of the precursors, which is followed by a gradual evolution, involving further densification parallel to optimizing molecular order and morphology.[289] Using cryo-cryo-scanning transmission electron microscope (STEM) tomography, also for protein such as ferritin, a gradual increase in both order and density from the surface of the precursor toward their interior was recently

reported.[89] Despite the progress in two-step nucleation theory, its application and our understanding of the preordered precursors in terms of their structural development as well as the exact role in crystal nucleation are still elusive.[74,272,276,285]

We have previously shown that trivalent salts such as YCl_3 or $CeCl_3$ can induce a reentrant condensation (RC) phase behavior in many acidic proteins like β-lactoglobulin (BLG) or human serum albumin (HSA).[34,40,41,43,46,48,50,214,248,290] Interestingly, depending on the position in the phase diagram, classical crystallization or a nonclassical crystallization process have been observed.[42,44–46] In a previous study,[44,45] the two-step nucleation process of protein crystallization in solutions was investigated by following the overall crystallization kinetics using real-time optical microscopy and small-angle X-ray scattering (SAXS).[44,45] For BLG-salt ($CdCl_2$) solutions in H_2O at the transition zone of $pseudo - c^{**}$, small aggregates formed after sample preparation. These protein aggregates were identified as a MIP during crystallization. The experimental results together with a consistent rate equation model provided solid evidence of two-step nucleation in the early stage of crystallization.[44,45] However, a detailed characterization of the MIP as a key ingredient in the crystallization and its evolution during crystallization is still missing.

In this work, we study BLG-$CdCl_2$, which was previously studied in H_2O only, in heavy water (D_2O). Establishing D_2O as a solvent responds to the fundamental interest in associating the physical differences of D_2O and H_2O with differences in the resulting biological assembly. Moreover, it permits subsequent small-angle neutron scattering (SANS) experiments to investigate the structural evolution of the MIP during a two-step crystallization process, as well as subsequent neutron spectroscopy investigations to explore the diffusive protein dynamics in situ during the crystallization. In addition, NMR studies may be aided as well by establishing D_2O as a solvent.[291] In general, real-time scattering techniques provide information on the ensemble average and structural information with good statistics,[42,44,45,292] which is in contrast to the real-space real-time techniques where details of the local domains of the system can be probed.[76,151,293] SANS has the advantage of being a noninvasive method with a large scattering volume. These are crucial aspects regarding the crystallization of (biological) protein solutions in which the crystal number density may be very small. Hence, this real-time study not only provides direct evidence for a two-step nucleation process, but also elucidates the role and the structural signature of the MIP in the nonclassical process of protein crystallization.

6.3 Experimental section

6.3.1 Materials and sample preparation

The protein β-lactoglobulin (BLG) from bovine milk, D_2O and the divalent salt $CdCl_2$ were purchased from Sigma-Aldrich (now Merck). For BLG (product no. L3908) a purity of $\geq$90 %, for D_2O (product no. 151882) a purity of $\geq$99.9 % and for $CdCl_2$ (product no. 202908) a purity of $\geq$99 % were guaranteed. In all experiments

of this study, D_2O was used as a solvent to obtain a good contrast in the neutron scattering experiments.

Stock solutions were prepared by dissolving the salt and protein powder, respectively, in D_2O. The protein concentration of the protein stock solutions was determined by UV-vis absorption measurements with an extinction coefficient of $0.961\,\mathrm{ml}\cdot\mathrm{mg}^{-1}\cdot\mathrm{cm}^{-1}$ at a wavelength of 278 nm.[178] For sample preparation, appropriate amounts of D_2O, protein stock solution and salt stock solution were mixed. In this work, the samples were prepared without additional buffer since buffers can affect the phase behavior of proteins and the solubility of salts. The pH values determined in H_2O were all in a range between 6 and 7. Using the relation $\mathrm{pH}_{D_2O} = \mathrm{pH}_{H_2O} + 0.4$,[294,295] the pH values were well above the isoelectric point of BLG of 5.2.[296] All experiments were performed at 20 ±1 °C.

6.3.2 Optical microscopy

Protein crystallization in real time was followed with an optical microscope (Axio Scope.
A1, Carl Zeiss AG) in the bright-field mode. The samples were mixed in 1.5 ml plastic tubes (Sarstedt, Germany), directly transferred into a Gene Frame (1×1 cm with a thickness of 0.25 mm and a volume of 25 µl from Thermo Scientific™, Germany) on a glass slide and subsequently covered with a cover slide to prevent evaporation. Images were taken by the microscope-included camera Axio-Cam ICc5 (Carl Zeiss AG) in time intervals according to the time scale of the investigated crystallization process. Since we are interested in the evolution of the sample, the focus area was kept constant to monitor the same spot for a few days. The software ZEN Lite 2012 was used to conduct the imaging as well as to measure the crystal lengths.

6.3.3 Small-angle neutron scattering (SANS)

SANS measurements were carried out at beamline D11 at the ILL, Grenoble, France.[182] The advantages of SANS are the negligible radiation damage and the large scattering volume containing a large amount of sample material, which ensure a good statistical average. The sample-to-detector distance was set to 2 m, which covers a q-range from 0.03 to $0.33\,\text{Å}^{-1}$ at a wavelength of 6 Å ($\Delta\lambda/\lambda = 10\,\%$). Protein-salt solutions in D_2O were filled in rectangular quartz cells with a path length of 2 mm. The beam size on the sample was 7 mm × 10 mm and the acquisition time per run was 240 s. Runs were repeated in appropriate time intervals to follow the crystallization process over a period of 3 days. H_2O was used as a secondary standard to calibrate the absolute scattering intensity. Data were stored in NEXUS data format.[183] The data correction and absolute intensity calibration were obtained using the software LAMP.[297] A detailed data analysis was performed by MATLAB and will be described in more detail in the results section. Data can be accessed via Refs. 185 and 298.

6.4 Results and discussion

6.4.1 Experimental phase diagram of BLG with $CdCl_2$ in D_2O

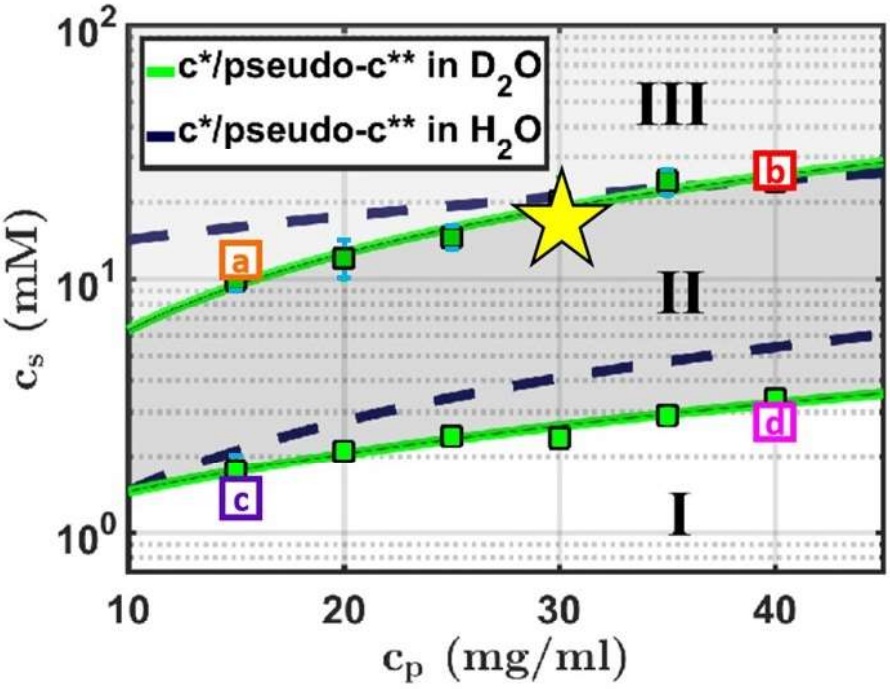


Figure 6.1: *Experimental phase diagram of BLG with $CdCl_2$ in D_2O at 21 °C. In regime I, the negatively charged proteins repel each other and the protein-salt solutions are clear. At $c_s > c^*$, they turn turbid due to the formation of aggregates (regime II). By further increasing c_s above $pseudo{-}c^{**}$, the turbidity decreases again, but does not vanish completely (regime III). In addition to the phase boundaries in D_2O, the phase boundaries in H_2O determined in our previous work are included as dashed lines.[42] The yellow star indicates the region selected for real-time SANS and optical microscopy experiments.*

We first present the phase diagram established in this context for the completely new system BLG with $CdCl_2$ in D_2O (see Fig. 6.1) to obtain an overview of the phase behavior, which will be compared with the phase diagram in H_2O in previous work.[44,45] Samples of different protein concentrations (c_p) and salt concentrations (c_s) were systematically prepared and probed for optical transmission. Depending on their grade of turbidity, they are assigned to regime I, II, or III. In regime I, the protein-salt solutions are clear, since the initially negatively charged proteins repel each other and are stable in solution.[43] Upon increasing c_s above c^*, a first sharp transition occurs from a clear to a turbid solution and one enters a condensed regime, referred to as regime II. By increasing c_s even further, a second phase boundary referred to as $pseudo - c^{**}$ is observed, above which the solutions become gradually

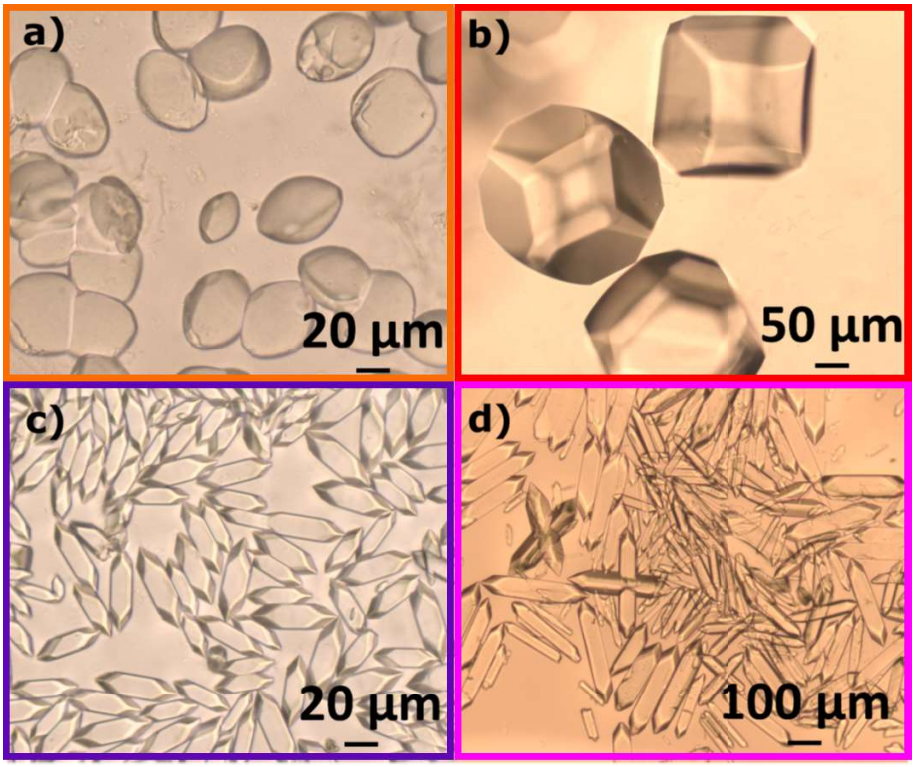


Figure 6.2: *Different crystal morphologies depending on the location in the phase diagram as indicated in Fig. 6.1. a) 15 mg/ml BLG with 13 mM $CdCl_2$, b) 40 mg/ml BLG with 25 mM $CdCl_2$, c) 15 mg/ml BLG with 1.5 mM $CdCl_2$ and d) 40 mg/ml BLG with 3 mM $CdCl_2$. All samples were prepared in D_2O.*

less turbid (regime III).[41,43] This phase behavior is denoted reentrant condensation (RC).[40,43] In contrast to what is observed in the presence of trivalent ions, the transition from regime II to III is not sharp and the solutions do not become completely clear again in regime III. Therefore, the mean c_s of the last clear and first turbid or last turbid and first clearer sample is referred to as c^* or $pseudo - c^{**}$, respectively. If not smaller than the symbols, the blue error bars indicate the standard deviations (see Fig. 6.1).

For comparison, the phase boundaries in H_2O determined in our previous work are included (Fig. 6.1, dashed lines).[42] Using D_2O instead of H_2O, c^* is slightly shifted toward lower salt concentrations. This deviation becomes stronger for higher protein concentrations and indicates that protein-protein interactions are stronger and the system is more attractive.[164] However, a substantial broadening of regime II when H_2O is replaced by D_2O, as reported recently for bovine and human serum albumin solutions in the presence of trivalent ions, is not observed for BLG.[164,214]

Crystallization was observed for samples in regime II. In agreement with our previous work, the resulting crystal morphology and growth kinetics depend strongly on the sample location in the phase diagram.[42,44–46] Fig. 6.2 shows representative crystal morphologies for the sample conditions labeled in the phase diagram (a–d).

Crystals grown close to c^* show elongated, bicapped prism morphologies whereas crystals grown at the $pseudo - c^{**}$ boundary are more roundish and compact. Regarding crystallization kinetics in H_2O, close to c^*, crystallization follows a classical one-step pathway.[42,44,45] Below $pseudo - c^{**}$, in regime II, an intermediate phase is observed before the crystals start to grow.[44,45] Note that Cd^{2+} ions were previously found to improve protein crystal size, morphology, and diffraction quality.[299,300] For this system, however, all crystals are twin crystals and therefore the structural elucidation is more challenging.

In the following, we focus on the characterization of crystal growth within a MIP. Thus, samples in the region just below $pseudo - c^{**}$ are selected as indicated by a yellow star in Fig. 6.1.

6.4.2 Crystallization followed by optical microscopy

We now present the kinetics of nonclassical protein crystallization using optical microscopy. Samples containing 30 mg/ml BLG with 16, 17, and 18 mM $CdCl_2$ in D_2O (indicated by a yellow star in Fig. 6.1) were prepared and followed by optical microscopy for several days. Directly after preparation, the solutions appear turbid due to the formation of aggregates developing a transient gel-like structure. The exact microscopic structure of the aggregates could not be resolved by optical microscopy due to the limited resolution. After roughly 1–2 h, the first crystals become visible and continue to grow for approximately 20 h. Simultaneously, the transient gel dissolves. Fig. 6.3 shows representative snapshots of a sample containing 30 mg/ml BLG and 17 mM $CdCl_2$ after 2.5 and 23 h. Furthermore, it shows the transient gel formed directly after preparation and the sedimented crystals in the final state (after the transient gel has apparently been consumed by crystal growth) within the quartz cuvettes, which were used for SANS measurements.

In Fig. 6.4, representative microscopy images of the real-time data of the crystallization process of 30 mg/ml BLG with 16 mM, 17 mM and 18 mM $CdCl_2$ in D_2O are presented. As expected, the final crystal morphology is highly similar for all conditions studied in this region in the phase diagram (close to $pseudo - c^{**}$), i.e., roundish and compact (see Figs. 6.2, 6.3 and 6.4).

Crystal growth kinetics were determined from the real-time microscopy images by measuring the crystal side-to-side lengths at each time interval. Note that the isotropic shape implies that the crystal volume scales approximately with the cube of this length. The respective lengths are plotted in Fig. 6.5 as a function of time. The linear portion of the data sets was fitted to obtain the growth rates and the induction times t_0. For all samples, an initial linear growth followed by a saturation of the length can be observed. The crystals for the 17 mM sample grew the largest with a final size of roughly 20 µm and had the fastest induction time ($t_0 = 1.3$ h). The induction times for 16 and 18 mM were 4.6 and 2.5 h, respectively, indicating that nucleation occurred in all samples within 5 h. The respective growth rates are also shown in Fig. 6.5. They denote that the samples containing 16 and 17 mM $CdCl_2$ grew approximately at the same speed, whereas the growth rate for the

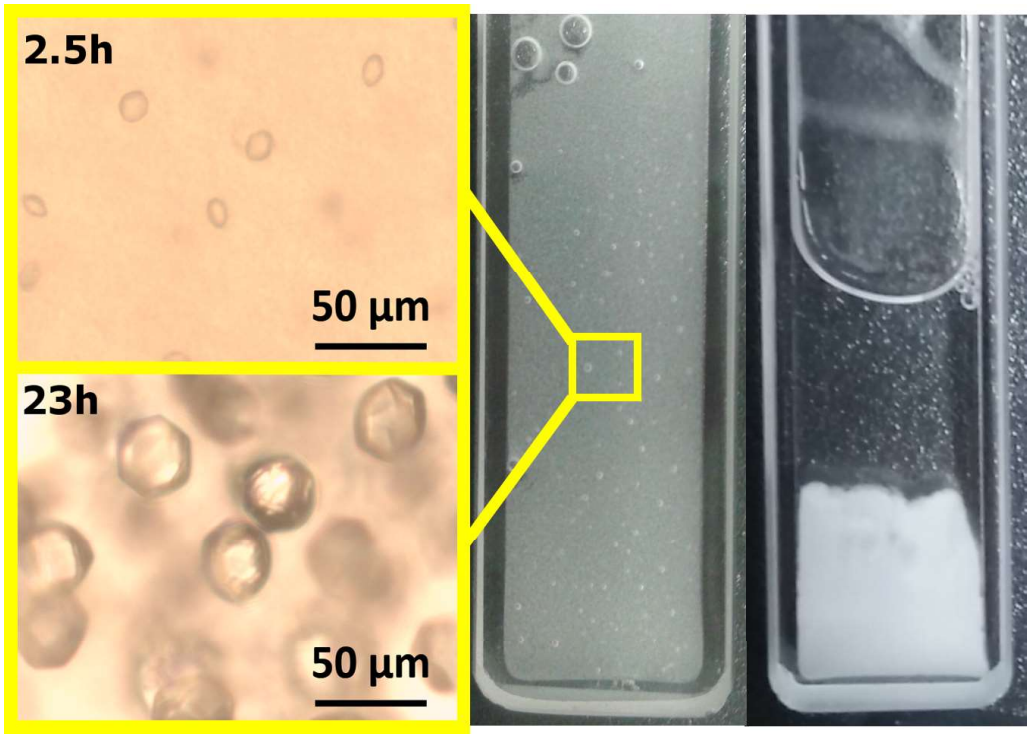


Figure 6.3: *Nonclassical crystallization of BLG close to pseudo − c^{**}. A representative sample containing 30 mg/ml BLG and 17 mM $CdCl_2$ in D_2O at 21 °C. In the early stage, a transient gel-like structure forms, which collapses due to consumption by crystal growth in the later stage, as can be seen in a quartz cuvette used for SANS experiments. Snapshots of the same sample are shown 2.5 and 23 h after preparation (left).*

18 mM sample was reduced. A clear trend as it can be observed for the system in H_2O that the crystal size increases with c_s is absent (see Fig. C.3). In comparison to H_2O, the induction time is longer, and the growth rate and the final crystal size are significantly reduced.

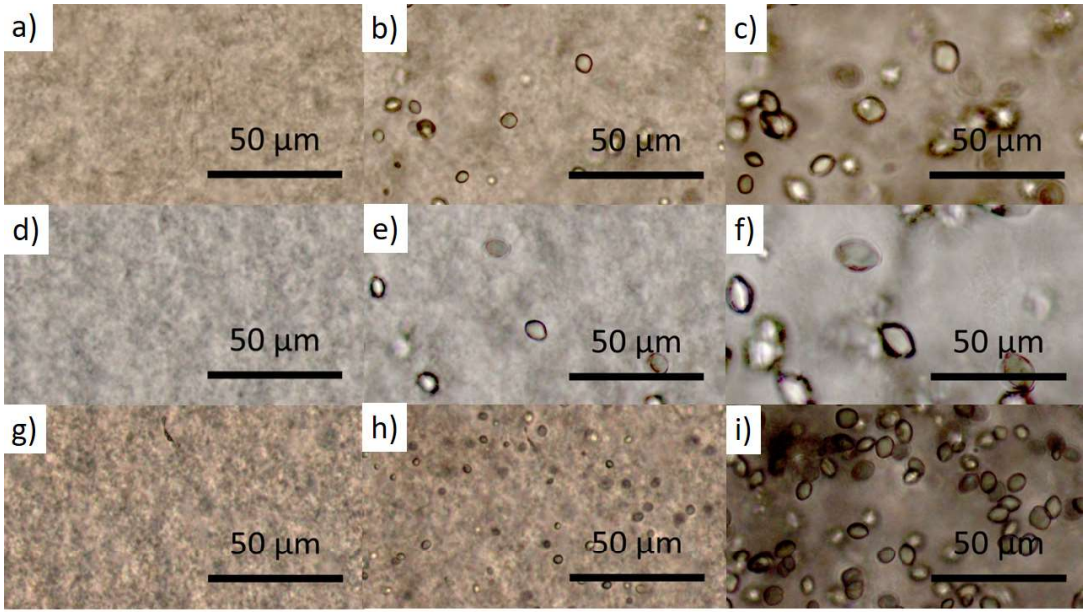


Figure 6.4: *Optical microscopy images of 30 mg/ml BLG with $CdCl_2$. (a–c) 16 mM $CdCl_2$, (d–f) 17 mM $CdCl_2$ and (g–i) 18 mM $CdCl_2$ in D_2O different times after preparation. a) Directly, b) 9.5 h, c) 23 h after preparation; d) directly, e) 11 h , f) 3 days after preparation; g) directly, h) 7 h, i) 1 day after preparation.*

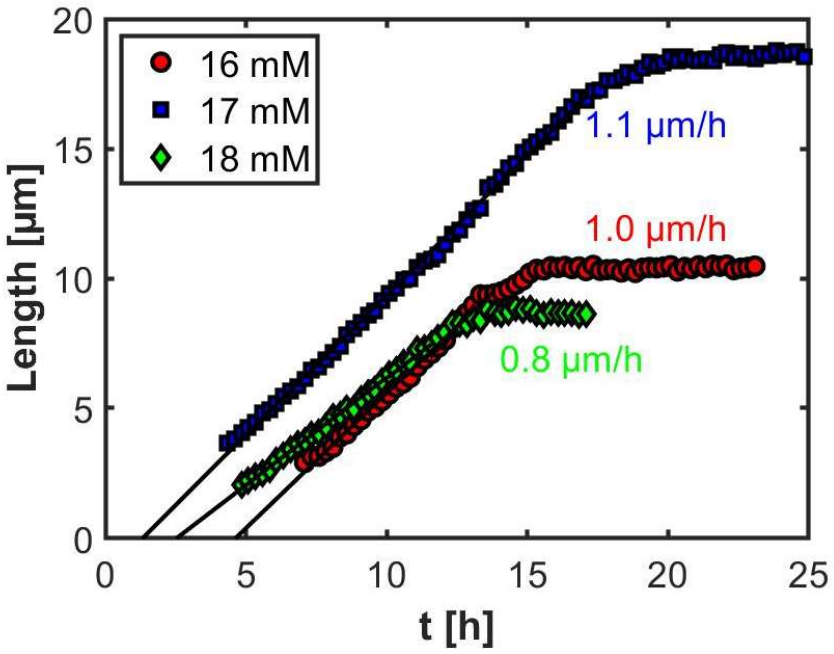


Figure 6.5: *Crystal length as function of time for 30 mg/ml BLG with 16, 17 and 18 mM $CdCl_2$ in D_2O.*

6.4.3 Crystallization followed by real-time SANS

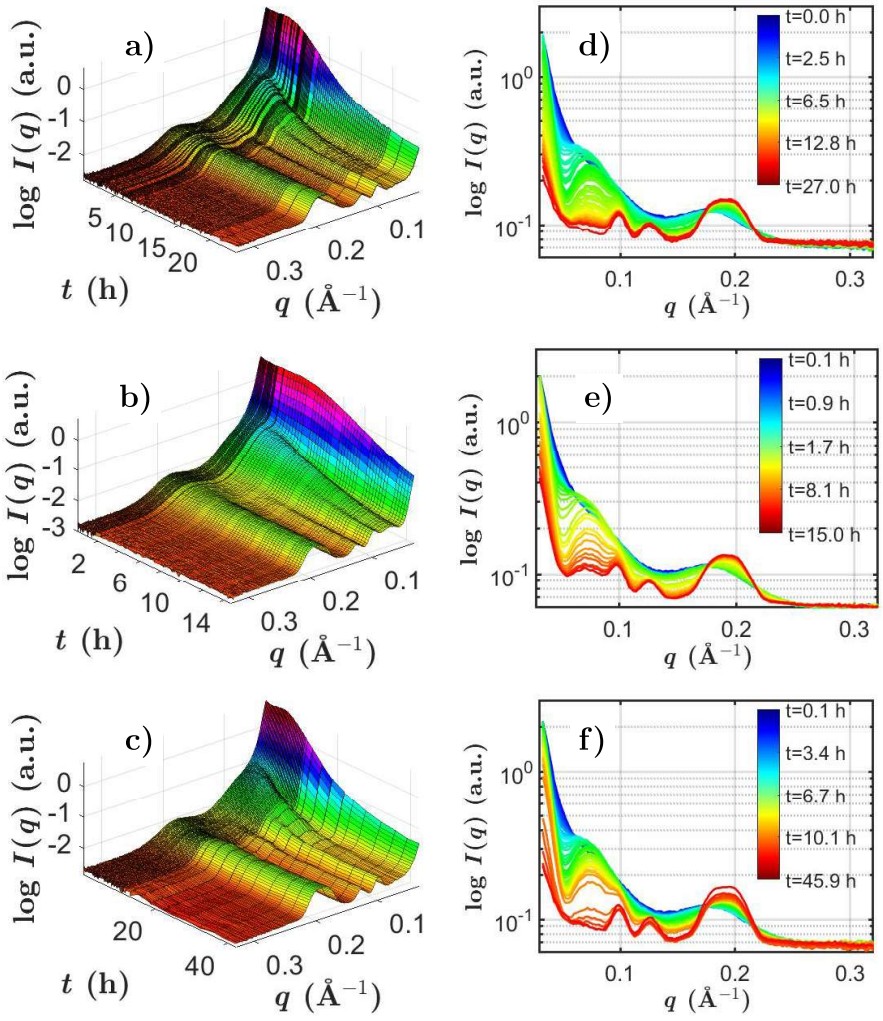


Figure 6.6: *Nonclassical crystallization of BLG close to pseudo − c** followed by real-time SANS: a,d) 30 mg/ml BLG with 16 mM, b,e) 17 mM and c,f) 18 mM $CdCl_2$ in D_2O at 20 °C. For each sample, SANS intensities $I(q,t)$ are plotted in two-dimensional (2D) and three-dimensional (3D) perspective. Note that the color code in 3D corresponds to the intensity, the color code in 2D illustrates the temporal evolution.*

The same sample conditions (30 mg/ml BLG with 16, 17, and 18 mM $CdCl_2$ in D_2O) were studied by real-time SANS to obtain further kinetic information of the crystallization process. Since the neutron beam is much larger than an X-ray beam or the field of view in optical microscopy, we could ensure an excellent statistical average of the sample. Fig. 6.6 shows the SANS intensities I as a function of scattering vector q and time t for each sample, respectively. Directly after preparation, the scattering intensity at very low q-values ($< 0.05\,\text{Å}^{-1}$) is strongly increased due to

the formation of amorphous aggregates. A broad correlation peak at $q \approx 0.175\,\text{Å}^{-1}$ is visible, corresponding to a particle-particle distance of 36 Å, which is the width of a BLG dimer.[301] An intermediate structural feature at $q \approx 0.075\,\text{Å}^{-1}$ starts to develop from the beginning, corresponding to a particle-particle correlation distance of $d_{MIP} \approx 84\,\text{Å}$. We identify this as the characteristic structural feature of the MIP, i.e., a local ordering of the proteins within the MIP. The MIP signal reaches a maximum in intensity after roughly 5 h and then decreases. Simultaneously to the decrease of MIP scattering, Bragg peaks appear at $q \approx 0.1$, 0.12, and $0.2\,\text{Å}^{-1}$ and the intensity at very low q-values decreases again. The positions of the Bragg peaks are consistent with our previous SAXS measurements of the system in H_2O, suggesting a similar unit cell.[44]

To identify possible correlations between the structural changes at different q-values and to clarify their role regarding crystallization, a two-phase analysis, originally known from the concept of crystallinity from semicrystalline polymer systems,[302] was applied. In the first step, all curves $I(q, t)$ were normalized by the first curve $I(q, t = 0)$, which reveals the newly developing structures more clearly (see Fig. 6.7 a). In the second step, the overall background signal was considered by subtracting an appropriate linear background from the normalized data. The background was determined for each single curve separately by a linear fit through $I(q = 0.05\,\text{Å}^{-1}, t)/I(q = 0.05\,\text{Å}^{-1}, t = 0)$ and $I(q = 0.11\,\text{Å}^{-1}, t)/I(q = 0.11\,\text{Å}^{-1}, t = 0)$, respectively (indicated in Fig. 6.7 a by purple arrows). This interval enclosed by two local minima contains both the signal of the MIP and a Bragg peak and can therefore be used to determine the amount of the respective phases (MIP and crystals) within the samples at a given time. Since the q-region of the MIP overlaps with the first Bragg peak, we fitted the interval enclosed by a sum of two Gaussians, fixed in center and width. One Gaussian is fitted to the broad correlation peak apparently corresponding to the MIP and the second Gaussian is fitted to the first Bragg peak representing the crystals in the sample. To clarify this step of analysis, the normalized background-corrected data with fits at selected points of time are shown for 30 mg/ml BLG with 17 mM $CdCl_2$ in Fig. 6.7 b. Note that we did not perform any data analysis of particle shape or size employing form factors, but instead we focus on the distinct scattering features of correlation and Bragg peaks. Using this method, we can minimize the effect of sedimentation on the results, because sedimentation only causes an overall shift of the scattering curves toward higher intensities due to the increase of the amount of material irradiated by the beam, which illuminates the bottom part of the cuvette. Since the analysis uses the area of well-defined peaks (correlation and Bragg peak) with an appropriate linear background correction, an overall upward shift of scattering profiles will not influence the analysis outcome. In addition, the illuminated area is big enough, and the medium viscosity is high enough that such sedimentation effects are minor.

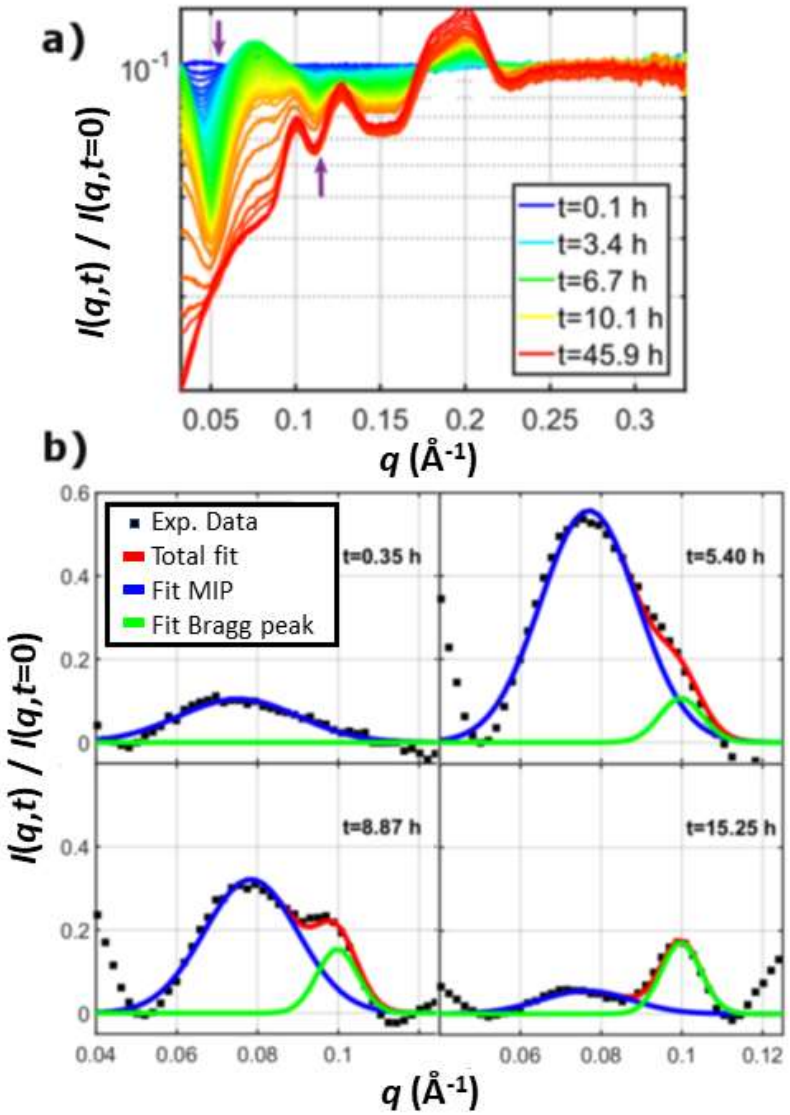


Figure 6.7: *a) Normalized SANS intensities $I(q,t)\,/\,I(q,t=0)$ of 30 mg/ml BLG with 17 mM $CdCl_2$. Normalization of the data reveals the newly developing structures more clearly. The interval for subsequent analysis is indicated by purple arrows. b) Fits of background-corrected normalized SANS data in the low q-region: a sum of two Gaussians (red) with fixed center and width is used to separate the signal of the MIP (blue) and the first Bragg peak (green).*

Furthermore, the signal of the Bragg peak feature at $q \approx 0.2\,\text{Å}^{-1}$ was evaluated in a model-free way. As a first step, a linear background through the intensity minima at $q_1 = 0.176\,\text{Å}^{-1}$ and $q_2 = 0.217\,\text{Å}^{-1}$ was subtracted from all normalized curves. In the second step, the normalized subtracted intensities were summed in the interval between the local minima for each time point. In the last step, the calculated sums were normalized by the maximum sum to obtain $A_{0.2\,\text{Å}^{-1}}(t)$. The temporal evolution of the Bragg peak feature obtained by this method was similar to the ones presented (see Fig. C.1).

With the method discussed above, we derive a measure A of the signal of the MIP (A_{MIP}) and the first Bragg peak (A_{Bragg}) by calculating the area under the respective Gaussian functions as a function of time. $A(t)$ thus provides information on crystal growth and the evolution of the MIP. Subsequently, we calculated the first time derivative of the Bragg peak signal $(d/dt)A_{Bragg}$ from the green guide to the eye in Fig. 6.8 to compare the crystal growth rate with the evolution of the MIP. The results are presented in Fig. 6.8 for 16, 17, and 18 mM $CdCl_2$.

In Fig. 6.8 one can see that the MIP starts to form directly after preparation, and 1–2 h later, the Bragg peaks start to grow, indicating the formation of crystals. The MIP passes a maximum after roughly 5 h and levels off again within the next 20 h. Simultaneously, crystal growth saturates. Both saturations are a clear sign against sedimentation of material into the beam. The analysis reveals that the crystal growth rates are at their respective maxima when a large amount of the MIP is available. It also reveals that the maximum of A_{MIP} is slightly delayed ($\approx$ 1–2 h) with respect to the maximum of $(d/dt)A_{Bragg}$, suggesting that crystals already start to form as soon as some amount of MIP is developed. We note that for the sample with the longest measurement time, we observed a second growth stage of the Bragg signal after 35 h, being consistent with our previous studies in H_2O using SAXS.[44,45] However, similar to the data in H_2O, no second growth step can be seen in the microscopy data either (see Figs. 6.5 and S3).

We note that the rate of crystallization strongly depends on the respective batch of protein since BLG has a purity of only 90 %. While the general phase behavior (RC) is observed for every batch, the phase transition boundaries and the crystallization speed vary. Investigating a similar condition (33 mg/ml BLG and 17 mM $CdCl_2$ in D_2O), measured with a different batch of protein on a different beamtime, resulted in a fast crystallization that was completed within 2 h (see Fig. C.2). In this case, the data analysis shows also a clear two-step crystal growth. In combination with Fig. 6.8 and the previous studies in H_2O,[44,45] we conclude that the second growth stage is a relevant feature and is caused by crystal growth within the dilute phase after all MIP is consumed and not only by crystals sedimenting into the beam. It is worth noting that the second growth stage (of the SANS signal) may only improve the crystal quality but not its size,[303] which would explain the absence of this growth stage in the microscopy data.

Finally, we analyze the structure of the MIP as a function of time. For this purpose, a Gaussian was fitted to the MIP correlation peak of the SANS data shown in Fig. 6.6. The q-values of the respective maxima (q^*) were transformed

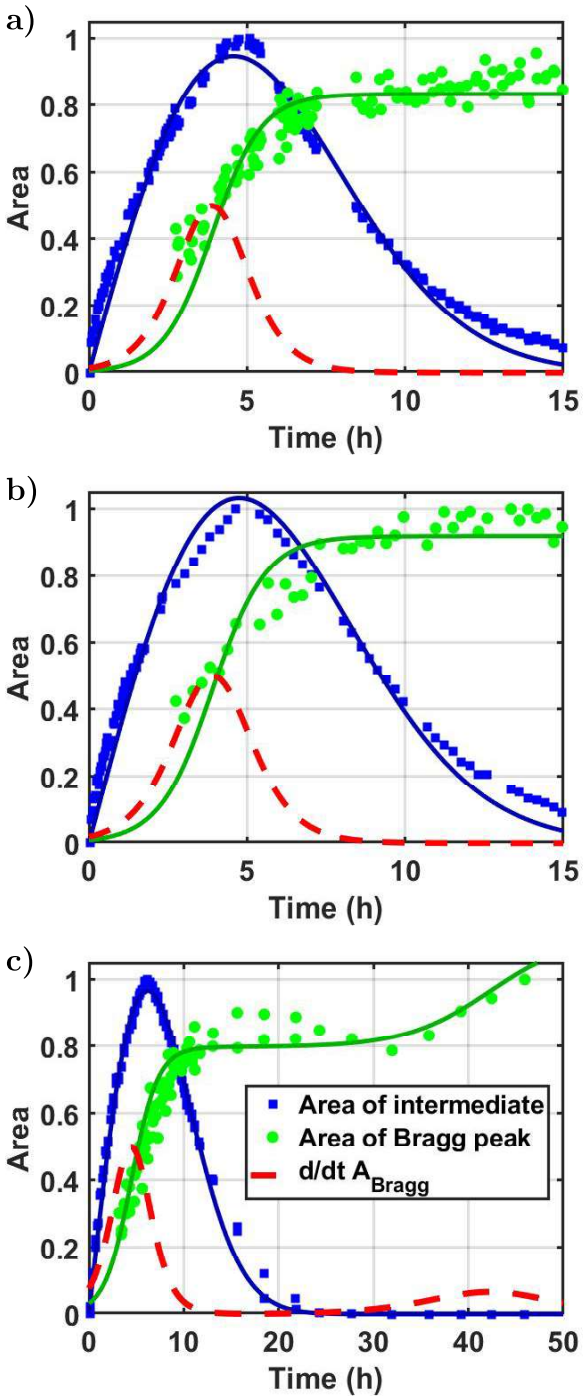


Figure 6.8: *Normalized kinetic analysis of 30 mg/ml BLG close to pseudo − c**: correlations between the evolution of the MIP and the Bragg peaks for 30 mg BLG with a) 16 mM $CdCl_2$, b) 17 mM $CdCl_2$ and c) 18 mM $CdCl_2$. The MIP starts to grow directly after preparation and passes a maximum. Bragg peaks start to grow slightly later. At the same time, as the amount of MIP decreases again, the growth of the Bragg peaks reaches saturation. A second growth stage of the Bragg peaks is observed after roughly 35 h. The colored lines are a guide to the eye.*

into real space distances by $d^* = 2\pi/q^*$. These values are plotted in Fig. 6.9 a. It is clearly visible that the proteins within the MIP are initially correlated within a range of 105–110 Å. With time, the average distance between the particles in the MIP decreases to 84 Å, where it saturates for all c_s investigated. Note that d^* is the average distance, but the correlation peak has a certain width, hence, shorter and longer distances are also present within the MIP and fully evolved domains may already serve as crystal precursors. Similarly, in a Lennard-Jones system at moderate supercooling, a local order parameter distribution was found.[277] Since d^* changes with time, the MIP is assumed to be protein aggregates with a certain flexibility. To compare the development of the MIP with the overall amount of MIP and crystals, all three parameters are plotted for 30 mg/ml BLG with 17 mM $CdCl_2$ in Fig. 6.9 b. Here, the maximum amount of dense phase present in the sample is close to the saturation time of d^*. Hence, when the maximum amount of MIP is present, the average distance between the proteins is at its final stage and a maximum amount of preordered precursor is available for crystallization. Roughly at this time, the crystallization rate is the highest, indicating the important role of a fully developed MIP as a preordered precursor. Based on the SANS analysis, we expect the MIP to be locally preordered domains. Hence, we conclude that in our system, first, the order changes within the clusters (see Fig. 6.9) and subsequently the density. However, the MIP does not necessarily already have the similar structure as the final crystal.

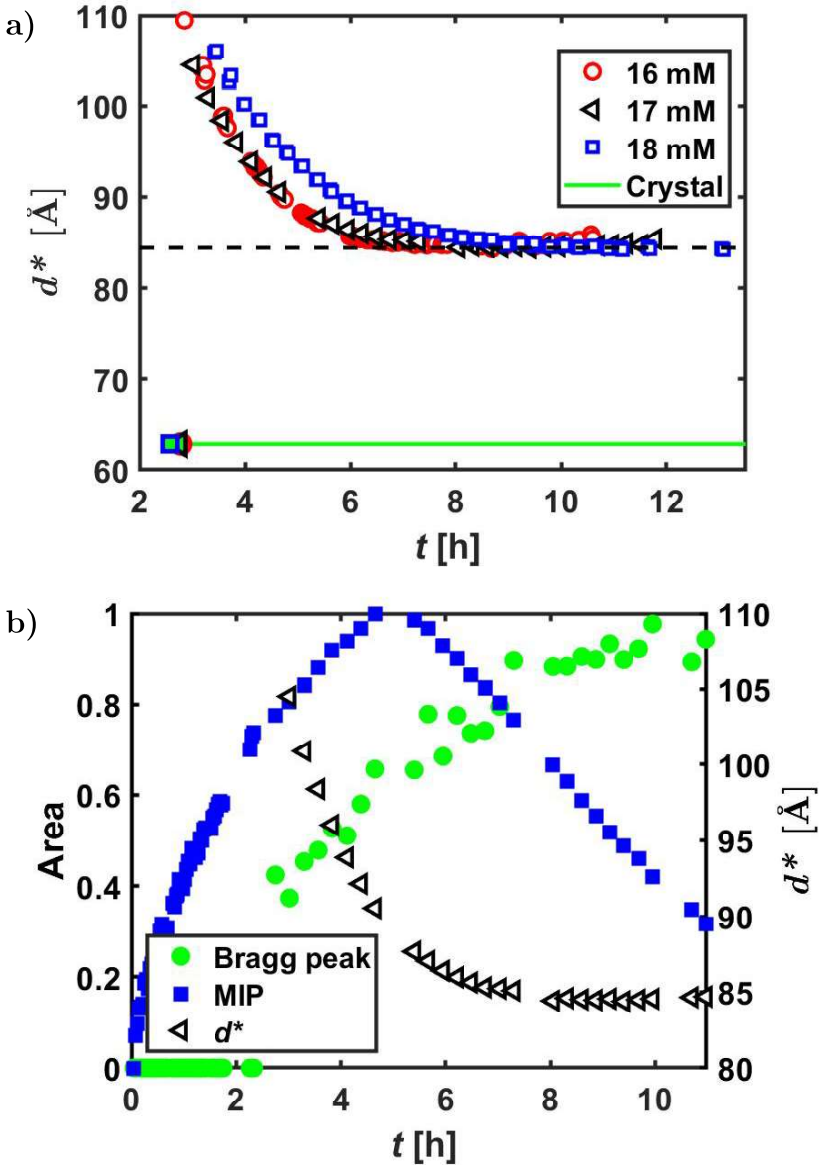


Figure 6.9: *a) Average distance between two proteins d^* within the MIP as function of time for samples containing 30 mg/ml BLG and 16, 17, and 18 mM $CdCl_2$. In green, the crystal distance corresponding to the first Bragg peak at 0.1 $Å^{-1}$ is shown with the respective symbols indicating when the Bragg peak was observed by SANS (see Fig. 6.8). The black dashed line at $d = 84$ Å indicates a similar final distance within the MIP for all three c_s. b) Amount of MIP (filled blue squares) and crystalline phase (filled green circles) as well as d^* (open black triangles) as function of time for a sample containing 30 mg/ml BLG and 17 mM $CdCl_2$. Filled symbols correspond to the left y-axis whereas open symbols correspond to the right y-axis.*

6.5 Discussion on the role and the development of the MIP

We discuss the significance of the preordered MIP observed in this work in comparison with other protein systems. In the BLG-$CdCl_2$ system, gel-like aggregates are formed in the condensed regime II instead of LLPS.[44,45] The metastable aggregates develop a correlation peak at $q \approx 0.075\,\text{Å}^{-1}$ in SANS and SAXS measurements, which is close to the first Bragg peak at $q = 0.1\,\text{Å}^{-1}$, indicating the preordered nature of this MIP. In our previous work on the system HSA with $CeCl_3$, a metastable LLPS with respect to crystallization was found.[214] Thus, dense liquid droplets were identified as metastable intermediates between solution and crystals.[214] However, these droplets seem to act only as reservoir rather than precursors and no structural feature such as a correlation peak was observed in SAXS/SANS data.[214] In BLG with $ZnCl_2$ solutions, amorphous aggregates form initially in regime II, but they relax into a dense liquid state.[42] Crystals appear at the interface of the dense phase and grow into the surrounding dilute phase.[42] Neither the initial amorphous aggregates nor the dense liquid phase show such correlation peak in scattering profiles. Interestingly, for BLG with YCl_3,[304] a correlation peak was observed at $q \approx 0.03\,\text{Å}^{-1}$ in comparison with the first Bragg peak at $q = 0.92\,\text{Å}^{-1}$.[48] This correlation peak was attributed to a local order of protein clusters caused by the fine balance between the bridging effect of metal ions and the electrostatic repulsion due to the accumulated net charges close to c^{**}.[304] Hence, it seems that the correlation peak observed here (and in H_2O[42,44]) is indeed a sign of preordering within the MIP, which cannot be seen for conditions close to c^*, which are believed to follow a one-step crystallization pathway.[42,44]

Similar preordering has been reported for ferritin crystallization in the presence of Cd^{2+}.[89] There, the preordered protein aggregates have an interparticle distance of less than 1.3 times the distance in the crystal and the crystalline order evolution is accompanied with the shortening of the interparticle distance.[89] This phenomenon has been observed also in mineralization processes and dehydration is proposed to be the driver of this change of distance.[89,275,286] In our system, the first Bragg peak corresponds to an interparticle distance of 62 Å and if we multiply it by 1.3, the nearest neighbors should be within a distance of roughly 80 Å. If water is expelled from the crystal during the final stage,[275] but is still present within the preordered MIP, the determined saturation interparticle distance of $d = 84\,\text{Å}$ within the MIP can be interpreted as the distance of nearest neighbors. Since d^* decreases from initially $\approx 110\,\text{Å}$ to the final value of $d_{MIP} = 84\,\text{Å}$, the number of nearest neighbors increases in this process as well, or, in other words, a densification occurs parallel to the structural changes. Based on these discussions, the crystallization pathway revealed in this work is illustrated in Fig. 6.10. Directly after preparation, randomly oriented clusters form. They undergo a preordering and a first densification in parallel, until an interparticle distance of $d = 84\,\text{Å}$ within the MIP is reached. As a second step, D_2O is expelled and therefore the density increases again, resulting in

the final crystal with an interparticle distance of $d = 62\,\text{Å}$. This $\approx 20\,\text{Å}$ difference between MIP and crystal is believed to correspond to the release of roughly two layers of water from each protein involved, since the first hydration layer of a protein was found to be $3 - 5\,\text{Å}$ thick while the overall hydration layer can be up to $8\,\text{Å}$.[305–308] We note that in this study heavy water (D_2O) and not H_2O was used as a solvent, which might influence the hydration slightly.

Another feature of the MIP is the mobility of molecules within the aggregates. Since the solutions investigated are extremely viscous and gel-like after preparation (see Fig. 6.3), a certain degree of mobility of molecules is assumed to be needed for crystallization. In an extreme case of glass, it was found that the rigidity of the network plays a crucial role in phase transitions (and therefore nucleation).[309] Nucleation is believed to occur in so-called "active centers", namely, the dynamic regions of the network, which are able to spatially rearrange and move within the rigid network.[309] Below a certain threshold, the sizes of these dynamic regions are too small for nucleation.[309] Ordering occurs first in these dynamic regions, followed by an increasing density (lowering of entropy).[309,310] A recent study on protein crystallization using time-resolved liquid-cell TEM demonstrated that proteins in the lattice are mobile throughout the crystal structure in the early stage of crystallization.[107] The intermolecular bonds or contacts can break and reform rapidly,[107] supporting the hypothesis of flexible and dynamic intermediates. Our previous work on the crystallization of BLG in the presence of YCl_3 showed that the protein clusters have not only a precrystalline structure but also an internal flexibility, which enables local reorientation within the clusters.[48] In consistency with this work, the temporal evolution of the ordering indicates that, although a local order exists, proteins are supposed to be still flexible within the MIP and can rearrange themselves, which is crucial for these aggregates being nucleation precursors.

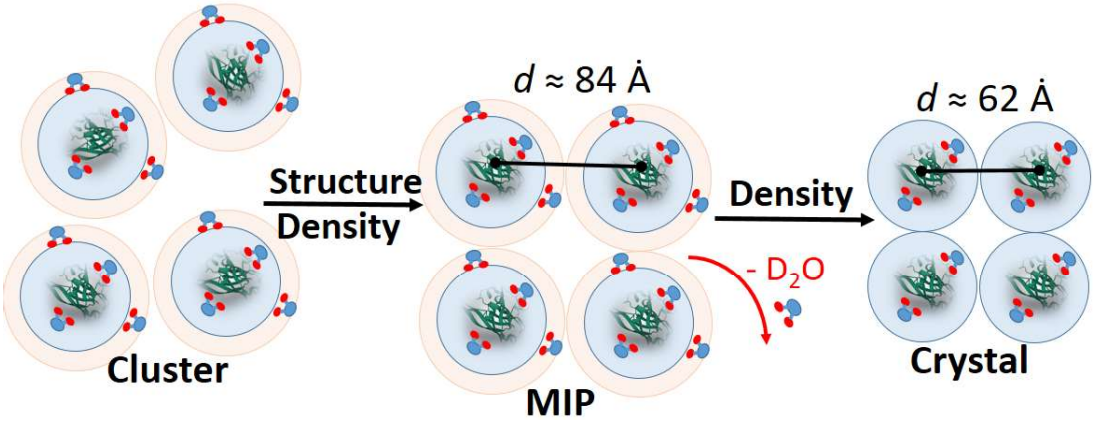


Figure 6.10: *Schematic pathway of protein crystallization from a metastable intermediate phase revealed in this work. The BLG monomers are drawn in green (PDB entry 4LZU, visualized by Mol*[311]). The oxygen atoms of D_2O are colored blue, whereas the deuterium atoms are colored red. For clarity, Cd^{2+} ions are not drawn.*

6.6 Conclusions

In summary, we demonstrate that the combination of real-time SANS and optical microscopy can be used to reveal new insights into the kinetics of protein crystallization. Based on our findings, we suggest the following nonclassical crystallization mechanism: Directly after preparation, the proteins form big amorphous aggregates. Within these aggregates, a preordered structure starts to develop (MIP) on a length scale slightly larger than the crystal unit cell. Since preordering lowers the nucleation barrier of the protein molecules, crystals start to nucleate within the MIP. Potentially, D_2O is expelled in the final stage as closing densification. During nucleation, the MIP is consumed. The crystals may grow further upon consuming a fraction of the proteins of the solution until a final equilibrium between solution and crystals is reached. These findings of a preordered precursor pave the way for understanding the crystallization pathway and the temporal role of a MIP during crystallization in aqueous protein solutions. This is not only relevant from a fundamental point of view but also has a huge impact on structural biology and potentially many other fields like biopharmaceutical formulation.

Part VII

Structural insights into polymer-bounded lipid nanodiscs

Chapter VII is based on a manuscript in preparation for submission:
Structural insights into polymer-bounded lipid nanodiscs
Ralph Maier#, Rodrigo Cuevas Arenas#, Ana García-Sáez, Fajun Zhang, and Frank Schreiber
#: These authors contributed equally to this work

Contributions:	
Research design	RCA, RM, ACS , FZ, FS
Experiments	RM, RCA
Data analysis and interpretation	RCA, RM, FZ
Paper writing	RCA, RM, FZ, FS

7.1 Abstract

Membrane proteins are an essential part of signalling and transport processes and are targeted by multiple drugs. To isolate and investigate them in their native state, polymer-bounded nanodiscs have become valuable tools. In this study, we investigate the model system dimyristoyl-phosphocholine (DMPC) as lipid with the nanodisc-forming copolymers styrene maleic acid (SMA) and diisobutylene maleic acid (DIBMA). Using small-angle X-ray scattering (SAXS) and dynamic light scattering (DLS), we studied the influence of polymer concentration and temperature on the nanodisc structure. In Tris buffer, the radius of the nanodiscs formed by the styrene group containing SMA is smaller compared to DIBMA and decreases monotonically with increasing polymer concentration, but to a stronger extent when using SMA. Measurements at temperatures T between 5–30 °C in phosphate buffer showed an incomplete solubilisation at high T even at polymer/lipid ratios above that required for complete lipid solubilisation with generally larger particles using SMA. For DIBMA, the nanodiscs developed at lower temperatures are stable and the net repulsion increases, while for SMA, aggregates/clusters of the nanodiscs are formed due to an increase in attraction at lower T. Interestingly, for both polymers, no drastic changes of the observable parameters are seen upon quenching, which would indicate a sharp (first order) phase transition from liquid crystalline to gel, but only gradual changes. Hence, we conclude that the transition from a gel toward a liquid-crystalline lipid phase proceeds over a broad T-range compared to a continuous lipid bilayer. These results can pave the way towards the development of better protocols for studying membrane proteins stabilised in this type of membrane mimics.

7.2 Introduction

Membrane proteins comprise approximately 26 % of the human proteome.[121] They play essential roles in signalling and transport across cellular membranes and are the

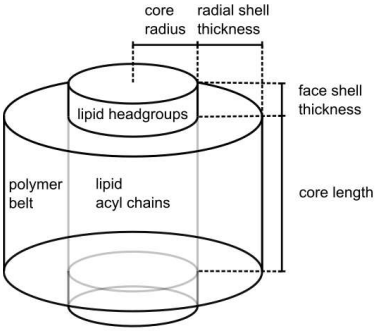
target of more than 60 % of all drugs.[312] Frequently, membrane proteins must be extracted from the membrane and purified for their study, which is commonly done using detergents that are composed of a hydrophilic headgroup and a hydrophilic tail. In general, detergents (also referred to as surfactants) solubilise lipid bilayers into mixed micelles. Despite their efficiency as solubilisers, detergents provide an environment which poorly mimics that of a lipid bilayer, often resulting in low protein stability, loss of conformation, or aggregation.[313] This can potentially lead to the denaturation of the membrane proteins.[313]

In 2002, so-called nanodiscs emerged as a solution to overcome these obstacles for membrane protein investigations.[127,128,133,314] For that, membrane scaffolding proteins (MSPs) have been used as a belt to surround a lipid bilayer and stabilize it.[127,128] These lipid-protein particles were on the order of $\approx$ 10 nm in diameter, and due to their architeture as nanosized lipid bilayers they gained their name nanodiscs.[127,315] Structural studies have been conducted to test different quantities. For example Morgan et al. could show that the respective scaffolding protein is able to undergo structural changes.[315] Protein-nanodiscs have enabled biophysical and chemical investigations of several different membrane proteins including ion transporters and cytochrome P450.[130–133]

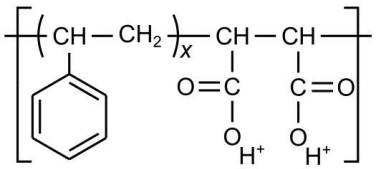
Using polymers as surrounding belt instead of MSPs has enabled the fine-tuning of the size of the nanodiscs.[316] Another advantage of using a polymer as belt compared to a MSP is the increased stability of the nanodiscs at low pH-values and in the presence of multivalent metal ions.[316] Also, no detergents are required for solubilisation, which have to be removed in the end, and since no MSP is present, it cannot interfere with absorbance studies of the desired membrane protein.[317] The architecture of such polymer nanodiscs, i.e., the model used for fitting the experimental data can be found in Fig. 7.1a. Recently, the amphiphilic copolymers styrene maleic acid (SMA) (Fig. 7.1b) and diisobutylene maleic acid (DIBMA) (Fig. 7.1c) have been applied in the solubilisation of model and natural lipid membranes.[134] In the presence of lipid membranes these copolymers spontaneously form polymer-bounded lipid nanodiscs termed SMA-lipid particles (SMALPs)[135] or DIBMA-lipid particles (DIBMALPs), respectively.[136] These polymer nanodiscs can stabilise membrane proteins and are amenable to biophysical methods requiring small particles sizes in suspension and allow to study the membrane proteins with methods/techniques typical of soluble proteins.[318] Additionally, the lipid core of the nanodiscs can undergo gel-to-liquid thermotropic phase transitions, indicating the presence of a true lipid bilayer.[136,319–321]

Despite efforts to address the structural details of polymer nanodiscs,[136,317,322–325] little is known about the structural and molecular changes at different temperatures, i.e., how the (possible) phase transitions can affect the structure, and polymer/lipid ratios. However, Bjørnestad et al. could show nicely by small-angle X-ray scattering (SAXS) how solubilisation from lipid vesicles proceeds upon polymer addition due to styrene units self-insertion into the lipid bilayer hydrocarbon (tail) region in a first step.[325] In the next step, upon increasing polymer (SMA(3:1), molar ratio of 3:1 styrene:maleic acid) concentration, the vesicle bilayers are saturated with polymer

a)



b)



c)

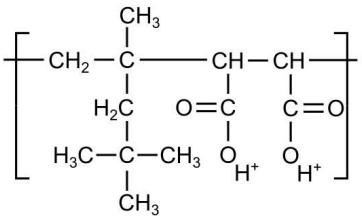


Figure 7.1: *(a) Core-shell cylinder model used to fit SAXS data showing the dimensions calculated from the model. Chemical structures of (b) SMA(2:1) (x ≈ 2, M_w = 7.0 kg/mol, M_n = 2.7 kg/mol) and (c) DIBMA (M_w = 15.3 kg/mol and M_n = 8.4 kg/mol).*

and SMA nanodiscs begin to form as the polymer molecules form a belt around the structure.[325] In this stage, the nanodiscs coexist with the polymer-saturated lipid vesicles.[325] In the last step, upon crossing the solubilisation polymer concentration, all lipid vesicles are fully transformed into SMA nanodiscs.[325] Similar observations were obtained by molecular dynamics simulations. There, SMA was found to bind to the lipid bilayer interface, which is caused by the hydrophobic effect.[326] Increasing the amount of adsorbed polymer leads to large membrane defects, including small, water-filled pores.[326] The rim of these pores can be stabilised by the SMA molecules, resulting in pore growth and further membrane disruption.[326] In their simulations, no complete nanodisc formation was seen due to the limited time scale of the simulations.[326] However, self-assembly simulations indicate that nanodiscs are the thermodynamically most favorable state of these systems.[326]

In the present work, we have exploited SAXS and dynamic light scattering (DLS) to systematically investigate the structural changes of polymer nanodiscs formed with the saturated phospholipid dimyristoylphosphocholine (DMPC) and either SMA(2:1) (2:1 styrene:maleic acid) or DIBMA (1:1 diisobutylene:maleic acid). Tak-

ing advantage of published pseudophase diagrams,[136,320] we produced SMALPs and DIBMALPs at copolymer/lipid molar ratios (R) above of that required to achieve complete lipid solubilisation (R^{SOL}) and analysed changes in their geometry and molecular arrangement at increasing R (case A), and the temperature of the system (case B). For SMALPs, R^{SOL} is 0.13 and for DIBMALPs 0.062 for the lipid concentration used in this work.[136,320] We found that the average diameter d of the polymer nanodiscs decreases monotonically when increasing R and that d(SMA) ¡ d(DIBMA) at the same R/R^{SOL} values. In contrast, the bilayer thickness is only reduced significantly for SMALPs, but to a much smaller extend for DIBMALPs. For case B, a reduction in the system temperature results in a contraction of the diameter and concomitant increment of the nanodisc thickness in both SMALPs and DIBMALPs. Importantly, quenching the temperature leads to a complete solubilisation and complete nanodisc formation while SMALPs can further aggregate into larger clusters.

7.3 Experimental

7.3.1 Materials

1,2-dimyristoyl-sn-glycero-3-phosphocholine (DMPC) was from Avanti (Alabaster, AL). Solutions of styrene/maleic acid 2:1 (SMA(2:1)) (tradename Xiran SZ30010) and diisobutylene/maleic acid (DIBMA) (tradename Sokalan CP9) were kindly provided by Polyscope (Geleen, Netherlands) and BASF (Ludwigshafen, Germany), respectively. NaCl, Na_2HPO_4, NaH_2PO_4, and tris(hydromethyl)-aminomethane (Tris) were purchased from Sigma–Aldrich (Steinheim, Germany). All chemicals were purchased at the highest purity available.

7.3.2 Polymer stock preparation

SMA(2:1) hydrolysed from styrene maleic anhydride (2:1) (mass-average molar mass $M_w = 7.0\,\mathrm{kg\,mol^{-1}}$ and number-average molar mass $M_n = 2.7\,\mathrm{kg\,mol^{-1}}$) and DIBMA ($M_w = 15.3\,\mathrm{kg\,mol^{-1}}$ and $M_n = 8.4\,\mathrm{kg\,mol^{-1}}$) were obtained as alkaline solution. The copolymers were prepared as described previously.[327] Briefly, copolymer in solution was precipitated by adding small amounts of concentrated HCl and gently shaking until the solution reached pH ≈ 5. The suspension was centrifuged at 11,000 g at room temperature (RT) for 15 min and the supernatant discarded. The copolymer was resuspended in 100 mL ultrapure water by vigorous shaking and centrifuged at 11,000 g at RT. The copolymer was resuspended in ultrapure water and centrifuged twice again. Precipitated copolymer was resuspended in 0.5 M NaOH at 37 °C under gentle shaking. After complete resuspension, the copolymer was frozen at -80 °C and freeze-dried for at least 24 h. Dried copolymer powder was stored in a dark sealed glass container at RT and resuspended in buffer before use.

7.3.3 Preparation of polymer-lipid nanodiscs

DMPC in the form of dried lipid powder was resuspended in Tris-saline (TS) buffer (50 mM Tris, 200 mM NaCl, pH 7.4) or phosphate-saline (PS) buffer (50 mM Na_2HPO_4/-NaH_2PO_4, 200 mM NaCl, pH 7.4) to a final concentration of 20 mM. The lipid suspension was thoroughly vortexed and equilibrated at 30 °C for 15 min prior to a 31-fold extrusion through a 100 nm polycarbonate membrane using a LiposoFast extruder (Avestin, Ottawa, Canada) to form large unilamellar vesicles (LUVs). LUVs were mixed and incubated with either SMA(2:1) or DIBMA in TS buffer for concentration-dependent experiments or in PS buffer for temperature-dependent experiments at 30 °C for at least 1 h to form SMALPs or DIBMALPs, respectively. The reason we used phosphate buffer for temperature-dependent experiments is that Tris buffer undergoes pH changes at different temperatures and, thus, can affect nanodisc shape/formation. SMALPs and DIBMALPs were always produced with a final lipid concentration of 10 mM and a R above of that required for complete lipid solubilisation (R^{SOL}).[320,321]

7.3.4 SAXS measurements

SAXS measurements were performed at P12, PETRA III at DESY, Hamburg, Germany.[223] The data were reduced according to standard procedures using the beamline software and scaled to absolute scattering intensity, $I(q)$, with units of 1/cm as a function of q with $q = 4\pi\sin\theta/\lambda$ where θ is half the scattering angle and λ the wavelength of the incoming bean. The incident beam had an energy of 10 keV. Calibration of the intensity was made using bovine serum albumin as protein standard or ultrapure water.

7.3.5 SAXS data analysis

SAXS data were analysed in both a model-free and a model-dependent way in order to obtain as much information as possible. For the model-free approach, the pair density distribution function (PDDF, $P(r)$) and the radius of gyration R_g of the respective SAXS curves were calculated by GNOM (Version 4.6).[328] An effective bilayer thickness could be obtained by the position of the second maximum in each curve representing the correlation between the headgroups. After having confirmed that the shape of the particles can be indeed assumed as flat discs, a poly core shell cylinder model was applied to fit the SAXS curves using IGOR Pro 6.37 in combination with the NIST analysis package.[225] The scattering length density (SLD) of the core, i.e., the hydrophobic tails of the lipids, was calculated to be 4.7×10^{-8} Å^{-2} and set constant. The SLD of the shell (taking into account the polymer belt as well as the hydrophilic headgroups of the lipids) was set to $\approx 8 \times 10^{-8}$ Å^{-2}. All other parameters were left free for fitting, sometimes within a given reasonable range. The bilayer thickness, t, was subsequently calculated as 2 × face shell thickness + core length, whereas the diameter of the nanodiscs, d, was calculated by 2 × core radius

+ 2 × radial shell thickness.

7.3.6 DLS

DLS measurements were performed on a Zetasizer Nano ZS (Malvern Instruments, Worcestershire, UK) equipped with a 633 nm He–Ne laser and a photodetector placed at an angle of 173 °. Measurements were carried out in a quartz cuvette with a 3 × 3 mm cross-section (ZEN2112, Malvern Instruments). Samples were measured with the attenuator position automatically optimised for determination of size distributions. Data analysis was performed by fitting the experimentally determined autocorrelation function with a non-negative constrained least-squares function[329] to obtained the intensity-weighted particle size distribution and by cumulant analysis[329] to yield the z-average particle size and size distribution width as derived from the associated polydispersity index (PDI). Assuming Gaussians distributions of both the decay rate and particle size, the standard deviation of the z-average particle size was determined as $\sigma = z\sqrt{\text{PDI}}$.

7.4 Results

7.4.1 Case A: Membrane architecture is affected with increasing copolymer concentrations

To test the influence of copolymer type on nanodisc formation, we produced SMALPs and DIBMALPs by solubilising large unilamellar vesicles (LUVs) made up of DMPC. Both polymers are similar except the fact that SMA contains a styrene residue whereas DIBMA's residue is aliphatic (see Fig. 7.1b,c). It has been reported that combining lipids with SMA or DIBMA at subsolubilising polymer/lipid ratios below R^{SOL} leads to incomplete vesicle solubilisation and subsequent formation of large aggregates which are incompatible with methods requiring small particle sizes.[330] Thus, we produced SMALPs and DIBMALPs at R greater than R^{SOL}.[320,321,331] SMALPs and DIBMALPs produced with increasing R were first analysed by DLS to determine their mean hydrodynamic size (z-average) and polydispersity.[332] The z-average sizes of the SMALPs ranged from 13 ± 6 nm up to 29 ± 14 nm (Fig. 7.2a) and of the DIBMALPs from 26 ± 12 nm up to 43 ± 21 nm (Fig. 7.2b). Notably, the polydispersity of both systems remained consistently low at all R, as reflected on the relatively narrow peak widths derived for each particle population. These results confirm the dependence of particle size with copolymer/lipid ratio of formation and the ability of DIBMA to form larger nanoparticles as compared with SMA. This information can be relevant for exploiting DIBMA's potential to directly extract large molecular complexes from biological membranes or use it as platform for membrane protein reconstitution.

Although DLS is a valuable method for gaining information about globular particle sizes, it is not able to resolve smaller-scale characteristics of the particles

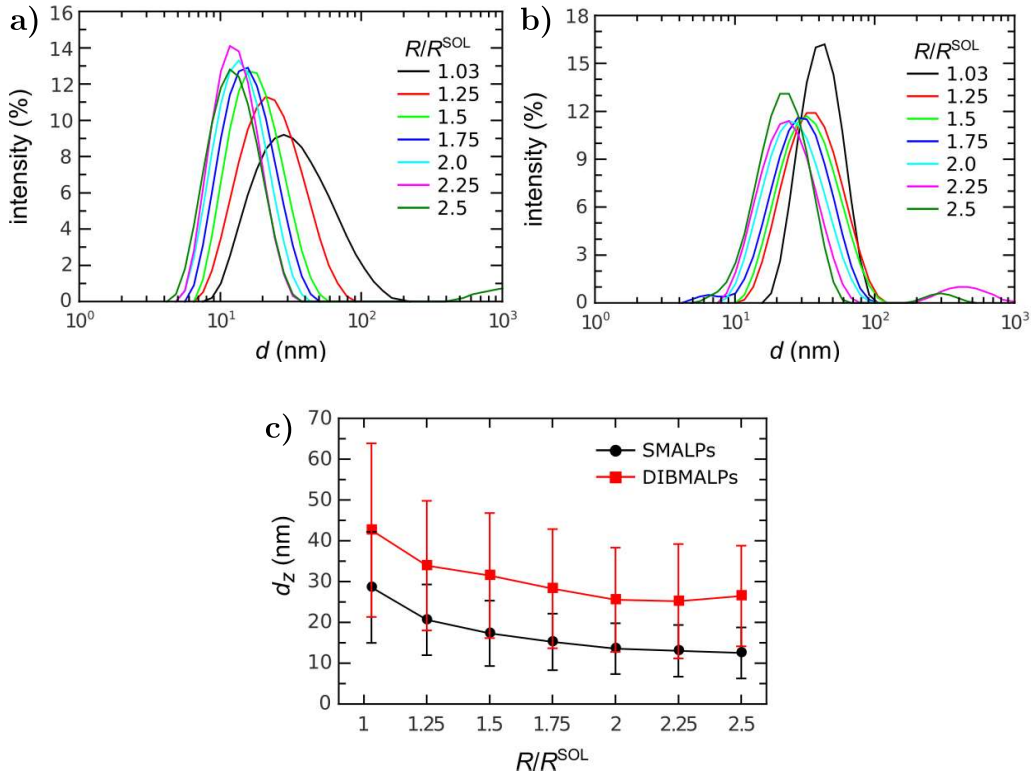


Figure 7.2: *Size of SMALPs and DIBMALPs as monitored by DLS at 30 °C. Intensity-weighted particle size distributions as function of hydrodynamic diameter, d, for (a) SMALPS and (b) DIBMALPs. Legend indicates normalised polymer/lipid ratio of nanodisc formation with the corresponding solubilising polymer/lipid ratio (R/R^{SOL}). (c) z-average particle size, d_z, as obtained from curves in (a) and (b). Error bars indicate the peak distribution width as determined from $\sigma = \sqrt{PDI}d$. Nanodiscs were formulated in TS buffer.*

of interest.[333] Hence, we used SAXS to obtain detailed information on the size and structure of nanodiscs in solution. The recorded SAXS data show an oscillating behaviour of the scattering intensity arising from negative excess scattering length density from the hydrocarbon chains at the nanodisc core and positive excess length densities from both the phosphocholine headgroups and the copolymer belt on both SMALPs and DIBMALPs (Fig. 7.3).[325,334–336] The SAXS pattern is similar to that of structurally similar particles such as, lipoprotein–lipid complexes[337] and protein-bounded nanodiscs,[338,339] evidencing the discoidal shape of SMALPs and DIBMALPs. The data for SMALPs show a local minimum at the scattering vector $q = 0.6\,\mathrm{nm}^{-1}$, which shifts to higher q-values accompanied by a reduction in its depth with increasing SMA concentrations (Fig. 7.3a). A shift of the minimum from $q = 0.6\,\mathrm{nm}^{-1}$ to $q = 0.8\,\mathrm{nm}^{-1}$ represents a decrease in the nanodisc radius from $d = 2\pi/q_{\mathrm{min}} = 2\pi/0.6\,\mathrm{nm}^{-1} = 12.4\,\mathrm{nm}$ to $d = 2\pi/0.8\,\mathrm{nm}^{-1} = 7.8\,\mathrm{nm}$. Conversely, DIBMALPs only present a marginal shift of the local minimum at $q = 0.6\,\mathrm{nm}^{-1}$, but

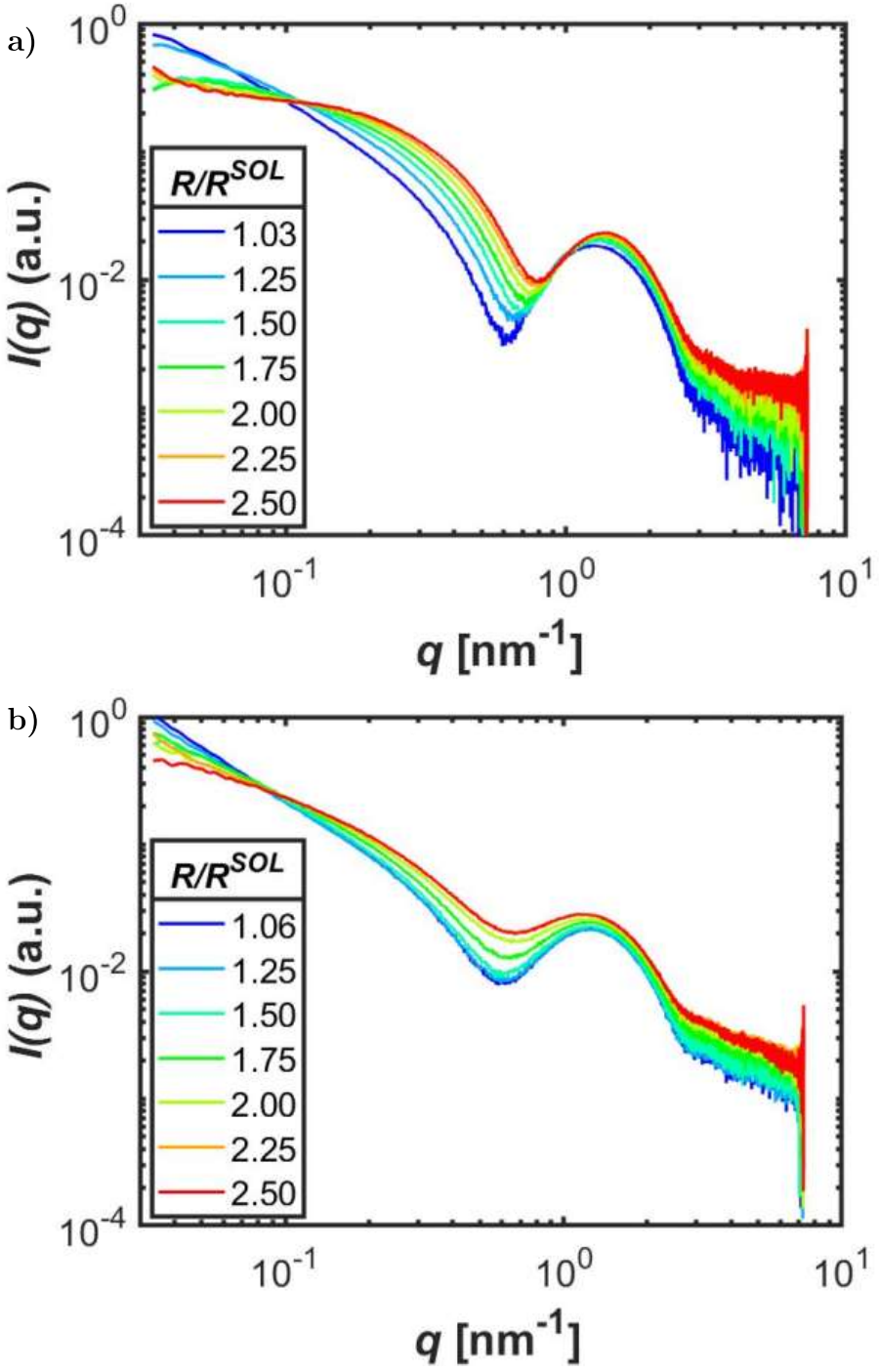


Figure 7.3: *SAXS scans for (a) SMALPs and (b) DIBMALPs produced at increasing copolymer/lipid ratio, measured at 30°C. Nanodiscs were formulated in TS buffer.*

a noticeable reduction of its depth with increasing copolymer fractions (Fig. 7.3b). The shift of the minimum to higher q-values indicates a decrease in size of the particles with increasing R/R^{SOL} ratio, which seems to be more pronounced for SMALPs. In addition, both systems change their behaviour similarly at low q-values. There, the slope of the SAXS curves decreases and becomes more and more flat, indicating that the molecular weight for the individual nanodiscs decreases with increasing R, being consistent with a reduction of their size.

Real-space representations of the SAXS data in the form of pair density distribution functions were determined via indirect Fourier transform (Fig. 7.4a,b).[340] All curves display a similar shape at low r-values, indicating similar distribution densities for all nanodiscs: a minimum flanked by two local maxima which are followed by a long tail at about 12 nm. The shape of these curves is typical for lipid bilayers,[341] which have negative scattering contrast at the central part of the particle and a positive one at the edges. Since X-rays scatter at the electrons of the atoms, the scattering contrast refers to as the difference in electron density between the particles investigated and the respective solvent of the system, and only the difference between these two electron densities is detectable. The local maximum at 5.5–6.5 nm is of particular importance as is determined by the lipid bilayer thickness (Fig. 7.4c), which corresponds to the sum of the core length and two times the lipid head groups represented by the face shell thickness (Fig. 7.1a). It decreases steadily from 6.5 to 5.3 nm for SMALPS, while the thickness of the DIBMALPs seem to be unaffected upon increasing the polymer/lipid ratio on the particles. Since the r-value at which the pair density distribution function declines to zero again indicates the maximum dimensions within the particle, the tail at high r-values is most likely emerging from copolymer chains protruding from the nanodisc. Since it decays to zero at much lower R/R^{SOL} for SMALPs than for DIBMALPs, we assume that the SMA molecules interact more strongly with the bilayer core due to their styrene residue and do not protrude as much as the DIBMA molecules do. This is also supported by the bilayer thickness decrease of the SMALPs, but not of the DIBMALPs (Fig. 7.4c). Due to the strong interactions with the hydrocarbon chains of the nanodiscs, potentially their effective length and therefore the bilayer thickness could be reduced.

Furthermore, the calculated radius of gyration (R_g), corresponding to the radial distance of the nanodiscs to their centre of mass (or, equivalently, the diameter (d, expressed as 2 x R_g) shows that this parameter is more affected by the copolymer molar fraction on SMALPs as compared with DIBMALPs (Fig. 7.4d). These results are in agreement with the DLS and raw SAXS data which generally show a decreasing size with increasing polymer concentration for both systems.

Taken together, these results indicate that the generally smaller SMALPs undergo a reduction of both the nanodisc diameter and bilayer thickness populating the core with increasing polymer/lipid ratios. In contrast, the average DIBMALP diameter is less affected by an increment of the DIBMA ratio, whereas the bilayer thickness remains virtually unaffected. However, a detailed nanodisc structure is far too complex to allow for a model-free interpretation based only in the inspection of

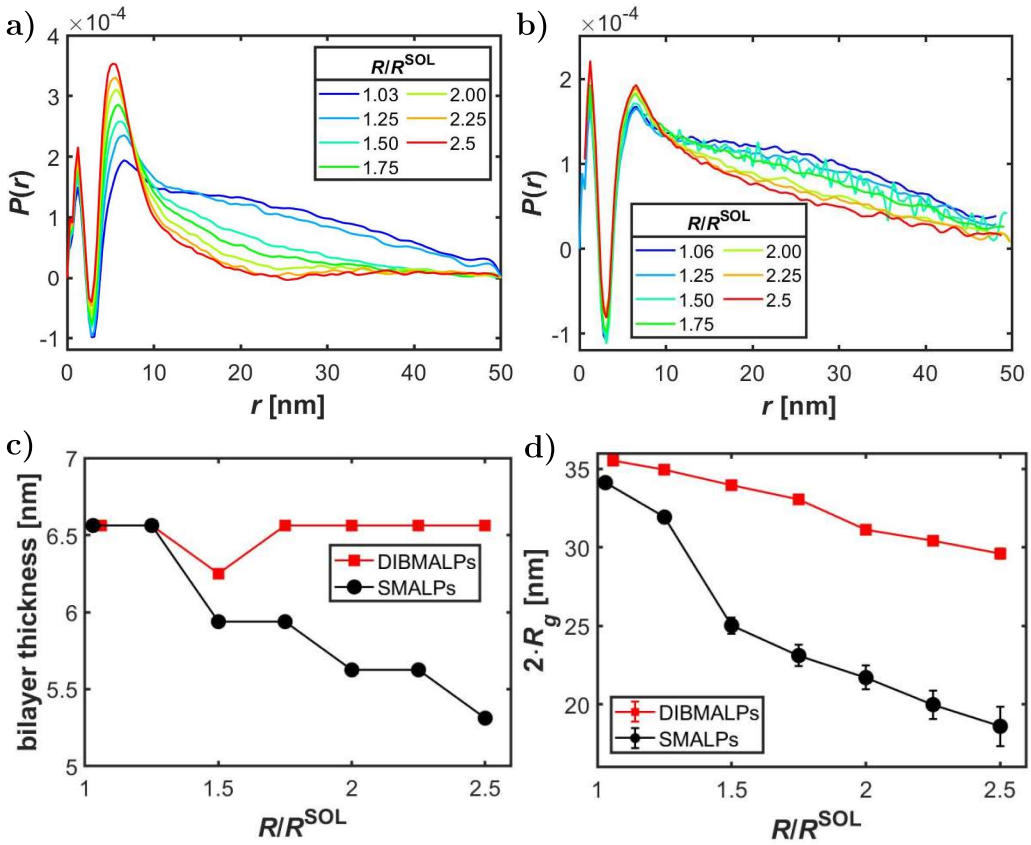


Figure 7.4: *Pair density distribution functions, $P(r)$, of (a) SMALPs and (b) DIBMALPs determined from SAXS scans presented in Fig. 7.3a and 7.3b, respectively. (c) Bilayer thickness as a function of R/R^{SOL}, and (d) nanodisc size, expressed in terms of radii of gyration, R_g. Nanodiscs were formulated in TS buffer.*

the SAXS and DLS data.

To gain further insights, we analysed the SAXS data using a core-shell cylinder model (Fig. 7.1a). The fit results (Fig. S1, Table S1) show that for both SMALPs and DIBMALPs, the radius of the nanodisc core is quickly reduced upon increasing the polymer/lipid ratio (Fig. 7.5a,b). In SMALPs, it decreases from ≈ 9 nm at $R/R^{\mathrm{SOL}} = 1.03$ and seemingly saturates at ≈ 3 nm, whereas DIBMALPs are bigger with a core radius of ≈ 13 nm at low R and ≈ 6 nm at $R/R^{\mathrm{SOL}} = 2.5$. Conversely, the nanodisc thickness increases slightly from ≈ 4 to ≈ 5 nm for SMALPs, but is apparently unaffected for DIBMALPs. To split the different contributions of each component and gain further insight, we analysed the core length and face shell thickness (see Fig. 7.1a). For SMALPs, the core length decreases with increasing polymer concentration while the face shell thickness increases. On the other hand, for DIBMALPs, the core length increases while the face shell thickness decreases. In the latter case, the modulus of these two changes is similar, compensating each other. Thus, in total, the bilayer thickness does not change. As already mentioned above, this behaviour is consistent with the literature, which states less perturbation of the DMPC

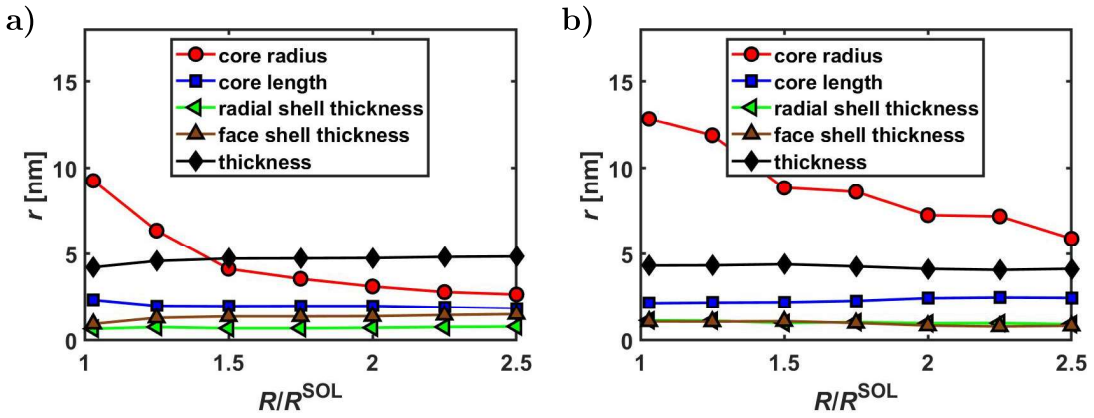


Figure 7.5: *Fit parameters calculated for (a) SMALPs and (b) DIBMALPs from SAXS data fit to model (Fig. 7.1a). Fitted values are detailed in Tab. D.1. Nanodiscs were formulated in TS buffer.*

phospholipids populating the nanodisc core compared to SMA.[136,320] Similar to the model-free analysis (Fig. 7.4d), a larger radius for the DIBMALPs is obtained and a decrease of the radius due to the addition of more polymer (Fig. 7.5b). In contrast, the thickness of the SMALPs increases in the core-shell cylinder model (Fig. 7.5a), whereas it decreases in the model-free analysis (Fig. 7.4c). This can be explained by the fact that the pair density distribution function takes into account the most probable or frequent distance between the lipid headgroups, whereas the model assumes an average or mean for the same distance. Furthermore, since a decrease in the core length is visible for SMALPs, but the lipid head groups do not change their size and therefore may also be surrounded by polymer (see Fig. 7.1a), a distinction between the scattering signal contribution of different parts of the nanodiscs is extremely difficult. We note that, similar to a recent study, we observe a rather constant thick polymer belt (here: radial shell thickness, see Fig. 7.1a).[325] Therefore, we also conclude that the number of SMA particles within the belt decreases with decreasing radius as the excess copolymer distributes mainly in the belt structure after solubilization.[325]

7.4.2 Case B: Influence of temperature on size and shape of nanodiscs

To study the influence of temperature and check for possible phase transitions of the lipid within the nanodiscs, SMALPs and DIBMALPs produced at $R/R^{\mathrm{SOL}} = 1.25$ were analysed using DLS and SAXS between 30 and 5 °C, that is, above and well below the melting temperature T_m of DMPC bilayers (24 °C).[317,321] Note that for the temperature measurements PS instead of TS buffer was used to minimise pH effects upon quenching.[342]

DLS analysis on SMALPs and DIBMALPs produced at $R/R^{\mathrm{SOL}} = 1.25$ show a

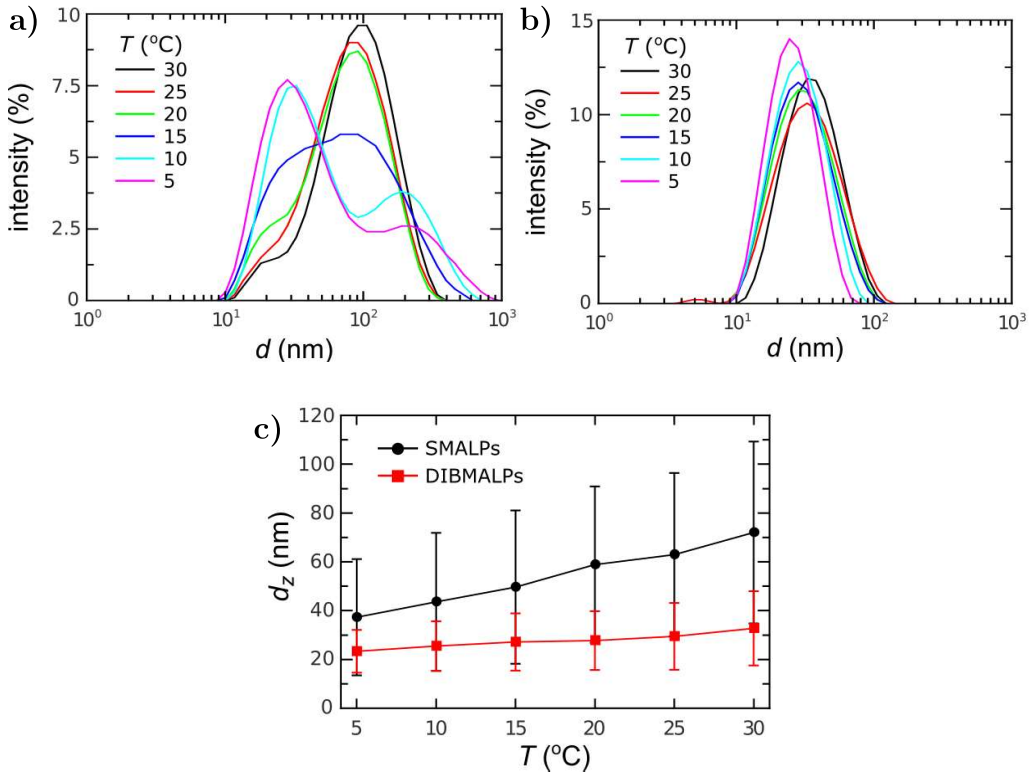


Figure 7.6: *SMALP and DIBMALP sizes as monitored by DLS at decreasing temperatures. Intensity-weighted particle size distributions as function of hydrodynamic diameter, d, for (a) SMALPs and (b) DIBMALPs measured between 5–30 °C. (c) z-average particle diameter, d_z, as calculated from curves in (a) and (b). Vertical bars indicate peak widths derived from the corresponding polydispersity values. Nanodiscs were formulated at $R/R^{SOL} = 1.25$ in PS buffer.*

reduction in the z-average mean size of both types of nanoparticles with decreasing temperature (Fig. 7.6a-c). However, we shall discuss the effect of exchanging the buffer. First, the maximum intensity-weighted particle size of SMALPs and DIBMALPs is changed, that is, SMALPs are the larger species and PS, whereas DIBMALPs are larger in TS buffer at this polymer/lipid ratio (Fig. 7.2c and 7.6c). Additionally, SMALPs show a clear bimodal size distribution in PS, especially at lower temperatures (Fig. 7.6a). The peak for the larger particles is roughly at 100 nm and shifts towards larger sizes, whereas the smaller particles consist dominantly of sizes between 20 and 30 nm. Upon quenching down to 5 °C, the peak for the larger length decreases and the smaller peak becomes dominant. We conclude that initially, at 30 °C, large aggregates/clusters of nanodiscs and/or an incomplete solubilisation of the LUVs are still present. Upon quenching, single/separated nanodiscs emerge (indicated by the 20 nm peak) as well as clusters/aggregates of the nanodiscs (as indicated by the 200 nm peak). For DIBMALPs, the effect of temperature (and solvent) seems weaker (Fig. 7.6b,c). Nevertheless, the nanodiscs are smaller in size

in PS buffer and a decrease of the intensity-weighted particle size (and distribution) is found. Hence, we speculate that the phosphate buffer in particular hinders the styrene group of SMA to interact with not only the lipid core (at elevated temperatures), but also with other nanodiscs/polymers to prevent aggregation at lower temperatures.

SAXS curves arising from SMALPs show a steady increment of the signal intensity at low q-values with decreasing temperatures (Fig. 7.7a). As stated above, this indicates a transition towards a system with particles having a higher molecular weight. This is consistent with the shift of the larger particle peak in the bimondal DLS data towards larger sizes. This effect dominates the scattering signal at low q-values and the increase in amount of solubilised nanodiscs cannot be observed in contrast with the DLS data (see Fig. 7.6a). However, the minimum at $q = 0.6\,\mathrm{nm}^{-1}$ shifts slightly towards higher q-values upon quenching, indicating the reduction of the nanodisc sizes, which is also consistent with DLS data showing the formation of single and separated nanodiscs. SAXS scattering curves arising from DIBMALPs exhibit a different behaviour at low and intermediate q-values (¡ $0.6\,\mathrm{nm}^{-1}$) with decreasing temperatures (Fig. 7.7b). We note that the raw SAXS data of DIBMALPs suggest an incomplete solubilisation at higher temperatures,[325] whereas quenching leads to a more complete solubilisation and formation of nanodiscs (Fig. 7.7b, 7.8b). This is supported by the shift of the minimum toward higher q-values and therefore smaller particles in solution. Similar observations have been made for lipid vesicles in the presence of polymer concentrations below the solubility limit R^{SOL}.[325] The straight line at 30 °C transforms into a shoulder at roughly $q = 0.1\,\mathrm{nm}^{-1}$, corresponding to a real-space distance ($r = 2\pi/q$) of $r \approx 60\,\mathrm{nm}$. It becomes more pronounced with decreasing temperature and mirrors the maximum size/length of the nanodiscs: from large, polydisperse particles at 30 °C, the system transforms into smaller, more monodisperse particles with a length of roughly 60 nm upon quenching (see also DLS data (Fig. 7.6b,c)). Hence, the scattering curves reflect the interparticle correlation; at high temperatures, an effective attraction resulting in a melt or an extended polymer chain entanglement is present. In contrast, at low temperatures, this entanglement dissolves into single/separated nanodiscs because of a net repulsion within the system. Thus, the raw data at high temperatures as well as the corresponding PDDFs do not exhibit a behaviour expected for nanodiscs and are therefore difficult to analyse. At $R/R^{\mathrm{SOL}} = 1.25$, we would assume that the formation of nanodiscs is complete, but the different buffer used for the temperature measurements (PS vs. TS) appears to play a role.

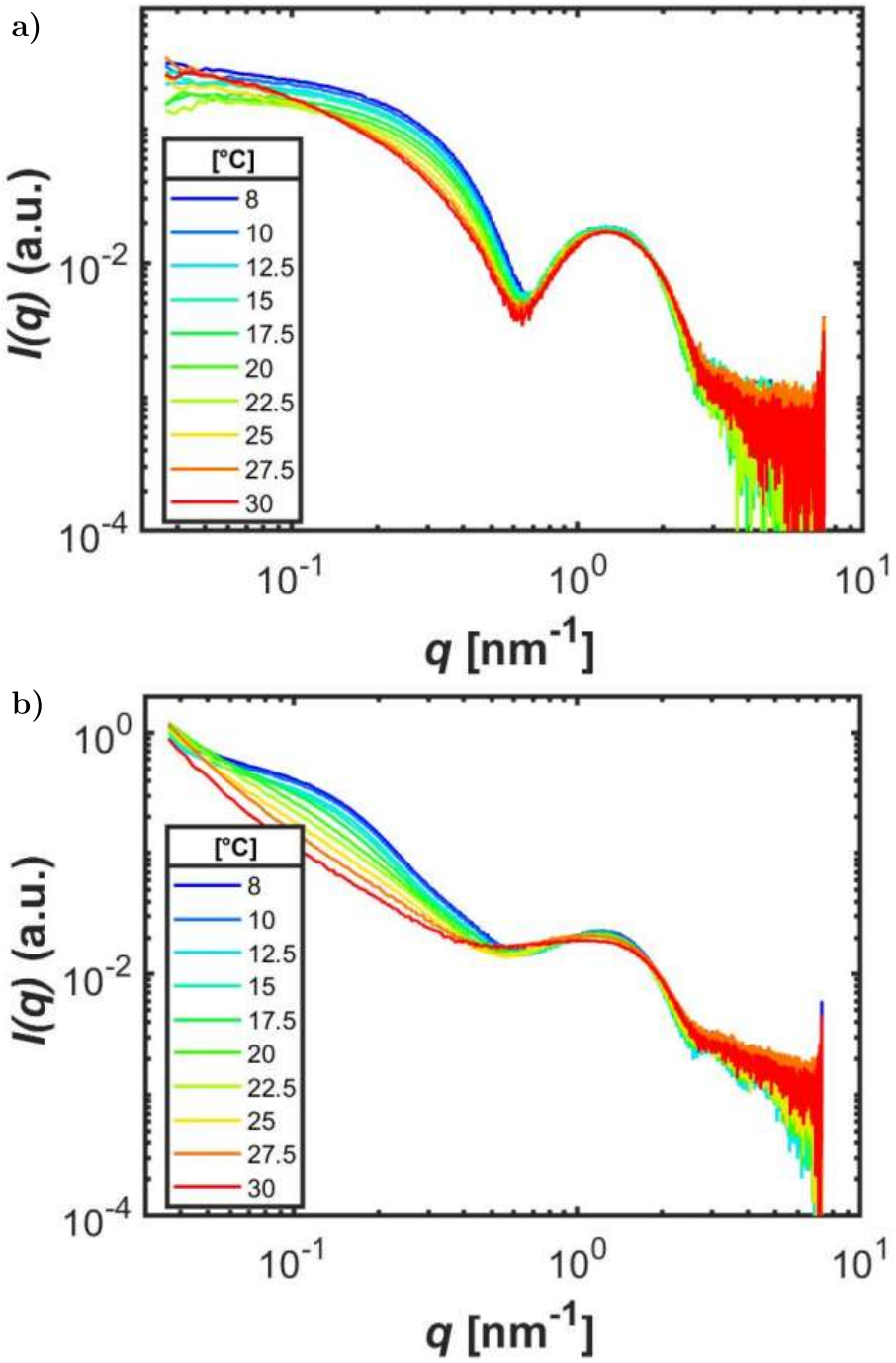


Figure 7.7: *SAXS scans for (a) SMALPs and (b) DIBMALPs measured between 8–30°C. Nanodiscs were formulated at $R/R^{SOL} = 1.25$ in PS buffer.*

The calculated PDDFs indicate a strong temperature-dependent effect on the nanodisc morphology. At 30 °C, the SMALPs exhibit a single peak at $r \approx 7$ nm, which broadens and evolves into two peaks upon temperature reduction (Fig. 7.8a). As a result, the DMPC bilayer thickness determined for SMALPs is 6.5 nm at 30 °C and transitions towards two distinctive bilayer thicknesses with decreasing temperature (Fig. 7.8d). Additionally, the long tail at high r-values decreases and vanishes at lower r-values with decreasing temperature, indicating a reduction in size (Fig. 7.8a), consistent with DLS and SAXS data. DIBMALPs present a more complex pattern; at 30 °C, the small peak at ≈4.7 nm has nearly disappeared and a broad peak with a local maximum at $r \approx 13$ nm appears at lower temperatures (Fig. 7.8b). Since a complete solubilisation of the lipid vesicles occurs only for lower temperatures (¡ 20 °C), it is impossible to determine the maximum of the PDDF curves as before. Nevertheless, for further quenching and, hence, finalising solubilisation, the bilayer thickness of DIBMALPs remains constant at 5.3 nm. The calculated R_g for SMALPs indicates particles with an average diameter of ≈25 nm at 30 °C, which decreases quickly upon temperature reduction to ≈15 nm (Fig. 7.8c), whereas DIBMALPs' average diameter was 38 nm at 30 °C and was reduced in a more stepped manner until reaching 27 nm (Fig. 7.8c).

Using again the core-shell cylinder model, we observe first an increase of the core radius of SMALPs upon quenching, until a gradual decrease is observed (Fig. 7.9). During the quenching process, the bilayer thickness increases slightly, suggesting a liquid crystalline to gel-phase transition. This increase in bilayer thickness is even visible for DIBMALPs in the reasonable low temperature regime, where a complete solubilisation took place (Fig. 7.9). The following parameters are essentially unchanged, and thus, are not plotted for clarity, but are mentioned in the following. For SMALPs, the core length is in a range between 1.2 and 1.4 nm, the radial shell thickness between 0.6 and 1 nm, and the face shell thickness is 2.1 nm. In contrast, for DIBMALPs, the core length is in the interval 0.7-0.8 nm, the radial shell thickness between 1.9 and 3 nm (decreasing with decreasing T), and the face shell thickness is ≈ 2.4 nm. As the radial shell thickness of the SMALPs decreases with decreasing T, we speculate that more SMA molecules are transferred from the polymer belt towards the interior of the nanodiscs due to quenching.

Taken together, these results indicate that SMALPs and DIBMALPs undergo a reduction in the average diameter with decreasing temperatures and that the buffer used plays a non-negligible role. In TS buffer, SMALPs are 2-3 times larger than DIBMALPs in the temperature range investigated. Due to the buffer exchange, both systems seem to be not completely solubilised at 30 °C. For DIBMALPs, solubilisation seems to improve upon quenching, whereas SMALPs can aggregate at lower temperatures. Moreover, the DMPC bilayers most likely transition from the liquid crystalline to gel-phase below 24 °C. SANS studies performed on DMPC bilayers have shown that lipids in the gel-phase occupy less area per molecule as compared with fluid-phase lipids and have increased hydrocarbon thickness.[343,344] This leads to closer lipid packing and can account for the reduction in the average nanodisc diameter with concomitant increment in the bilayer thickness. Additionally, EPR

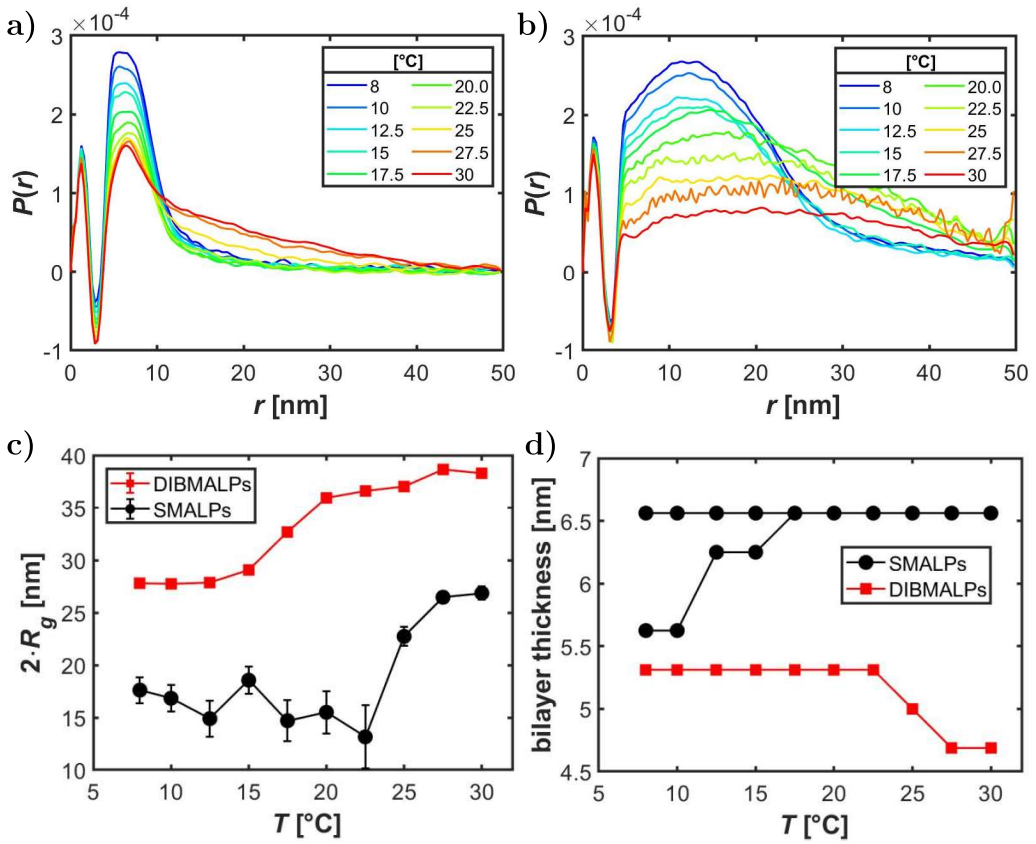


Figure 7.8: *Calculated pair density distribution functions, $P(r)$, of (a) SMALPs and (b) DIBMALPs at increasing temperatures as derived from SAXS curves in Fig. 7a and 7b, respectively. (c) Particle radii of gyration, R_g, (expressed as $2\,R_g$) and (d) bilayer thickness of SMALPs and DIBMAPs as function of temperature. Nanodiscs were formulated at $R/R^{SOL} = 1.25$ in PS buffer.*

studies on SMA-stabilised nanodiscs have shown that the copolymer styrene groups strongly interact with the phospholipids' acyl chains.[345,346] We speculate that, at low temperatures, the two membrane thicknesses observed in SMALPs can be a result of phase separation of the gel- and liquid crystalline-phase lipids coexisting within individual nanodiscs as a result of strong local SMA–DMPC interactions at the nanodisc rim. Due to these strong interactions and additional incorporation of SMA into the nanodisc core, the thickness could be effectively decreased as the SMA molecules occupy positions of lipids. This can be a result of the polymer interacting dominantly with the nanodisc core (i.e., the hydrophobic part). Hence, as the SMA molecules are located there, some of the lipids (and therefore also their headgroups) are displaced and are absent compared to the nanodiscs formed at higher T, which may lead to the two thicknesses observed (Fig. 7.8d). Note that already in Case A, an increase in SMA concentration led to a decrease in the bilayer thickness of the nanodiscs (see Fig. 7.4c), supporting this hypothesis.

We note that neither in the raw data nor in the analysis a jump of the respective

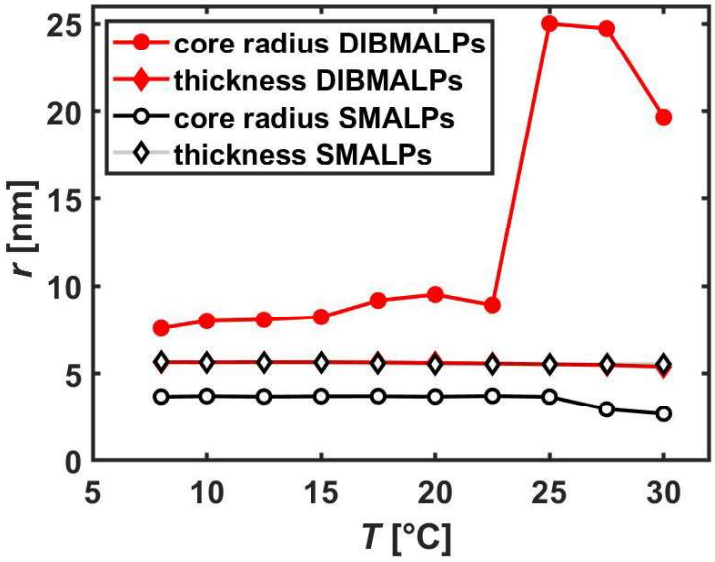


Figure 7.9: *Selected fit parameters calculated for SMALPs (black) and DIBMALPs (red) obtained from SAXS data fit to core–shell cylinder model (Fig. 7.1a). All fit parameters can be found in Tab. D.2 and the fits are shown in Fig. D.2. Nanodiscs were formulated at* $R/R^{SOL} = 1.25$ *in PS buffer.*

parameters was seen, but always a continuous change. We assume that the phase transition of the lipid within the nanodiscs is therefore not as sharp as for the pure lipid itself, but the phase transition temperature is rather smeared out. Already in 2012, a non-cooperative thermotropic phase transition was reported for nanodiscs consisting of DMPC and SMA.[347] The authors attributed this to the smaller size of the nanodiscs compared to the pure DMPC vesicles, and the presence of lipids that probably do not participate in the cooperative phase transition due to their interactions with the polymer and therefore their increased ordering compared with DMPC vesicles.[347,348] Similar to Bjørnestad et al. who recently reported that gel-like membranes more easily solubilise with SMA(3:1), we observe a seemingly higher solubilisation at low temperatures.[325] This is not only true for SMA(2:1), but also for DIBMA. However, we assume a further aggregation of the SMALPs at low temperatures, leading to a species of particles with a size of 200 nm in addition to the separated and solubilised nanodiscs.

We note that different models for the analysis of small-angle scattering data of nanodiscs have been applied in the past. While Bjørnestad et al. applied an ellipsoidal core-shell mixed micelle model, a mixed lipid:SMA disc model, a lipid disc with SMA belt model and a mixed lipid:SMA disc with SMA belt model to fit the data and the latter one had the best results, Skar-Gislinge et al. developed a completely new model themselves.[334,335] Since the nanodiscs used by Skar-Gislinge et al. consisted of lipids and MSPs, they constructed their model with two histidine-tags protruding out from the belt, the MSP as belt, and two caps from the lipid

head groups.[334] In addition, they separated the hydrophobic interior into a central low-density methyl group region, sandwiched between two higher density leaflets composed of the $(CH_2)_n$ chains.[334] To catch the important parameters, but keep the model as simple as possible, we decided to use the core-shell cylinder model as it was proven before that the nanodiscs exhibit a disc-like architecture and the model fits the experimental data well.[325,334]

7.5 Conclusion

In summary, we have investigated the structure of membrane-mimicing nanodiscs composed of the lipid DMPC with two different polymers SMA(2:1) and DIBMA by SAXS and DLS. In a first approach, the polymer/lipid ratio was increased continuously (in TS buffer), starting from ratios above that required for complete lipid vesicle solubilisation ($R/R^{\mathrm{SOL}} \approx 1$) up to a ratio of $R/R^{\mathrm{SOL}} = 2.5$. Here, DIBMALPs are larger for the same R/R^{SOL}-ratios. The nanodisc radii formed by both polymers decrease with increasing R, but stronger when using SMA, suggesting a stronger interaction of SMA with DMPC. In a second approach, temperature-dependent measurements between 5 and 30 °C were performed to study the effect of temperature on the architecture as well as on the (possible) phase transitions. For this purpose, PS buffer was used to not influence the pH dramatically. Nevertheless, this buffer exchange seems to have crucial effects. First, in PS buffer, SMALPs are the larger species at the polymer/lipid ratio used. Second, the lipid vesicles are not completely solubilised, even at $R/R^{\mathrm{SOL}} = 1.25$ at 30 °C. Quenching leads in both cases to a complete solubilisation and nanodisc formation. In this regard, DIBMALPs are stable at low T due to an increase in net repulsion. In contrast, nanodiscs formed with SMA aggregate further at low T due to an increase in attraction. Interestingly, no sudden changes can be observed, which would indicate the presence of a sharp phase transition temperature. All changes are gradual and mirror a broad melting temperature range. These results are not only relevant from a fundamental point of view, but also have a huge impact on structural biology of proteins and potentially many other fields such as biopharmaceutical formulation.

Part VIII

Concluding discussion and outlook

The aim of this dissertation was to get an in-depth insight into the mechanisms driving protein crystallization and its correlation with the phase behavior and parameters such as protein and salt concentration. In multiple studies, the phase behavior and (nonclassical) crystallization of globular proteins in the presence of multivalent salts were thoroughly investigated, which lead to new findings in this field. Furthermore, the characterization of nanodiscs, which enable biophysical and chemical investigations, extending these studies to membrane proteins, was performed. In this chapter, the results of Chapters IV–VII are comprehensively discussed based on the initially asked questions in Chapter II. While many questions could be answered in the scope of this dissertation, there are still open questions, which need further investigation, and consequential new questions, which are addressed and discussed as an outlook at the end of this chapter.

Putting a pin in Chapter II, the following questions were point of investigation in Chapter IV: Does crystallization indeed occur within the dense phase or not? Are there any other precursors? Does the exchange in solvent alter the phase behavior and/or the crystallization pathway, i.e., are there any isotope effects due to the exchange of H_2O by D_2O as the solvent?

Investigating the crystallization kinetics outside and inside the LLPS binodal, the data suggests that the dense phase after LLPS only acts as a reservoir and that nucleation actually starts within the dilute phase. During crystal growth, the dense phase dissolves and facilitates further growth. This is in strong contrast to simulations and theoretical studies, which predict another nonclassical crystallization pathway, in which the dense phase acts as crystal precursor by lowering the energy barrier for nucleation.[78,137,138] Similar observations to the ones presented here (i.e., the dissolution of the MIP to facilitate crystal growth, but no nucleation within the MIP) have been made for, e.g., amorphous calcium carbonate crystallization, water condensation processes at high altitudes, and the fluid-solid phase transition in colloidal systems.[77,203] However, SAXS and SANS always provide a time-averaged two-dimensional scattering image at the detector. Hence, possible precursors with a short lifetime cannot be detected, which would be an indicator for a different nonclassical crystallization pathway where the intermediate phase acts as crystal precursor and not only as a reservoir. For example high-speed in situ electron microscopy experiments revealed that gold clusters form on graphene through multiple reversible structural fluctuations between disordered and crystalline states on the order of milliseconds.[349] These structural fluctuations emerge due to a size-dependent thermodynamic stability of the two states.[349] Due to the temporal limitations of the techniques used in this thesis, these phenomena cannot be observed. In addition, each SANS and SAXS experiment is limited by the experimental set-up, meaning the length scales that can be investigated are fixed and only a certain q-range (and therefore length scale in real space) is available to study. In particular larger length scales were not investigated here, which may be important for crystal precursors. Hence, the possibility of larger and/or short-lived crystal precursors cannot be ruled out. In spite of that, the results do show that HSA crystallization is triggered by the

multivalent cations, which not only diminish the charge due to protein binding, but are also an integral part of the crystal lattice by forming crystal contacts between the proteins. Although the effective attractions are stronger and the dense phase is rather a liquid network than dense droplets in D_2O compared to H_2O, the crystallization kinetics are resembling for both solvents. To summarize, the main question whether nucleation takes place within the dense phase can be conclusively negated for these systems. These findings show that theoretical calculations are an extreme benefit in many cases, but experimental systems do not necessarily follow theoretical predictions, because it is extremely difficult to include every experimental parameter into the theory and therefore the experimental and theoretical systems can differ a lot.

In Chapter V, we proceeded to the following main questions that should be answered within this study: Why does HSA crystallize so readily in the presence of multivalent cations, but BSA does not? What are the differences and similarities between the two proteins?

Studying there the phase behavior of BSA and HSA shows that both proteins undergo RC with $CeCl_3$ and exhibit LLPS. The shift of the LLPS binodal toward lower protein concentrations already indicates less attractive forces for BSA compared to HSA in the second regime. SAXS measurements have further supported this statement. As BSA is slightly more negatively charged, a stronger adsorption at an interface due to cation bridging with the surface was observed. Similar to previous studies, no BSA crystals, but only HSA crystals were found. Since HSA is more hydrophobic than BSA,[220] and the crystal structure of HSA with Y^{3+} shows many protein-protein contacts (without cation bridging), the conclusive answer was that the additional hydrophobic forces of HSA drive crystallization and enable crystal contact formation. As BSA is lacking these hydrophobic forces (at least in the same fashion/extent as HSA), no crystallization does occur. Hence, the electrostatic interactions seem to play a dominant role in the overall protein phase and adsorption behavior, but one has to take into account the whole set of interactions to properly explain all phase phenomena observed, in particular crystallization.

Afterward in Chapter VI, the focus was set on the nonclassical crystallization of the BLG-$CdCl_2$ system in D_2O to answer the following question: Does the system behave similarly in the new solvent (i.e., D_2O)? Can we obtain new insights into the crystallization pathway using neutron scattering experiments? Does the system still crystallize according to a two-step crystallization process in D_2O? How do the crystal precursors evolve with time? What is their exact role during crystallization?

The phase behavior of the BLG-$CdCl_2$ system is extremely similar in D_2O compared to H_2O. Again, a RC phase behavior and a nonclassical two-step crystallization pathway could be observed close to the $pseudo - c^{**}$ border. Analyzing not only the amount of precursor, but also its structural evolution during crystallization enabled the conclusion of a preordered metastable intermediate phase serving as crystal precursor. This preordering takes some time, since the average distance between

the protein molecules decreases with time. A final value is reached, which is only slightly larger than the typical distances within the crystal lattice. Interestingly, preordering of liquid water has been also observed for example in the crystallization pathway of H_2O on graphitic surfaces at ambient pressure.[82] However, the authors claim that the preordered domains do not show an additional free energy minimum, i.e., have only one single transition state, and therefore, the crystallization process is supposed to follow a one-step, heterogeneous crystallization.[82] This is in strong contrast to our conclusions, since we assume the preordered domains to be metastable and therefore to have an additional free energy minimum in between that of the initial solution and the crystal. As a last step for the BLG-$CdCl_2$ crystallization in D_2O, it is proposed that the hydration layer of the proteins is expelled and a final densification occurs. The same procedure was found in DNA-functionalized gold nanoparticle crystallization and was also reported in QCM-D studies investigating the self-assembly of iron oxide nanocubes.[350,351] In the latter case, the authors based their hypothesis on an increase in shear modulus during the assembly.[351] Hence, additional QCM-D studies could help to strengthen our hypothesis. Unfortunately, similar to H_2O, no crystal structure resolution was possible in D_2O due to crystal twinning. These results again highlight that different nonclassical crystallization pathways are followed, depending on the system (compared to, e.g., the HSA-$CeCl_3$ system). Hence, there seems to be no general pathway applicable for all protein-multivalent systems, potentially due to differences in the surface and size of the proteins, although they show a resembling phase behavior.

In the last result chapter (Chapter VII), the structure of polymer-bounded lipid nanodiscs was studied upon varying the nature of the polymer, the polymer concentration, and the temperature to solve the following questions: Are there differences between the structure of the nanodiscs using different polymers? What happens to the nanodisc structure if one increases the polymer concentration? How does a temperature change alter the structure of the nanodiscs? Do lipid bilayer phase transitions also occur within the nanodiscs? Do additional charges (due to the addition of multivalent ions) affect the nanodisc architecture?

For this project, similar to the previous topics, most of the initial questions could be answered. The data suggest that in Tris buffer, nanodiscs formed by the lipid DMPC with the polymer DIBMA are generally larger than those formed with the polymer SMA(2:1). Nevertheless, for both polymers, a decrease of the nanodisc radius was observed upon increasing the respective polymer/lipid ratio. This effect was stronger when using SMA. Interestingly, exchanging the buffer to phosphate buffer to perform temperature-dependent experiments without changing the pH led to an extremely different nanodisc formation behavior. First of all, the lipid vesicles were not completely solubilized into nanodiscs (at 30 °C), although the conditions used were above that required for complete lipid vesicle solubilization. Besides, SMALPs were the larger species here for the same sample compositions. The strong effect of the buffer on the nanodisc solubilization is not understood yet. Quenching down to 8 °C led to a complete solubilization for both polymers. In the case of DIBMA, the

nanodiscs formed were stable due to an increase in the net repulsion, whereas for SMA, aggregates/clusters of nanodiscs were formed due to an increase in attraction. No sudden changes in any parameter were found when quenching below the melting temperature of the pure lipid, but gradual changes. Since the lipid bilayer thickness increased slightly for both systems upon quenching, suggesting a transition from the liquid-crystalline toward the gel phase, we assume that the additional interactions with the polymers broaden the phase transition (temperature) compared to the pure lipid vesicles. Unfortunately, for the increase of ionic strength, no reliable data sets could be recorded, and hence, the possible effect of increasing the concentration of (multivalent) ions could not be determined. Although complementary SAXS and DLS data help to understand the structure much better, a lot of the analysis depends on models. Therefore, additional TEM experiments would be beneficial to support the assumptions. Nevertheless, these results enable the biophysical and chemical investigation of membrane proteins in a much more controlled way.

Within this dissertation, different crystallization kinetics and nucleation sites have been reported. For HSA-$CeCl_3$ (Chapter IV), the crystal nucleation site was found to be outside the dense MIP, whereas for BLG-$CdCl_2$ in D_2O (Chapter VI), it was located within the preordered MIP. Nevertheless, in Chapter II, the following question was also asked: Where exactly does nucleation occur, meaning in bulk, both in bulk and at the interface or only at the interface? Is there a dominant pathway? In two studies, we could already show that a dense packing at a hydrophilic, negatively charged surface occurs for proteins which are able to crystallize (BLG and HSA (Ref. 238 and Chapter V, respectively)). In contrast, BSA, which does not crystallize in the presence of multivalent cations, packs loosely at the same surface. If this densely-packed layer of adsorbed proteins acts or can act as precursor for subsequent crystallization or not is a question, which is still unanswered. According to theoretical studies performed by Nanev, heterogeneous (2D) nuclei at hydrophobic surfaces can be as small as two proteins.[119] Therefore, although this number increases as the supersaturation of the solution decreases,[119] it is extremely difficult to solve this question and further investigations are needed, which are out-of-scope for this dissertation. Please note that, nevertheless, both scenarios have been reported, meaning heterogeneous nucleation at glass surfaces was observed as well as homogeneous nucleation in bulk.[68,352–354] Decreasing the width between two glass plates to $\leq 0.05\,\mathrm{cm}$, however, makes it impossible to distinguish these two scenarios.[68] Surprisingly, the authors report lower free energy barriers for nucleation in bulk than on the glass surface.[68] Importantly, heterogeneous nucleation does not only have to occur on solid surfaces. In a recent study, BSA crystallization at the interface of microbubbles filled with oxygen, nitrogen and carbon dioxide was observed.[254] The authors believe that BSA can enrich and reorient at the interface of the hydrophobic gas microbubbles with the protein solution, leading to a gas-liquid interface-induced crystallization.[254] Such aggregation and crystallization of proteins at an interface of a solution with a hydrophobic counterpart/medium (independent of its aggregation state) was already observed previously.[355,356] In these

cases, the proteins are "anchored" at the hydrophobic medium-solution interface, with the anchor being the strongest hydrophobic patches.[356] Hence, due to accumulation of protein at the interface, protein adsorption facilitates 2D crystal nucleation there.[356] In contrast, for 3D crystal nucleation, Nanev concludes that only if the interactions of the protein molecules with the hydrophobic interface are weaker than the protein-protein intracrystalline contacts, a hydrophobic surface promotes crystallization and does not solely result in an enhanced protein adsorption.[356] Hence, the following questions remain unsolved: Does nucleation in the systems investigated dominantly occur in bulk or at an interface? In case nucleation occurs at an interface, is there still nucleation in bulk? Or is it the other way round? QCM-D, ellipsometer, and X-ray or neutron reflectometry experiments could help to shed light onto these questions.

There are multiple research topic, which were touched upon within in the different chapters, yet were not within the scope of this dissertation. These can be used as a starting point for future studies and investigations. One topic is the formulation of extremely large crystals. Complementary neutron and X-ray diffraction can enable atomistic resolution as well as the possibility to monitor the hydration of the protein molecules within the crystal in D_2O. These information would help to better understand ion binding and therefore the phase behavior as well as the crystallization pathway. Such studies could help answer the following question: Are there systems, which grow naturally larger crystals? So far, none of the systems investigated (BLG-YCl_3 in H_2O and D_2O, BLG-YI_3 in H_2O, BLG-$LaCl_3$ in H_2O and D_2O, BLG-$ZnCl_2$ in H_2O and D_2O, BLG- $CdCl_2$ in H_2O and D_2O, HSA-$CeCl_3$ in H_2O and D_2O, HSA-$LaCl_3$ in H_2O, HSA-YCl_3 in H_2O) resulted in large, high-quality crystals suitable for neutron diffraction at the conditions tested. Are there maybe certain conditions within the phase diagram that favor the growth of larger, high-quality single crystals?

Another research topic might be the crystallization of BLG with $ZnCl_2$. Interestingly, for this system in both H_2O and D_2O, two different polymorphs can be obtained, which was not seen so far in similar systems. It seems that temperature, solvent, salt and protein concentration influence the preferred polymorph formation. Another approach to control polymorphism tested by Parambil et al. was template-induced nucleation.[357] There, the surface itself acts as an anchoring point at which the molecules aggregate, forming prenucleation clusters.[357] Depending on the surface–molecule interaction and the hydrodynamic conditions, the solute cluster can either grow into a stable nucleus while still interacting with the surface or detach from the surface and move into the bulk solution.[357] The question, which are still unanswered for the BLG-$ZnCl_2$ system in both solvents, are: Are there different precursors, which lead to the different crystal structures? Since mostly polymorph mixtures are formed, how close are their free energies? Do different surfaces induce/favor different polymorphs similar to Parambil et al.? Interestingly, the Bragg peaks of one polymorph overlap with the Bragg peaks of BLG-$CdCl_2$ crystals, whose

structure could not yet be resolved due to crystal twinning (see Chapter VI). Thus, one further question is whether one can resolve this polymorph structure and transfer the information to the $CdCl_2$ crystals.

To summarize, this dissertation provides new insights into the phase behavior of globular protein solutions in the presence of multivalent salts and a better understanding of the nonclassical crystallization behavior, e.g., the role of hydrophobic interactions in the crystallization pathway. These findings are crucial from a fundamental point, but also for research areas ranging from structural biology to pharmaceutical drug formulation.

List of publications

- Following protein dynamics in real-time during crystallization
  C. Beck, M. Grimaldo, F. Roosen-Runge, R. Maier, O. Matsarskaia, M. Braun, B. Sohmen, O. Czakkel, R. Schweins, F. Zhang, T. Seydel, and F. Schreiber *Cryst. Growth Des.* **2019** *19*, 7036-7045

- Protein crystallization in the presence of a metastable liquid-liquid phase separation
  R. Maier, G. Zocher, A. Sauter, S. Da Vela, O. Matsarskaia, R. Schweins, M. Sztucki, F. Zhang, T. Stehle, and F. Schreiber *Cryst. Growth Des.* **2020** *20*, 7951-7962

- Human versus bovine serum albumin: A subtle difference in hydrophobicity leads to large differences in bulk and interface behavior
  R. Maier, M.R. Fries, C. Buchholz, F. Zhang, and F. Schreiber *Cryst. Growth Des.* **2021** *21*, 5451-5459

- Protein crystallization from a preordered metastable intermediate phase followed by real-time small-angle neutron scattering
  R. Maier, B. Sohmen, S. Da Vela, O. Matsarskaia, C. Beck, R. Schweins, T. Seydel, F. Zhang, F. Schreiber *Cryst. Growth Des.* **2021** *21*, 6971–6980

- Bulk phase behaviour vs interface adsorption: Effects of anions and isotopes on β-lactoglobulin (BLG) interactions
  M.R. Fries, M.W.A. Skoda, N.F. Conzelmann, R.M.J. Jacobs, R. Maier, N. Scheffczyk, F. Zhang, F. Schreiber *J. Colloid Interface Sci.* **2021** *598*, 430-443

- Molecular flexibility of antibodies preserved even in dense phase after macroscopic phase separation
  A. Girelli, C. Beck, F. Bäuerle, O. Matsarskaia, R. Maier, F. Zhang, B. Wu, C. Lang, O. Czakkel, T. Seydel, F. Schreiber, and F. Roosen-Runge *Mol. Pharm.* **2021** *18*, 4162-4169

- Structural insights into polymer-bounded lipid nanodiscs
  R. Maier#, R.C. Arenas#, A. García-Sáez, F. Zhang, F. Schreiber *in preparation*
  #: These authors contributed equally to this work

- Kinetics of HSA crystallization and its relationship with the phase diagram
  C. Buchholz, L.F. Reichart, F. Surfaro, R. Maier, F. Zhang, A. Gerlach, F. Schreiber *submitted*

- Effective interactions and phase behavior of protein solutions in the presence of hexamine cobalt(III) chloride
  M.D. Senft, R. Maier, F. Zhang, and F. Schreiber *in preparation*

- Tuning crystal polymorphs of BLG using salt, temperature and solvent
  R. Maier, M.D. Senft, G. Zocher, A. Girelli, A. Idrees, C. Simo, C. Lang, B. Wu, F. Zhang, T. Stehle, and F. Schreiber *in preparation*

Bibliography

[1] C. Zhang, Y. Wang, Y. Zhu, C. Liu, C. Gu, S. Xu, Y. Wang, Y. Zhou, Y. Wang, W. Han, et al., *Development and structural basis of a two-Mab cocktail for treating SARS-CoV-2 infections*, Nat. Commun. **12** (2021), 1–16.

[2] M. Yuan, H. Liu, N. C. Wu, C.-C. D. Lee, X. Zhu, F. Zhao, D. Huang, W. Yu, Y. Hua, H. Tien, T. F. Rogers, E. Landais, D. Sok, J. G. Jardine, D. R. Burton, and I. A. Wilson, *Structural basis of a shared antibody response to SARS-CoV-2*, Science **369** (2020), 1119–1123.

[3] J. Ge, R. Wang, B. Ju, Q. Zhang, J. Sun, P. Chen, S. Zhang, Y. Tian, S. Shan, L. Cheng, et al., *Antibody neutralization of SARS-CoV-2 through ACE2 receptor mimicry*, Nat. Commun. **12** (2021), 1–9.

[4] L. Zhang, D. Lin, X. Sun, U. Curth, C. Drosten, L. Sauerhering, S. Becker, K. Rox, and R. Hilgenfeld, *Crystal structure of SARS-CoV-2 main protease provides a basis for design of improved α-ketoamide inhibitors*, Science **368** (2020), 409–412.

[5] N. E. Chayen and E. Saridakis, *Protein crystallization: from purified protein to diffraction-quality crystal*, Nat. Methods **5** (2008), 147–153.

[6] S. D. Durbin and G. Feher, *Protein crystallization*, Annu. Rev. Phys. Chem. **47** (1996), 171–204.

[7] H. Qi, X. Liu, D. M. Henn, S. Mei, M. C. Staub, B. Zhao, and C. Y. Li, *Breaking translational symmetry via polymer chain overcrowding in molecular bottlebrush crystallization*, Nat. Commun. **11** (2020), 1–9.

[8] S. Kato, S. Furukawa, D. Aoki, R. Goseki, K. Oikawa, K. Tsuchiya, N. Shimada, A. Maruyama, K. Numata, and H. Otsuka, *Crystallization-induced mechanofluorescence for visualization of polymer crystallization*, Nat. Commun. **12** (2021), 1–7.

[9] G. Bodo, *Crystalline cytochrome c from the king penguin*, Nature **176** (1955), 829–830.

[10] B. Hagihara, K. Tagawa, M. Nozaki, I. Morikawa, J. Yamashita, and K. Okunuki, *Crystalline cytochrome c: Crystallization of cytochrome c from fish*, Nature **179** (1957), 249–250.

[11] T. Morimoto, G. Blobel, and D. Sabatini, *Ribosome crystallization in chicken embryos: II. conditions for the formation of ribosome tetramers in vivo*, J. Cell Biol. **52** (1972), 355–366.

[12] B. Clark, B. Doctor, K. C. Holmes, A. Klug, K. Marcker, S. Morris, and H. Paradies, *Crystallization of transfer RNA*, Nature **219** (1968), 1222–1224.

[13] S. Nosaki, T. Terada, A. Nakamura, K. Hirabayashi, Y. Xu, T. B. C. Bui, T. Nakano, M. Tanokura, and T. Miyakawa, *Highlighting the potential utility of MBP crystallization chaperone for arabidopsis BIL1/BZR1 transcription factor-DNA complex*, Sci. Rep. **11** (2021), 1–9.

[14] Z. Wang, K. Gao, Y. Kan, M. Zhang, C. Qiu, L. Zhu, Z. Zhao, X. Peng, W. Feng, Z. Qian, et al., *The coupling and competition of crystallization and phase separation, correlating thermodynamics and kinetics in OPV morphology and performances*, Nat. Commun. **12** (2021), 1–14.

[15] L.-J. Chan, A. Gandhirajan, L. L. Carias, M. H. Dietrich, O. Vadas, R. Visentin, C. T. França, S. Menant, D. Soldati-Favre, I. Mueller, C. L. King, and W.-H. Tham, *Naturally acquired blocking human monoclonal antibodies to Plasmodium vivax reticulocyte binding protein 2b*, Nat. Commun. **12** (2021), 1–14.

[16] A. Watson, H. Li, B. Ma, R. Weiss, D. Bendayan, L. Abramovitz, N. Ben-Shalom, M. Mor, E. Pinko, M. B. Oz, et al., *Human antibodies targeting a mycobacterium transporter protein mediate protection against tuberculosis*, Nat. Commun. **12** (2021), 1–11.

[17] K. E. Blow, D. Quigley, and G. C. Sosso, *The seven deadly sins: when computing crystal nucleation rates, the devil is in the details*, Chem. Phys. **155** (2021), 040901.

[18] T. Storelvmo and I. Tan, *The Wegener-Bergeron-Findeisen process - its discovery and vital importance for weather and climate*, Meteor. Z **24** (2015), 455–461.

[19] K. Lau and H. Wu, *Warm rain processes over tropical oceans and climate implications*, Geophys. Res. Lett. **30** (2003), 2290.

[20] G. C. Sosso, G. Miceli, S. Caravati, F. Giberti, J. Behler, and M. Bernasconi, *Fast crystallization of the phase change compound gete by large-scale molecular dynamics simulations*, J. Phys. Chem. Lett. **4** (2013), 4241–4246.

[21] W. Chen, H. Yang, and J. Y. Yew Heng, *Chapter 10 continuous protein crystallization*, The Handbook of Continuous Crystallization, The Royal Society of Chemistry, 2020, pp. 372–392.

[22] A. Schiefner, R. Walser, M. Gebauer, and A. Skerra, *Proline/alanine-rich sequence (PAS) polypeptides as an alternative to PEG precipitants for protein crystallization*, Acta Crystallogr. F **76** (2020), 320–325.

[23] Y. Hata, X. Li, U.-i. Chung, and T. Sakai, *Molecular crystallization directed by polymer size and overlap under dilute and crowded macromolecular conditions*, Polym. J. (2021), 1–10.

[24] S. Stroobants, M. Callewaert, M. Krzek, S. Chinnu, P. Gelin, I. Ziemecka, J. F. Lutsko, W. De Malsche, and D. Maes, *Influence of shear on protein crystallization under constant shear conditions*, Cryst. Growth Des. **20** (2020), 1876–1883.

[25] S. Bhattacharya, P. Kundu, J. Liu, W.-C. Wang, and F.-G. Tseng, *Feedback-system-control integrated microfluidic system for fast screening of protein crystallization conditions*, Cryst. Growth Des. **20** (2020), 4325–4334.

[26] M. Kang, G. Lee, K. Jang, D. W. Jeong, J.-O. Lee, H. Kim, and Y. J. Kim, *Graphene quantum dots as nucleants for protein crystallization*, Cryst. Growth Des. **22** (2021), 269–276.

[27] M. Polino, H. Rho, M. Pina, R. Mallada, A. Carvalho, M. Romão, I. Coelhoso, J. Gardeniers, J. Crespo, and C. A. Portugal, *Protein crystallization in a microfluidic contactor with Nafion 117 membranes*, Membranes **11** (2021), 549.

[28] Y. Mao, F. Li, T. Wang, X. Cheng, G. Li, D. Li, X. Zhang, and H. Hao, *Enhancement of lysozyme crystallization under ultrasound field*, Ultrason. Sonochem. **63** (2020), 104975.

[29] R. Chowdhury, M. I. Abboud, T. E. McAllister, B. Banerji, B. Bhushan, J. L. Sorensen, A. Kawamura, and C. J. Schofield, *Use of cyclic peptides to induce crystallization: case study with prolyl hydroxylase domain 2*, Sci. Rep. **10** (2020), 1–11.

[30] X.-Z. Yang, C.-Y. Zhang, Q.-J. Wang, Y.-Z. Guo, C. Dong, E.-K. Yan, W.-J. Liu, X.-W. Zheng, and D.-C. Yin, *Utilization of cyclodextrins and its derivative particles as nucleants for protein crystallization*, Cryst. Growth Des. **17** (2017), 6189–6200.

[31] R. C. Stevens, *High-throughput protein crystallization*, Curr. Opin. Struct. Biol. **10** (2000), 558–563.

[32] T. X. Tran, M. L. Pusey, and R. S. Aygun, *Protein crystallization segmentation and classification using subordinate color channel in fluorescence microscopy images*, J. Fluoresc. **30** (2020), 637–656.

[33] Y.-R. Liang, L.-N. Zhu, J. Gao, H.-X. Zhao, Y. Zhu, S. Ye, and Q. Fang, *3D-printed high-density droplet array chip for miniaturized protein crystallization screening under vapor diffusion mode*, ACS Appl. Mater. Interfaces **9** (2017), 11837–11845.

[34] O. Matsarskaia, F. Roosen-Runge, and F. Schreiber, *Multivalent ions and biomolecules: Attempting a comprehensive perspective*, ChemPhysChem **21** (2020), 1742–1767.

[35] B. V. Derjaguin and L. Landau, *Theory of the stability of strongly charged lyophobic sols and of the adhesion of strongly charged particles in solutions of electrolytes*, Acta Physicochim. USSR **14** (1941), 633–662.

[36] E. Verwey and J. Overbeek, *Theory of the Stability of Lyophobic Colloids*, Elsevier, Amsterdam, 1948.

[37] M. Gouy, *Sur la constitution de la charge électrique à la surface d'un électrolyte*, J. Phys. Theor. Appl. **9** (1910), 457–468.

[38] D. L. Chapman, *A contribution to the theory of electrocapillarity*, Phil. Mag. **25** (1913), 475–481.

[39] F. Hofmeister, *Zur Lehre von der Wirkung der Salze*, N-S Arch. Pharmacol. **24** (1888), 247–260.

[40] F. Zhang, M. W. A. Skoda, R. M. J. Jacobs, S. Zorn, R. A. Martin, C. M. Martin, G. F. Clark, S. Weggler, A. Hildebrandt, O. Kohlbacher, and F. Schreiber, *Reentrant condensation of proteins in solution induced by multivalent counterions*, Phys. Rev. Lett. **101** (2008), 148101.

[41] F. Roosen-Runge, F. Zhang, F. Schreiber, and R. Roth, *Ion-activated attractive patches as a mechanism for controlled protein interactions*, Sci. Rep. **4** (2014), 7016.

[42] A. Sauter, M. Oelker, G. Zocher, F. Zhang, T. Stehle, and F. Schreiber, *Nonclassical pathways of protein crystallization in the presence of multivalent metal ions*, Cryst. Growth Des. **14** (2014), 6357–6366.

[43] F. Zhang, S. Weggler, M. J. Ziller, L. Ianeselli, B. S. Heck, A. Hildebrandt, O. Kohlbacher, M. W. A. Skoda, R. M. J. Jacobs, and F. Schreiber, *Universality of protein reentrant condensation in solution induced by multivalent metal ions*, Proteins **78** (2010), 3450–3457.

[44] A. Sauter, F. Roosen-Runge, F. Zhang, G. Lotze, R. M. J. Jacobs, and F. Schreiber, *Real-time observation of nonclassical protein crystallization kinetics*, J. Am. Chem. Soc. **137** (2015), 1485–1491.

[45] A. Sauter, F. Roosen-Runge, F. Zhang, G. Lotze, A. Feoktystov, R. M. J. Jacobs, and F. Schreiber, *On the question of two-step nucleation in protein crystallization*, Faraday Discuss. **179** (2015), 41–58.

[46] F. Zhang, G. Zocher, A. Sauter, T. Stehle, and F. Schreiber, *Novel approach to controlled protein crystallization through ligandation of yttrium cations*, J. Appl. Cryst. **44** (2011), 755–762.

[47] F. Zhang, R. Roth, M. Wolf, F. Roosen-Runge, M. W. A. Skoda, R. M. J. Jacobs, M. Sztucki, and F. Schreiber, *Charge-controlled metastable liquid-liquid phase separation in protein solutions as a universal pathway towards crystallization*, Soft Matter **8** (2012), 1313–1316.

[48] F. Zhang, F. Roosen-Runge, A. Sauter, R. Roth, M. W. A. Skoda, R. Jacobs, M. Sztucki, and F. Schreiber, *The role of cluster formation and metastable liquid-liquid phase separation in protein crystallization*, Faraday Discuss. **159** (2012), 313–325.

[49] F. Zhang, F. Roosen-Runge, A. Sauter, M. Wolf, R. M. J. Jacobs, and F. Schreiber, *Reentrant condensation, liquid-liquid phase separation and crystallization in protein solutions induced by multivalent metal ions*, Pure Appl. Chem. **86** (2014), 191–202.

[50] M. Wolf, F. Roosen-Runge, F. Zhang, R. Roth, M. W. Skoda, R. M. Jacobs, M. Sztucki, and F. Schreiber, *Effective interactions in protein–salt solutions approaching liquid–liquid phase separation*, J. Mol. Liq. **200** (2014), 20–27.

[51] S. Da Vela, C. Exner, R. S. Schäufele, J. Moller, Z. Fu, F. Zhang, and F. Schreiber, *Arrested and temporarily arrested states in a protein-polymer mixture studied by USAXS and VSANS*, Soft Matter **13** (2017), 8756–8765.

[52] F. Cardinaux, T. Gibaud, A. Stradner, and P. Schurtenberger, *Interplay between spinodal decomposition and glass formation in proteins exhibiting short-range attractions*, Phys. Rev. Lett. **99** (2007), 118301.

[53] H. Liu, S. K. Kumar, and F. Sciortino, *Vapor-liquid coexistence of patchy models: Relevance to protein phase behavior*, J. Chem. Phys. **127** (2007), 084902.

[54] J. R. Espinosa, J. A. Joseph, I. Sanchez-Burgos, A. Garaizar, D. Frenkel, and R. Collepardo-Guevara, *Liquid network connectivity regulates the stability and composition of biomolecular condensates with many components*, Proc. Natl. Acad. Sci. U.S.A. **117** (2020), 13238–13247.

[55] V. A. Bloomfield, *DNA condensation*, Curr. Opin. Struct. Biol. **6** (1996), 334.

[56] H. Dong, J. F. Snyder, K. S. Williams, and J. W. Andzelm, *Cation-induced hydrogels of cellulose nanofibrils with tunable moduli*, Biomacromolecules **14** (2013), 3338–3345.

[57] K. J. Henderson, T. C. Zhou, K. J. Otim, and K. R. Shull, *Ionically cross-linked triblock copolymer hydrogels with high strength*, Macromolecules **43** (2010), 6193–6201.

[58] L. Valencia, E. M. Nomena, S. Monti, W. Rosas-Arbelaez, A. P. Mathew, S. Kumar, and K. P. Velikov, *Multivalent ion-induced re-entrant transition of carboxylated cellulose nanofibrils and its influence on nanomaterials' properties*, Nanoscale **12** (2020), 15652–15662.

[59] P. K. Jha, J. W. Zwanikken, and M. O. De La Cruz, *Understanding swollen–collapsed and re-entrant transitions in polyelectrolyte nanogels by a modified Donnan theory*, Soft Matter **8** (2012), 9519–9522.

[60] C. E. Sing, J. W. Zwanikken, and M. Olvera de la Cruz, *Effect of ion–ion correlations on polyelectrolyte gel collapse and reentrant swelling*, Macromolecules **46** (2013), 5053–5065.

[61] E. Raspaud, M. O. De La Cruz, J.-L. Sikorav, and F. Livolant, *Precipitation of DNA by polyamines: a polyelectrolyte behavior*, Biophys. J. **74** (1998), 381–393.

[62] J. Widom and R. L. Baldwin, *Cation-induced toroidal condensation of DNA: studies with Co^{3+} $(NH_3)_6$*, J. Mol. Biol. **144** (1980), 431–453.

[63] C. E. Sing, J. W. Zwanikken, and M. Olvera de la Cruz, *Effect of ion–ion correlations on polyelectrolyte gel collapse and reentrant swelling*, Macromolecules **46** (2013), 5053–5065.

[64] M. G. Poirier, T. Monhait, and J. F. Marko, *Reversible hypercondensation and decondensation of mitotic chromosomes studied using combined chemical–micromechanical techniques*, J. Cell. Biochem. **85** (2002), 422–434.

[65] E. Raspaud, I. Chaperon, A. Leforestier, and F. Livolant, *Spermine-induced aggregation of DNA, nucleosome, and chromatin*, Biophys. J. **77** (1999), 1547–1555.

[66] M. Olvera de la Cruz, L. Belloni, M. Delsanti, J. P. Dalbiez, O. Spalla, and M. Drifford, *Precipitation of highly charged polyelectrolyte solutions in the presence of multivalent salts*, J. Chem. Phys. **103** (1995), 5781–5791.

[67] H. Fu, X. Gao, X. Zhang, and L. Ling, *Recent advances in nonclassical crystallization: Fundamentals, applications, and challenges*, Cryst. Growth Des. **22** (2022), 1476–1499.

[68] C. N. Nanev, *Kinetics and intimate mechanism of protein crystal nucleation*, Prog. Cryst. Growth Charact. Mater. **59** (2013), 133–169.

[69] J. W. Gibbs, *On the equilibrium of heterogeneous substances*, Trans. Connect. Acad. Sci. **16** (1876), 343–524.

[70] J. W. Gibbs, *On the equilibrium of heterogeneous substances*, Trans. Connect. Acad. Sci. **3** (1878), 108–248.

[71] J. De Yoreo, *A perspective on multistep pathways of nucleation*, Crystallization via Nonclassical Pathways Volume 1: Nucleation, Assembly, Observation & Application, ACS Publications, 2020, pp. 1–17.

[72] S.-T. Yau and P. G. Vekilov, *Direct observation of nucleus structure and nucleation pathways in apoferritin crystallization*, J. Am. Chem. Soc. **123** (2001), 1080–1089.

[73] S. T. Yau and P. G. Vekilov, *Quasi-planar nucleus structure in apoferritin crystallization*, Nature **406** (2000), 494–497.

[74] M. Sleutel, J. Lutsko, A. E. van Driessche, M. A. Durán-Olivencia, and D. Maes, *Observing classical nucleation theory at work by monitoring phase transitions with molecular precision*, Nat. Commun. **5** (2014), 1–8.

[75] A. E. Van Driessche, N. Van Gerven, R. R. Joosten, W. L. Ling, M. Bacia, N. Sommerdijk, and M. Sleutel, *Nucleation of protein mesocrystals via oriented attachment*, Nat. Commun. **12** (2021), 1–8.

[76] A. E. Van Driessche, N. Van Gerven, P. H. Bomans, R. R. Joosten, H. Friedrich, D. Gil-Carton, N. A. Sommerdijk, and M. Sleutel, *Molecular nucleation mechanisms and control strategies for crystal polymorph selection*, Nature **556** (2018), 89.

[77] Q. Hu, M. H. Nielsen, C. Freeman, L. Hamm, J. Tao, J. Lee, T. Y.-J. Han, U. Becker, J. Harding, P. Dove, and J. De Yoreo, *The thermodynamics of calcite nucleation at organic interfaces: Classical vs. non-classical pathways*, Faraday Discuss. **159** (2012), 509–523.

[78] P. R. ten Wolde and D. Frenkel, *Enhancement of protein crystal nucleation by critical density fluctuations*, Science **277** (1997), 1975–1978.

[79] W. Ostwald, *Studien über die bildung und umwandlung fester körper*, Z. Phys. Chem. **22** (1897), 289–330.

[80] S.-Y. Chung, Y.-M. Kim, J.-G. Kim, and Y.-J. Kim, *Multiphase transformation and Ostwald's rule of stages during crystallization of a metal phosphate*, Nat. Phys. **5** (2009), 68–73.

[81] C. Desgranges and J. Delhommelle, *Can ordered precursors promote the nucleation of solid solutions?*, Phys. Rev. Lett. **123** (2019), 195701.

[82] L. Lupi, B. Peters, and V. Molinero, *Pre-ordering of interfacial water in the pathway of heterogeneous ice nucleation does not lead to a two-step crystallization mechanism*, J. Chem. Phys. **145** (2016), 211910.

[83] M. Kaissaratos, L. Filobelo, and P. G. Vekilov, *Two-step crystal nucleation is selected because of a lower surface free energy barrier*, Cryst. Growth Des. **21** (2021), 5394–5402.

[84] C. A. Stifler, C. E. Killian, and P. U. Gilbert, *Evidence for a liquid precursor to biomineral formation*, Cryst. Growth Des. **21** (2021), 6635–6641.

[85] N. D. Loh, S. Sen, M. Bosman, S. F. Tan, J. Zhong, C. A. Nijhuis, P. Král, P. Matsudaira, and U. Mirsaidov, *Multistep nucleation of nanocrystals in aqueous solution*, Nat. Chem. **9** (2017), 77–82.

[86] G. Li, N. He, J. Deng, J. Liu, Y. Sun, M. Qu, Y. Jiang, T. Zhao, S.-Y. Zhou, H. Zeng, Z. Qizheng, H.-G. Liao, and S.-G. Sun, *Observations of dense liquid phase-assisted nanocrystal growth and coalescence*, Cryst. Growth Des. **21** (2021), 6025–6030.

[87] D. G. Greene, S. Modla, N. J. Wagner, S. I. Sandler, and A. M. Lenhoff, *Local crystalline structure in an amorphous protein dense phase*, Biophys. J. **109** (2015), 1716–1723.

[88] T. H. Zhang and X. Y. Liu, *How does a transient amorphous precursor template crystallization*, J. Am. Chem. Soc. **129** (2007), 13520–13526.

[89] L. Houben, H. Weissman, S. G. Wolf, and B. Rybtchinski, *A mechanism of ferritin crystallization revealed by cryo-STEM tomography*, Nature **579** (2020), 540–543.

[90] J. F. Lutsko, *How crystals form: A theory of nucleation pathways*, Sci. Adv. **5** (2019), eaav7399.

[91] E. W. Martin, T. S. Harmon, J. B. Hopkins, S. Chakravarthy, J. J. Incicco, P. Schuck, A. Soranno, and T. Mittag, *A multi-step nucleation process determines the kinetics of prion-like domain phase separation*, Nat. Commun. **12** (2021), 1–12.

[92] A. Dey, P. H. Bomans, F. A. Müller, J. Will, P. M. Frederik, G. de With, and N. A. Sommerdijk, *The role of prenucleation clusters in surface-induced calcium phosphate crystallization*, Nat. Mater. **9** (2010), 1010–1014.

[93] A. F. Wallace, L. O. Hedges, A. Fernandez-Martinez, P. Raiteri, J. D. Gale, G. A. Waychunas, S. Whitelam, J. F. Banfield, and J. J. De Yoreo, *Microscopic evidence for liquid-liquid separation in supersaturated $CaCO_3$ solutions*, Science **341** (2013), 885–889.

[94] P. J. Smeets, A. R. Finney, W. J. Habraken, F. Nudelman, H. Friedrich, J. Laven, J. J. De Yoreo, P. M. Rodger, and N. A. Sommerdijk, *A classical view on nonclassical nucleation*, Proc. Natl. Acad. Sci. USA **114** (2017), E7882–E7890.

[95] W. Dachraoui, D. Keller, T. R. Henninen, O. J. Ashton, and R. Erni, *Atomic mechanisms of nanocrystallization via cluster-clouds in solution studied by liquid-phase scanning transmission electron microscopy*, Nano Lett. **21** (2021), 2861–2869.

[96] R. R. Steendam and P. J. Frawley, *Secondary nucleation of sodium chlorate: the role of initial breeding*, Cryst. Growth Des. **19** (2019), 3453–3460.

[97] S. Xu, Z. Hou, X. Chuai, and Y. Wang, *Overview of secondary nucleation: From fundamentals to application*, Ind. Eng. Chem. Res. **59** (2020), 18335–18356.

[98] G. Zhu, M. L. Sushko, J. S. Loring, B. A. Legg, M. Song, J. A. Soltis, X. Huang, K. M. Rosso, and J. J. De Yoreo, *Self-similar mesocrystals form via interface-driven nucleation and assembly*, Nature **590** (2021), 416–422.

[99] L. Liu, E. Nakouzi, M. L. Sushko, G. K. Schenter, C. J. Mundy, J. Chun, and J. J. De Yoreo, *Connecting energetics to dynamics in particle growth by oriented attachment using real-time observations*, Nat. Commun. **11** (2020), 1–11.

[100] J.-O. Henck, U. Griesser, and A. Burger, *Polymorphie von Arzneistoffen: Eine wirtschaftliche Herausforderung?*, Pharm. Ind. **59** (1997), 165–169.

[101] K. Kersten, R. Kaur, and A. Matzger, *Survey and analysis of crystal polymorphism in organic structures*, IUCrJ **5** (2018), 124–129.

[102] G. P. Stahly, *Diversity in single-and multiple-component crystals. the search for and prevalence of polymorphs and cocrystals*, Cryst. Growth Des. **7** (2007), 1007–1026.

[103] R. Thakuria and T. Thakur, *Crystal polymorphism in pharmaceutical science*, Comprehensive Supramolecular Chemistry II, Elsevier: Oxford, UK, 2017, pp. 283–309.

[104] R. Hilfiker, *Polymorphism: In the pharmaceutical industry*, Wiley-VCH, Weinheim, Germany, 2006.

[105] A. J. Cruz-Cabeza, N. Feeder, and R. J. Davey, *Open questions in organic crystal polymorphism*, Commun. Chem. **3** (2020), 1–4.

[106] D. James, S. Beairsto, C. Hartt, O. Zavalov, I. Saika-Voivod, R. K. Bowles, and P. H. Poole, *Phase transitions in fluctuations and their role in two-step nucleation*, J. Chem. Phys. **150** (2019), 074501.

[107] T. Yamazaki, A. E. Van Driessche, and Y. Kimura, *High mobility of lattice molecules and defects during the early stage of protein crystallization*, Soft Matter **16** (2020), 1955–1960.

[108] Y. Peng, F. Wang, Z. Wang, A. M. Alsayed, Z. Zhang, A. G. Yodh, and Y. Han, *Two-step nucleation mechanism in solid–solid phase transitions*, Nat. Mater. **14** (2015), 101–108.

[109] G. E. Dale, C. Oefner, and A. D'Arcy, *The protein as a variable in protein crystallization*, J. Struct. Biol. **142** (2003), 88–97.

[110] C. N. Nanev, *Phenomenological consideration of protein crystal nucleation; the physics and biochemistry behind the phenomenon*, Crystals **7** (2017), 193.

[111] S. Fudo, F. Qi, M. Nukaga, and T. Hoshino, *Influence of precipitants on molecular arrangements and space groups of protein crystals*, Cryst. Growth Des. **17** (2017), 534–542.

[112] Y. Guo, N. Nishida, and T. Hoshino, *Quantifying the separation of positive and negative areas in electrostatic potential for predicting feasibility of ammonium sulfate for protein crystallization*, J. Chem. Inf. Model. **61** (2021), 4571–4581.

[113] Z. S. Derewenda and P. G. Vekilov, *Entropy and surface engineering in protein crystallization*, Acta Crystallogr. D **62** (2006), 116–124.

[114] C. Jelsch, S. Longhi, and C. Cambillau, *Packing forces in nine crystal forms of cutinase*, Proteins **31** (1998), 320–333.

[115] A. Elbasir, R. Mall, K. Kunji, R. Rawi, Z. Islam, G.-Y. Chuang, P. R. Kolatkar, and H. Bensmail, *BCrystal: an interpretable sequence-based protein crystallization predictor*, Bioinformatics **36** (2020), 1429–1438.

[116] O. Carugo and P. Argos, *Protein–protein crystal-packing contacts*, Protein Sci. **6** (1997), 2261–2263.

[117] A. George and W. W. Wilson, *Predicting protein crystallization from a dilute solution property*, Acta Crystallogr. D **50** (1994), 361–365.

[118] G. A. Vliegenthart and H. N. W. Lekkerkerker, *Predicting the gas–liquid critical point from the second virial coefficient*, J. Chem. Phys. **112** (2000), 5364–5369.

[119] C. N. Nanev, *Advancements (and challenges) in the study of protein crystal nucleation and growth; thermodynamic and kinetic explanations and comparison with small-molecule crystallization*, Prog. Cryst. Growth Charact. Mater. (2020), 100484.

[120] J. D. Schmit and K. Dill, *Growth rates of protein crystals*, J. Am. Chem. Soc. **134** (2012), 3934–3937.

[121] L. Fagerberg, K. Jonasson, G. von Heijne, M. Uhlén, and L. Berglund, *Prediction of the human membrane proteome*, Proteomics **10** (2010), 1141–1149.

[122] C.-J. Tsai and G. F. Schertler, *Membrane protein crystallization*, 187–210, Wiley Online Library, 2020, pp. 187–210.

[123] T. M. Bakheet and A. J. Doig, *Properties and identification of human protein drug targets*, Bioinformatics **25** (2009), 451–457.

[124] M. A. Yıldırım, K.-I. Goh, M. E. Cusick, A.-L. Barabási, and M. Vidal, *Drug-target network*, Nat. Biotechnol. **25** (2007), 1119–1126.

[125] M. Caffrey, *Membrane protein crystallization*, J. Struct. Biol. **142** (2003), 108–132.

[126] A. Nath, W. M. Atkins, and S. G. Sligar, *Applications of phospholipid bilayer nanodiscs in the study of membranes and membrane proteins*, Biochemistry **46** (2007), 2059–2069.

[127] T. H. Bayburt, Y. V. Grinkova, and S. G. Sligar, *Self-assembly of discoidal phospholipid bilayer nanoparticles with membrane scaffold proteins*, Nano Lett. **2** (2002), 853–856.

[128] T. H. Bayburt and S. G. Sligar, *Membrane protein assembly into nanodiscs*, FEBS Lett. **584** (2010), 1721–1727.

[129] K. A. Morrison, A. Doekhie, G. M. Neville, G. J. Price, P. Whitley, J. Doutch, and K. J. Edler, *Ab initio reconstruction of small angle scattering data for membrane proteins in copolymer nanodiscs*, BBA Advances **2** (2022), 100033.

[130] A. Z. Kijac, Y. Li, S. G. Sligar, and C. M. Rienstra, *Magic-angle spinning solid-state NMR spectroscopy of nanodisc-embedded human CYP3A4*, Biochemistry **46** (2007), 13696–13703.

[131] F. Hagn, M. Etzkorn, T. Raschle, and G. Wagner, *Optimized phospholipid bilayer nanodiscs facilitate high-resolution structure determination of membrane proteins*, J. Am. Chem. Soc. **135** (2013), 1919–1925.

[132] P. J. Mak, M. C. Gregory, I. G. Denisov, S. G. Sligar, and J. R. Kincaid, *Unveiling the crucial intermediates in androgen production*, Proc. Natl. Acad. Sci. U.S.A. **112** (2015), 15856–15861.

[133] I. G. Denisov and S. G. Sligar, *Nanodiscs for structural and functional studies of membrane proteins*, Nat. Struct. Mol. Biol. **23** (2016), 481–486.

[134] J. M. Dörr, S. Scheidelaar, M. C. Koorengevel, J. J. Dominguez, M. Schäfer, C. A. van Walree, and J. A. Killian, *The styrene–maleic acid copolymer: a versatile tool in membrane research*, Eur. Biophys. J. **45** (2016), 3–21.

[135] T. J. Knowles, R. Finka, C. Smith, Y.-P. Lin, T. Dafforn, and M. Overduin, *Membrane proteins solubilized intact in lipid containing nanoparticles bounded by styrene maleic acid copolymer*, J. Am. Chem. Soc. **131** (2009), 7484–7485.

[136] A. O. Oluwole, B. Danielczak, A. Meister, J. O. Babalola, C. Vargas, and S. Keller, *Solubilization of membrane proteins into functional lipid-bilayer nanodiscs using a diisobutylene/maleic acid copolymer*, Angew. Chemie Int. Ed. **56** (2017), 1919–1924.

[137] P. G. Vekilov, *Dense liquid precursor for the nucleation of ordered solid phases from solution*, Cryst. Growth Des. **4** (2004), 671–685.

[138] R. P. Sear, *The non-classical nucleation of crystals: microscopic mechanisms and applications to molecular crystals, ice and calcium carbonate*, Int. Mater. Rev. **57** (2012), 328–356.

[139] A. Bujacz, *Structures of bovine, equine and leporine serum albumin*, Acta Crystallogr. D **68** (2012), 1278–1289.

[140] D. I. Svergun, M. H. J. Koch, P. A. Timmins, and R. P. May, *Small angle X-ray and neutron scattering from solutions of biological macromolecules*, Oxford University Press, 2013.

[141] P. Lindner and T. Zemb, *Neutrons, X-rays, and light: Scattering methods applied to soft condensed matter*, Elsevier North-Holland, 2002.

[142] C. E. Blanchet and D. I. Svergun, *Small-angle x-ray scattering on biological macromolecules and nanocomposites in solution.*, Ann. Rev. Phys. Chem. **64** (2013), 37 – 54.

[143] M. Kotlarchyk and S.-H. Chen, *Analysis of small angle neutron scattering spectra from polydisperse interacting colloids*, J. Chem. Phys. **79** (1983), 2461–2469.

[144] S. Doniach, *Changes in biomolecular conformation seen by small angle X-ray scattering*, Chem. Rev. **101** (2001), 1763–1778.

[145] B. Jacrot and G. Zaccai, *Determination of molecular weight by neutron scattering*, Biopolymers **20** (1981), 2413–2426.

[146] M. J. Hollamby, *Practical applications of small-angle neutron scattering*, Phys. Chem. Chem. Phys. **15** (2013), 10566–10579.

[147] B. Linder, *Thermodynamics and introductory statistical mechanics*, John Wiley & Sons, 2004.

[148] L. Rayleigh, *Form factor of a homogenous sphere*, Proc. R. Soc. London, Ser. A **84** (1911), 25–38.

[149] D. Bendedouch and S.-H. Chen, *Structure and interparticle interactions of bovine serum albumin in solution studied by small-angle neutron scattering*, J. Chem. Phys. **87** (1983), 1473–1477.

[150] M. Volmer and A. Weber, *Keimbildung in übersättigten Gebilden*, Z. Phys. Chem. **119** (1926), 277–301.

[151] R. Schubert, A. Meyer, D. Baitan, K. Dierks, M. Perbandt, and C. Betzel, *Real-time observation of protein dense liquid cluster evolution during nucleation in protein crystallization*, Cryst. Growth Des. **17** (2017), 954–958.

[152] F. Zhang, *Nonclassical nucleation pathways in protein crystallization*, J. Phys. Condens. Matter **29** (2017), 443002.

[153] F. C. Meldrum and R. P. Sear, *Now you see them*, Science **322** (2008), 1802–1803.

[154] D. Erdemir, A. Y. Lee, and A. S. Myerson, *Nucleation of crystals from solution: Classical and two-step models*, Acc. Chem. Res. **42** (2009), 621–629.

[155] J. Russo and H. Tanaka, *Crystal nucleation as the ordering of multiple order parameters*, J. Chem. Phys. **145** (2016), 211801.

[156] S. Karthika, T. K. Radhakrishnan, and P. Kalaichelvi, *A review of classical and nonclassical nucleation theories*, Cryst. Growth Des. **16** (2016), 6663–6681.

[157] M. Sleutel and A. E. S. van Driessche, *Role of clusters in nonclassical nucleation and growth of protein crystals.*, Proc. Nat. Sci. USA **111** (2014), E546–E553.

[158] J. Russo and H. Tanaka, *The microscopic pathway to crystallization in supercooled liquids*, Sci. Rep. **2** (2012), 505.

[159] M. H. J. Hagen and D. Frenkel, *Determination of phase diagrams for the hard-core attractive Yukawa system*, J. Chem. Phys. **101** (1994), 4093–4097.

[160] N. Begam, O. Matsarskaia, M. Sztucki, F. Zhang, and F. Schreiber, *Unification of lower and upper critical solution temperature phase behavior of globular protein solutions in the presence of multivalent cations*, Soft Matter **16** (2020), 2128–2134.

[161] C. Gripon, L. Legrand, I. Rosenman, O. Vidal, M. C. Robert, and F. Boué, *Lysozyme solubility in H_2O and D_2O solutions: A simple relationship*, J. Cryst. Growth **177** (1997), 238–247.

[162] C. Gripon, L. Legrand, I. Rosenman, O. Vidal, M. C. Robert, and F. Boué, *Lysozyme-lysozyme interactions in under- and super-saturated solutions: a simple relation between the second virial coefficients in H_2O and D_2O*, J. Cryst. Growth **178** (1997), 575–584.

[163] S. Bucciarelli, N. Mahmoudi, L. Casal-Dujat, M. Jéhannin, C. Jud, and A. Stradner, *Extended law of corresponding states applied to solvent isotope effect on a globular protein*, J. Phys. Chem. Lett. **7** (2016), 1610–1615.

[164] M. K. Braun, M. Wolf, O. Matsarskaia, S. Da Vela, F. Roosen-Runge, M. Sztucki, R. Roth, F. Zhang, and F. Schreiber, *Strong isotope effects on effective interactions and phase behavior in protein solutions in the presence of multivalent ions*, J. Phys. Chem. B **121** (2017), 1731–1739.

[165] P. G. Vekilov, *Nucleation*, Cryst. Growth Des. **10** (2010), 5007–5019.

[166] K. Djinović-Carugo and O. Carugo, *Structural biology of the lanthanides - Mining rare earths in the Protein Data Bank*, J. Inorg. Biochem. **143** (2015), 69–76.

[167] L. J. Daumann, *Essential and ubiquitous: the emergence of lanthanide metallobiochemistry*, Angew. Chem., Int. Ed. **58** (2019), 12795–12802.

[168] Y. W. Deng, S. Y. Ro, and A. C. Rosenzweig, *Structure and function of the lanthanide-dependent methanol dehydrogenase XoxF from the methanotroph methylomicrobium buryatense 5GB1C*, J. Biol. Inorg. Chem. **23** (2018), 1037–1047.

[169] T. T. Nguyen, I. Rouzina, and B. I. Shklovskii, *Reentrant condensation of DNA induced by multivalent counterions*, J. Chem. Phys. **112** (2000), 2562–2568.

[170] O. Matsarskaia, F. Roosen-Runge, G. Lotze, J. Möller, A. Mariani, F. Zhang, and F. Schreiber, *Tuning phase transitions of aqueous protein solutions by multivalent cations*, Phys. Chem. Chem. Phys. **20** (2018), 27214–27225.

[171] S. Pandit and S. Kundu, *Optical responses of BSA protein under re-entrant condensation in presence of trivalent ions*, J. Mol. Liq. **276** (2019), 954–960.

[172] A. Bijelic and A. Rompel, *The use of polyoxometalates in protein crystallography – an attempt to widen a well-known bottleneck*, Coord. Chem. Rev. **299** (2015), 22 – 38.

[173] M. Muschol and F. Rosenberger, *Liquid–liquid phase separation in supersaturated lysozyme solutions and associated precipitate formation/crystallization*, J. Chem. Phys. **107** (1997), 1953–1962.

[174] B. Zhang and Q. Wang, *Quartz crystal microbalance with dissipation*, Nanotechnology Research Methods for Food and Bioproducts, Wiley Online Library, 2012, p. 181.

[175] Q. Chen, P. G. Vekilov, R. L. Nagel, and R. E. Hirsch, *Liquid-liquid phase separation in hemoglobins: Distinct aggregation mechanisms of the $\beta 6$ mutants*, Biophys. J. **86** (2004), 1702–1712.

[176] W. J. Ray and C. Bracker, *Polyethylene glycol: catalytic effect on the crystallization of phosphoglucomutase at high salt concentration*, J. Cryst. Growth **76** (1986), 562–576.

[177] Y. Liu, X. Wang, and C. B. Ching, *Toward further understanding of lysozyme crystallization: Phase diagram, protein-protein interaction, nucleation kinetics, and growth kinetics*, Cryst. Growth Des. **10** (2010), 548–558.

[178] H. A. Sober, *CRC Handbook of Biochemistry: Selected data for molecular biology*, The Chemical Rubber Co. Cleveland, Ohio, 1970.

[179] T. Narayanan, M. Sztucki, P. Van Vaerenbergh, J. Léonardon, J. Gorini, L. Claustre, F. Sever, J. Morse, and P. Boesecke, *A multipurpose instrument for time-resolved ultra-small-angle and coherent X-ray scattering*, J. App. Cryst. **51** (2018), 1511–1524.

[180] T. Narayanan, *17: Synchroton small-angle X-ray scattering*, 899, Springer New York, 2008, p. 899.

[181] L. Ianeselli, F. Zhang, M. W. A. Skoda, R. M. J. Jacobs, R. A. Martin, S. Callow, S. Prévost, and F. Schreiber, *Protein-protein interactions in ovalbumin solutions studied by small-angle scattering: effect of ionic strength and the chemical nature of cations*, J. Phys. Chem. B **114** (2010), 3776–3783.

[182] K. Lieutenant, P. Lindner, and R. Gahler, *A new design for the standard pinhole small-angle neutron scattering instrument D11*, J. Appl. Cryst. **40** (2007), 1056–1063.

[183] M. Könnecke, F. A. Akeroyd, H. J. Bernstein, A. S. Brewster, S. I. Campbell, B. Clausen, S. Cottrell, J. U. Hoffmann, P. R. Jemian, and D. Männicke, *The nexus data format*, J. Appl. Cryst. **48** (2015), 301–305.

[184] D. Richard, M. Ferrand, and G. J. Kearley, *Analysis and visualisation of neutron-scattering data*, J. Neutron Res. **4** (1996), 33–39.

[185] F. Zhang, C. Beck, M. Feustel, S. Da Vela, R. Maier, O. Matsarskaia, M. Mikorski, F. Roosen-Runge, F. Schreiber, R. Schweins, T. Seydel, and B. Sohmen, *Kinetics of two-step nucleation in protein crystallization studied by real-time SANS*, http://dx.doi.org/10.5291/ILL-DATA.9-13-672, 2016, Institut Laue-Langevin (ILL) doi:10.5291/ILL-DATA.9-13-672.

[186] W. Kabsch, *XDS*, Acta Cryst. D **66** (2010), 125–132.

[187] A. J. McCoy, R. W. Grosse-Kunstleve, P. D. Adams, M. D. Winn, L. C. Storoni, and R. J. Read, *Phaser crystallographic software*, J. Appl. Crystallogr. **40** (2007), 658–674.

[188] P. V. Afonine, R. W. Grosse-Kunstleve, N. Echols, J. J. Headd, N. W. Moriarty, M. Mustyakimov, T. C. Terwilliger, A. Urzhumtsev, P. H. Zwart, and P. D. Adams, *Towards automated crystallographic structure refinement with phenix.refine*, Acta Cryst. D **68** (2012), 352–367.

[189] G. N. Murshudov, P. Skubák, A. A. Lebedev, N. S. Pannu, R. A. Steiner, R. A. Nicholls, M. D. Winn, F. Long, and A. A. Vagin, *REFMAC5 for the refinement of macromolecular crystal structures*, Acta Cryst. D **67** (2011), 355–367.

[190] P. Emsley, B. Lohkamp, W. G. Scott, and K. Cowtan, *Features and development of Coot*, Acta Cryst. D **66** (2010), 486–501.

[191] V. B. Chen, W. B. Arendall, III, J. J. Headd, D. A. Keedy, R. M. Immormino, G. J. Kapral, L. W. Murray, J. S. Richardson, and D. C. Richardson, *MolProbity: all-atom structure validation for macromolecular crystallography*, Acta Cryst. D **66** (2010), 12–21.

[192] L. Schrödinger, *The PyMOL molecular graphics system, version 1.8*, The PyMOL Molecular Graphics System, Version 1.8, Schrödinger, LLC., 2015.

[193] M. K. Braun, A. Sauter, O. Matsarskaia, M. Wolf, F. Roosen-Runge, M. Sztucki, R. Roth, F. Zhang, and F. Schreiber, *Reentrant phase behavior in protein solutions induced by multivalent salts: Strong effect of anions Cl^- versus NO^{3-}*, J. Phys. Chem. B **122** (2018), 11978–11985.

[194] M. R. Fries, D. Stopper, M. K. Braun, A. Hinderhofer, F. Zhang, R. M. Jacobs, M. W. Skoda, H. Hansen-Goos, R. Roth, and F. Schreiber, *Multivalent-ion-activated protein adsorption reflecting bulk reentrant behavior*, Phys. Rev. Lett. **119** (2017), 228001.

[195] M. R. Fries, D. Stopper, M. W. A. Skoda, M. Blum, C. Kertzscher, A. Hinderhofer, F. Zhang, R. M. J. Jacobs, R. Roth, and F. Schreiber, *Enhanced protein adsorption upon bulk phase separation*, Sci. Rep. **10** (2020), 1–9.

[196] P.-G. De Gennes, *Wetting: statics and dynamics*, Rev. Mod. Phys. **57** (1985), 827.

[197] P.-F. Verhulst, *Notice sur la loi que la population suit dans son accroissement*, Corresp. Math. Phys. **10** (1838), 113–126.

[198] V. A. Kritsman, *Ludwig Wilhelmy, Jacobus H. van't Hoff, Svante Arrhenius und die Geschichte der chemischen Kinetik*, Chem. unserer Zeit **31** (1997), 291–300.

[199] Y. Kuznetsov, A. Malkin, and A. McPherson, *Atomic-force-microscopy studies of phase separations in macromolecular systems*, Phys. Rev. B **58** (1998), 6097–6103.

[200] D. Vivarès, E. W. Kaler, and A. M. Lenhoff, *Quantitative imaging by confocal scanning fluorescence microscopy of protein crystallization via liquid–liquid phase separation*, Acta Crystallogr. D **61** (2005), 819–825.

[201] O. Galkin and P. G. Vekilov, *Are nucleation kinetics of protein crystals similar to those of liquid droplets?*, J. Am. Chem. Soc. **122** (2000), 156–163.

[202] T. Yamazaki, Y. Kimura, P. G. Vekilov, E. Furukawa, M. Shirai, H. Matsumoto, A. E. S. Van Driessche, and K. Tsukamoto, *Two types of amorphous protein particles facilitate crystal nucleation*, Proc. Natl. Acad. Sci. U.S.A. **114** (2017), 2154–2159.

[203] H. Tsurusawa, J. Russo, M. Leocmach, and H. Tanaka, *Formation of porous crystals via viscoelastic phase separation*, Nat. Mater. **16** (2017), 1022–1028.

[204] C. Mueller-Dieckmann, S. Panjikar, A. Schmidt, S. Mueller, J. Kuper, A. Geerlof, M. Wilmanns, R. K. Singh, P. A. Tucker, and M. S. Weiss, *On the routine use of soft X-rays in macromolecular crystallography. Part IV. Efficient determination of anomalous substructures in biomacromolecules using longer X-ray wavelengths*, Acta Cryst. D **63** (2007), 366–380.

[205] E. Krissinel and K. Henrick, *Inference of macromolecular assemblies from crystalline state*, J. Mol. Biol. **372** (2007), 774–797.

[206] S. Curry, H. Mandelkow, P. Brick, and N. Franks, *Crystal structure of human serum albumin complexed with fatty acid reveals an asymmetric distribution of binding sites*, Nat. Struct. Biol. **5** (1998), 827–835.

[207] S. Sugio, A. Kashima, S. Mochizuki, M. Noda, and K. Kobayashi, *Crystal structure of human serum albumin at 2.5Å resolution*, Protein Eng. **12** (1999), 439–446.

[208] X. M. He and D. C. Carter, *Atomic structure and chemistry of human serum albumin*, Nature **358** (1992), 209–215.

[209] I. M. Klotz and J. M. Urquhart, *The binding of organic ions by proteins. comparison of native and of modified proteins*, J. Am. Chem. Soc. **71** (1949), 1597–1603.

[210] I. M. Klotz and J. Ayers, *Interactions of some neutral organic molecules with proteins*, J. Am. Chem. Soc. **74** (1952), 6178–6180.

[211] S. Wang, S. Liu, Y. Zhang, J. He, D. H. Coy, and L. Sun, *Human serum albumin (HSA) and its applications as a drug delivery vehicle*, Health Sci. J. **14** (2020), 1–8.

[212] P. Kandagal, S. Ashoka, J. Seetharamappa, S. Shaikh, Y. Jadegoud, and O. B. Ijare, *Study of the interaction of an anticancer drug with human and bovine serum albumin: spectroscopic approach*, J. Pharm. Biomed. Anal. **41** (2006), 393–399.

[213] A. Sułkowska, J. Równicka, B. Bojko, and W. Sułkowski, *Interaction of anticancer drugs with human and bovine serum albumin*, J. Mol. Struct. **651** (2003), 133–140.

[214] R. Maier, G. Zocher, A. Sauter, S. Da Vela, O. Matsarskaia, R. Schweins, M. Sztucki, F. Zhang, T. Stehle, and F. Schreiber, *Protein crystallization in the presence of a metastable liquid–liquid phase separation*, Cryst. Growth Des. **20** (2020), 7951–7962.

[215] M. R. Fries, N. F. Conzelmann, L. Günter, O. Matsarskaia, M. W. Skoda, R. M. Jacobs, F. Zhang, and F. Schreiber, *Bulk phase behavior vs interface adsorption: Specific multivalent cation and anion effects on BSA interactions*, Langmuir **37** (2021), 139–150.

[216] S. Hadichegeni, B. Goliaei, M. Taghizadeh, S. Davoodmanesh, F. Taghavi, and M. Hashemi, *Characterization of the interaction between human serum albumin and diazinon via spectroscopic and molecular docking methods*, Hum. Exp. Toxicol. **37** (2018), 959–971.

[217] E. Gelamo and M. Tabak, *Spectroscopic studies on the interaction of bovine (BSA) and human (HSA) serum albumins with ionic surfactants*, Spectrochim. Acta A **56** (2000), 2255–2271.

[218] W. Bal, J. Christodoulou, P. J. Sadler, and A. Tucker, *Multi-metal binding site of serum albumin*, J. Inorg. Biochem. **70** (1998), 33–39.

[219] A. Michnik, K. Michalik, A. Kluczewska, and Z. Drzazga, *Comparative DSC study of human and bovine serum albumin*, J. Therm. Anal. Calorim. **84** (2006), 113–117.

[220] Y. Akdogan, J. Reichenwallner, and D. Hinderberger, *Evidence for water-tuned structural differences in proteins: an approach emphasizing variations in local hydrophilicity*, PLoS One **7** (2012), e45681.

[221] S. Da Vela, M. K. Braun, A. Dorr, A. Greco, J. Moller, Z. Fu, F. Zhang, and F. Schreiber, *Kinetics of liquid-liquid phase separation in protein solutions exhibiting lcst phase behavior studied by time-resolved USAXS and VSANS*, Soft Matter **12** (2016), 9334–9341.

[222] O. Matsarskaia, M. K. Braun, F. Roosen-Runge, M. Wolf, F. Zhang, R. Roth, and F. Schreiber, *Cation-induced hydration effects cause lower critical solution temperature behavior in protein solutions*, J. Phys. Chem. B **120** (2016), 7731–7736.

[223] C. E. Blanchet, A. Spilotros, F. Schwemmer, M. A. Graewert, A. Kikhney, C. M. Jeffries, D. Franke, D. Mark, R. Zengerle, F. Cipriani, S. Fiedler, M. Roessle, and D. I. Svergun, *Versatile sample environments and automation for biological solution X-ray scattering experiments at the P12 beamline (PETRA III, DESY)*, J. Appl. Crystallogr. **48** (2015), 431–443.

[224] R. J. Baxter, *Percus–Yevick equation for hard spheres with surface adhesion*, J. Chem. Phys. **49** (1968), 2770–2774.

[225] S. R. Kline, *Reduction and analysis of SANS and USANS data using IGOR Pro*, J. Appl. Cryst. **39** (2006), 895–900.

[226] S. V. G. Menon, C. Manohar, and K. S. Rao, *A new interpretation of the sticky hard sphere model*, J. Chem. Phys. **95** (1991), 9186–9190.

[227] J. Lee and S. Timasheff, *Partial specific volumes and interactions with solvent components of proteins in guanidine hydrochloride*, Biochemistry **13** (1974), 257–265.

[228] T. Hianik, S. Poniková, J. Bágel'ová, and M. Antalík, *Specific volume and compressibility of human serum albumin–polyanion complexes*, Bioorg. Med. Chem. Lett. **16** (2006), 274–279.

[229] M. K. Braun, M. Wolf, O. Matsarskaia, S. Da Vela, F. Roosen-Runge, M. Sztucki, R. Roth, F. Zhang, and F. Schreiber, *Strong isotope effects on effective interactions and phase behavior in protein solutions in the presence of multivalent ions*, J. Phys. Chem. B **121** (2017), 1731–1739.

[230] J.-P. Hansen and J. B. Hayter, *A rescaled MSA structure factor for dilute charged colloidal dispersions*, Mol. Phys. **46** (1982), 651–656.

[231] J. B. Hayter and J. Penfold, *An analytic structure factor for macroion solutions*, Mol. Phys. **42** (1981), 109–118.

[232] F. Zhang, F. Roosen-Runge, M. W. A. Skoda, R. M. J. Jacobs, M. Wolf, P. Callow, H. Frielinghaus, V. Pipich, S. Prevost, and F. Schreiber, *Hydration and interactions in protein solutions containing concentrated electrolytes studied by small-angle scattering*, Phys. Chem. Chem. Phys. **14** (2012), 2483–2493.

[233] I. Reviakine, D. Johannsmann, and R. P. Richter, *Hearing what you cannot see and visualizing what you hear: interpreting quartz crystal microbalance data from solvated interfaces*, Anal. Chem. **83** (2011), 8838–8848.

[234] M. V. Voinova, M. Rodahl, M. Jonson, and B. Kasemo, *Viscoelastic acoustic response of layered polymer films at fluid-solid interfaces: continuum mechanics approach*, Phys. Scr. **59** (1999), 391.

[235] A. A. Feiler, A. Sahlholm, T. Sandberg, and K. D. Caldwell, *Adsorption and viscoelastic properties of fractionated mucin (BSM) and bovine serum albumin (BSA) studied with quartz crystal microbalance (QCM-D)*, J. Colloid Interface Sci. **315** (2007), 475–481.

[236] E. Rojas, M. Gallego, and I. Reviakine, *Effect of sample heterogeneity on the interpretation of quartz crystal microbalance data: impurity effects*, Anal. Chem. **80** (2008), 8982–8990.

[237] J.-P. Hansen and I. R. McDonald, *Theory of simple liquids*, 3rd ed., Academic Press Amsterdam, 2006.

[238] M. R. Fries, M. W. Skoda, N. F. Conzelmann, R. M. Jacobs, R. Maier, N. Scheffczyk, F. Zhang, and F. Schreiber, *Bulk phase behaviour vs interface adsorption: Effects of anions and isotopes on β-lactoglobulin (BLG) interactions*, J. Colloid Interface Sci. **598** (2021), 430–443.

[239] R. Kurrat, J. Prenosil, and J. Ramsden, *Kinetics of human and bovine serum albumin adsorption at silica–titania surfaces*, J. Colloid Interface Sci. **185** (1997), 1–8.

[240] S. von Bülow, M. Siggel, M. Linke, and G. Hummer, *Dynamic cluster formation determines viscosity and diffusion in dense protein solutions*, Proc. Nat. Acad. Sci. USA **116** (2019), 9843–9852.

[241] B. Jachimska, M. Wasilewska, and Z. Adamczyk, *Characterization of globular protein solutions by dynamic light scattering, electrophoretic mobility, and viscosity measurements*, Langmuir **24** (2008), 6866–6872.

[242] M. Dockal, D. C. Carter, and F. Rüker, *Conformational transitions of the three recombinant domains of human serum albumin depending on pH*, J. Biol. Chem. **275** (2000), 3042–3050.

[243] M. Dockal, D. C. Carter, and F. Rüker, *The three recombinant domains of human serum albumin: structural characterization and ligand binding properties*, J. Biol. Chem. **274** (1999), 29303–29310.

[244] K. Murayama and M. Tomida, *Heat-induced secondary structure and conformation change of bovine serum albumin investigated by Fourier transform infrared spectroscopy*, Biochemistry **43** (2004), 11526–11532.

[245] K. Schomäcker, D. Mocker, R. Münze, and G.-J. Beyer, *Stabilities of lanthanide-protein complexes*, Appl. Radiat. Isot. **39** (1988), 261–264.

[246] K. O. Ramberg, S. Engilberge, T. Skorek, and P. B. Crowley, *Facile fabrication of protein–macrocycle frameworks*, J. Am. Chem. Soc. **143** (2021), 1896–1907.

[247] E. Ohyoshi and S. Kohata, *The binding of Yb (III) and Gd (III) to bovin serum albumin by a competitive spectrophotometry*, J. Inorg. Biochem. **52** (1993), 157–163.

[248] F. Roosen-Runge, B. S. Heck, F. Zhang, O. Kohlbacher, and F. Schreiber, *Interplay of pH and binding of multivalent metal ions: Charge inversion and reentrant condensation in protein solutions*, J. Phys. Chem. B **117** (2013), 5777–5787.

[249] M. Blaber, X. J. Zhang, and B. W. Matthews, *Structural basis of amino acid alpha helix propensity*, Science **260** (1993), 1637–1640.

[250] S. Whitelam, *Control of pathways and yields of protein crystallization through the interplay of nonspecific and specific attractions*, Phys. Rev. Lett. **105** (2010), 088102.

[251] I. Staneva and D. Frenkel, *The role of non-specific interactions in a patchy model of protein crystallization*, J. Chem. Phys. **143** (2015), 194511.

[252] H. Rosenbach, J. Victor, J. Borggräfe, R. Biehl, G. Steger, M. Etzkorn, and I. Span, *Expanding crystallization tools for nucleic acid complexes using U1A protein variants*, J. Struct. Biol. **210** (2020), 107480.

[253] K. A. Majorek, P. J. Porebski, A. Dayal, M. D. Zimmerman, K. Jablonska, A. J. Stewart, M. Chruszcz, and W. Minor, *Structural and immunologic characterization of bovine, horse, and rabbit serum albumins*, Mol. Immunol. **52** (2012), 174–182.

[254] Q. Wang, C. Xue, Y. Qin, X. Zhang, Y. Li, et al., *The fabrication of protein microbubbles with diverse gas core and the novel exploration on the role of interface introduction in protein crystallization*, Colloids Surf. A Physicochem. Eng. Asp. **589** (2020), 124471.

[255] M. Rosseneu-Motreff, V. Blaton, B. Declercq, D. Vandamme, and H. Peeters, *Size and shape determination of native and detatted bovine serum albumin monomers: I. chemical characterization of lipids bound to native and defatted-bovine serum albumin monomers*, J. Biochem. **68** (1970), 369–377.

[256] S. Puhl, L. Meinel, and O. Germershaus, *Recent advances in crystalline and amorphous particulate protein formulations for controlled delivery*, Asian J. Pharm. Sci. **11** (2016), 469–477.

[257] R. Vaishya, V. Khurana, S. Patel, and A. K. Mitra, *Long-term delivery of protein therapeutics*, Expert Opin. Drug Deliv. **12** (2015), 415–440.

[258] M. Volmer and A. Weber, *Nucleus formation in supersaturated systems*, Z. Phys. Chem. **119** (1926), 277–301.

[259] D. Kashchiev, *Nucleation*, Butterworth-Heinemann, 2000.

[260] D. Gebauer and H. Cölfen, *Prenucleation clusters and non-classical nucleation*, Nano Today **6** (2011), 564–584.

[261] V. J. Anderson and H. N. W. Lekkerkerker, *Insights into phase transition kinetics from colloid science*, Nature **416** (2002), 811–815.

[262] R. Sear, *Nucleation at contact lines where fluid–fluid interfaces meet solid surfaces*, J. Phys.: Condens. Matter **19** (2007), 466106.

[263] D. Maes, M. A. Vorontsova, M. A. C. Potenza, T. Sanvito, M. Sleutel, M. Giglio, and P. G. Vekilov, *Do protein crystals nucleate within dense liquid clusters?*, Acta Cryst. F **F71** (2015), 815–822.

[264] J. L. Harland, S. I. Henderson, S. M. Underwood, and W. van Megen, *Observation of accelerated nucleation in dense colloidal fluids of hard sphere particles*, Phys. Rev. Lett. **75** (1995), 3572–3575.

[265] S. Martin, G. Bryant, and W. van Megen, *Crystallization kinetics of polydisperse colloidal hard spheres: Experimental evidence for local fractionation*, Phys. Rev. E **67** (2003), 061405.

[266] S. Martin, G. Bryant, and W. van Megen, *Crystallization kinetics of polydisperse colloidal hard spheres. II. Binary mixtures*, Phys. Rev. E **71** (2005), 021404.

[267] H. J. Schöpe, G. Bryant, and W. van Megen, *Two-step crystallization kinetics in colloidal hard-sphere systems*, Phys. Rev. Lett. **96** (2006), 175701.

[268] T. Schilling, H. J. Schöpe, M. Oettel, G. Opletal, and I. Snook, *Precursor-mediated crystallization process in suspensions of hard spheres*, Phys. Rev. Lett. **105** (2010), 025701.

[269] O. Galkin and P. G. Vekilov, *Control of protein crystal nucleation around the metastable liquid–liquid phase boundary*, Proc. Natl. Acad. Sci. USA **97** (2000), 6277–6281.

[270] D. Gebauer, A. Völkel, and H. Cölfen, *Stable prenucleation calcium carbonate clusters*, Science **322** (2008), 1819–1822.

[271] M. Sleutel, J. F. Lutsko, D. Maes, and A. E. S. Van Driessche, *Mesoscopic impurities expose a nucleation-limited regime of crystal growth*, Phys. Rev. Lett. **114** (2015), 245501.

[272] D. Gebauer and S. E. Wolf, *Designing solid materials from their solute state: a shift in paradigms toward a holistic approach in functional materials chemistry*, J. Am. Chem. Soc. **141** (2019), 4490–4504.

[273] D. Gebauer, M. Kellermeier, J. D. Gale, L. Bergström, and H. Cölfen, *Pre-nucleation clusters as solute precursors in crystallisation*, Chem. Soc. Rev. **43** (2014), 2348–2371.

[274] K. G. Soga, J. R. Melrose, and R. C. Ball, *Metastable states and the kinetics of colloid phase separation.*, J. Chem. Phys. **110** (1999), 2280–2289.

[275] F. Sebastiani, S. L. Wolf, B. Born, T. Q. Luong, H. Cölfen, D. Gebauer, and M. Havenith, *Water dynamics from thz spectroscopy reveal the locus of a liquid–liquid binodal limit in aqueous $CaCO_3$ solutions*, Angew. Chem. Int. Ed. **56** (2017), 490–495.

[276] F. Zhang, J. A. Gavira, G. W. Lee, and D. Zahn, *Nonclassical nucleation - role of metastable intermediate phase in crystal nucleation: An editorial prefix*, Crystals **11** (2021), 174.

[277] P. R. Ten Wolde, M. J. Ruiz-Montero, and D. Frenkel, *Numerical evidence for bcc ordering at the surface of a critical fcc nucleus*, Phys. Rev. Lett. **75** (1995), 2714.

[278] B. Ranguelov and C. Nanev, *2D monte carlo simulation of patchy particles association and protein crystal polymorph selection*, Crystals **9** (2019), 508.

[279] B. C. Park, J. Cho, M. S. Kim, M. J. Ko, L. Pan, J. Y. Na, and Y. K. Kim, *Strategy to control magnetic coercivity by elucidating crystallization pathway-dependent microstructural evolution of magnetite mesocrystals*, Nat. Commun. **11** (2020), 1–10.

[280] Y. Kezuka, K. Kawai, K. Eguchi, and M. Tajika, *Fabrication of single-crystalline calcite needle-like particles using the aragonite–calcite phase transition*, Minerals **7** (2017), 133.

[281] G. Mirabello, A. Ianiro, P. H. Bomans, T. Yoda, A. Arakaki, H. Friedrich, G. de With, and N. A. Sommerdijk, *Crystallization by particle attachment is a colloidal assembly process*, Nat. Mater. **19** (2020), 391–396.

[282] Y. Tidhar, H. Weissman, D. Tworowski, and B. Rybtchinski, *Mechanism of crystalline self-assembly in aqueous medium: a combined cryo-tem/kinetic study*, Chem. Eur. J. **20** (2014), 10332–10342.

[283] J. J. De Yoreo, P. U. P. A. Gilbert, N. A. J. M. Sommerdijk, R. L. Penn, S. Whitelam, D. Joester, H. Zhang, J. D. Rimer, A. Navrotsky, J. F. Banfield, A. F. Wallace, F. M. Michel, F. C. Meldrum, H. Cölfen, and P. M. Dove, *Crystallization by particle attachment in synthetic, biogenic, and geologic environments*, Science **349** (2015), aaa6760.

[284] H. Wu, Y. Yang, Y. Ou, B. Lu, J. Li, W. Yuan, Y. Wang, and Z. Zhang, *Early stage growth of rutile titania mesocrystals*, Cryst. Growth Des. **18** (2018), 4209–4214.

[285] M. Jehannin, A. Rao, and H. Cölfen, *New horizons of nonclassical crystallization*, J. Am. Chem. Soc. **141** (2019), 10120–10136.

[286] R. S. Lam, J. M. Charnock, A. Lennie, and F. C. Meldrum, *Synthesis-dependant structural variations in amorphous calcium carbonate*, CrystEngComm **9** (2007), 1226–1236.

[287] E. Wiedenbeck, M. Kovermann, D. Gebauer, and H. Cölfen, *Liquid metastable precursors of ibuprofen as aqueous nucleation intermediates*, Angew. Chem. Int. Ed. **58** (2019), 19103–19109.

[288] Y. Lu, X. Lu, Z. Qin, and J. Shen, *Experimental evidence for ordered precursor foreshadowing crystal nucleation in colloidal system*, Solid State Commun. **217** (2015), 13–16.

[289] Y. Tsarfati, S. Rosenne, H. Weissman, L. J. Shimon, D. Gur, B. A. Palmer, and B. Rybtchinski, *Crystallization of organic molecules: Nonclassical mechanism revealed by direct imaging*, ACS Cent. Sci. **4** (2018), 1031–1036.

[290] D. Soraruf, F. Roosen-Runge, M. Grimaldo, F. Zanini, R. Schweins, T. Seydel, F. Zhang, R. Roth, M. Oettel, and F. Schreiber, *Protein cluster formation in aqueous solution in the presence of multivalent metal ions - a light scattering study*, Soft Matter **10** (2014), 894–902.

[291] C. Haas and J. Drenth, *Understanding protein crystallization on the basis of the phase diagram*, J. Cryst. Growth **196** (1999), 388–394.

[292] C. Beck, M. Grimaldo, F. Roosen-Runge, R. Maier, O. Matsarskaia, M. Braun, B. Sohmen, O. Czakkel, R. Schweins, F. Zhang, T. Seydel, and F. Schreiber, *Following protein dynamics in real time during crystallization*, Cryst. Growth Des. **19** (2019), 7036–7045.

[293] Z. Ou, Z. Wang, B. Luo, E. Luijten, and Q. Chen, *Kinetic pathways of crystallization at the nanoscale*, Nat. Mater. **19** (2020), 450–455.

[294] A. Krçżel and W. Bal, *A formula for correlating pK_a values determined in D_2O and H_2O*, J. Inorg. Biochem. **98** (2004), 161–166.

[295] A. K. Covington, M. Paabo, R. A. Robinson, and R. G. Bates, *Use of the glass electrode in deuterium oxide and the relation between the standardized pD (pa_D) scale and the operational pH in heavy water*, Anal. Chem. **40** (1968), 700–706.

[296] U. M. Elofsson, M. A. Paulsson, and T. Arnebrant, *Adsorption of β-lactoglobulin A and B in relation to self-association: Effect of concentration and pH*, Langmuir **13** (1997), 1695–1700.

[297] D. Richard, M. Ferrand, and G. J. Kearley, *Analysis and visualisation of neutron-scattering data*, J. Neutron Res. **4** (1996), 33–39.

[298] F. Zhang, S. Da Vela, M. Feustel, M. Grimaldo, O. Matsarskaia, F. Roosen-Runge, F. Schreiber, R. Schweins, T. Seydel, and B. Sohmen, *Kinetics of two-step nucleation in protein crystallization studied by real-time SANS*, http://dx.doi.org/10.5291/ILL-DATA.9-13-620, 2015, Institut Laue-Langevin (ILL) doi:10.5291/ILL-DATA.9-13-620.

[299] S. Trakhanov and F. A. Quiocho, *Influence of divalent cations in protein crystallization*, Protein Sci. **4** (1995), 1914–1919.

[300] S. Trakhanov, D. I. Kreimer, S. Parkin, G. F.-L. Ames, and B. Rupp, *Cadmium-induced crystallization of proteins: II. Crystallization of the salmonella typhimurium histidine-binding protein in complex with L-histidine, L-arginine, or L-lysine*, Protein Sci. **7** (1998), 600–604.

[301] M. Verheul, J. S. Pedersen, S. P. F. M. Roefs, and K. G. de Kruif, *Association behavior of native β-lactoglobulin*, Biopolymers **49** (1999), 11–20.

[302] G. Strobl, *Concepts for understanding their structures and behavior*, ch. 5, Springer, third ed., 2007.

[303] A. E. Flood, *Feedback between crystal growth rates and surface roughness*, CrystEngComm **12** (2010), 313–323.

[304] A. Sauter, F. Zhang, N. K. Szekely, V. Pipich, M. Sztucki, and F. Schreiber, *Structural evolution of metastable protein aggregates in the presence of trivalent salt studied by (V)SANS and SAXS*, J. Phys. Chem. B **120** (2016), 5564–5571.

[305] S. K. Sinha, S. Chakraborty, and S. Bandyopadhyay, *Thickness of the hydration layer of a protein from molecular dynamics simulation*, J. Phys. Chem. B **112** (2008), 8203–8209.

[306] S. Bandyopadhyay, S. Chakraborty, S. Balasubramanian, S. Pal, and B. Bagchi, *Atomistic simulation study of the coupled motion of amino acid residues and water molecules around protein HP-36: fluctuations at and around the active sites*, J. Phys. Chem. B **108** (2004), 12608–12616.

[307] F. Merzel and J. C. Smith, *Is the first hydration shell of lysozyme of higher density than bulk water?*, Proc. Natl. Acad. Sci. USA **99** (2002), 5378–5383.

[308] B. Bagchi, *Water dynamics in the hydration layer around proteins and micelles*, Chem. Rev. **105** (2005), 3197–3219.

[309] I. Avramov, R. Keding, C. Rüssel, and R. Kranold, *Precipitate particle size distribution in rigid and floppy networks*, J. Non-Cryst. Solids **278** (2000), 13–18.

[310] M. E. McKenzie, B. Deng, D. Van Hoesen, X. Xia, D. E. Baker, A. Rezikyan, R. E. Youngman, and K. Kelton, *Nucleation pathways in barium silicate glasses*, Sci. Rep. **11** (2021), 1–15.

[311] D. Sehnal, S. Bittrich, M. Deshpande, R. Svobodová, K. Berka, V. Bazgier, S. Velankar, S. K. Burley, J. Koča, and A. S. Rose, *Mol* viewer: modern web app for 3d visualization and analysis of large biomolecular structures*, Nucleic Acids Res. **49** (2021), W431–W437.

[312] G. C. Terstappen and A. Reggiani, *In silico research in drug discovery*, Trends Pharmacol. Sci. **22** (2001), 23–26.

[313] A. M. Seddon, P. Curnow, and P. J. Booth, *Membrane proteins, lipids and detergents: not just a soap opera*, Biochim. Biophys. Acta - Biomembr. **1666** (2004), 105–117.

[314] J. Borch and T. Hamann, *The nanodisc: a novel tool for membrane protein studies*, Biol. Chem. **390** (2009), 805–814.

[315] C. R. Morgan, C. M. Hebling, K. D. Rand, D. W. Stafford, J. W. Jorgenson, and J. R. Engen, *Conformational transitions in the membrane scaffold protein of phospholipid bilayer nanodiscs*, Mol. Cell. Proteom. **10** (2011), 10.1074/mcp.M111.010876.

[316] T. Ravula, N. Z. Hardin, and A. Ramamoorthy, *Polymer nanodiscs: Advantages and limitations*, Chem. Phys. Lipids **219** (2019), 45–49.

[317] M. Orwick-Rydmark, J. E. Lovett, A. Graziadei, L. Lindholm, M. R. Hicks, and A. Watts, *Detergent-free incorporation of a seven-transmembrane receptor protein into nanosized bilayer lipodisq particles for functional and biophysical studies*, Nano Lett. **12** (2012), 4687–4692.

[318] J. Thoma and B. M. Burmann, *Fake it 'till you make it—the pursuit of suitable membrane mimetics for membrane protein biophysics*, Int. J. Mol. Sci. **22** (2021), 50.

[319] R. Adão, P. F. Cruz, D. C. Vaz, F. Fonseca, J. N. Pedersen, F. Ferreira-da Silva, R. M. Brito, C. H. Ramos, D. Otzen, S. Keller, and M. Bastos, *DIBMA nanodiscs keep α-synuclein folded*, Biochim. Biophys. Acta - Biomembr. **1862** (2020), 183314.

[320] A. Grethen, A. O. Oluwole, B. Danielczak, C. Vargas, and S. Keller, *Thermodynamics of nanodisc formation mediated by styrene/maleic acid (2:1) copolymer*, Sci. Rep. **7** (2017), 1–14.

[321] A. O. Oluwole, J. Klingler, B. Danielczak, J. O. Babalola, C. Vargas, G. Pabst, and S. Keller, *Formation of lipid-bilayer nanodiscs by diisobutylene/maleic acid (DIBMA) copolymer*, Langmuir **33** (2017), 14378–14388.

[322] S. C. Hall, C. Tognoloni, G. J. Price, B. Klumperman, K. J. Edler, T. R. Dafforn, and T. Arnold, *Influence of poly (styrene-co-maleic acid) copolymer structure on the properties and self-assembly of SMALP nanodiscs*, Biomacromolecules **19** (2017), 761–772.

[323] M. Jamshad, V. Grimard, I. Idini, T. J. Knowles, M. R. Dowle, N. Schofield, P. Sridhar, Y. Lin, R. Finka, M. Wheatley, et al., *Structural analysis of a nanoparticle containing a lipid bilayer used for detergent-free extraction of membrane proteins*, Nano Res. **8** (2015), 774–789.

[324] R. Zhang, I. D. Sahu, L. Liu, A. Osatuke, R. G. Comer, C. Dabney-Smith, and G. A. Lorigan, *Characterizing the structure of lipodisq nanoparticles for membrane protein spectroscopic studies*, Biochim. Biophys. Acta - Biomembr. **1848** (2015), 329–333.

[325] V. A. Bjørnestad, M. Orwick-Rydmark, and R. Lund, *Understanding the structural pathways for lipid nanodisc formation: How styrene maleic acid copolymers induce membrane fracture and disc formation*, Langmuir **37** (2021), 6178–6188.

[326] M. Xue, L. Cheng, I. Faustino, W. Guo, and S. J. Marrink, *Molecular mechanism of lipid nanodisk formation by styrene-maleic acid copolymers*, Biophys. J. **115** (2018), 494–502.

[327] S. C. Lee, T. J. Knowles, V. L. Postis, M. Jamshad, R. A. Parslow, Y.-P. Lin, A. Goldman, P. Sridhar, M. Overduin, S. P. Muench, and T. R. Dafforn, *A method for detergent-free isolation of membrane proteins in their local lipid environment*, Nat. Protoc. **11** (2016), 1149–1162.

[328] D. Svergun, *Determination of the regularization parameter in indirect-transform methods using perceptual criteria*, J. Appl. Crystallogr. **25** (1992), 495–503.

[329] D. E. Koppel, *Analysis of macromolecular polydispersity in intensity correlation spectroscopy: the method of cumulants*, J. Chem. Phys. **57** (1972), 4814–4820.

[330] C. Vargas, R. C. Arenas, E. Frotscher, and S. Keller, *Nanoparticle self-assembly in mixtures of phospholipids with styrene/maleic acid copolymers or fluorinated surfactants*, Nanoscale **7** (2015), 20685–20696.

[331] R. C. Arenas, J. Klingler, C. Vargas, and S. Keller, *Influence of lipid bilayer properties on nanodisc formation mediated by styrene/maleic acid copolymers*, Nanoscale **8** (2016), 15016–15026.

[332] P. Atkins and J. de Paula, *Physical Chemistry*, 8th ed., Oxford University Press, Oxford, 2006.

[333] W. Winter, *Measurement of suspended particles by quasi-elastic light scattering*, J. Polym. Sci. Polym. Lett. Ed. **21** (1983), 1020–1020.

[334] N. Skar-Gislinge, J. B. Simonsen, K. Mortensen, R. Feidenhans'l, S. G. Sligar, B. Lindberg Møller, T. Bjørnholm, and L. Arleth, *Elliptical structure of phospholipid bilayer nanodiscs encapsulated by scaffold proteins: casting the roles of the lipids and the protein*, J. Am. Chem. Soc. **132** (2010), 13713–13722.

[335] N. Skar-Gislinge and L. Arleth, *Small-angle scattering from phospholipid nanodiscs: derivation and refinement of a molecular constrained analytical model form factor*, Phys. Chem. Chem. Phys. **13** (2011), 3161–3170.

[336] N. Skar-Gislinge, N. T. Johansen, R. Høiberg-Nielsen, and L. Arleth, *Comprehensive study of the self-assembly of phospholipid nanodiscs: what determines their shape and stoichiometry?*, Langmuir **34** (2018), 12569–12582.

[337] D. Atkinson, H. M. Smith, J. Dickson, and J. P. Austin, *Interaction of apoprotein from porcine high-density lipoprotein with dimyristoyl lecithin: 1. the structure of the complexes*, Eur. J. Biochem. **64** (1976), 541–547.

[338] I. G. Denisov, M. A. McLean, A. W. Shaw, Y. V. Grinkova, and S. G. Sligar, *Thermotropic phase transition in soluble nanoscale lipid bilayers*, J. Phys. Chem. B **109** (2005), 15580–15588.

[339] M. Zhang, M. Gui, Z.-F. Wang, C. Gorgulla, J. Y. James, H. Wu, J. S. Zhen-yu, C. Klenk, L. Merklinger, L. Morstein, F. Hagn, A. Plückthun, A. Brown, M. L. Nasr, and G. Wagner, *Cryo-EM structure of an activated GPCR–G protein complex in lipid nanodiscs*, Nat. Struct. Mol. Biol. **28** (2021), 258–267.

[340] J. S. Pedersen, *Determination of size distribution from small-angle scattering data for systems with effective hard-sphere interactions*, J. Appl. Cryst. **27** (1994), 595–608.

[341] D. Svergun, C. Barberato, and M. H. J. Koch, *CRYSOL – a program to evaluate X-ray solution scattering of biological macromolecules from atomic coordinates*, J. Appl. Cryst. **28** (1995), 768–773.

[342] N. E. Good, G. D. Winget, W. Winter, T. N. Connolly, S. Izawa, and R. M. Singh, *Hydrogen ion buffers for biological research*, Biochemistry **5** (1966), 467–477.

[343] S. Tristram-Nagle, Y. Liu, J. Legleiter, and J. F. Nagle, *Structure of gel phase DMPC determined by X-ray diffraction*, Biophys. J. **83** (2002), 3324–3335.

[344] J. Pencer, M.-P. Nieh, T. A. Harroun, S. Krueger, C. Adams, and J. Katsaras, *Bilayer thickness and thermal response of dimyristoylphosphatidylcholine unilamellar vesicles containing cholesterol, ergosterol and lanosterol: a small-angle neutron scattering study*, Biochim. Biophys. Acta - Biomembr. **1720** (2005), 84–91.

[345] B. D. Harding, G. Dixit, K. M. Burridge, I. D. Sahu, C. Dabney-Smith, R. E. Edelmann, D. Konkolewicz, and G. A. Lorigan, *Characterizing the structure of styrene-maleic acid copolymer-lipid nanoparticles (SMALPs) using RAFT polymerization for membrane protein spectroscopic studies*, Chem. Phys. Lipids **218** (2019), 65–72.

[346] A. P. Bali, I. D. Sahu, A. F. Craig, E. E. Clark, K. M. Burridge, M. T. Dolan, C. Dabney-Smith, D. Konkolewicz, and G. A. Lorigan, *Structural characterization of styrene-maleic acid copolymer-lipid nanoparticles (SMALPs) using EPR spectroscopy*, Chem. Phys. Lipids **220** (2019), 6–13.

[347] M. C. Orwick, P. J. Judge, J. Procek, L. Lindholm, A. Graziadei, A. Engel, G. Gröbner, and A. Watts, *Detergent-free formation and physicochemical characterization of nanosized lipid–polymer complexes: Lipodisq*, Angew. Chemie Int. Ed. **51** (2012), 4653–4657.

[348] L. M. R. Hernandez and I. Levental, *Comparing lipid packing between nanodiscs and native membranes*, Biophys. J. **121** (2022), 485a.

[349] S. Jeon, T. Heo, S.-Y. Hwang, J. Ciston, K. C. Bustillo, B. W. Reed, J. Ham, S. Kang, S. Kim, J. Lim, K. Lim, J. S. Kim, M.-H. Kang, R. S. Bloom, S. Hong, K. Kim, A. Zettl, W. Y. Kim, P. Ercius, J. Park, and W. C. Lee, *Reversible disorder-order transitions in atomic crystal nucleation*, Science **371** (2021), 498–503.

[350] H. Sumi, N. Ohta, H. Sekiguchi, S. Harada, T. Ujihara, K. Tsukamoto, and M. Tagawa, *Two-step nanoparticle crystallization via dna-guided self-assembly and the nonequilibrium dehydration process*, Cryst. Growth Des. **21** (2021), 4506–4515.

[351] M. Kapuscinski, M. Agthe, and L. Bergström, *Time-resolved viscoelastic properties of self-assembling iron oxide nanocube superlattices probed by quartz crystal microbalance with dissipation monitoring*, J. Colloid Interface Sci. **522** (2018), 104–110.

[352] C. N. Nanev, I. Dimitrov, and D. Tsekova, *Adhesion of protein crystals: Measurement of the detachment force*, Crystal Research and Technology: Journal of Experimental and Industrial Crystallography **41** (2006), 505–509.

[353] D. Tsekova, S. Dimitrova, and C. N. Nanev, *Heterogeneous nucleation (and adhesion) of lysozyme crystals*, J. Cryst. Growth **196** (1999), 226–233.

[354] C. N. Nanev, F. V. Hodzhaoglu, and I. L. Dimitrov, *Kinetics of insulin crystal nucleation, energy barrier, and nucleus size*, Cryst. Growth Des. **11** (2011), 196–202.

[355] S. Rudiuk, L. Cohen-Tannoudji, S. Huille, and C. Tribet, *Importance of the dynamics of adsorption and of a transient interfacial stress on the formation of aggregates of IgG antibodies*, Soft Matter **8** (2012), 2651–2661.

[356] C. N. Nanev, E. Saridakis, L. Govada, S. C. Kassen, H. V. Solomon, and N. E. Chayen, *Hydrophobic interface-assisted protein crystallization: Theory and experiment*, ACS Appl. Mater. Interfaces **11** (2019), 12931–12940.

[357] J. V. Parambil, S. K. Poornachary, J. Y. Heng, and R. B. Tan, *Template-induced nucleation for controlling crystal polymorphism: from molecular mechanisms to applications in pharmaceutical processing*, CrystEngComm **21** (2019), 4122–4135.

Appendix A

Supporting information: Protein crystallization in the presence of a metastable liquid-liquid phase separation

Table A.1: *Data collection and refinement statistics.*

	HSA:Yttrium (2mM)
Data collection statistics	
Resolution [Å]	40 - 2.75 (2.82 - 2.75)
Space group	$P2_12_12_1$
Unit cell [Å]	$a = 55.27$, $b = 71.93$, $c = 180.13$
No. of unique reflections	35814 (2442)
R_{meas} [%]	13.0 (183.0)
$CC(1/2)$	99.9 (64.1)
Completeness [%]	99.5 (93.8)
Multiplicity	16.1 (11.1)
$I/\sigma(I)$	16.8 (1.6)
Wilson B-factor [Å^2]	75.7
Refinement statistics	
R_{work} / R_{free} [%]	24.7 / 29.6
rmsd bond length	0.020
rmsd bond angle	1.20
Ramachandran angles	
Favored [%]	93.9
Outliers [%]	1.0

Values for the highest resolution shell are given in parentheses

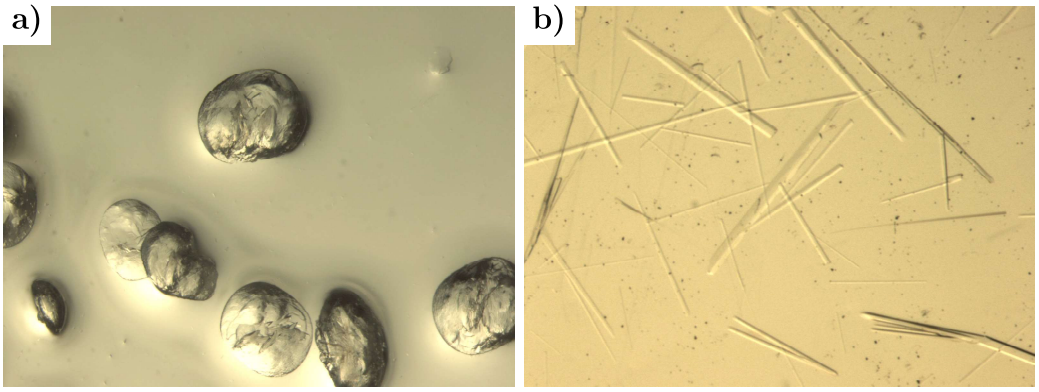


Figure A.1: *Crystal morphology of HSA crystals with YCl_3 grown at different conditions in the experimental phase diagram several days after preparation. a) Crystallization near the LLPS boundary (50 mg/ml HSA with 4 mM YCl_3), b) crystallization slightly below c^* (50 mg/ml HSA with 2 mM YCl_3).*

Table A.2: *Parameters for the logistic function (Eq. 1, main text) fitted to the integrated intensities measured by SANS/SAXS.*

sample	A	k [h^{-1}]	t_1 [h]
20 mg/ml HSA with 2 mM $CeCl_3$ in H_2O (Fig. 4.4 b)			
Bragg peak	0.97	0.41	15.59
Overall material	0.99	−0.48	16.04
10 mg/ml HSA with 2 mM $CeCl_3$ in D_2O (Fig. 4.7 b)			
Bragg peak	0.93	0.27	61.48
Overall material	0.97	−0.14	62.27
50 mg/ml HSA with 3.5 mM $CeCl_3$ in D_2O (Fig. A.3 b)			
Bragg peak	0.91	0.31	32.86
Overall material	0.89	−0.27	28.64

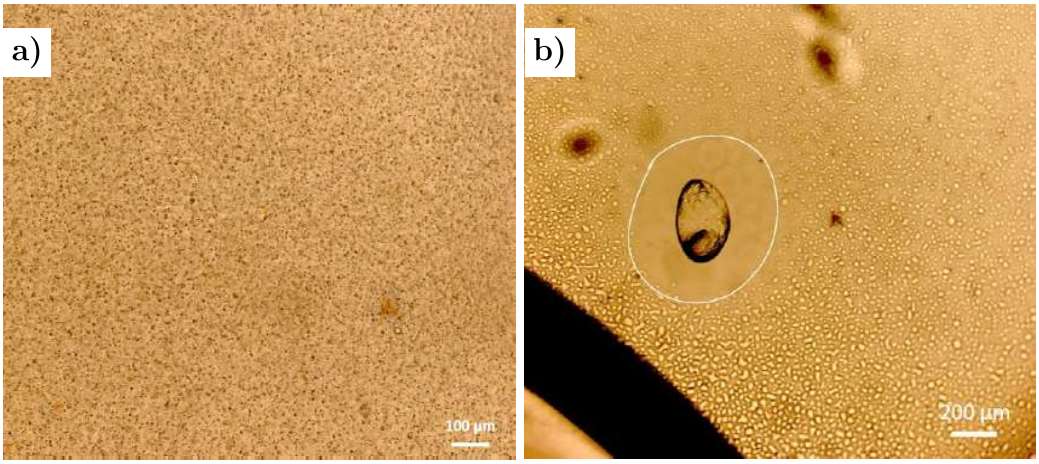


Figure A.2: *Crystal growth from unstable LLPS. The sample contains 20 mg/ml HSA and 1.5 mM $CeCl_3$ in H_2O. a) Formation of dense wetting layer via deposition of tiny droplets formed after mixing, b) crystals form and grow at the solid surface and a depletion zone is visible due to consumption of protein in the dense wetting layer several days after preparation.*

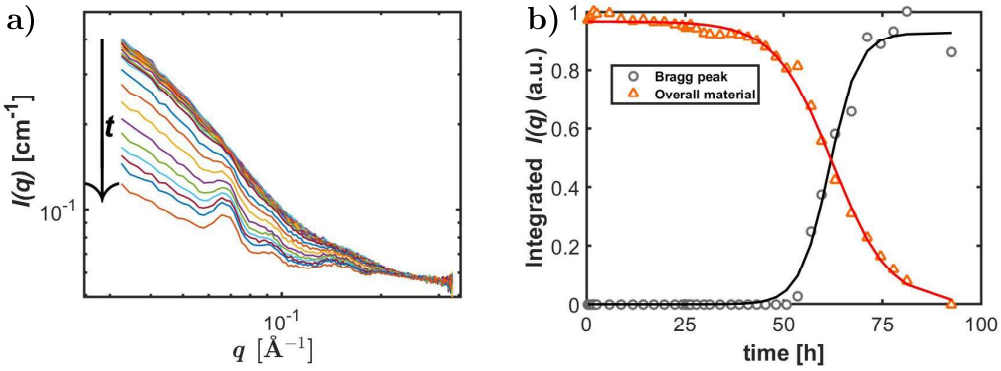


Figure A.3: *Another example of crystal growth outside of the LLPS binodal, but in regime II. a) SANS data for a sample containing 10 mg/ml HSA and 2 mM $CeCl_3$ in D_2O. Scattering intensity is shown as a function of q. b) Kinetics analysis based on the integrated area covered by Bragg peak at $q = 0.07\,Å^{-1}$ and the low q-intensity between 0.03 and 0.06 $Å^{-1}$. The solid lines represent the corresponding fits (Eq. 1).*

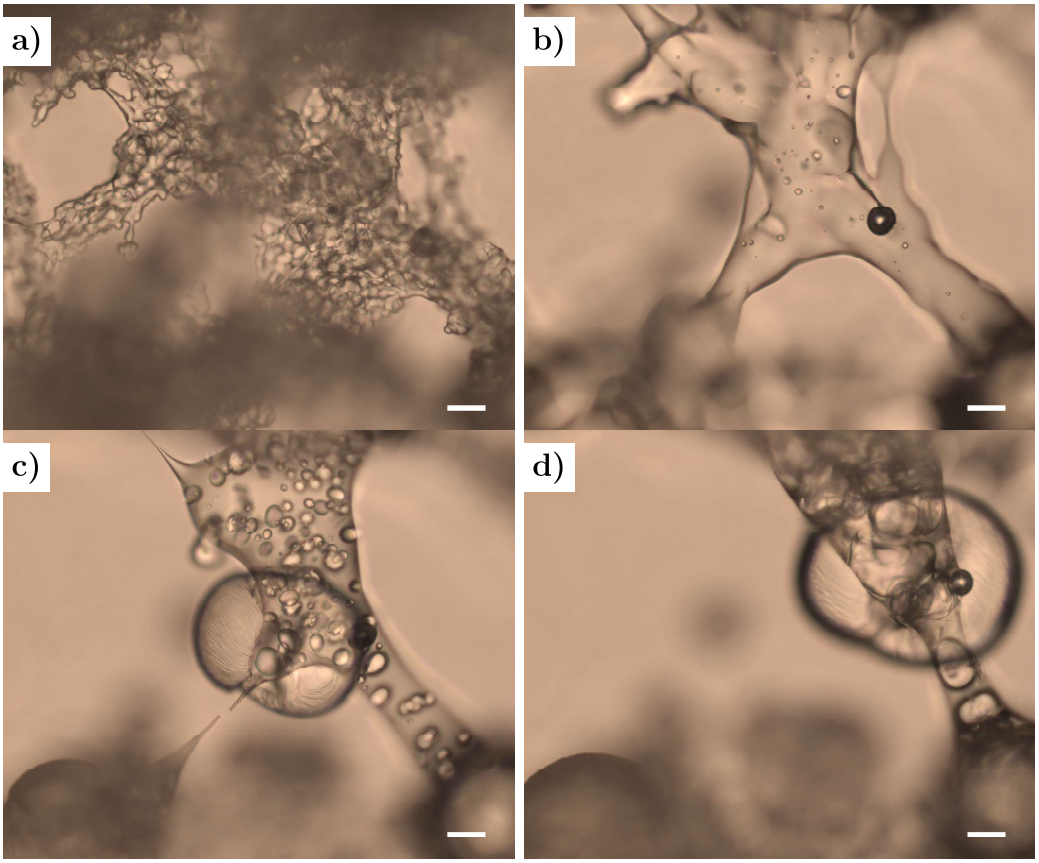


Figure A.4: *Crystal growth in D_2O of a sample containing 50 mg/ml HSA with 3.5 mM $CeCl_3$ at different times after sample preparation: a) 2.15 h; b) 12.5 h; c) 1 day; d) 2 days. The increased interprotein attractions in D_2O lead to a network structure of the dense phase compared to the dense droplets in H_2O. The scale bar corresponds to 50 µm.*

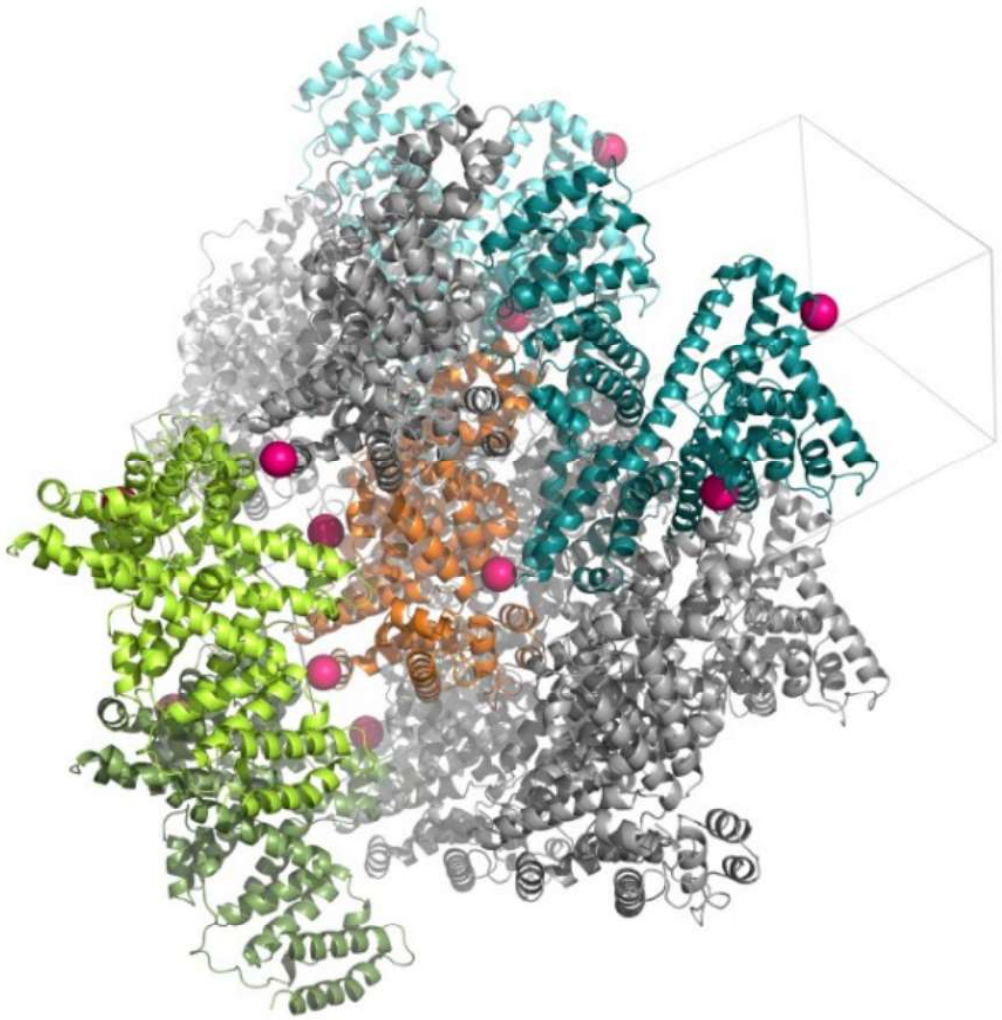


Figure A.5: *Crystal structure of HSA crystallized in the presence of yttrium ions. The representation shows that each HSA protomer is in contact to ten symmetry-related protomers. All protomers which contact the central protomer (orange) by metal (pink) coordination are colored (green, blue). Protomers interacting exclusively by protein-protein interactions are colored grey.*

Appendix B

Supporting information: Human versus bovine serum albumin: A subtle difference in hydrophobicity leads to large differences in bulk and interface behavior



Figure B.1: *Dilution series of BSA with $CeCl_3$. The glass vials contain samples with c(BSA) = 150 mg/ml and the $CeCl_3$ concentration as labeled on the vials. Macroscopic LLPS is visible for the samples in the middle (1.2-25 mM $CeCl_3$).*

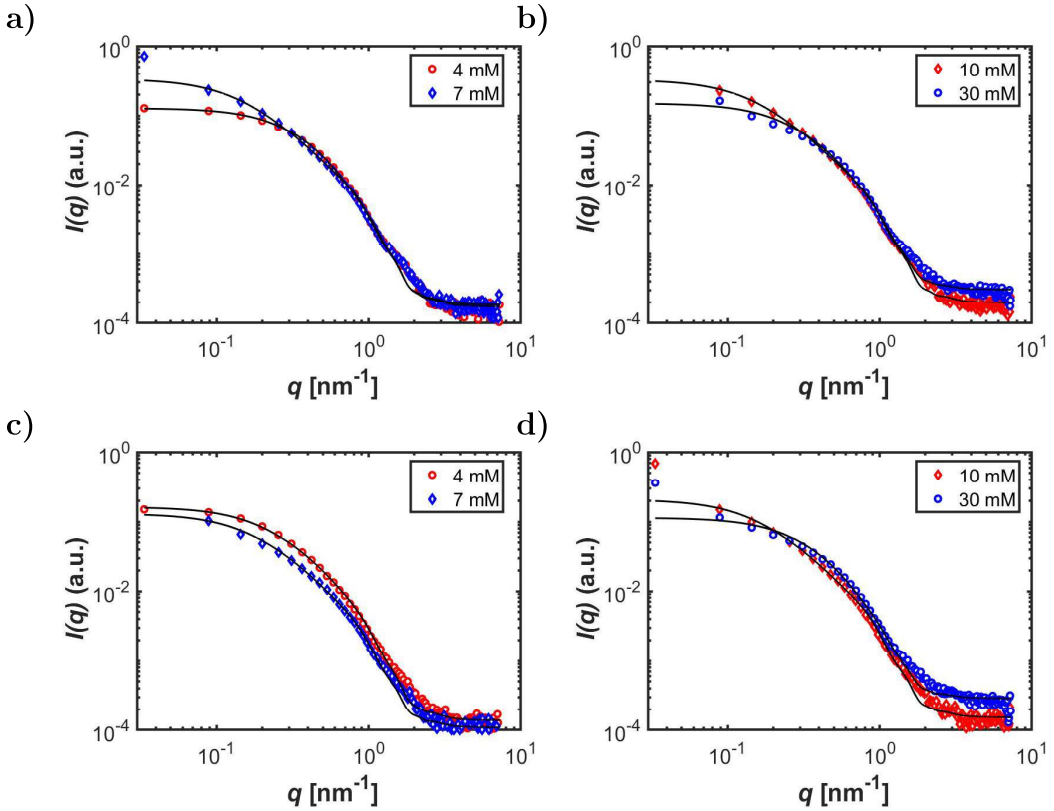


Figure B.2: *Raw SAXS intensity data (symbols) and SHS fits (lines) of samples containing a,b) 50 mg/ml BSA and c,d) 50 mg/ml HSA and varying $CeCl_3$ concentrations. For better visualization, only every 20th data point is plotted and for each protein system, four representative c_s are selected, i.e., three in regime II and one in regime III. The raw data can be found in Fig. 3. Fitting parameters can be found in the Materials and methods section in the main text.*

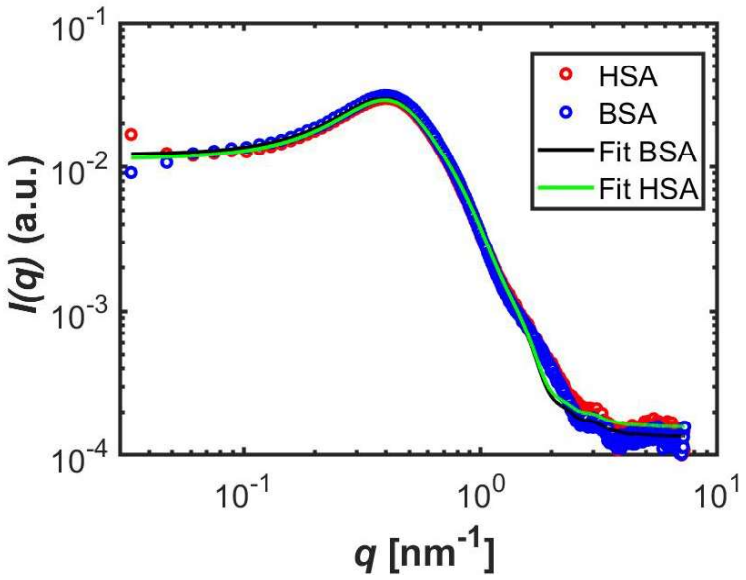


Figure B.3: *Raw SAXS intensity data (symbols) and corresponding SC fits (lines) of 50 mg/ml BSA (blue and black) and 50 mg/ml HSA (red and green) with 1 mM $CeCl_3$. For better visualization, only every 5th data point is shown. Fitting parameters can be found in the Materials and methods section in the main text.*

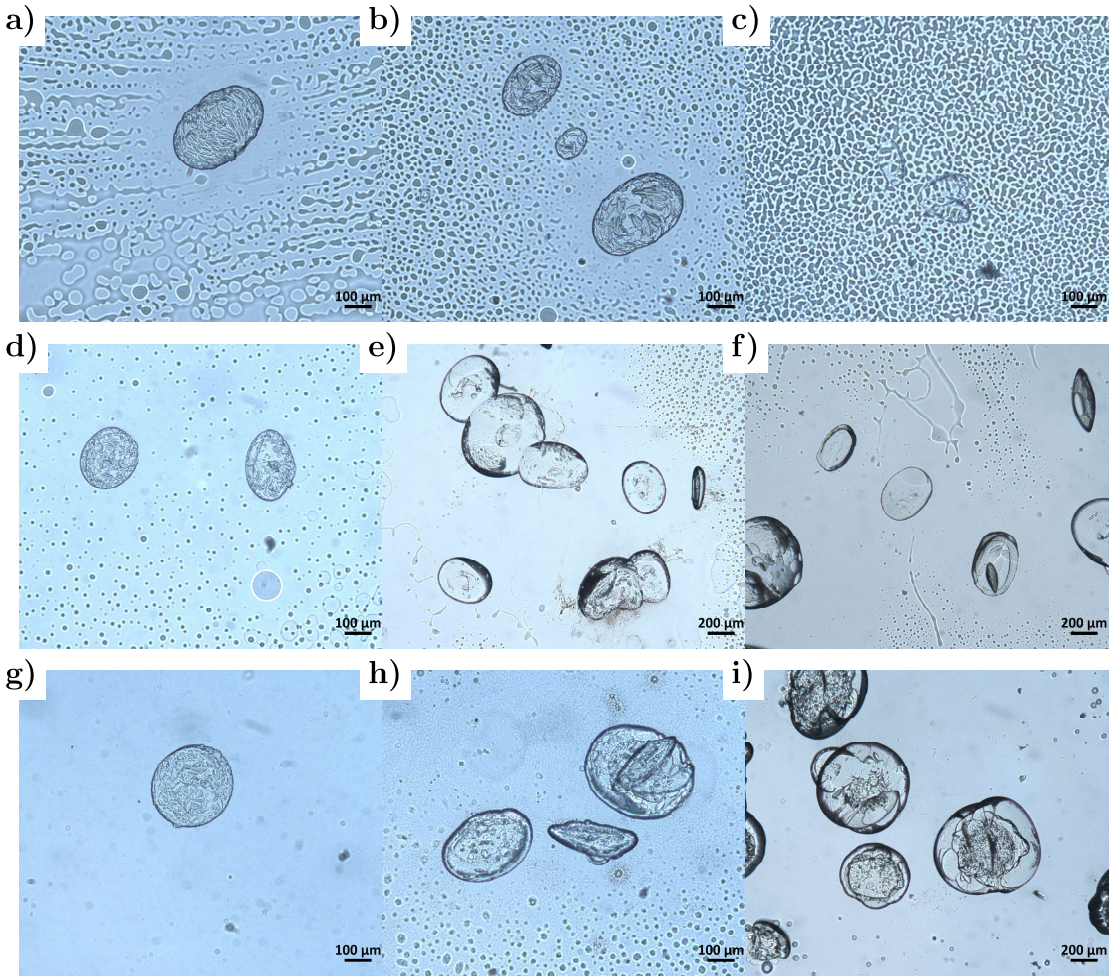


Figure B.4: *Microscopy images of different HSA-$CeCl_3$ crystals 14 days after sample preparation. a) 20 mg/ml HSA with 2.5 mM $CeCl_3$, b) 20 mg/ml HSA with 3 mM $CeCl_3$, c) 20 mg/ml HSA with 4 mM $CeCl_3$; d) 50 mg/ml HSA with 3.5 mM $CeCl_3$, e) 50 mg/ml HSA with 5 mM $CeCl_3$, f) 50 mg/ml HSA with 6 mM $CeCl_3$; g) 80 mg/ml HSA with 4.5 mM $CeCl_3$, h) 80 mg/ml HSA with 6 mM $CeCl_3$, and i) h) 80 mg/ml HSA with 7 mM $CeCl_3$.*

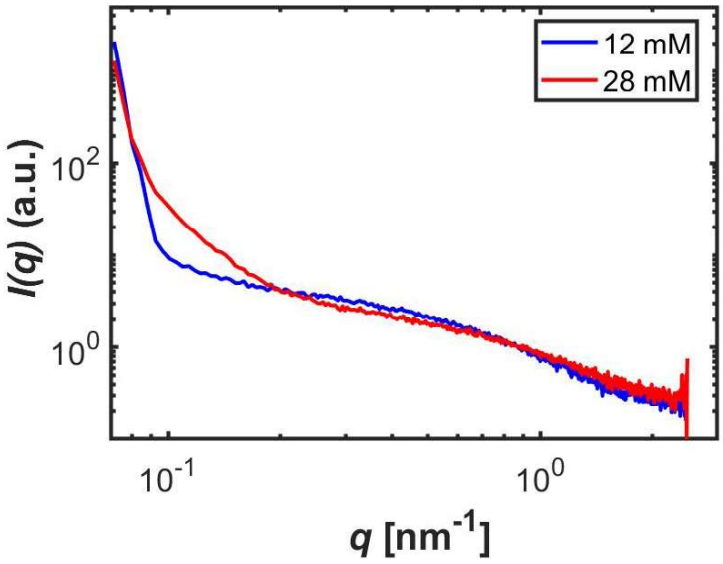


Figure B.5: *SAXS intensity curves of samples containing 20 mg/ml BSA and 12 mM LaI_3 (blue) and 28 mM LaI_3 (red). The curves were recorded a week after sample preparation. No Bragg peaks are visible, which would indicate the presence of crystals.*

Appendix C

Supporting information: Protein crystallization from a preordered metastable intermediate phase followed by real-time small-angle neutron scattering

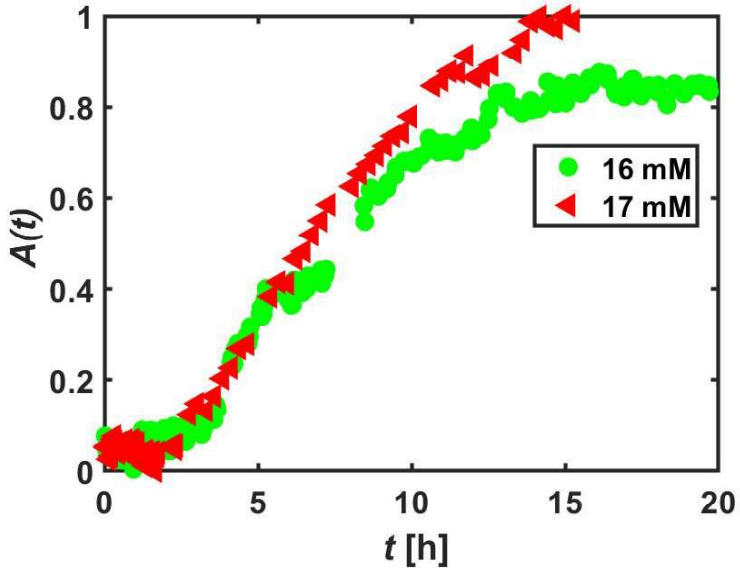


Figure C.1: *Summed intensities $A(t)$ of the Bragg peak feature at $q \approx 0.2\,\text{Å}^{-1}$ as function of time. After subtracting a linear background between $q_1 = 0.176\text{Å}^{-1}$ and $q_2 = 0.217\text{Å}^{-1}$, the scattering intensities within this interval were summed up to obtain $A(t)$. This analysis was performed for samples containing 30 mg/ml BLG with 16 mM (green circles) and 17 mM (red triangles) $CdCl_2$ in D_2O.*

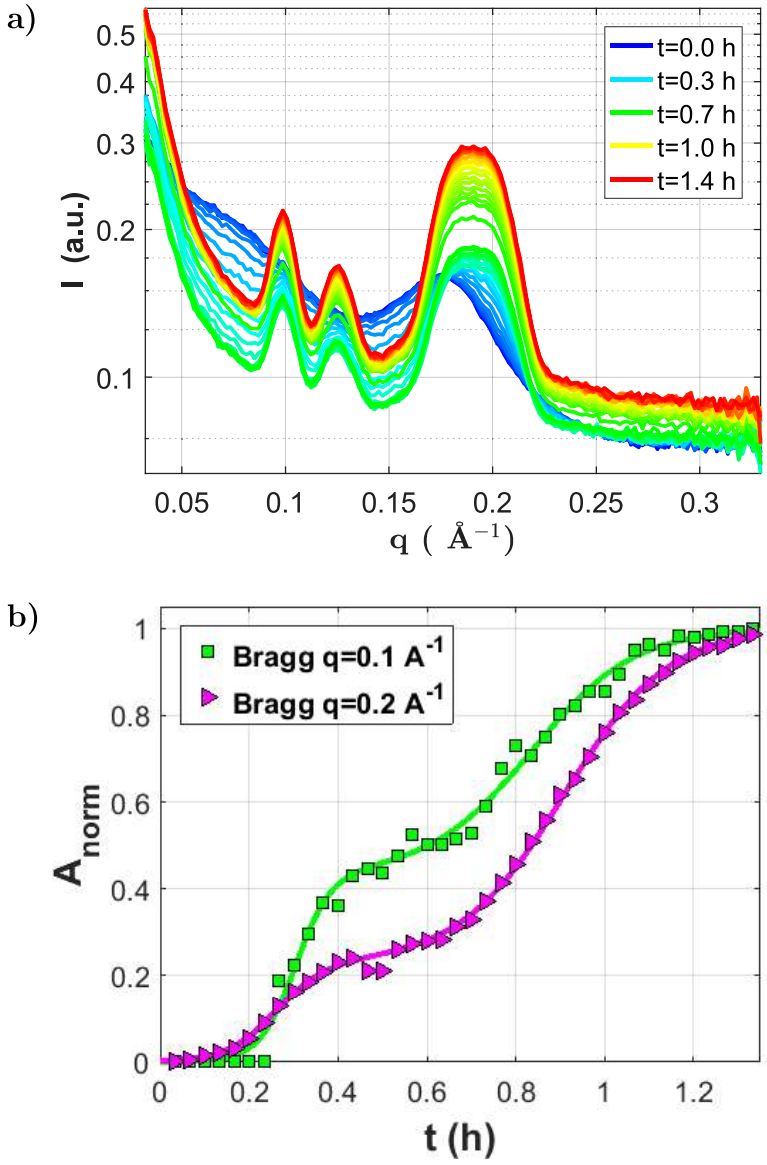


Figure C.2: *Real-time SANS follows the crystal growth of a sample containing 33 mg BLG with 17 mM $CdCl_2$. Crystallization is fast and completed within 2 h. Kinetics analysis shows a clear two-step growth.*

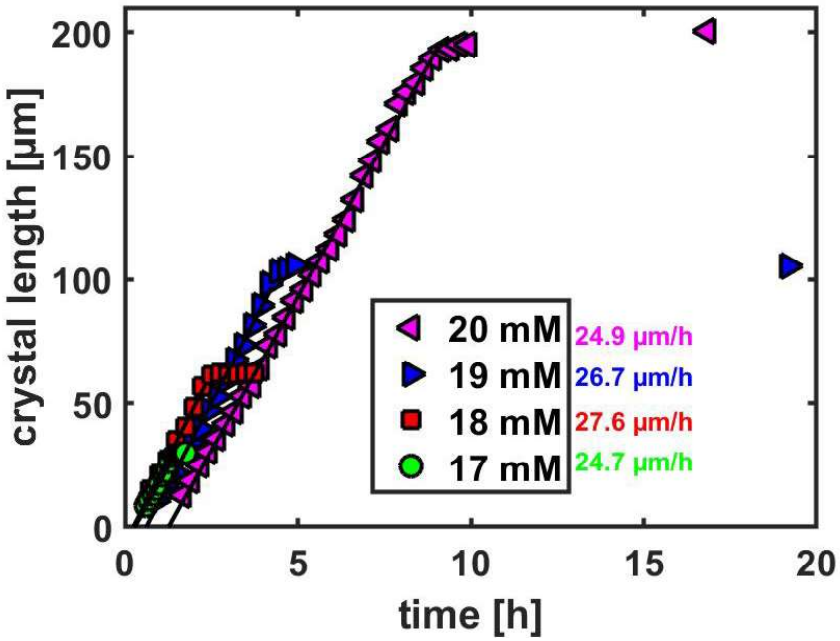


Figure C.3: *Crystal length as function of time of samples containing 33 mg/ml BLG with 17-20 mM $CdCl_2$ in H_2O. For the 19 and 20 mM samples it was ensured with the last image of the respective series that no second growth step occurred. The respective growth rates are implemented in the figure. The corresponding microscopy data were already published in Ref. 45.*

Appendix D

Supporting information: Structural insights into polymer-bounded lipid nanodiscs

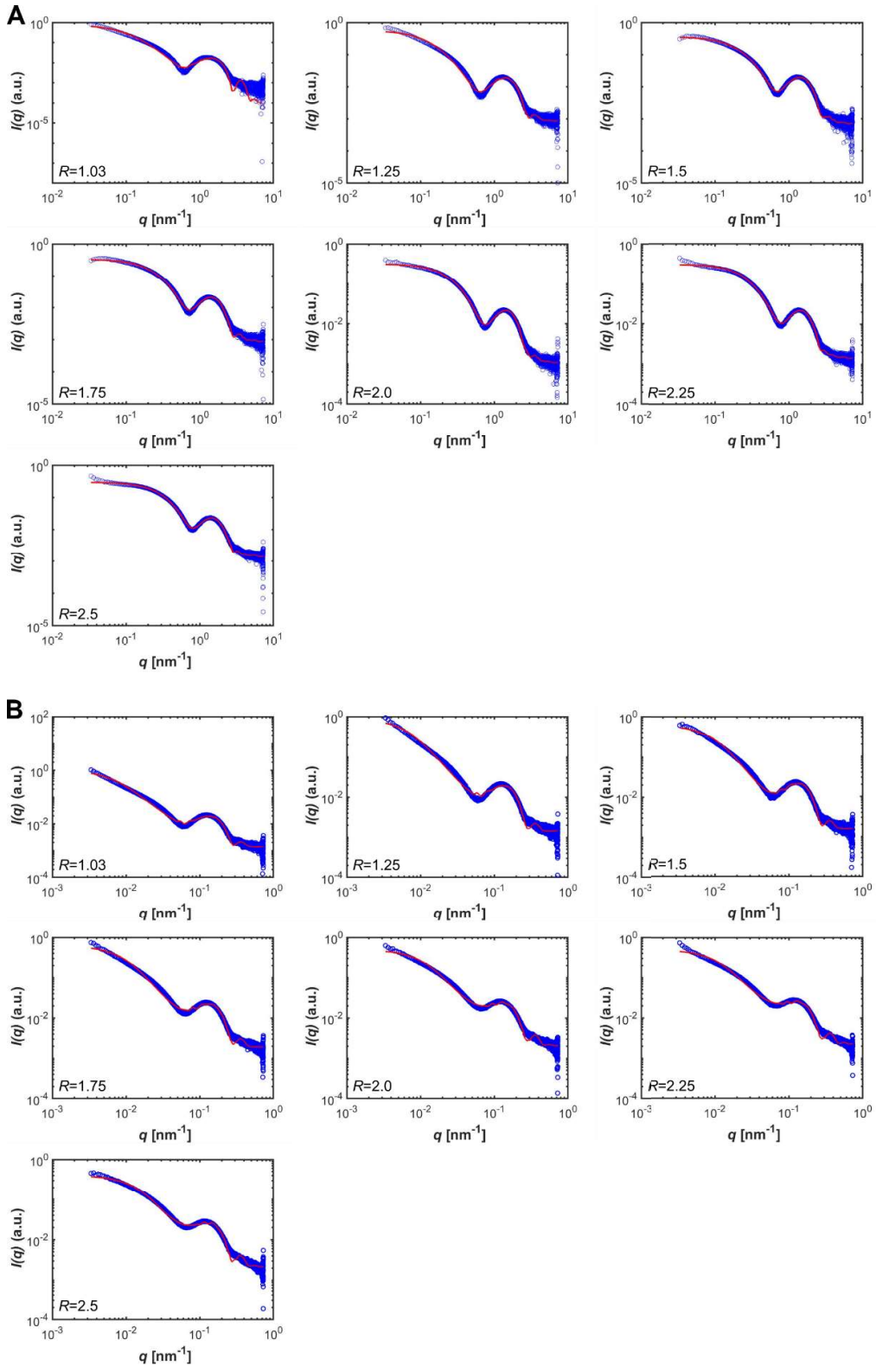


Figure D.1: *Experimental SAXS data (blue dots) for measured mixtures with model fits (red line) of (A) SMALPs and (B) DIBMALPs produced at increasing copolymer/DMPC ratios (R/R^{SOL}) at 30°C.*

Table D.1: *Fit parameters for fitting SAXS data obtained from SMALPs (top) and DIBMALPs (bottom) produced at increasing polymer/DMPC ratios (R/R^{SOL}) at 30°C to a core-shell cylinder model.*

R/R^{SOL} (SMALPs)	1.03	1.25	1.5	1.75	2.0	2.25	2.5
scale	0.27	0.25	0.27	0.29	0.31	0.33	0.36
core radius [Å]	92.6	63.7	41.5	35.8	31.4	28.2	26.8
radial polydispersity	0.5	0.5	0.5	0.5	0.5	0.5	0.5
core length [Å]	23.6	20.2	20.0	20.1	20.1	19.3	18.6
radial shell thickness [Å]	6.6	7.6	6.9	6.9	7.2	7.6	7.9
face shell thickness [Å]	9.4	12.9	13.7	13.7	13.8	14.5	15
SLD core [$Å^{-2}$]	$4.7 \cdot 10^{-8}$	$4.7 \cdot 10^{-8}$	$4.7 \cdot 10^{-8}$	$4.7 \cdot 10^{-8}$	$4.7 \cdot 10^{-8}$	$4.7 \cdot 10^{-8}$	$4.7 \cdot 10^{-8}$
SLD shell [$Å^{-2}$]	$7.98 \cdot 10^{-7}$	$7.97 \cdot 10^{-7}$	$7.97 \cdot 10^{-7}$	$7.97 \cdot 10^{-7}$	$7.97 \cdot 10^{-7}$	$7.97 \cdot 10^{-7}$	$7.975 \cdot 10^{-7}$
SLD solvent [$Å^{-2}$]	$3.30 \cdot 10^{-7}$	$4.11 \cdot 10^{-7}$	$4.20 \cdot 10^{-7}$	$4.18 \cdot 10^{-7}$	4.2 ·t 10^{-7}	$4.38 \cdot 10^{-7}$	$4.52 \cdot 10^{-7}$
incoh. bkg [cm^{-1}]	$8.43 \cdot 10^{-5}$	$8.49 \cdot 10^{-4}$	$6.85 \cdot 10^{-4}$	$8.54 \cdot 10^{-4}$	$1.03 \cdot 10^{-3}$	$1.38 \cdot 10^{-3}$	$1.37 \cdot 10^{-7}$
R/R^{SOL} (DIBMALPs)	1.03	1.25	1.5	1.75	2.0	2.25	2.5
scale	0.25	0.25	0.27	0.30	0.36	0.40	0.40
core radius [Å]	128.3	118.8	88.5	86.1	72.6	71.9	59.1
radial polydispersity	0.5	0.5	0.5	0.5	0.5	0.5	0.5
core length [Å]	21.8	22.1	22.3	23.1	24.7	25.1	24.9
radial shell thickness [Å]	11.4	11.2	9.9	10.4	9.7	9.8	9.2
face shell thickness [Å]	10.8	10.7	10.9	9.9	8.4	7.9	8.3
SLD core [$Å^{-2}$]	$4.7 \cdot 10^{-8}$	$4.7 \cdot 10^{-8}$	$4.7 \cdot 10^{-8}$	$4.7 \cdot 10^{-8}$	$4.7 \cdot 10^{-8}$	$4.7 \cdot 10^{-8}$	$4.7 \cdot 10^{-8}$
SLD shell [$Å^{-2}$]	$8.0 \cdot 10^{-7}$	$8.0 \cdot 10^{-7}$	$8.0 \cdot 10^{-7}$	$8.0 \cdot 10^{-7}$	$8.0 \cdot 10^{-7}$	$8.0 \cdot 10^{-7}$	$8.0 \cdot 10^{-7}$
SLD solvent [$Å^{-2}$]	$3.9 \cdot 10^{-7}$	$3.8 \cdot 10^{-7}$	$3.9 \cdot 10^{-7}$	$3.7 \cdot 10^{-7}$	$3.4 \cdot 10^{-7}$	$3.3 \cdot 10^{-7}$	$3.4 \cdot 10^{-7}$
incoh. bkg [cm^{-1}]	$1.4 \cdot 10^{-3}$	$1.4 \cdot 10^{-3}$	$1.6 \cdot 10^{-3}$	$1.9 \cdot 10^{-3}$	$2.1 \cdot 10^{-3}$	$2.3 \cdot 10^{-3}$	$2.1 \cdot 10^{-3}$

Table D.2: *Fit parameters for fitting SAXS data obtained from SMALPs (top) and DIBMALPs (bottom) produced at decreasing 30-8°C at a polymer/DMPC ratio (R/R^{SOL}) of 1.25 to a core-shell cylinder model.*

T [°C] (SMALPs)	30	27.5	25	22.5	20	17.5	15	12.5	10	8
scale	0.39	0.37	0.38	0.39	0.37	0.36	0.37	0.36	0.35	0.36
core radius [Å]	26.8	29.5	36.9	37.3	37.0	37.2	37.2	37.0	37.2	36.9
radial polydispersity	0.67	0.62	0.45	0.31	0.28	0.28	0.30	0.30	0.30	0.31
core length [Å]	11.7	12.1	12.5	12.9	13.7	13.7	13.7	13.6	14.0	13.7
radial shell thickness [Å]	5.9	6.7	8.4	9.9	10.3	10.2	10.1	10.1	9.9	10.0
face shell thickness [Å]	21.8	21.6	21.4	21.3	20.83	21.0	21.2	21.4	21.2	21.5
SLD core [Å^{-2}]	$4.7 \cdot 10^{-8}$	$4.7 \cdot 10^{-8}$	$4.7 \cdot 10^{-8}$	$4.7 \cdot 10^{-8}$	$4.7 \cdot 10^{-8}$	$4.7 \cdot 10^{-8}$	$4.7 \cdot 10^{-8}$	$4.7 \cdot 10^{-8}$	$4.7 \cdot 10^{-8}$	$4.7 \cdot 10^{-8}$
SLD shell [Å^{-2}]	$8.0 \cdot 10^{-7}$	$8.0 \cdot 10^{-7}$	$8.0 \cdot 10^{-7}$	$8.0 \cdot 10^{-7}$	$8.0 \cdot 10^{-7}$	$8.0 \cdot 10^{-7}$	$8.0 \cdot 10^{-7}$	$8.0 \cdot 10^{-7}$	$8.0 \cdot 10^{-7}$	$8.0 \cdot 10^{-7}$
SLD solvent [Å^{-2}]	$5.9 \cdot 10^{-7}$	$5.9 \cdot 10^{-7}$	$5.9 \cdot 10^{-7}$	$5.9 \cdot 10^{-7}$	$5.9 \cdot 10^{-7}$	$5.8 \cdot 10^{-7}$	$5.8 \cdot 10^{-7}$	$5.8 \cdot 10^{-7}$	$5.6 \cdot 10^{-7}$	$5.7 \cdot 10^{-7}$
incoh. bkg [cm^{-1}]	$4.7 \cdot 10^{-4}$	$7.8 \cdot 10^{-4}$	$6.0 \cdot 10^{-4}$	$3.1 \cdot 10^{-4}$	$5.3 \cdot 10^{-4}$	$3.4 \cdot 10^{-4}$	$8.0 \cdot 10^{-4}$	$5.2 \cdot 10^{-4}$	$6.0 \cdot 10^{-4}$	$6.7 \cdot 10^{-4}$
T [°C] (DIBMALPs)	30	27.5	25	22.5	20	17.5	15	12.5	10	8
scale	0.79	0.81	0.88	0.86	0.83	0.90	0.94	0.94	1.09	1.11
core radius [Å]	196.57	247.25	250.11	89.30	95.27	91.86	82.30	80.73	80.04	75.82
radial polydispersity	0.37	0.27	0.26	0.58	0.53	0.44	0.38	0.38	0.38	0.46
core length [Å]	7.87	7.90	7.49	7.93	8.11	7.97	7.84	7.81	7.42	7.30
radial shell thickness [Å]	27.51	28.89	29.32	21.59	21.70	20.7	19.53	19.34	19.35	19.69
face shell thickness [Å]	22.99	23.47	23.88	23.92	23.97	24.21	24.36	24.37	24.51	24.58
SLD core [Å^{-2}]	$4.7 \cdot 10^{-8}$	$4.7 \cdot 10^{-8}$	$4.7 \cdot 10^{-8}$	$4.7 \cdot 10^{-8}$	$4.7 \cdot 10^{-8}$	$4.7 \cdot 10^{-8}$	$4.7 \cdot 10^{-8}$	$4.7 \cdot 10^{-8}$	$4.7 \cdot 10^{-8}$	$4.7 \cdot 10^{-8}$
SLD shell [Å^{-2}]	$8.0 \cdot 10^{-7}$	$8.0 \cdot 10^{-7}$	$8.0 \cdot 10^{-7}$	$8.0 \cdot 10^{-7}$	$8.0 \cdot 10^{-7}$	$8.0 \cdot 10^{-7}$	$8.0 \cdot 10^{-7}$	$8.0 \cdot 10^{-7}$	$8.0 \cdot 10^{-7}$	$8.0 \cdot 10^{-7}$
SLD solvent [Å^{-2}]	$6.9 \cdot 10^{-7}$	$6.8 \cdot 10^{-7}$	$6.8 \cdot 10^{-7}$	$6.8 \cdot 10^{-7}$	$6.8 \cdot 10^{-7}$	$6.8 \cdot 10^{-7}$	$6.8 \cdot 10^{-7}$	$6.8 \cdot 10^{-7}$	$6.8 \cdot 10^{-7}$	$6.8 \cdot 10^{-7}$
incoh. bkg [cm^{-1}]	$1.1 \cdot 10^{-3}$	$1.6 \cdot 10^{-3}$	$9.3 \cdot 10^{-4}$	$9.4 \cdot 10^{-4}$	$8.3 \cdot 10^{-4}$	$1.1 \cdot 10^{-3}$	$9.6 \cdot 10^{-4}$	$6.9 \cdot 10^{-4}$	$1.0 \cdot 10^{-3}$	$1.1 \cdot 10^{-3}$

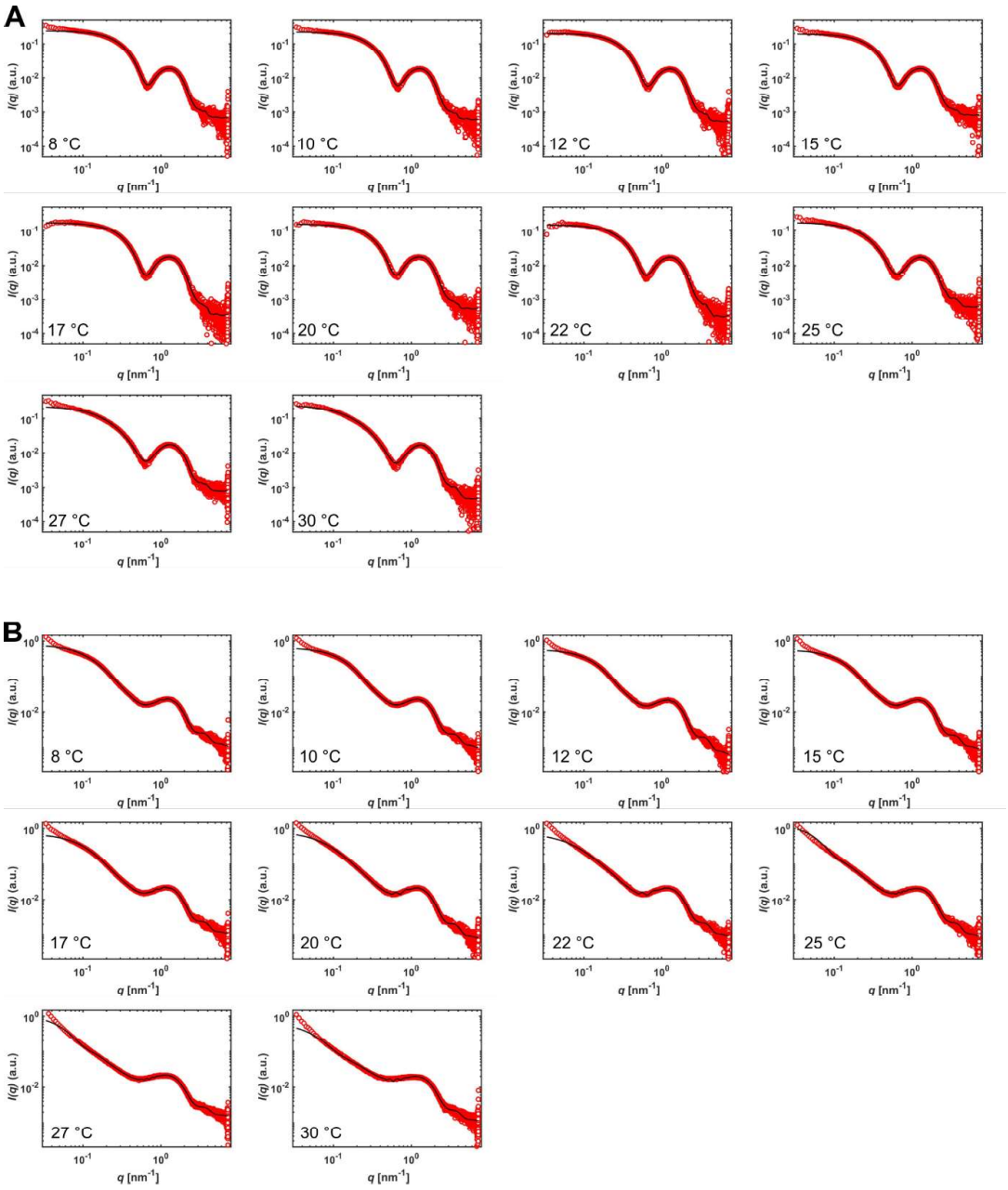


Figure D.2: *Experimental SAXS data (red dots) and fits (black line) for (A) SMALPs and (B) DIBMALPs produced at* $R/R^{SOL} = 1.25$*, measured at 8–30°C.*

Acknowledgements

First of all, I would like to thank Prof. Dr. Frank Schreiber, the head of the group, for the opportunity to work on this interesting project. Thank you for all your trust in my abilities and for giving me plenty of freedom while always contributing with good advice.

Second, I want to thank my first supervisor PD Dr. Fajun Zhang. Your passion for this topic (as well as other topics) was very inspiring and I appreciate every conversation we had. Thank you for your guidance through the whole time. I also enjoyed playing football with you a lot.

Third, I want to thank Prof. Dr. Roland Roth, who kindly agreed to be my second reviewer and part of my defense committee.

Then, I would like to express my sincere gratitude to former and current colleagues, who helped me not only in the times as a PhD student, but also as a bachelor and master student in this group. These include especially Dr. Olga Matsarskaia, Dr. Benedikt Sohmen, Dr. Stefano Da Vela, Dr. Madeleine Fries, Anita Girelli, Dr. Christian Beck, and Dr. Martin Hodas. Concerning this matter, I want to particularly thank Dr. Madeleine Fries and Anita Girelli for all the scientific discussions in these years and their input.

I am also grateful for all the great work of the students who worked at least partially under my supervision, namely Aafiya Idrees, Lennart Rieger, Christian Simo, Yannick Palmowski, Cara Buchholz, Maximilian Senft, Alexander Krauth, Resul Akyüz, Famke Bäuerle, Dragana Galevska, and Pasupathi Rajendran. Thanks for your great work, this thesis truly benefited from it.

Furthermore, I thank Dr. Georg Zocher and Prof. Dr. Thilo Stehle for the productive collaboration during the last years. Similarly, I want to thank Dr. Rodrigo Cuevas Arenas and Prof. Dr. Ana García-Sáez for their trust and collaboration on a completely new topic for me.

My sincere gratitude goes to all scientific staff members I have worked with at neutron or X-ray facilities, whose support has been invalubale. These include in particular Dr. Aurel Radulescu, Dr. Ralf Schweins, Dr. Vitaly Pipich, Dr. Baohu Wu, Dr. Christian Lang, Dr. Tilo Seydel, Dr. Markus Appel, Dr. Orsolya Czakkel, Dr. Olga Matsarskaia, Dr. Alexey Kikhney, and Dr. Stefano da Vela.

I thank Bernd Hofferberth and Ralf Zenke for their technical support and their help whenever needed.

Next, I immensely appreciate the feedback from all of my proofreaders: Dr. Madeleine Fries, Maximilian Senft, Furio Surfaro, Hadra Banks Machado, Anita Girelli, Sebastian Retzbach, Cara Buchholz, Lara Reichart, Dr. Nafisa Begam, Ingrid Dax, Frederik Unger, Christoph Theurer, Julian Hausch, Michael Zimmermann, Michael Maier, and Nina Conzelmann. Thank you a lot for your time and your work, which you put into this dissertation, helping to improve and finalize it.

This work profited a lot from the help and the environment of friendly and supportive people. I am immensely thankful for everything they have done and want to acknowledge their support. I also enjoyed the group activities in which I participated a lot.

Last but not least, I want to thank my family and friends for their support during the past years.